Dissociation of Oxygen Molecules on the Al(111) Surface

Diplom-Chemiker
Jörg Behler

Von der Fakultät II-Mathematik und Naturwissenschaften
der Technischen Universität Berlin
zur Erlangung des akademischen Grades
DOCTOR RERUM NATURALIUM
genehmigte Dissertation

Promotionsausschuss:

Vorsitzender: Prof. Dr. Christian Thomsen
Berichter: Prof. Dr. Eckehard Schöll
Berichter: Prof. Dr. Matthias Scheffler

Tag der wissenschaftlichen Aussprache: 24.11.2004

Berlin 2004
D 83

Abstract

The dissociation of oxygen molecules on the Al(111) surface is an important model reaction for the adsorption of simple molecules on metal surfaces. Numerous experiments have shown that the initial sticking probability of thermal oxygen molecules impinging onto Al(111) is only about one percent. An obvious explanation would be the existence of energy barriers along the dissociation pathway that could only be overcome by molecules of higher energy. In fact, sticking coefficients of almost unity have been measured at higher kinetic energies. However, previous density-functional theory (DFT) studies on this system did not yield sizeable energy barriers.

To investigate this problem the well established "divide and conquer" approach is employed. First, the adiabatic full-potential six-dimensional potential-energy surface (PES) taking into account all molecular degrees of freedom is calculated on a dense grid using DFT. Subsequent presentation of the PES by a neural network technique enables to perform extensive molecular dynamics runs and thereby to take reliable statistical averages. A sticking coefficient close to unity is obtained independent of the kinetic energy, in agreement with the conclusion from preceding DFT studies, but in strong disagreement with experimental data.

Concluding that essential physics is missing in the adiabatic description of the dissociation process, the standard approach is extended by implementing a spin-constrained DFT method into the DMol^3 code. This approach is an improvement over standard fixed-spin-moment calculations as it allows to keep the spin-triplet located on the oxygen molecule while keeping the metal surface in a singlet state. With this new tool the possible role of non-adiabatic effects during the dissociation event is explored, which could arise from a low transition probability from the initial triplet state of the gas phase O_2 molecule to the singlet ground state of the adsorbed atoms. The resulting triplet-constrained PES exhibits energy barriers in most entrance channels towards dissociation, and molecular dynamics runs confined to this diabatic PES yield a significantly reduced sticking coefficient. Non-adiabatic effects in form of a non-instantaneous spin-flip during the dissociation process could therefore well account for the low sticking probability of thermal oxygen molecules. A quantitative determination of the sticking curve is, however, prevented by the inaccuracies in the energetics provided by present-day DFT functionals.

Zusammenfassung

Die Dissoziation von Sauerstoffmolekülen auf der Al(111) Oberfläche ist eine wichtige Modellreaktion für die Adsorption einfacher Moleküle auf Metalloberflächen. Zahlreiche Experimente haben gezeigt, dass die anfängliche Haftwahrscheinlichkeit thermischer Sauerstoffmoleküle beim Auftreffen auf die Al(111) Oberfläche nur etwa ein Prozent beträgt. Eine einfache Erklärung wäre die Existenz von Energiebarrieren auf dem Dissoziationsweg, die nur von Molekülen höherer kinetischer Energie überwunden werden können. Tatsächlich wurden für höhere kinetische Energien Haftkoeffizienten nahe eins gemessen. Im Gegensatz dazu ergaben bisherige Untersuchungen dieses Systems mit Dichtefunktional-Theorie (DFT) keine nennenswerten Energiebarrieren.

Um dieses Problem zu untersuchen wird der etablierte „divide and conquer" Ansatz verwendet. Zuerst wird dazu unter Berücksichtigung aller molekularen Freiheitsgrade die sechsdimensionale Energiehyperfläche (PES) mit Hilfe von DFT auf einem dichten Gitter von Punkten berechnet. Die anschließende Darstellung dieser PES durch ein Neuronales Netz ermöglicht die Durchführung umfangreicher, statistisch verlässlicher Molekulardynamik Simulationen. Unabhängig von der kinetischen Energie wird ein Haftkoeffizient von etwa eins erhalten, der gut mit Folgerungen aus früheren DFT Studien übereinstimmt, aber im Widerspruch zum Experiment steht.

Da in der adiabatischen Beschreibung des Dissoziationsprozesses anscheinend wesentliche Physik nicht berücksichtigt wird, wird dieses Standardverfahren durch die Implementierung einer Randbedingung für den Spin in das DMol^3 Programm erweitert. Dies ist eine Verbesserung des üblichen „fixed-spin-moment" Verfahrens, die ermöglicht, den Triplett-Spin auf dem Sauerstoffmolekül zu lokalisieren, während die Metalloberfläche im Singulett-Zustand bleibt. Mit diesem neuen Verfahren wird die mögliche Rolle nicht-adiabatischer Effekte während des Dissoziationsvorgangs untersucht. Diese Effekte können auftreten, wenn die Übergangswahrscheinlichkeit vom anfänglichen Triplett-Zustand des O_2 Moleküls in der Gasphase zum Singulett-Zustand der adsorbierten Atome klein ist. Die resultierende Triplett-PES weist Energiebarrieren in den meisten Dissoziationskanälen auf. Aus diesem Grund ergeben auf diese diabatische PES beschränkte Molekulardynamik Simulationen einen deutlich reduzierten Haftkoeffizienten. Die niedrige Haftwahrscheinlichkeit thermischer Sauerstoffmoleküle könnte daher durch nicht-adiabatische Effekte in Form eines verzögerten Spin-Umklapp-Prozesses erklärt werden. Eine quantitative Bestimmung der Haftkurve ist allerdings aufgrund der unzureichenden Genauigkeit gegenwärtiger DFT Funktionale nicht möglich.

For Alexandra
and my parents

One thing I have learned in a long life:
that all our science, measured against reality,
is primitive and childlike
- and yet it is the most precious thing we have.

Albert Einstein

Contents

List of Figures

List of Tables

Chapter 1

Introduction

In recent years the interaction of oxygen molecules with metal surfaces has gained a central role in surface science due to its fundamental importance for many technologically relevant processes like heterogeneous catalysis and corrosion. Only a detailed investigation of the underlying elementary steps at an atomic scale, e.g. physisorption, chemisorption, dissociation, diffusion, and desorption, can yield a deeper understanding, which at present is still very limited even for the most basic process, namely the interaction of an individual molecule with a surface. For these studies "simple" and well-defined model systems are required, which allow to address all aspects of the adsorption event in a concerted effort by experiment and theory and help to establish a firm basis for further investigations.

One such, and maybe even the most important, model system for the interaction of oxygen molecules with metal surfaces is the dissociative adsorption of oxygen on the single-crystal Al(111) surface. This system is appealing for both, theory and experiment, since aluminium has a rather simple electronic structure and because the low-index Al(111) surface offers a comparably simple geometric arrangement. In the past 30 years a wealth of experimental data has been accumulated using essentially all available techniques, and also numerous theoretical studies of many aspects of this interaction have been performed. Yet, in spite of these efforts still several key aspects of this apparently simple system have not been understood. Two prominent examples are the adsorption mechanism and the sticking probability, which is the ratio of successful sticking events to the total number of molecule-surface collisions. Concerning the mechanism, several contradictory models like abstraction [1, 2], dissociative chemisorption [3] and the so-called "hot atom" motion [4, 5] have been proposed mainly based on different interpretations of scanning tunnelling microscopy (STM) results.

Both quantities are entangled and one can view the sticking probability as maybe the more basic one. It is typically determined by the very first interaction of the molecule with the surface, and only if this is understood, a proper discussion about the ensuing adsorption mechanism can be attempted. With respect to molecular sticking, it has been unambiguously shown in many independent experiments that the sticking probability of thermal oxygen molecules is only about 1 % [6–12]. Furthermore, using a molecular beam experiment [9] it was found that the sticking probability increases with translational kinetic energy[1] and reaches a saturation value of about 90 % only for kinetic energies higher than 0.5 eV. A likely explanation for this finding would be the existence of energy barriers towards dissociation that cannot be overcome by low energy, thermal molecules. Inspired by these experiments theoretical studies addressed the oxygen-aluminium interaction by calculating parts of the multi-dimensional potential-energy surface (PES), which in principle should contain all information on the energy barriers. For this purpose usually density-functional theory (DFT) [13, 14] is used, which is presently established as a standard tool for large systems, in particular in theoretical surface science, often offering a reliable compromise between accuracy and efficiency. The result, however, was very surprising in that basically no energy barriers could be identified, which could account for the low sticking probability. In contrast to experiment, the sticking probability was accordingly expected to be very high and independent of the kinetic energy of the oxygen molecule. This discrepancy between experiment and theory reflects a lack of understanding of this elementary process that is very disturbing, and affects also further theoretical studies on other, more involved aspects of the adsorption process like the dissociation mechanism. Additionally, consequences for similar systems are completely uncertain as long as the origin of this discrepancy has not been found.

Consequently, the main objective of this thesis is to gain a deeper understanding of the dissociation process and to identify the origin of the low sticking probability of thermal oxygen molecules. Several scenarios are possible: So far, only parts of the PES of the oxygen dissociation on Al(111) have been calculated for a limited number of molecular orientations in rather small surface unit cells. Additionally, all conclusions about the sticking probability have been drawn from a mere inspection of the PES without an explicit calculation of the sticking curve from first-principles, i.e. all dynamic aspects of the dissociation event have hitherto not been addressed. It might well be that slow molecules are steered systematically to non-dissociative pathways by the multi-dimensional surface potential. This can only be taken into account by molecular dynamics (MD) simulations based on this PES, which allow to explicitly follow the molecular trajectories by solving the classical equations of motion. That a full treatment of the dynamics can be important for understanding sticking has indeed been shown e.g. for the H_2 dissociation at metal surfaces [15–17]. Another approximation that is often made is the neglect of the mobility of substrate atoms, which has been shown to be valid for example for the adsorption of H_2 on Pd(100) [18], while the mobility is important for H_2 on Si(100) [19]. For O_2 on Al(111) the applicability of this frozen surface approximation cannot be taken for granted considering the almost equal masses of O_2 and aluminium atoms. Besides, all calculations for this

[1] Since the present work is mainly concerned with the determination of the sticking probability as a function of the translational kinetic energy of the molecules towards the surface, the term “kinetic energy” in this work generally refers to translational energy. It has also been shown in experiment that the sticking probability increases slightly for vibrationally excited molecules [9].

system so far have been based on density-functional theory, which is often accurate enough, but also has some prominent failures due to the only approximate treatment of exchange and correlation in its current implementations. Finally, the adiabatic nature of the PES *per se* has been questioned for this system [9, 20–24]. The adiabatic description of the dissociation process is equivalent to a molecular trajectory on the Born-Oppenheimer PES [25], assuming an instantaneous relaxation of the electronic structure to its ground state with the changing nuclear coordinates. Due to the dynamic nature of the adsorption process, which necessarily gives rise to a competition of time scales of nuclear and electronic motion, non-adiabatic effects might play an important role. According to this model, the oxygen molecule, which in the gas phase has a spin-triplet ground state, could be confined to the initial diabatic neutral, spin-triplet PES for some time during its approach to the surface. In contrast to the hitherto studied adiabatic potential-energy surface, this triplet PES might show energy barriers, which could provide an explanation for the low sticking probability of thermal oxygen molecules.

In the present work most of these aspects have been addressed to investigate the origin of the low sticking probability of thermal oxygen molecules. First, to establish a firm reference, the adiabatic potential-energy surface has been calculated as accurately as possible and far more detailed than before. The almost complete absence of sizeable energy barriers towards dissociation could be confirmed. Using a neural network [26, 27] interpolation technique a continuous representation of this PES could be obtained, which allowed to calculate a statistically significant number of MD trajectories and in turn a sticking curve based on first-principles for this system for the first time. The sticking probability was found to be about unity, independent of the kinetic energy, in contrast to experiment. Consequently, dynamical steering effects can be excluded as origin of the low sticking probability. Tests including the substrate motion via direct *ab initio* MD have also eliminated the mobility of substrate atoms as a possible explanation. Substrate motion only becomes sizeable and relevant at a later stage of the adsorption process, when the oxygen has come much closer to the surface. The description of the system by the approximate exchange-correlation functional in DFT has been assessed by reference calculations on the free oxygen molecule, bulk aluminium and the clean and oxygen-covered Al(111) surface. Comparison of the obtained structures and energetics with experimental data shows a good agreement, an exception being the well-known overestimation of the binding energy of the free oxygen molecule. Yet, this should not sensitively affect the sticking probability, since the PES represents differences of DFT energies and the errors are expected to cancel. Closer to the surface a strong interaction with the aluminium sets in, the electronic structure becomes very different from the free molecule and the well understood reasons for the overbinding in O_2 do not apply anymore. This seems confirmed by our calculations applying different exchange-correlation functionals, which yield basically the same sticking curve, while the binding energy of the free oxygen molecule shows a sizeable functional dependence. However, one should stress that the small remaining uncertainty can only be ruled out by an improved treatment of exchange and correlation being more accurate than present-day functionals used in DFT, which is beyond the scope of this work.

Having thus shown that the adiabatic PES is most probably not able to explain the experimental sticking curve, a model has been developed to assess the possible role of non-adiabatic effects. The basic idea is that the molecule might continue approaching the metal surface on the initial diabatic neutral spin-triplet PES, even when the adiabatic ground state becomes energetically more favorable. This idea is not new, but while previous studies mainly focussed on charge transfer from the surface to the molecule as source of non-adiabaticity [21, 28, 29], in this work the molecular spin has a central role. This comes about, since the free oxygen molecule has a triplet ground state, whereas the adsorbed atoms are in a singlet state. In the suggested two-state model the molecule approaches the surface on the diabatic, neutral spin-triplet PES and a relaxation to the adiabatic ground state is assumed to be inhibited as long as the coupling between the diabatic triplet and singlet PESs is weak. This should be a good approximation beyond a certain distance from the surface, before the coupling to other diabatic PESs (e.g. for charged molecules) starts to play a role. To be able to account for the low sticking probability in this non-adiabatic model, the neutral triplet PES necessarily has to exhibit energy barriers towards dissociation. Validating the possible existence of such energy barriers requires the detailed calculation of this diabatic PES, for which before the beginning of this thesis appropriate methods were hardly (or only conceptionally) available. A complete description of the dissociation process then could be accomplished by including further diabatic PESs. A spin-triplet could be imposed on the system by using the fixed-spin-moment approach [30–33]. Unfortunately, tests showed that at small molecule-surface separations the majority of the spin is transferred to the aluminium surface. This does not correspond to the spin-triplet PES we want to describe, in which the molecule is in a triplet state while the surface is in a singlet state for all configurations. Following an early concept suggested by Dederichs *et al.* [34], a very general constrained density-functional method has been developed and tested in the course of this project, which in principle allows for the calculation of diabatic potential-energy surfaces of arbitrary charge and spin states of the oxygen molecule within the limitations provided by DFT. This constrained DFT approach has been applied to calculate the neutral spin-triplet potential-energy surface using two different exchange-correlation functionals to evaluate the reliability of the results. Sizeable energy barriers of up to almost 1 eV have been found, and subsequent MD simulations yielded a significantly reduced sticking probability for kinetic energies lower than 0.5 eV in excellent agreement with experiment. This clearly shows that in principle non-adiabatic effects could indeed explain the experimental findings. However, the absolute height of the energy barriers shows some dependence on the chosen exchange-correlation functional and for one functional a few barrier-free dissociation channels exist, which has substantial effects on the calculated sticking curve. Due to this uncertainty a quantitative agreement with experiment could not be obtained, and further calculations building on the results of this thesis, but employing an improved description of exchange and correlation would be desirable.

The computed sticking curves for molecular motion confined to either the adiabatic or the spin-triplet diabatic PES represent extreme cases with an immediate and an infinitely slow relaxation of the electronic structure to the adiabatic ground state. The real dissociation process likely involves transitions between the triplet and further diabatic PESs. From the idea of a hindered spin-relaxation, the spin-singlet PES appears as a most appropriate alternative diabatic PES. While the developed constrained DFT method would in principle allow to compute this singlet PES, the singlet energy obtained from DFT itself is unfortunately not accurate enough to provide a reliable description of the singlet PES due to a well known deficiency of current jellium-based exchange-correlation functionals. Consequently, the crossing of the singlet and the triplet PES can be determined only in an approximate way, which does not allow to calculate transition matrix elements quantitatively. So far, therefore transitions between the diabatic states have not been included in our model. Still, it is very likely that the reduced sticking probability of thermal molecules found in the triplet MD is untouched by these transitions, because the onset of the energy barriers is rather far away from the surface, in a region where the coupling between the triplet PES and other diabatic PESs is still very small.

The main conclusion of the present work is therefore that non-adiabatic effects could well be able to describe the low sticking probability of thermal oxygen molecules at Al(111), while other remaining explanations like dynamic effects or substrate mobility could be ruled out. The framework for the calculation of diabatic PESs has been laid out, and subsequent work will have to focus on an improved description of exchange and correlation to conclusively settle the prevailing discrepancy with the experimental data by a quantitative calculation of the sticking curve based on diabatic energy surfaces.

—

The present work is organized as follows: In Chapter 2 the state of current research on the interaction of oxygen molecules with the Al(111) surface is summarized showing that non-adiabatic effects, which are explained in Chapter 3, may play an important role for this system. The "divide and conquer" approach for the calculation of sticking curves employed in this work is presented in Chapter 4. The required potential-energy surfaces are calculated using density-functional theory, the basics of which are given in Chapter 5, followed by a description of its implementation in the DMol^3 code in Chapter 6. The neural network technique used for the interpolation of the potential-energy surface is briefly summarized in Chapter 7 together with its application in molecular dynamics simulations in Chapter 8. Before these methods are applied to the oxygen dissociation on Al(111) the description of oxygen and aluminium provided by density-functional theory is tested by calculations for the free oxygen molecule, bulk aluminium, and clean and oxygen-covered Al(111) surfaces in

Chapter 9. The calculation of the adiabatic potential-energy surface for the oxygen dissociation on Al(111), its interpolation and the resulting sticking curve are presented in Chapter 10, completed by a study of the role of surface mobility. The model for the inclusion of non-adiabatic effects is introduced in Chapter 11. It requires the development of a constrained DFT formalism, which is explained in detail in Chapter 12 and has been applied to the calculation of the sticking curve based on the spin-triplet potential-energy surface reported in Chapter 13. The applicability to other diabatic potential-energy surfaces is critically reviewed in Chapter 14, and the effect of transitions between these diabatic energy surfaces is discussed in Chapter 15. Finally, some aspects of the adsorption mechanism are investigated in Chapter 16. The results are summarized in Chapter 17 and perspectives for further studies are given. Appendix A contains the benchmark calculations that have been performed to identify a suitable DFT code, whose accuracy is illustrated by the convergence tests in Appendix B. Finally, Appendix C gives additional information on the mapping of the potential-energy surfaces.

Chapter 2

Oxygen on Al(111): Status of Current Research

One of the most important model reactions for the interaction of oxygen molecules with metal surfaces is the dissociative adsorption of oxygen on the Al(111) surface. In the past 30 years a large number of experimental as well as theoretical studies has been carried out for this system. Aluminium is an important construction material, which is very light and has the interesting property that it is protected from corrosion by the formation of a thin oxide layer, which is only a few atomic layers thick [35] and can be generated in a controlled way by exposing aluminium to a highly oxidizing environment. Aluminium oxide, Al_2O_3, is abundant on earth and forms an important support for catalysts in chemical industry. Therefore, the interest in its structural and electronic properties is very high, and soon the interaction of oxygen with aluminium became a prototype system for studying metal oxide formation.

Of all low index surfaces of aluminium, the (111) surface is energetically most favorable [36, 37]. Its structure is shown in Fig. 2.1. The atoms are arranged in a face centered cubic (fcc) lattice with ABCABC stacking along the (111) direction and an approximate interlayer spacing of 2.3 Å. Neither the clean nor the oxygen-covered Al(111) surface shows any reconstruction making this system a good candidate to gain a deeper understanding of the interaction of oxygen with metals. From a theoretical point of view the Al(111) surface is very appealing, because aluminium is a simple *sp* band nearly-free electron metal and may be well described even by the jellium approximation. Therefore, understanding the interaction of oxygen molecules with the Al(111) surface could establish a valuable reference system for the adsorption on more complex metals, higher index surfaces or pre-covered surfaces like in transition metal catalyzed processes.

The investigation of the dissociative adsorption of oxygen on the Al(111) surface started in the 1970's [6], and in the past decades almost every available experimental technique has been used to gain insight into the elementary steps of this process [38]. Surprisingly, the experimental characterization of the phases formed by adsorbed oxygen turned out to be very difficult, which has several reasons. First of all, the Al(111)

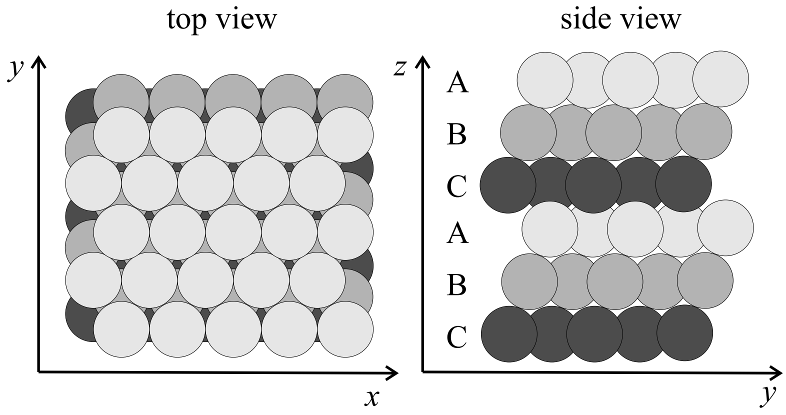

Figure 2.1: The Al(111) surface.

surface shows a strong affinity to oxygen and other elements making the preparation of well defined clean surfaces with low defect and impurity concentrations and reproducible experimental results very hard. To obtain a clean Al(111) surface many repeated cycles of sputtering and annealing at about 700 K are required [10, 39]. It has been shown by Brune *et al.* [5, 8] by the analysis of scanning tunnelling microscope (STM) images that even in the absence of signals in Auger electron spectroscopy (AES), which indicates a "clean" surface, still a remarkable amount of impurities can be present. Additionally, experiments are complicated by the coverage-dependent complex coexistence of different oxygen species like isolated atoms, islands of chemisorbed atoms and oxide grains. Accordingly, the first experiments focussed on structural aspects, i.e. the determination of the preferred adsorption sites. Low energy electron diffraction (LEED) investigations have shown [40, 41] that the (1×1) overlayer structure of the clean Al(111) surface is preserved in the initial stages of oxygen adsorption, but the intensity of the diffraction spots increases. From these data it was concluded that well ordered islands of oxygen atoms are formed, which was also concluded from X-ray photoelectron spectroscopy (XPS) [42, 43]. At increasing oxygen coverage the LEED pattern disappears, because an amorphous oxide is formed [40, 44]. To identify the adsorption site of oxygen in the initial adsorption stage high-resolution electron energy loss spectroscopy (HREELS), AES and XPS have been used. Two different HREELS peaks were found and the existence of an oxygen double layer with oxygen atoms being adsorbed in the fcc hollow sites and subsurface sites was concluded [45–48]. The existence of a subsurface site was also supported by work function measurements, which yielded only a small increase and in some cases even a decrease in the work function upon adsorption [6, 7, 42, 49]. On the other hand, the existence of subsurface oxygen was excluded by medium energy ion scattering (MEIS) [49, 50] and negative direct recoil spectroscopy [51]. In spite of these contradictory results it was commonly agreed that at 300 K the oxygen islands slowly start to transform into the oxide, which can be identified by a characteristic vibrational mode at 820-865 cm^{-1} in HREELS spectra [39]. This process can be accelerated by increasing the surface temperature.

A new era of experimental studies began when the first STM images of the oxygen-covered Al(111) surface became available in 1992 [5, 8, 52]. Atomically resolved images by Brune *et al.* showed single isolated oxygen atoms with an average distance of about 80 Å at very low oxygen coverages (θ_O=0.0014 monolayers), when the surface was at room temperature in ultra high vacuum (UHV). At increased oxygen exposure small islands of chemisorbed oxygen start to form, confirming the attractive interaction between the oxygen atoms as had been earlier found by LEED, and at a coverage of about 0.2 monolayers (ML) the first oxide nuclei form at the borders of the islands, i.e. long before a coverage of 1 ML has been reached. By comparison of STM images with theoretical results it was found that the STM images might well be explained without referring to subsurface oxygen atoms [8]. This very detailed information stimulated further experimental work and a closer investigation of the existing HREELS and XPS data. Finally, the HREELS modes were reassigned to on-surface chemisorbed oxygen atoms in different local environments [53], i.e. at the interior and the perimeter of islands. By a close examination of oxygen 1s XPS spectra and comparison to Hartree-Fock cluster calculations also the XPS data could be reassigned to these species [54], and the postulated subsurface oxygen in the early adsorption stage was abandoned. The reason for this long standing discussion was identified as the immobility of the oxygen atoms at room temperature, which inhibits the island growth by oxygen diffusion on the surface. Consequently, an exceptionally high ratio of oxygen atoms is located at the borders of small islands, resulting in unexpectedly strong peak intensities of this species in XPS and HREELS. Now it is commonly agreed that oxygen chemisorbs at the fcc site both experimentally [55] and theoretically [4, 56]. The determined distance of the oxygen atoms in the fcc sites from the surface atoms varies strongly with experiment, but the most accepted layer distance is about 0.7 Å above the surface as determined by LEED [57, 58], normal incidence standing X-ray wavefield absorption (NISXW) [35] and surface extended X-ray absorption fine structure (SEXAFS) [44, 59]. This has also been confirmed by density-functional calculations [4, 56, 60].

Having established the structure of the initial on-surface adsorption phase formed on Al(111), the interest turned to the dynamics of the adsorption process. This was again initiated by the STM images of Brune *et al.* [5, 8, 52]. By comparing images taken at different surface temperatures they showed that the immobility of the chemisorbed oxygen atoms at room temperature is caused by a diffusion barrier of about 1 eV. Thus, to explain the large separation of the isolated oxygen atoms at low coverages, they postulated a “hot atom” (also called “hot dimer” or “high transient mobility”) mechanism, in which the excess energy freed during adsorption is transferred into a transient mobility of the oxygen atoms along the surface. Due to the inability to dissipate the energy gained on adsorption instantaneously, this mobility was expected to explain the large distance between the atoms. The likelihood of this mechanism was investigated theoretically employing molecular dynamics simulations based on

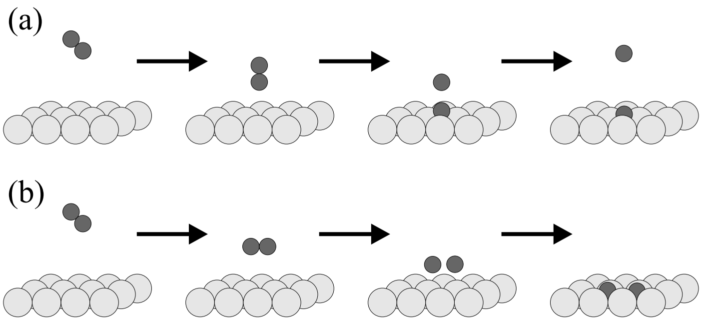

Figure 2.2: Models proposed for the adsorption mechanism of oxygen on Al(111). In (a) the abstraction mechanism is shown, in which the molecule is steered towards a perpendicular orientation with respect to the surface. This leads to an adsorption of the atom being closer to the surface while the second atom is reflected back into to gas phase as a neutral atom. (b) is the "normal" dissociative chemisorption, which is the consequence of a parallel approach to the surface. In this case both atoms are adsorbed close to each other on the surface.

model potentials [61, 62]. They showed that the mechanism suggested by Brune *et al.* is not able to explain the atomic separations, since the strong corrugation of the surface soon leads to a randomization of the diffusion yielding a much smaller average distance. Results from Monte Carlo simulations, which aimed to reproduce the distribution of oxygen atoms on the surface, are contradictory in that some simulations are compatible to the hot atom mechanism [63, 64] while others suggest the dominance of different mechanisms [65] like abstraction or "normal" dissociative chemisorption. Both mechanisms are shown schematically in Fig. 2.2. In the abstraction mechanism [66] the approaching molecule is steered into a perpendicular orientation to the surface. Then the atom being closer to the surface adsorbs while the second atom is ejected back into the gas phase [1, 20, 61]. This process is energetically allowed, because the adsorption energy of a single oxygen atom exceeds the O_2 binding energy by about 1-2 eV, which has been obtained from density-functional theory [4, 67]. A variation of the abstraction mechanism is the "cannon-ball" mechanism, in which the ejected atom does not possess a kinetic energy component perpendicular to the surface high enough to escape into the gas phase. Still, due to its high kinetic energy, it is able to fly over the surface at a larger distance where the potential-energy surface corrugation is small, and finally it is adsorbed far away from the original impact site. Consequently, the trajectories of both atoms are very different, in contrast to the "hot atom" mechanism, in which the adsorption energy is transferred into kinetic energy of both atoms. On the other hand, in the "normal" dissociative chemisorption mechanism the approaching oxygen molecule is steered into a parallel orientation towards the surface and both atoms adsorb close to each other.

In recent years there have also been several experiments questioning the validity of the "hot atom" mechanism. Schmid *et al.* [3] performed STM studies under the same conditions (300 K) as Brune *et al.*, but interpreted the images as pairs of adsorbed oxygen atoms. As the two oxygen atoms of the pairs are separated by only 1 to 3 lattice constants they doubted a high transient mobility. They also excluded the abstraction mechanism by their interpretation of the STM features as dimers. In return the validity of these statements was questioned by Binetti *et al.* [1, 68] and Komrowski *et al.* [2] by the detection of single oxygen atoms ejecting from the Al(111) surface by laser spectroscopy, thus supporting the abstraction model. Additionally, Binetti *et al.* [1, 68] and Komrowski *et al.* [2] performed further STM experiments. In order to investigate the energy dependence of the absorption mechanism they used a molecular beam of defined kinetic energy to deposit the oxygen molecules. At low kinetic energies they found mainly isolated oxygen atoms and concluded that the abstraction mechanism dominates, while at a kinetic energy of 0.5 eV the ratio of abstraction to normal dissociative chemisorption becomes unity. The identification of the depressions in the STM as single oxygen atoms by Brune *et al.* was confirmed by illustrating that the apparently elongated shape attributed to dimers by Schmid *et al.* [3] could in fact be a snapshot of a continuously changing shape. At present these contradictory interpretations of the STM data have not been resolved and conclusive theoretical investigations of the adsorption mechanism based on first-principles do not exist.

Another fundamental property of the oxygen-aluminium system is the initial sticking probability of oxygen molecules impinging on the clean Al(111) surface. The initial sticking coefficient S_0 is defined as the ratio of successful adsorption events to the total number of molecule-surface collisions on a clean surface. It has been measured for the first time in 1977 by Gartland to be about 0.03 for thermal molecules at room temperature [6]. Many other experiments, which are listed in Table 2.1, have confirmed this surprisingly low value. The most detailed sticking data have been provided by Österlund *et al.* [9] using a molecular beam experiment employing the method of King and Wells [69]. In this experiment the initial sticking probability has been measured as a function of the kinetic energy of the oxygen molecules. The obtained sticking curve is shown in Fig. 2.3. For thermal energies the sticking probability is found to be about 1 %, while the sticking probability rises continuously with increasing kinetic energy and reaches a saturation value of 90 % at about 0.5 eV. From this data it has been concluded that the sticking is an activated process, i.e. there are energy barriers towards dissociation which efficiently prevent slow molecules from dissociative adsorption. A significant dependence of the sticking probability on the surface temperature has not been found, but vibrational excitation can enhance the sticking probability.

In contrast to this study Zhukov *et al.* measured the sticking probability as a function of the surface temperature using HREELS and XPS [10, 11] and found slight variations of the sticking probability with a minimum value of 0.015 at 250 K and a maximum value of 0.07 at 600 K. They concluded the existence of a weakly bound mobile molecular precursor, which accounts for the increase of the sticking probability between 250 K and 600 K, because a higher surface temperature promotes the passage of the barrier towards adsorption. For higher temperatures, when the oxide becomes the dominating structure on the surface, the sticking probability decreases again, suggesting that the sticking at the oxide is a non-activated process.

S_0	Ref.	Method
0.03	Gartland 1977 [6]	Auger Electron Spectroscopy
0.02	Bradshaw *et al.* 1977 [7]	X-ray Photoelectron Spectroscopy
0.005	Brune *et al.* 1993 [8]	Scanning Tunnelling Microscopy
0.014	Österlund *et al.* 1997 [9]	Molecular Beam Experiment
0.01	Zhukov *et al.* 1999 [10]	X-ray Photoelectron Spectroscopy
0.02	Zhukov *et al.* 1999 [11]	X-ray Photoelectron Spectroscopy
0.0051	Lee and Lin 2001 [12]	Ion Bombardment Induced Light Emission

Table 2.1: Sticking probabilities of oxygen on Al(111) obtained by different experimental techniques.

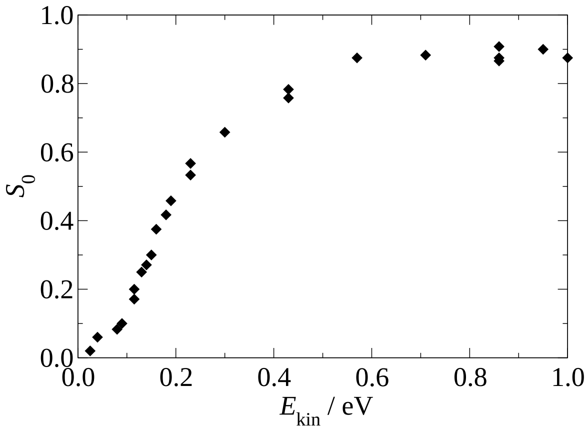

Figure 2.3: Initial sticking probability S_0 for an oxygen molecule impinging on a clean Al(111) surface as a function of its kinetic energy for normal incidence. The data have been obtained in a molecular beam experiment [9] employing the method of King and Wells [69].

In general, the low sticking probability of oxygen on Al(111) could be explained by the existence of energy barriers towards dissociation. To identify these barriers several groups calculated parts of the adiabatic potential-energy surface using density-functional theory [22, 24, 70–73]. Unfortunately, almost no energy barriers could be found. According to theory the sticking probability should then be very high and independent of the kinetic energy of the molecule. There are several possible explanations for this failure of adiabatic density-functional theory. One possibility would be the inability of current implementations of density-functional theory to describe the energetics of the interaction of an oxygen molecule with the aluminium surface accurately enough to determine the barriers. This assumption would be supported by the rather poor description of the gas phase oxygen molecule by state-of-the-art density-functional theory [74, 75]. Another possibility is that the adiabatic nature of the DFT potential-energy surface does not properly describe the physics of the adsorption process, and that non-adiabatic effects would have to be taken into account to explain the experimental data. A dominant role of non-adiabatic effects in this system has been suggested in several studies [9, 20–24].

Part I

Theoretical Background

Chapter 3

Non-Adiabatic Effects

The adiabatic description of the dissociation process in standard density-functional theory is based on the Born-Oppenheimer approximation [25]. It states that for each configuration of the nuclei during the molecular approach to the surface the electronic structure instantaneously relaxes to the ground state. This cannot be taken for granted due to the dynamic nature of the adsorption process [76], which leads to a competition of time scales for the nuclear and electronic motion. If the time scales do not decouple perfectly, this could result in a continued motion on the initial diabatic state, which becomes an excited state due to the presence of the aluminium surface.

The first studies of such non-adiabatic effects were carried out for the case of crossing energy levels during the collision of two atoms [77–82]. In such a collision event a charge transfer from one atom to the other can occur when the energy of an ion pair becomes lower than the energy of the two neutral atoms below a certain distance Z_c. In this case, the neutral and the ionic potential-energy surfaces form two diabatic states ψ_1^d and ψ_2^d of the system, which cross at the atomic separation Z_c. This is shown schematically in Fig. 3.1. For an interatomic distance smaller than Z_c the state ψ_2^d is lower in energy, and for a distance larger than Z_c state ψ_1^d is energetically favorable. By a combination of ψ_1^d and ψ_2^d the adiabatic ground state ψ_1^a can be constructed, if the coupling H'_{12} of the two diabatic states is known. The adiabatic ground state has the lowest energy for all interatomic separations and approaches the diabatic states asymptotically for very large and very small distances. A second combination of the diabatic states yields the excited adiabatic state ψ_2^a, which forms an upper bound to the diabatic energies. Both adiabatic states do not cross, they have an "avoided crossing", and the energy difference of both adiabatic states at Z_c is twice the coupling $|H'_{12}|$ of the two diabatic states [83]. The energies $E_{1,2}^\mathrm{a}$ of the adiabatic states are related to the diabatic energies $E_{1,2}^\mathrm{d}$ [84] by

$$E_{1,2}^\mathrm{a} = \frac{E_1^\mathrm{d} + E_2^\mathrm{d}}{2} \pm \frac{1}{2}\sqrt{\left(E_1^\mathrm{d} - E_2^\mathrm{d}\right)^2 + 4|H'_{12}|^2} \quad . \tag{3.1}$$

Therefore both, the adiabatic and the diabatic states, are apt to describe a two-state system, and the Hamiltonian is typically expressed in the adiabatic basis $\{\psi_1^\mathrm{a}, \psi_2^\mathrm{a}\}$ or

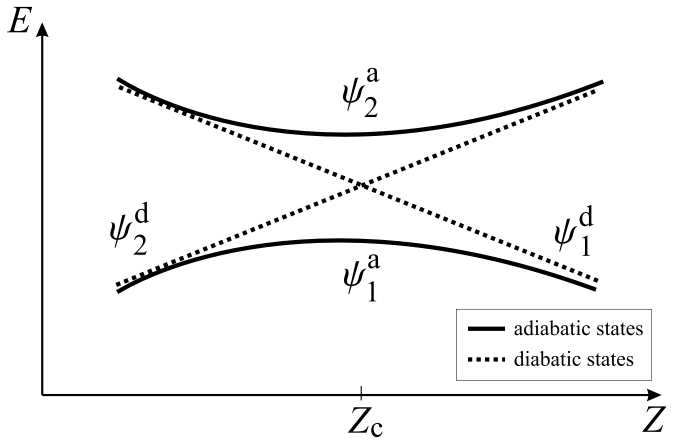

Figure 3.1: General two-state curve crossing problem.

equivalently in the diabatic basis $\{\psi_1^d, \psi_2^d\}$. For an increasing interatomic distance both representations become identical due to the absence of coupling. The Hamiltonian $\mathbf{H}$ in the adiabatic representation is diagonal, while the Hamiltonian $\mathbf{H}'$ in the diabatic representation contains the off-diagonal coupling matrix elements H'_{12} and H'_{21}, which have the same absolute value, but are complex conjugate.

$$\mathbf{H} = \begin{pmatrix} H_{11} & 0 \\ 0 & H_{22} \end{pmatrix} \qquad \mathbf{H}' = \begin{pmatrix} H'_{11} & H'_{12} \\ H'_{21} & H'_{22} \end{pmatrix} \tag{3.2}$$

If the atoms move infinitely slow, the system will follow the adiabatic ground state ψ_1^a, and this is exactly what is assumed in the prevalent description of dissociation processes at surface. However, in case of a finite velocity the state of the system will become a linear combination of both adiabatic states, i.e. a certain probability for a non-adiabatic transition exists. A non-adiabatic transition is defined as a transition from the adiabatic state ψ_1^a to state ψ_2^a [83], and is equivalent to a continued motion on the initial diabatic energy surface beyond the crossing point. The probability of such a non-adiabatic transition increases with the atomic velocities, since less time is available for the electrons to adapt to the rapidly changing nuclear positions, and has the highest value at the crossing distance Z_c, because then the required energy for the transition is smallest.

The importance of non-adiabatic effects is not restricted to atomic collisions. Also for the interaction of molecules with surfaces non-adiabatic effects have been accounted for experimental observations. In this case the two or more states are energy levels of the molecule[1], and their energetic order is modified by the presence of the surface finally giving rise to level crossings. In particular for metal surfaces the

[1]In general, also excited states of the surface could be taken into account.

validity of the Born-Oppenheimer approximation is questionable, because the continuum of energy levels allows for electronic excitations by an infinitesimal amount of energy [84–86]. A prominent example is the dissociative adsorption of Cl_2 molecules on a potassium surface [20, 87]. It has been suggested that the Cl_2 dissociates into a Cl^- ion and a neutral chlorine atom by a harpooning mechanism, which is basically a tunnelling of an electron from the metal surface to the molecule at a comparably large distance, e.g. approximately 4 Å for the dissociation of chlorine on potassium. The emerging unoccupied $3p$ level of the chlorine atom is below the Fermi level of the metal. This excited state decays by the emission of Auger electrons, which are called exoelectrons, if their kinetic energy is higher than the work function of the metal enabling them to leave the surface. There are also several studies about non-adiabatic effects in the oxygen adsorption on metals like cesium [88], magnesium [89], lithium [90] and silver [91]. In case of the oxygen molecule another possible source of non-adiabatic effects apart from charge transfer is its spin-triplet ground state. It has been shown by Kato *et al.* [92, 93] that the energy dependence of the initial sticking probability of oxygen on the Si(001) surface may be explained by a hindered spin-flip from the triplet ground state of the free molecule to the singlet ground state of the adsorbed atoms, because the probability of a change of the spin state, which would be required for an adiabatic approach to the surface, is very low.

The assumption that non-adiabatic effects are important for the oxygen dissociation on Al(111) is supported by several experiments. In 1974 Kasemo had shown that upon the adsorption of oxygen on Al(111) photons are emitted [89]. This chemiluminescence results from electronic transitions from excited molecular states into the ground state. These excited states could be created when unoccupied molecular states are shifted below the Fermi level of the metal during the approach of the molecule to the surface. A prerequisite for this model is that charge transfer is slow compared to the molecular motion. Another experimental evidence is the detection of exoelectrons [94], which form another possibility for electronic relaxation. Both experiments have been interpreted as clear evidence for non-adiabatic effects. First attempts based on simple theoretical models have also been made to include non-adiabatic effects in the calculation of the sticking curve of oxygen on Al(111) [21, 28]. Yet, even a qualitative understanding of the experimental sticking curve based on first-principles is still lacking. This is particularly disturbing, because the sticking probability is strongly related to other interesting aspects of the adsorption process like the heavily disputed adsorption mechanism. As long as the first interaction of the oxygen molecule with the surface, which determines the sticking probability, is not described correctly, it is also not possible to make reliable statements about other aspects of the dissociation process. A major obstacle for a detailed theoretical investigation of non-adiabatic effects in molecular sticking is the problem of calculating the relevant diabatic potential-energy surfaces accurately from first-principles [85]. The purpose of the present work is therefore to examine the possible role of non-adiabatic effects in the interaction of oxygen molecules with the Al(111) surface based on DFT, and to analyze if these effects can provide an explanation for the low sticking probability found in experiment.

Chapter 4

Calculation of Sticking Curves

To gain a deeper understanding of the origin of the discrepancy between theory and experiment concerning the sticking probability, the sticking curve of oxygen molecules impinging on the clean Al(111) surface has to be calculated from first-principles, i.e. using DFT. This way the effect of molecular steering can be analyzed, which is particularly important when slow molecules approach the surface [15–17], and cannot be deduced from a mere inspection of the potential-energy surface as done in previous work [24].

In general, sticking curves can be obtained from molecular dynamics simulations. These simulations have to take into account that the sticking probability is a statistically averaged quantity, which in experiment is composed of a macroscopic number of individual molecular trajectories. To obtain statistically relevant sticking probabilities that can be compared with experiment, a large number of trajectories has to be calculated, covering the whole configuration space of the molecule when it approaches the surface. This large number of trajectories, typically several thousand for the sticking of a diatomic molecule, has furthermore to be calculated for many different initial kinetic (translational) energies of the molecule possibly taking into account also different vibrational and rotational states. This would require a prohibitive computational effort, if direct *ab initio* [95–97] molecular dynamics simulations would be employed, i.e. if for each intermediate configuration of the molecule the energies and forces would have to be calculated from first-principles. For large systems, this approach typically allows for a calculation of about 50 trajectories only. An alternative way to provide the energies and forces would be to construct an empirical potential, which would allow for a very fast calculation of the energy and forces. However, the price for such an efficient potential is still a far lower accuracy in the energies and forces, since no existing functional form can reliably treat the effects of hybridization that so much determine the molecule surface interaction. To overcome these problems and to combine the advantages of *ab initio* molecular dynamics with the efficiency of empirical potentials, a "divide and conquer" approach has been proposed [17]. In this approach the evaluation of the potential-energy surface from first-principles is decoupled from the molecular dynamics in that the procedure is split up into three independent steps.

In the first step the potential-energy surface for the molecule-surface interaction is calculated for a dense grid of configurations in six dimensions taking into account only the degrees of freedom of the oxygen molecule. The validity of this frozen surface approximation has to be tested carefully, e.g. by comparing the shape of the PESs obtained from a calculation with a frozen and a fully relaxed substrate. Typically, density-functional theory is presently used for the mapping of the potential-energy surface, because it is very accurate but also efficient enough to handle large systems, which are necessary to model the interaction of an isolated molecule with the surface. Still, only a finite number of about 1000 energy points can be calculated. To provide energies and forces for arbitrary molecular configurations, which is required for the molecular dynamics simulations, the discrete mesh of energy points is interpolated to a continuous potential-energy surface. The interpolation of high-dimensional potential-energy surfaces is a formidable task, but in recent years several methods have been developed for this purpose. In this work a neural network technique has been applied, that has proven to be very well suited for the interpolation of potential-energy surfaces [26, 27]. It provides energies and forces about five orders of magnitude faster than direct *ab initio* calculations with only a small fitting error. In the final step, classical molecular dynamics simulations are performed for thousands of different trajectories and for many different kinetic energies to obtain a statistically significant sticking curve.

This approach is general and can be applied to any type of potential-energy surface, adiabatic and diabatic. In the following chapters the methods employed in the individual steps of the "divide and conquer" technique will be introduced and finally employed in the calculation of the sticking curves based on the adiabatic ground state as well as on the diabatic spin-triplet potential-energy surface.

Chapter 5

Density-Functional Theory

5.1 The Many-Body Problem

Understanding and predicting material properties without relying on experimental data has been the aim of first-principles calculations since their advent about 80 years ago. All information about a system composed of N electrons and M nuclei can in principle be obtained from the many-body Schrödinger equation. In its time-independent, non-relativistic version it is given by

$$H\Psi\left(\mathbf{r}_i,\mathbf{R}_j\right) = E\Psi\left(\mathbf{r}_i,\mathbf{R}_j\right) \quad . \tag{5.1}$$

H is the many-body Hamilton operator providing the total energy E of the system when applied to the many-body wave-function $\Psi\left(\mathbf{r}_i,\mathbf{R}_j\right)$ that depends on the nuclear positions $\mathbf{R}_j$ and the electron coordinates $\mathbf{r}_i$ [86]. The Hamiltonian itself has five main contributions: The kinetic energy operators T_n and T_e of the nuclei and the electrons, the electron-electron interaction V_ee, the repulsion of the nuclei V_nn and the electrostatic interaction between the electrons and the nuclei V_ne.

$$H = T_\mathrm{n} + T_\mathrm{e} + V_\mathrm{ee} + V_\mathrm{nn} + V_\mathrm{ne} \tag{5.2}$$

In atomic units the components of the Hamilton operator are

$$T_\mathrm{n} = -\frac{1}{2}\sum_{j=1}^{M}\frac{1}{m_j}\nabla_j^2 \quad , \tag{5.3a}$$

$$T_\mathrm{e} = -\frac{1}{2}\sum_{i=1}^{N}\nabla_i^2 \quad , \tag{5.3b}$$

$$V_\mathrm{ee} = \sum_{i=1}^{N}\sum_{j>i}^{N}\frac{1}{|\mathbf{r}_i-\mathbf{r}_j|} \quad , \tag{5.3c}$$

$$V_{\mathrm{nn}} = \sum_{i=1}^{M}\sum_{j>i}^{M} \frac{Z_i Z_j}{|\mathbf{R}_i - \mathbf{R}_j|} \quad , \tag{5.3d}$$

$$\text{and} \quad V_{\mathrm{ne}} = \sum_{i=1}^{N}\sum_{j=1}^{M} \frac{-Z_j}{|\mathbf{r}_i - \mathbf{R}_j|} \quad , \tag{5.3e}$$

where m_j is the mass of nucleus j in multiples of the electron mass, Z_j the nuclear charge and ∇_i^2 the Laplacian operator acting on particle i.

The difficulties in solving Eq. (5.1) arise from the large number of variables the many-body wave-function Ψ depends on. For a system consisting of N electrons and M nuclei there are $3N+3M$ degrees of freedom, i.e. three spatial coordinates for each electron and for each nucleus. A first simplification can be achieved by taking into account the large difference in masses between the electrons and the nuclei. Therefore, the electrons move much faster than the nuclei and to a good approximation the positions of the nuclei can be assumed to be static, i.e. they can be treated as parameters. In this way the motion of the electrons is separated from the motion of the nuclei, which now form an "external" potential to the electrons. The kinetic energy of the nuclei can be set to zero and the nuclear-nuclear repulsion term in Eq. (5.2) enters the total energy expression as a constant. This is the Born-Oppenheimer approximation (BOA) [25]. Even though the number of degrees of freedom has now been reduced to $3N$, the remaining electronic many-body problem is still far too involved to be solved exactly, except for the simplest cases like a free hydrogen atom or one-electron ions. The remaining electronic Hamiltonian is given by

$$H_{\mathrm{e}} = T_{\mathrm{e}} + V_{\mathrm{ne}} + V_{\mathrm{ee}} = -\frac{1}{2}\sum_{i=1}^{N}\nabla_i^2 - \sum_{i=1}^{N}\sum_{j=1}^{M}\frac{Z_j}{|\mathbf{r}_i - \mathbf{R}_j|} + \sum_{i=1}^{N}\sum_{j>i}^{N}\frac{1}{|\mathbf{r}_i - \mathbf{r}_j|} \quad . \tag{5.4}$$

The electronic Schrödinger equation is

$$H_{\mathrm{e}}\Psi_{\mathrm{e}}(\mathbf{r}_i) = E_{\mathrm{e}}\Psi_{\mathrm{e}}(\mathbf{r}_i) \quad , \tag{5.5}$$

with $\Psi_{\mathrm{e}}(\mathbf{r}_i)$ being the electronic wave-function. The first numerical scheme to solve this equation quantitatively to obtain an approximate wave-function and the total energy has been suggested by Hartree and Fock [98, 99] in the 1930's. Since the introduction of the Hartree-Fock (HF) method wave-function based techniques have undergone an enormous development [100, 101]. More advanced approaches to solve the many-body problem based on wave-functions are for example the Møller Plesset perturbation theory (MP2, MP4, ...) [102], configuration interaction (CI) [100], coupled cluster methods (CC) [100] and multi-configuration self-consistent field methods (MCSCF and CASSCF) [103].

Additionally, with density-functional theory (DFT) a powerful alternative based on the electron density as the central quantity instead of the wave-function has become a very popular and successful quantum mechanical approach to solve the many-body problem [13, 14, 104].

5.2 The Early Days of Density-Functional Theory: The Thomas-Fermi Model

The electron density was used for the first time to calculate the total energy of a system by Thomas and Fermi in the late 1920's. The electron density ρ is defined as the integral of the many-body wave-function over all but one spatial coordinates of all electrons multiplied by the number of electrons N.

$$\rho\left(\mathbf{r}\right) = N \int ... \int \left|\Psi\left(\mathbf{r}_1, \mathbf{r}_2, ..., \mathbf{r}_N\right)\right|^2 d\mathbf{r}_2 ... d\mathbf{r}_N \quad , \tag{5.6}$$

where $\mathbf{r}$ refers to the spatial coordinates of the density and the $\mathbf{r}_i$ to the coordinates of the individual electrons. The justification for this approach has been given be Hohenberg and Kohn about 35 years later [105]. In contrast to the wave-function the electron density ρ is an observable, and like the wave-function it contains all information required to define the system: cusps in the electron density mark the positions of the nuclei, the value of ρ at the nuclei contains information on the nuclear charges [106] and the integration of the electron density is the electron number N.

$$\int \rho\left(\mathbf{r}\right) d\mathbf{r} = N \tag{5.7}$$

Thomas and Fermi tried to express the energy of a system as a functional of the electron density [107, 108]. This ansatz leads to a reduction from $3N$ to 3 coordinates. The energy is given by the Thomas-Fermi kinetic energy functional depending only on the density as well as by classical terms for the electron-electron and electron-nucleus interaction. Then the energy is minimized with respect to the density to obtain the ground state energy of the system.

However, for many-electron atoms and many-atom systems the results were not very satisfying. Molecules calculated with the Thomas-Fermi approach are unstable, because the sum of the energies of the isolated atoms is lower than the energy of the molecule. The reasons are that in the Thomas-Fermi model exchange and correlation are completely neglected and that the kinetic energy is approximated by the kinetic energy of non-interacting electrons in the homogeneous electron gas. In 1930 Dirac added an expression for the exchange energy [109] depending only on the density but still the correlation was not taken into account. Nevertheless, this model is historically very important, because it was the first attempt to establish an energy expression using exclusively the electron density as the basic variable.

5.3 From a Model to a Theory: The Hohenberg-Kohn Theorems

In 1964 density-functional theory was established as a theory by two theorems of Hohenberg and Kohn [105], who showed that the ground state density can indeed be used to replace the complex wave-function. They showed that the external potential *"V_{ext} is (to within a constant) a unique functional of ρ; since, in turn, V_{ext} fixes H we see that the full many-particle ground state is a unique functional of ρ."* [105]. So the density uniquely defines the Hamilton operator and therefore the energy of a system. Hohenberg and Kohn have given a simple proof of this theorem. Accordingly, the electronic ground state energy E_0 can be obtained as a functional of the ground state density ρ_0.

$$E_0 = E[\rho_0] = T_{\mathrm{e}}[\rho_0] + E_{\mathrm{ee}}[\rho_0] + E_{\mathrm{ne}}[\rho_0] = E_{\mathrm{ne}}[\rho_0] + F_{\mathrm{HK}}[\rho_0] \tag{5.8}$$

This equation defines the Hohenberg-Kohn functional $F_{\mathrm{HK}}[\rho]$, which is independent of the system, i.e. it is universal, but unfortunately no exact expressions for its components $E_{\mathrm{ee}}[\rho]$ and $T_{\mathrm{e}}[\rho]$ are known. However, $E_{\mathrm{ee}}[\rho]$ can be written as a sum of the Hartree energy $E_{\mathrm{H}}[\rho]$, which is the interaction of a charge distribution with itself

$$E_{\mathrm{H}}[\rho] = \frac{1}{2}\int \frac{\rho(\mathbf{r})\,\rho(\mathbf{r}')}{|\mathbf{r}-\mathbf{r}'|} d\mathbf{r}d\mathbf{r}' \quad , \tag{5.9}$$

and a non-classical part $E_{\mathrm{ncl}}[\rho]$, which contains the self-interaction correction, the exchange and the Coulomb correlation. In summary, there is a one-to-one correspondence between the external potential and the ground state density of a system. Consequently, the expectation value of any observable is also a unique functional of the exact ground state electron density. This is often called the first Hohenberg-Kohn theorem.

The second Hohenberg-Kohn theorem states that the energy is minimal for the ground state density resulting from the external potential. This enables the use of the variational principle to calculate the exact ground state density if the energy functional is known. Any density different from the ground state density yields a higher total energy than the *true* ground state density. However, it should be noted that the functional $F_{\mathrm{HK}}[\rho]$ is not known and instead approximations have to be used. As a consequence the obtained ground state energy is not an upper bound to the true ground state energy any more, but within a given approximation to $F_{\mathrm{HK}}[\rho]$ the variational principle can only be used to find the ground state density and its corresponding energy for this approximated functional form of $F_{\mathrm{HK}}[\rho]$.

5.4 From a Theory to a Practical Tool: The Kohn-Sham Equations

The Hohenberg-Kohn theorems set the foundations of density-functional theory, but still an efficient scheme to obtain the ground state density and energy was missing. This was developed in 1965 when DFT turned from a theory to a practical tool by the introduction of the concept of a non-interacting reference system by Kohn and Sham [110]. With this approach it is not required anymore to use the unknown kinetic energy density-functional $T_{\mathrm{e}}[\rho]$. Instead the kinetic energy is separated into the kinetic energy T_{S} of a system of non-interacting electrons, which can be calculated exactly using

$$T_{\mathrm{S}} = -\frac{1}{2}\sum_i \phi_i^*(\mathbf{r})\,\nabla^2\phi_i(\mathbf{r})\,d\mathbf{r} \quad , \tag{5.10}$$

and an unknown component T_{C}, which contains the corrections resulting from the electronic interaction. The single-particle Kohn-Sham orbitals ϕ_i are determined under the constraint to reproduce the density of the fully interacting many-body system in a self-consistent way from the Kohn-Sham equations

$$f_{\mathrm{KS}}\phi_i(\mathbf{r}) = \epsilon_i\phi_i(\mathbf{r}) \quad . \tag{5.11}$$

The Kohn-Sham operator f_{KS} is an effective one-electron operator and is given by

$$f_{\mathrm{KS}} = -\frac{1}{2}\nabla^2 + V_{\mathrm{ext}}[\rho] + V_{\mathrm{H}}[\rho] + V_{\mathrm{XC}}[\rho] \quad . \tag{5.12}$$

$V_{\mathrm{ext}}[\rho]$ is the external potential due to the nuclei and is often combined with the classical Hartree potential $V_{\mathrm{H}}[\rho]$ and the exchange-correlation potential $V_{\mathrm{XC}}[\rho]$ to the effective potential $V_{\mathrm{eff}}[\rho]$. The eigenvalues ϵ_i are Lagrange multipliers that ensure the orthonormality of the Kohn-Sham orbitals. The density constructed from the Kohn-Sham orbitals ϕ_i and their occupation numbers f_i is the same as the density of the interacting system.

$$\rho(\mathbf{r}) = \sum_{i=1}^{N}\phi_i^*(\mathbf{r})\cdot\phi_i(\mathbf{r})\cdot f_i \tag{5.13}$$

The ϕ_i are functionals of ρ and consequently the kinetic energy is still given as a functional of ρ in an indirect way. The remaining part T_{C} of the true kinetic energy is combined with the non-classical contributions to the electron-electron interaction $E_{\mathrm{ncl}}[\rho]$ in the exchange-correlation functional $E_{\mathrm{XC}}[\rho]$. Therefore, $E_{\mathrm{XC}}[\rho]$

contains everything that is unknown, and it is related to the exchange-correlation potential V_{XC} in Eq. (5.12) in that the latter is its functional derivative with respect to the density.

$$V_{\mathrm{XC}}\left[\rho(\mathbf{r})\right] = \frac{\delta E_{\mathrm{XC}}[\rho(\mathbf{r})]}{\delta\rho\left(\mathbf{r}\right)} \tag{5.14}$$

In summary, the Kohn-Sham equations replace the minimization of $E\left[\rho\right]$ by the solution of the single-particle Schrödinger equations of non-interacting electrons. This means that the universal Hohenberg-Kohn functional is expressed in the form

$$F_{\mathrm{HK}} = T_{\mathrm{S}} + E_{\mathrm{H}} + E_{\mathrm{XC}} \quad , \tag{5.15}$$

and all many-body effects are included in $E_{\mathrm{XC}}[\rho]$. It should be noted that the single-particle orbitals ϕ_i are not the wave-functions of electrons, nor are the eigenvalues single-electron energies in a strict physical sense. Only the density and the total energy have a physical meaning. So far the Kohn-Sham equations do not contain any approximation and are in principle exact. However, we still do not know the exact form of the exchange-correlation functional, which is required to calculate the ground state density and energy.

5.5 Exchange-Correlation Functionals

With the introduction of the Kohn-Sham formalism most contributions to the total energy can be calculated exactly. The remaining unknown parts are assembled in the exchange-correlation functional. Therefore good approximations to $E_{\mathrm{XC}}[\rho]$ are crucial to obtain reliable results in a DFT calculation. Unfortunately, in contrast to wave-function based methods there is no systematic way how better and better results can be obtained.

The first attempt to find an explicit expression for $E_{\mathrm{XC}}[\rho]$ was based on the homogeneous electron gas. This is a uniform electron distribution on a positive background charge distribution for overall charge neutrality. The basic assumption is that exchange and correlation depend only on the local value of the density. Consequently, this is called the local-density approximation (LDA). One approximates the real inhomogeneous electron density as a sum of small cells each of which has a homogeneous electron density. It is assumed that $E_{\mathrm{XC}}[\rho(\mathbf{r})]$ at position $\mathbf{r}$ is identical to $E_{\mathrm{XC}}^{\mathrm{LDA}}[\rho(\mathbf{r})]$ of the homogeneous electron gas of the same density. The exchange-correlation functional is then given by

$$E_{\mathrm{XC}}^{\mathrm{LDA}}\left[\rho(\mathbf{r})\right] = \int \rho\left(\mathbf{r}\right)\mathcal{E}_{\mathrm{XC}}\left(\rho\left(\mathbf{r}\right)\right)d\mathbf{r} \quad , \tag{5.16}$$

where $\mathcal{E}_{\mathrm{XC}}(\rho(\mathbf{r}))$ is the exchange-correlation energy per particle of the homogeneous electron gas. $E_{\mathrm{XC}}^{\mathrm{LDA}}$ can further be split up into the exchange and the correlation contributions $E_{\mathrm{X}}^{\mathrm{LDA}}$ and $E_{\mathrm{C}}^{\mathrm{LDA}}$. The exchange part can be given analytically in case of the homogeneous electron gas.

$$E_{\mathrm{X}}^{\mathrm{LDA}}[\rho(\mathbf{r})] = \int \rho(\mathbf{r}) \left(-\frac{3}{4}\right) \sqrt[3]{\frac{3\rho(\mathbf{r})}{\pi}} d\mathbf{r} \tag{5.17}$$

The correlation energy is only numerically known from quantum Monte Carlo calculations by Ceperley and Alder [111] and can be parameterized to be used in DFT calculations. The two most prominent parameterizations have been done by Vosko, Wilk and Nusair [112] and by Perdew and Wang [113], which give usually very similar results.

Although the local-density approximation is a rather unrealistic model for real systems, it has been the standard functional until the 1990's with often surprisingly good results comparable to Hartree-Fock for many systems. However, the LDA typically overestimates binding energies and underestimates bond lengths, and for systems with less homogeneous electron densities the results using the LDA are often disappointing. Still, the importance of the LDA lies in that the homogeneous electron gas is the only system for which the exchange-correlation functional is known, and all improved functionals to date are based on this approach. Such improvements can be achieved by including the first derivative of the electron density $\nabla\rho(\mathbf{r})$ yielding the generalized gradient approximation (GGA), in which $E_{\mathrm{XC}}[\rho(\mathbf{r})]$ is given by

$$E_{\mathrm{XC}}^{\mathrm{GGA}}[\rho(\mathbf{r})] = \int f(\rho(\mathbf{r}), \nabla\rho(\mathbf{r}))\, d\mathbf{r} \quad . \tag{5.18}$$

Including the gradient of the density results in much better binding energies compared to the LDA making GGA functionals the most important class of functionals in current DFT. Many GGAs exist differing in the functional form of exchange and correlation. In most cases GGA energies are more reliable than LDA results, but due to their non-unique definition there is typically a certain variation in the energies obtained from different GGA functionals.

These days the development of new and better functionals is still an active field of research. E_{XC} is far smaller in value than all other contributions to the total energy, and usually density-functional theory is used to calculate the energy difference between different systems. In this case the errors in the exchange-correlation energy often cancel to a large extent, and this is the reason why approximations to E_{XC} lead to reliable results in most cases.

Two important GGA functionals, which have been used in this work, have been proposed by Perdew, Burke and Ernzerhof in 1996 (PBE) [114] and by Hammer, Hansen and Nørskov in 1999 (RPBE) [74]. The PBE functional has been constructed in a way to fulfill physical constraints rather than fitting to experimental data [115]. The basic idea behind this functional was to mimic the PW91 functional of Perdew and Wang [116], which is basically an analytical fit to a numerically determined first-principles GGA, but to find a simpler functional form by neglecting energetically irrelevant terms. The RPBE functional is based on the same expression for correlation as PBE, but the functional form of the exchange term is different, while the same physical boundary conditions as in the PBE case are still fulfilled [74]. Therefore, both functionals have the same physical justification, and differences in the obtained results are indicative of the uncertainty in present GGA functionals.

5.6 Spin-Density-Functional Theory

Many systems of interest possess an odd number of electrons and even some systems with an even number of electrons have to be treated as radicals, when two electrons occupy a doubly degenerate orbital [117], the oxygen molecule being a prominent example. While the results obtained from DFT as described so far are quite satisfactory for closed-shell systems, for the investigation of these open-shell systems an extension is required. Improved results can be obtained by using approximate functionals that depend on the spin-densities $\rho^{\uparrow}$ and $\rho^{\downarrow}$ instead of the total density ρ. This leads to the formalism of spin-density-functional theory [118, 119]. In analogy to restricted and unrestricted Hartree-Fock calculations one can define restricted (RKS) and unrestricted (UKS) Kohn-Sham methods, which use the same spatial orbitals or different spatial orbitals for both spin orientations, respectively, representing non-spin-polarized and spin-polarized DFT. In unrestricted Kohn-Sham calculations the $\phi_i^{\uparrow}$ and $\phi_i^{\downarrow}$ Kohn-Sham orbitals experience different potentials which provides additional flexibility in the calculations resulting in a better description of open shell systems [120].

Spin-density-functionals are used for exchange and correlation and therefore two effective potentials $V_{\text{eff}}^{\uparrow}$ and $V_{\text{eff}}^{\downarrow}$ appear in the Kohn-Sham equations.

$$\left[-\frac{1}{2}\nabla^2 + V_{\text{eff}}^{\sigma}\right]\phi_i^{\sigma}(\mathbf{r}) = \epsilon_i^{\sigma}\phi_i^{\sigma}(\mathbf{r}) \quad , \tag{5.19}$$

where σ represents the spin. The spin orbitals ϕ_i^{σ} are formed by a spatial orbital and a spin function. The spin-polarized version of LDA is called local-spin-density approximation (LSD) [118] and the exchange-correlation functional is then given by

$$E_{\text{XC}}^{\text{LSD}}\left[\rho^{\uparrow}(\mathbf{r}), \rho^{\downarrow}(\mathbf{r})\right] = \int \rho(\mathbf{r})\,\mathcal{E}_{\text{XC}}\left(\rho^{\uparrow}(\mathbf{r}), \rho^{\downarrow}(\mathbf{r})\right) d\mathbf{r} \quad . \tag{5.20}$$

Like in the restricted Kohn-Sham scheme, in this case the Hohenberg-Kohn theorem is valid stating that there exists a one-to-one correspondence of the spin-dependent potentials V_{eff}^{σ} and the spin densities. For calculations on spin-polarized species like most free atoms and some molecules like O_2 the use of the UKS scheme is mandatory to obtain meaningful energies.

5.7 Applications in Solid State Theory

Crystalline solids and surfaces are characterized by a practically infinite number of atoms, and their positions are related by certain symmetries inherent to the crystal structure. The only way to describe these systems within density-functional theory is to make use of these symmetry properties in order to reduce the system size to the unit cell of the bulk solid or the surface by applying periodic boundary conditions (PBC). The translational symmetry is taken into account in the construction of the Hamiltonian and the wave-functions by applying the Bloch theorem [121]. It states that the wave-function of a periodic system can be written as a product of a plane wave $e^{i\mathbf{kr}}$ and a function with the lattice periodicity $u_{\mathbf{k}}(\mathbf{r})$.

$$\phi_{\mathbf{k}}(\mathbf{r}) = e^{i\mathbf{kr}} u_{\mathbf{k}}(\mathbf{r}) \tag{5.21}$$

$$u_{\mathbf{k}}(\mathbf{r}) = u_{\mathbf{k}}(\mathbf{r} + \mathbf{T}) \tag{5.22}$$

$\mathbf{k}$ is a wave vector within the first Brillouin zone and $\mathbf{T}$ is a vector of the Bravais lattice. The one-electron wave-functions $\phi_{\mathbf{k}}(\mathbf{r})$ are called Bloch functions.

To determine the total energy of a crystal a summation over the eigenvalues of the occupied single-particle states has to be performed. For periodic systems this sum over orbitals generalizes into an integration over the first Brillouin zone. By making use of the symmetry in the unit cell the integration over the Brillouin zone can be further reduced to the integration of the irreducible part of the Brillouin zone. In practical calculations the latter is replaced by a summation over discrete points in reciprocal space, called k-points, which have to be as representative as possible for the whole Brillouin zone. Several methods have been suggested for an efficient summation, a prominent example being the tetrahedron method [122].

While the description of surfaces by density-functional calculations would in principle be possible by using just two-dimensional periodicity, in practice the same procedure as for bulk solids is often applied. The surfaces are then modeled by slabs, which consist of several layers of atoms of infinite extension in two dimensions by applying appropriate boundary conditions. Additionally, the periodicity is artificially maintained also in the third dimension by infinitely repeating the slab in the direction perpendicular to the surface as shown in Fig. 5.1. This approach leads to two surfaces on both sides of the slab, and one has to make sure that the slab is thick enough to avoid interactions between these surfaces. Ideally, the atoms in the middle of the slab should have the physical properties of bulk atoms. The interaction between different slabs is prevented by a large vacuum region. By the formation of ordered adsorbate layers or reconstructions the symmetry of the surface can be reduced necessitating the use of larger surface unit cells, called supercells.

Another approach to model surfaces is to use large clusters. While the geometries of adsorbed molecules are usually satisfying (if the clusters are large enough), the binding energies show a very slow convergence making clusters a less appropriate model for metal [86] and semiconductor surfaces [123].

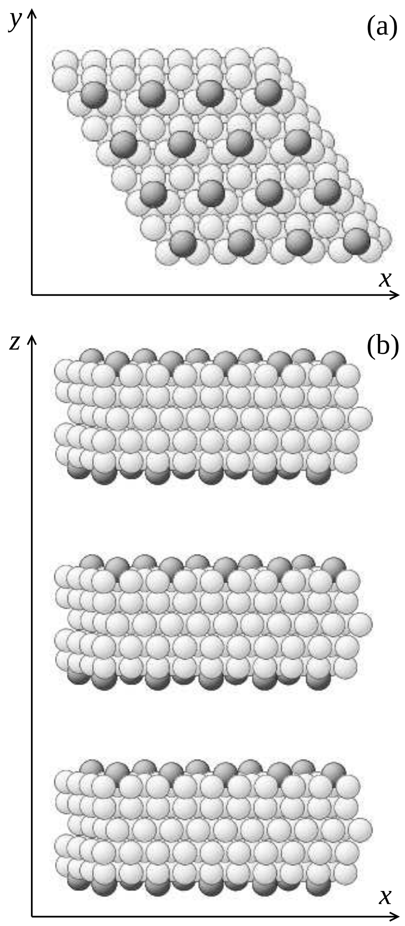

Figure 5.1: Top view (a) and side view (b) of Al(111) slabs with $\frac{1}{4}$ monolayer of oxygen atoms adsorbed on both sides.

5.8 Summary

Density-functional theory offers a way to perform calculations on all types of systems with generally good accuracy and efficiency. Exchange and correlation are in principle included, but in practical implementations only in an approximate way, which is the major source of error of this method. The construction of reliable exchange-correlation functionals is a difficult task. Some prominent deficiencies of density-functional theory using LDA and GGA functionals are the severe underestimation of band gaps in semiconductors [124], the inability to describe van der Waals interactions [125, 126], the instability of negative ions and the prediction of metallic properties of strongly correlated systems such as NiO and FeO [127], which are antiferromagnetic insulators. The accuracy of structural parameters and binding energies strongly depends on the employed functional. The LDA typically tends to overestimate binding energies and underestimate bond lengths, while GGAs show the opposite behavior.

Additionally, in density-functional theory the many-body wave-function is not accessible, and the single-particle eigenvalues of the Kohn-Sham orbitals strictly have no physical meaning, although they are often very good approximations to the energy levels of the electrons. The great success of *ab initio* methods and density-functional theory in particular has lead to the 1998 Nobel prize for John Pople and Walter Kohn underlining the importance of these techniques.

Chapter 6

The Density-Functional Implementation DMol^3

6.1 Introduction

Due to the steadily growing importance of density-functional theory in many fields, a large number of implementations has become available. Although they are all based on the same theoretical foundation, the actual realizations of density-functional theory can be significantly different. Historically, there are two main types of implementations either using plane waves or localized basis functions as basis set or as part of the basis set. While the first have their origin in calculations on solids applying periodic boundary conditions, for which plane waves are particularly useful, the latter have mainly been used in the chemistry community which is primarily interested in the properties of molecules. In recent years, however, the borders have started to vanish. Codes employing plane waves have been extended by localized functions establishing highly accurate all-electron approaches like the "linearized augmented plane wave" method (LAPW) [128–130] and the "augmented plane wave + local orbital" (APW+lo) method [131, 132]. On the other hand, many DFT codes employing localized basis sets have been extended to handle periodic boundary conditions. For the project of this thesis, intensive benchmark calculations have been performed to find the optimal density-functional code for the problems to be studied. The requirements are high both in accuracy, as accurate barrier heights are crucial for the correct description of the dynamics of the adsorption process, and in efficiency, as the mapping of six-dimensional potential-energy surfaces requires the calculation of a huge number of energy points based on rather large unit cells. Finally, the all-electron code DMol^3 [133] has been chosen because of its high efficiency and accuracy. Details of the performed benchmark calculations and comparisons to other DFT codes are given in Appendix A.

In almost all density-functional codes employing localized basis sets the molecular orbitals $\phi_i(\mathbf{r})$ are constructed as a linear combination of n basis functions $\chi_j(\mathbf{r})$, which do not change during the calculation.

$$\phi_i(\mathbf{r}) = \sum_{j=1}^{n} c_{ij}\chi_j(\mathbf{r}) \tag{6.1}$$

To obtain these Kohn-Sham orbitals the expansion coefficients c_{ij} have to be optimized. Practically all DFT codes are based on this equation, but they differ in the type of basis functions $\chi(\mathbf{r})$ employed. In the case of DMol^3 the basis functions are localized numerical atomic orbitals.

The name DMol is an abbreviation for "density-functional calculations on molecules", and in fact the original DMol code [133] was intended to do only calculations on atoms, molecules and clusters without periodic boundary conditions. Recently, an extension to handle periodic boundary conditions was implemented and the code was renamed to DMol^3, now being able to handle calculations with and without periodic boundary conditions [134] on an equal footing. In the following sections the characteristic methods used in the DMol^3 approach to density-functional theory are introduced. The focus will be primarily on aspects of the DMol^3 approach which differ from other density-functional implementations, namely the basis set, the numerical integration schemes and the calculation of the electrostatic potential.

6.2 The Atomic Orbital Basis Set

The most important feature of the DMol^3 approach is the use of localized atomic orbital basis functions. They are potentially the most efficient basis functions available, because they already show important properties like a cusp at the nucleus, square integrability and exponential decay for large distances from the nucleus, which are hard do reproduce with other basis sets. Another advantage is that in the limit of dissociating molecules the individual atoms are (almost) perfectly described by their own atomic orbitals as basis functions minimizing the basis set superposition error, which can be a serious source of error in other types of localized basis sets like the very popular Gaussian functions [100], if too small basis sets are chosen. However, atomic orbitals cannot be handled analytically, because their exact shape depends on the nuclear and atomic charges. Consequently, they require a purely numerical integration technique that will be described in the next section. The main philosophy behind the DMol^3 approach is that this technique is applied in a consistent way to all integrations involving the basis functions. Another advantage of atomic orbitals is that they are easily applicable to all types of compounds, with and without periodic boundary conditions, while the required number of basis functions is very small in both cases.

In the beginning of a DMol^3 calculation the basis functions are determined from a separate self-consistent density-functional calculation on free spherical atoms for all elements that are present in the system. With this approach the orbitals are

Basis set	Oxygen	N_B(O)	Aluminium	N_B(Al)
minimal	O: $1s$,$2s$,$2p$	5	Al: $1s$,$2s$,$2p$,$3s$,$3p$	9
dn	O^{2+}: $2s$,$2p$	9	Al^{2+}: $3s$,$3p$	13
dnd	N: $3d$	14	B: $3d$	18
dnp	=*dnd*	14	Be: $3p$, N: $4f$	28
all	B: $3d$	19	=*dnp*	28

Table 6.1: Basis sets for oxygen and aluminium. N_B(O) and N_B(Al) are the total numbers of basis functions per atom for oxygen and aluminium. The element symbols represent the nuclear charge used to construct the basis functions.

automatically adapted to the chosen exchange-correlation functional. Due to the spherically symmetric potential the basis functions can be calculated and fully defined by a radial grid which typically consists of 500 points. For the ensuing application of the basis functions to polyatomic systems the radial functions are multiplied with spherical harmonics.

The smallest possible basis set is called *minimal* and consists of all orbitals that are occupied in the ground state of the free atoms. They are determined in a calculation of a neutral atom. This basis set provides qualitative results at most. Basically, all functions that are bound eigenfunctions of some spherical potential can be used [135] to improve the basis set, which opens the way to use also other types of basis functions than the eigenfunctions of neutral atoms. Another important class of functions used in DMol^3 is formed by the atomic orbitals of free positive ions. Usually one or two electrons are removed from the neutral atom and in this way a second set of orbitals is obtained. Basis sets consisting of the *minimal* basis and of additional ionic basis functions for the valence electrons are called double numeric, *dn* for short, in analogy to double zeta basis functions frequently used in quantum chemistry. The basis set can be further improved by adding orbitals of a higher angular momentum, i.e. polarization functions. These are very important to accurately describe chemical bonding. Typically, polarization functions are determined from so-called hydrogenic atoms. These are one-electron atoms with an arbitrary nuclear charge and the electron being confined in a certain orbital, typically in d or f orbitals. This allows to generate a wide range of possible polarization functions by varying the nuclear charge, which also does not need to be integer. Basis sets including additional polarization functions are available in DMol^3 for the whole periodic table. They are called *dnd* (double numeric plus d-functions) and *dnp* (double numeric plus polarization functions). Even more polarization functions are added in the *all* basis set. In order to make the overlap matrix better conditioned, orbitals of the second and further basis subsets are Schmitt orthogonalized against the basis functions of the *minimal* set. As an example the radial parts of the basis functions of an aluminium atom are shown in Fig. 6.1. In Table 6.1 the basis sets for oxygen and aluminium as applied in this thesis are listed.

A clear disadvantage of an atomic orbital basis set is that there is no systematic

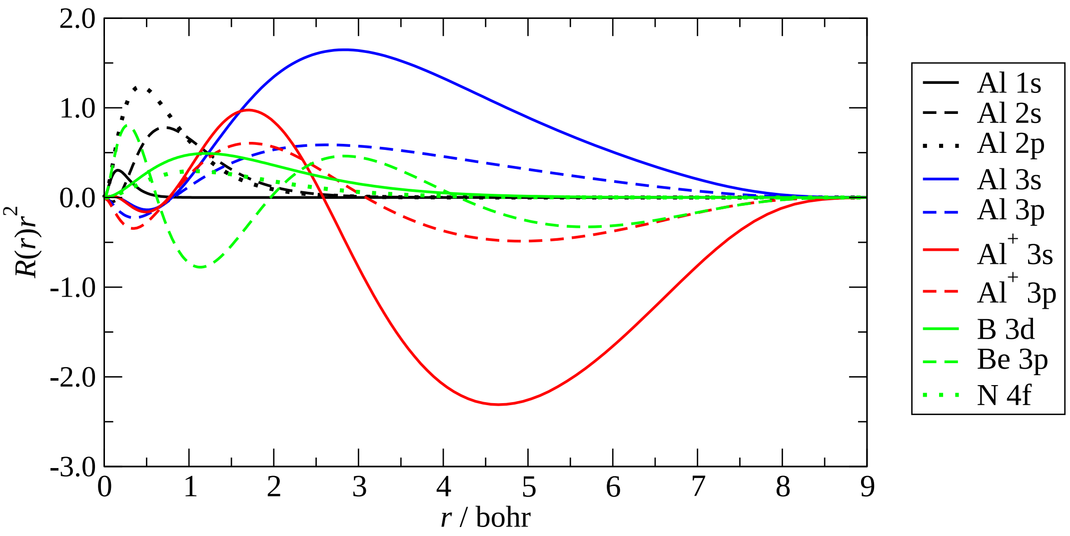

Figure 6.1: Radial basis functions of an aluminium atom. The basis functions of the *minimal* basis set are shown in black and blue. The additional basis functions taken from a positively charged aluminium atom in a *dn* basis set are shown in red. The polarization functions obtained from hydrogenic atoms included in the *dnd* and *dnp* basis sets are shown in green.

way to improve it. The construction of basis sets requires a lot of experience as well as testing and has a clear "trial and error" component. Several basis sets are available in the basis set library of DMol^3. Comparisons with highly accurate density-functional codes employing basis sets that can be systematically improved, like the LAPW method in the WIEN2k implementation [136], have been made for this project. They have shown that the basis sets available in the DMol^3 library provide basically the same accuracy. Details of these comparisons are given in Appendix A. However, the number of basis functions required for a given accuracy in case of DMol^3 is far smaller. As the bottleneck in DFT calculations on large systems is the diagonalization of the Hamiltonian, which scales like the cube of the number of basis functions, DMol^3 is therefore much faster than current LAPW and APW+lo implementations for large systems and makes the extensive potential-energy surface calculations required for the present work feasible.

At large distances from the nuclei the wave-functions decay exponentially. This can be exploited by truncating the basis functions at some cutoff radius. By a soft confining potential it is ensured that the basis functions do not have any discontinuities in value and in their derivatives at the cutoff radius. This real-space cutoff has to be tested carefully. The finite range of the basis functions drastically reduces the number of integrations as only matrix elements for nuclei have to be calculated, which are closer than twice the cutoff radius. For large systems this results in linear scaling. On the other hand, cutoff radii, which are too small, can affect the shape of the basis functions reducing the quality of the basis set. Typical cutoffs which are a good compromise between efficiency and accuracy are about 9-10 bohr.

While plane waves are a natural choice for calculations using periodic boundary conditions, the applicability of localized atomic orbitals in this case is less obvious. To fulfill the requirements of the Bloch theorem each basis function χ_μ centered at nucleus μ is translated to all positions of nucleus μ in all image unit cells at positions $\mathbf{n}$ by the lattice vectors $\mathbf{T_n}$. The basis functions now become the Bloch functions $\varphi_\mu^{\mathbf{k}}(\mathbf{r})$ depending on the k-point $\mathbf{k}$.

$$\varphi_\mu^{\mathbf{k}}(\mathbf{r}) = \sum_{\mathbf{n}=-\infty}^{\infty} e^{i\mathbf{k}\mathbf{T_n}} \chi_\mu^{\mathbf{n}}(\mathbf{r} - \mathbf{T_n}) \tag{6.2}$$

The Hamilton and overlap matrix elements are calculated by

$$\begin{aligned} H_{\mu\nu}^{\mathbf{k}} &= \sum_{\mathbf{n}=-\infty}^{\infty} e^{i\mathbf{k}\mathbf{T_n}} < \chi_\mu^0|H|\chi_\nu^{\mathbf{n}} >=< \varphi_\mu^{\mathbf{k}}|H|\varphi_\nu^{\mathbf{k}} > & (6.3) \\ \text{and} \quad S_{\mu\nu}^{\mathbf{k}} &= \sum_{\mathbf{n}=-\infty}^{\infty} e^{i\mathbf{k}\mathbf{T_n}} < \chi_\mu^0|\chi_\nu^{\mathbf{n}} >=< \varphi_\mu^{\mathbf{k}}|\varphi_\nu^{\mathbf{k}} > \quad . & (6.4) \end{aligned}$$

The single particle states $\phi_i^{\mathbf{k}\sigma}$ are constructed from the periodic Bloch basis functions.

$$\phi_i^{\mathbf{k}\sigma} = \sum_{j=1}^{n} c_{ij}^{\mathbf{k}\sigma} \varphi_j^{\mathbf{k}} \tag{6.5}$$

In summary, the use of atomic orbitals as basis functions offers a lot of advantages for the present study. First, the number of basis functions is smaller than for other basis sets like LAPW or APW+lo at the same accuracy. The basis set superposition error is minimized and molecules and solids can be handled with the same type of basis functions. Additionally, the use of atomic orbital basis functions enables to deal with the electrostatic interaction in a particularly efficient way as will be shown in Section 6.4. Drawbacks are the somewhat unsystematic construction of the basis set and the complicated numerical integration techniques that are required to calculate the matrix elements.

6.3 Numerical Integration

Once the basis functions have been defined, a way to represent them in a practical calculation has to be found. While other types of localized basis functions like Gaussian type orbitals [100] can be given analytically, atomic orbitals require a purely numerical treatment. Three-dimensional numerical integration is applied in most DFT codes for example to calculate the exchange-correlation matrix elements. In DMol^3 it has a particularly essential role, because it is used for the calculation of all matrix elements, which poses no limitations on the form of the basis functions, making the use of an atomic orbital basis possible at all.

An efficient way to calculate the integrals is to use a partitioning technique that is based on the fact that atoms retain much of their identity even in a molecular or solid environment. The idea is to decompose an integral of a complex function $f(\mathbf{r})$ over all space, i.e. over all atoms, to a summation of integrals over simpler functions $f_\alpha(\mathbf{r})$ centered at the nuclei α. f might be for example $f = \varphi_i(\mathbf{r})H\varphi_j(\mathbf{r})$.

$$\int f(\mathbf{r})d\mathbf{r} = \sum_\alpha \int f_\alpha(\mathbf{r})d\mathbf{r} = \sum_\alpha \int f(\mathbf{r})p_\alpha(\mathbf{r})d\mathbf{r} \tag{6.6}$$

The functions $f_\alpha(\mathbf{r})$ can be calculated from $f(\mathbf{r})$ by multiplying $f(\mathbf{r})$ with a partition function $p_\alpha(\mathbf{r})$ centered at atom α. Many partitioning schemes have been suggested in the literature. Bader introduced a scheme relying on density gradients [137], but the boundaries of the atomic regions are hard to calculate. Voronoi polyhedra or Wigner-Seitz cells are easy to construct, but these approaches make no use of the spherical symmetry close to the nuclei [138]. In DMol^3 a technique based on the partitioning scheme proposed by Hirshfeld [139] is employed. It is based on the "stockholder principle": The free atoms are used as reference and all changes in the density at a point in space due to the interaction of the atoms is partitioned among the individual atoms according to the ratio of the densities of the non-interacting free atoms at this point in space. Mathematically, a function $g_\alpha(\mathbf{r})$ is chosen for each center α. In case of a Hirshfeld charge analysis $g_\alpha(\mathbf{r})$ would be the atomic electron density. Then for each atom α the partition function can be defined as

$$p_\alpha(\mathbf{r}) = \frac{g_\alpha(\mathbf{r})}{\sum_\beta g_\beta(\mathbf{r})} \tag{6.7}$$

In general $g_\alpha(\mathbf{r})$ is a sharply peaked function which typically is large close to the atom it is centered at and small close to all other atoms. The denominator leads to a normalization of the partition functions making the functions $f_\alpha(\mathbf{r})$ sum up exactly to the original function $f(\mathbf{r})$. The partition functions can be made dependent on the atom sizes by including the electron densities ρ_α of the free atoms α. Typical choices for g_α are ρ_α^2 or ρ_α/r^2 [133]. There are no strict boundaries separating the space between the atoms and the partition functions of neighbored atoms can overlap. The resulting smooth decay of the partition functions is particularly apt for numerical integration. The principle of the partition functions is demonstrated in Fig. 6.2.

The atom-centered functions $f_\alpha(\mathbf{r})$ can easily be integrated with an angular-radial product scheme. For this purpose the integrals over the atom-centered functions can be evaluated numerically using suitable integration grids. The construction of these grids is crucial for the accuracy and efficiency of the whole method. Most current grids are based on the work of Becke [140]. The single-center integrations are separated

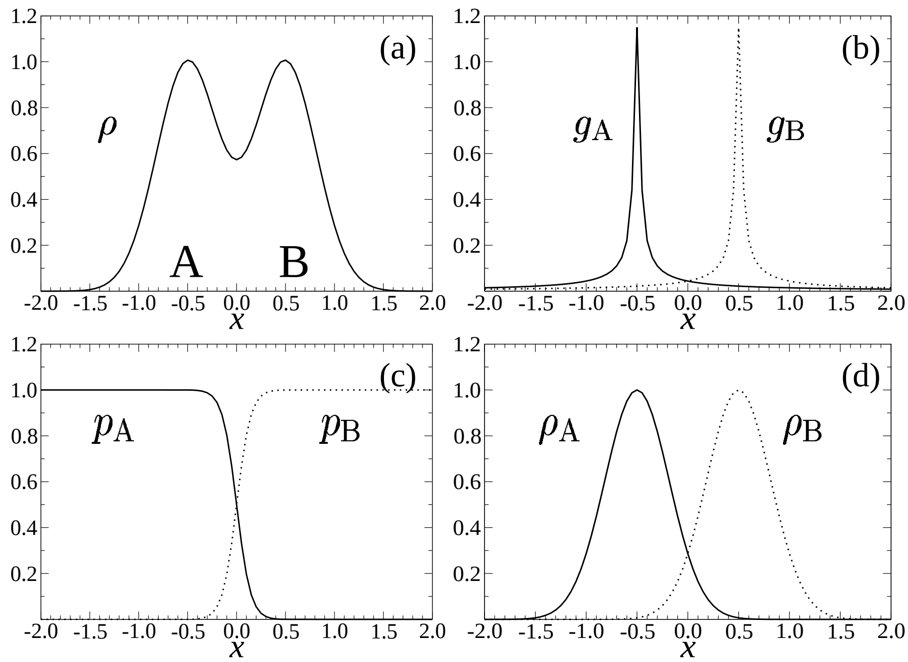

Figure 6.2: Principle of the partitioning scheme used in DMol^3. The function ρ around two centers A and B to be partitioned is shown in (a). In (b) examples for sharply peaked functions g_{A} and g_{B} centered at the atoms A and B are given, which can be used according to Eq. (6.7) to construct the partition functions p_{A} and p_{B} shown in (c). Multiplication of f with p_{A} and p_{B} leads to the atomic centered functions ρ_{A} and ρ_{B} which sum up to ρ and can be integrated individually.

into radial and angular parts. The angular part consists of integrations over points located on the surfaces of spheres of different radii centered at the nuclei. The radii of these shells are determined by the radial grid. Because of the fast oscillations of the wave-functions close to the nuclei a dense sequence of shells is required in this region. The lower values of the basis functions far from the nucleus are less critical in the numerical integration and fewer shells are sufficient. The number of radial points N_r is given by

$$N_r = s \cdot 14(Z+2)^{1/3} \quad . \tag{6.8}$$

s is a scaling factor that can be adapted to increase the radial density of the grid, but typically a value of 1 is sufficient. Z is the nuclear charge making sure that heavier elements with a more complex electronic structure are sampled more accurately by a denser sequence of integration shells.

The angular distribution of the integration points is done according to a scheme introduced by Lebedev [141–144]. He suggested grids on the unit sphere of various point densities, which are determined by spherical harmonics up to a certain order. Some examples are given in Fig. 6.3. Close to the nuclei only a few integration points

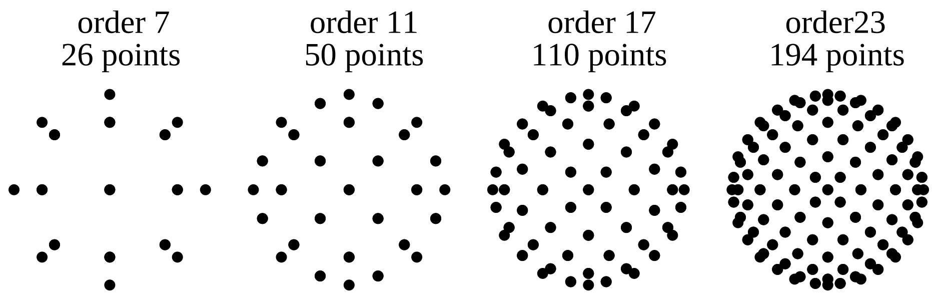

Figure 6.3: Integration points on the unit sphere. The point distributions of different orders introduced by Lebedev [141–144] possess octahedral symmetry and allow to reduce the computational effort by taking into account the molecular symmetry.

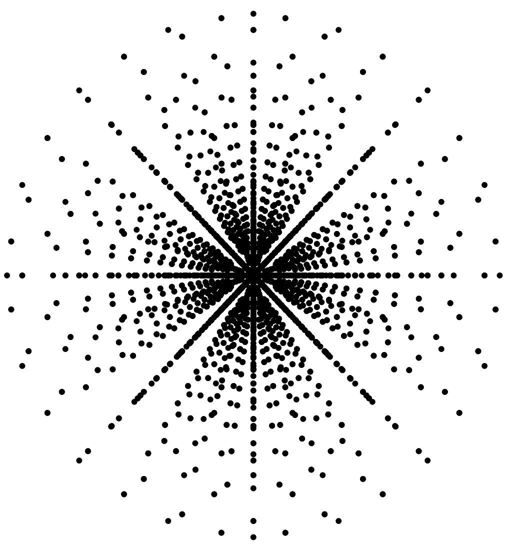

Figure 6.4: Integration grid for an oxygen atom. The full mesh is a superposition of all spherical Lebedev meshes of different radial distance from the nucleus and consists of 3287 points in this example.

on each sphere are sufficient because of the low angular dependence of the electronic structure, but far from the nuclei schemes of higher orders have to be applied. The Lebedev scheme is particularly useful, because the point arrangements possess octahedral symmetry. If the system of interest contains a high symmetry, it is possible to transfer the symmetry of the molecule to the grid points and integrate only over a irreducible wedge of points. The full system is then taken into account via weights assigned to these points. The full atomic integration mesh is a superposition of all spheres of different radii and typically consists of a few thousand points. In Fig. 6.4 the full integration mesh of an oxygen atom is shown. Finally, the three-dimensional integration mesh of the many-atom system is a superposition of individual atomic meshes. It should be noted that a too sparse integration mesh can result in "numerical noise", because inaccurate integrations can lead to arbitrary changes in the total energies as demonstrated in Fig. 6.5.

6.4 The Electrostatic Potential

The calculation of the electrostatic potential is often a time consuming step in a DFT calculation using localized basis sets. To simplify the calculation of the required inte-

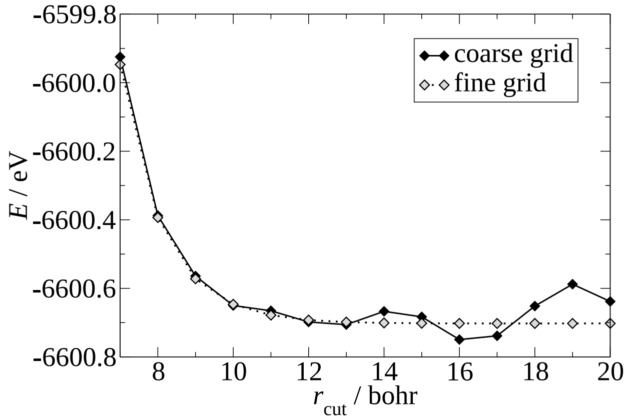

Figure 6.5: Total energy of an aluminium atom as a function of the real space cutoff for the basis functions for two different integration meshes. Both meshes consist of a constant number of points but as the cutoff increases the meshes have to cover more space, i.e. the point density decreases. While the fine mesh with many points provides accurate total energies for all cutoffs, the coarse mesh with fewer points is not dense enough for a precise integration beyond a cutoff of 10 bohr, and the total energies start to oscillate.

grals many DFT codes using localized basis sets replace the electron density obtained from the eigenstates by some fitted auxiliary density. This results in the introduction of an auxiliary fitting basis set with adherent fitting errors. In DMol^3 the partitioning scheme presented in the previous section paves the way for a very efficient and accurate calculation of the electrostatic potential without relying on a fitting technique. In a first step the total electron density is partitioned into atomic contributions $\rho_\alpha(\mathbf{r})$ for each atom α in the system. This enables the use of the single-center Poisson equation relating the electrostatic potential V_α to the density ρ_α at this center.

$$\nabla^2 V_\alpha = -4\pi\rho_\alpha \tag{6.9}$$

In a second step the atom-centered densities are projected onto spherical harmonics $Y_{\alpha,l,m}$ attached to the atoms.

$$\rho_{\alpha,l,m}(r) = \frac{1}{\sqrt{4\pi}}\frac{1}{\sqrt{2l+1}}\int Y_{\alpha,l,m}(\theta,\phi)\rho_\alpha(r,\theta,\phi)d\theta d\phi \tag{6.10}$$

In this way multipoles centered at the atoms are obtained, and for each multipole the density is represented by a one-dimensional radial density $\rho_{\alpha,l,m}(r)$. Sampling the projected density components at many radii gives a flexibility to the charge density representation which goes far beyond the one obtained with density fitting procedures. Although the multipolar expansion of the charge density has to be truncated, the truncation errors are usually far smaller than in density fitting procedures. For each of these one-dimensional multipole densities $\rho_{\alpha,l,m}(r)$, Poisson's equation is solved separately with high accuracy by replacing ρ_α and V_α in Eq. (6.9) by sums over all multipole densities and potentials. In the last step the resulting multipole potentials $V_{\alpha,l,m}(r)$ are reassembled to obtain the electrostatic potential of the atom-centered densities. Finally, these are combined to the electrostatic potential of the full system.

For calculations with periodic boundary conditions an Ewald summation [145] has been implemented [146]. In this method an auxiliary charge density consisting of Gaussian broadened point charges at the atomic sites and an exactly opposite second auxiliary charge density are introduced as well as a uniform background charge to compensate the point charges of the crystal lattice. Now the potential is calculated in two steps. The potential from the first auxiliary density and the uniform background charge density can be calculated in reciprocal space, whereas the potential of the second auxiliary density and the point charges rapidly converges in real space. To make use of the one-dimensional multipolar charge densities $\rho_{\alpha,l,m}(r)$ the Ewald method has been extended to multipole lattices. Because of the finite extent of the atom-centered charge densities only within the basis function cutoff radius the radial details of the electron density have to be taken into account resulting in a modified real space part of the Ewald summation [146].

In summary, DMol^3 uses a basis set free expansion and projection technique to decompose the total density into one-dimensional multipolar densities, for which Poisson's equation can be used to obtain one-dimensional potentials that are reassembled to obtain the electrostatic potential of the full system. In contrast to traditional density fitting schemes, which scale like the cube of the system size [138], for large systems this approach is very efficient and scales with the square of the system size for molecules and linearly with system size for calculations using periodic boundary conditions [146].

6.5 The Eigenvalue Problem

In contrast to plane wave basis sets, localized basis functions centered at different atoms are not orthogonal to each other. Therefore a special technique is required to determine the eigenvalues and the eigenvectors of a given Hamiltonian. The procedure will be described here in detail because this will be of importance for the implementation of the spin-constrained density-functional method described in Chapter 12. The non-orthogonality of the localized basis functions is reflected by an overlap matrix **S** which is not equal to the unit matrix **I**. To determine the eigenvectors and eigenvalues of a given Hamilton operator for each spin σ, first the Hamilton and overlap matrix elements are calculated by numerical integration.

$$H^\sigma_{ij} = < \chi_i | H^\sigma | \chi_j > \quad (6.11)$$

$$S_{ij} = < \chi_i | \chi_j > \quad (6.12)$$

The problem is that these matrix elements are not given in an orthonormal basis representation. Therefore the secular equation to be solved is

$$\mathbf{H}^\sigma - \lambda^\sigma \mathbf{S} = 0 \quad . \tag{6.13}$$

λ is the diagonal matrix containing all the eigenvalues. This eigenvalue problem has to be transformed into the standard form with an orthogonal basis representation. Therefore the matrix $\mathbf{U}$ has to be determined by a Cholesky factorization [147].

$$\mathbf{S} = \mathbf{U}^\mathrm{T}\mathbf{U} \tag{6.14}$$

Using $\mathbf{U}$, which now contains all information from the overlap matrix, the eigenvalue problem can be transformed to the standard form.

$$(\mathbf{U}^\mathrm{T})^{-1}\mathbf{H}\mathbf{U}^{-1} - \lambda(\mathbf{U}^\mathrm{T})^{-1}\mathbf{S}\mathbf{U}^{-1} = \mathbf{H}' - \lambda\mathbf{I} = 0 \tag{6.15}$$

Then the transformed Hamiltonian $\mathbf{H}'$ represented in an orthogonal basis can be diagonalized to yield the eigenvectors $\mathbf{c}'$ in the orthogonalized basis representation and the eigenvalues ϵ_i, which do not depend on the representation. In the last step the eigenvectors have to be transformed back to the non-orthogonal atom-centered basis.

$$\mathbf{c} = \mathbf{U}^{-1}\mathbf{c}' \tag{6.16}$$

6.6 The Harris Functional

In DMol^3 the total energy is not calculated according to the Kohn-Sham functional but using the Harris functional [148, 149]. Contrary to the usual applications of the Harris functional, in which non-selfconsistent charge densities are used to obtain crude energy estimates in just one iteration, in DMol^3 the Harris functional is applied to obtain accurate densities in a standard self-consistency cycle. The total energy E_tot according to the Harris functional is

$$\begin{aligned} E_\mathrm{tot}[\rho^\uparrow, \rho^\downarrow] &= \sum_{i,\sigma} f_i^\sigma \epsilon_i^\sigma + E_\mathrm{XC}[\rho^\uparrow, \rho^\downarrow] - \sum_\sigma \int \rho_\sigma (V_{\mathrm{XC},\sigma} + \frac{V_\mathrm{e}}{2}) d\mathbf{r} \\ &\quad + \sum_{\beta \neq \alpha} \frac{Z_\alpha Z_\beta}{|\mathbf{R}_\alpha - \mathbf{R}_\beta|} \end{aligned} \tag{6.17}$$

The f_i^σ are the occupation numbers of the Kohn-Sham orbitals ϕ_i^σ of spin σ. The reason for using the Harris functional instead of the Kohn-Sham functional is that then errors due to inaccuracies in the charge density enter the total energy only in second order. These inaccuracies can arise from imperfect self-consistency, basis set limitations and limitations of the numerical integration. In contrast to the Kohn-Sham functional the Harris functional has a saddle point at the correct Kohn-Sham density [138, 150, 151], but both functionals are stationary for the same densities and yield the same total energies, which is a basic requirement for the applicability of the Harris functional.

In a typical calculation the total energies are in the range of 10^5 eV. However, one is usually interested in binding energies with respect to some reference system. These binding energies, which are in the order of 1 eV and should have a precision of about 0.01 eV, are very sensitive to numerical noise as they are differences of large numbers. Instead of total energies only binding energies E_{bind} with respect to the free spherical atoms are calculated in DMol^3 to reduce the numerical noise, and when needed, the total energies are restored by adding the total energies $E_{\text{atom}}^{\text{ref}}$ of the free reference atoms.

$$E_{\text{tot}} = E_{\text{bind}} + \sum E_{\text{atom}}^{\text{ref}} \tag{6.18}$$

The direct calculation of the binding energy is done by subtracting the densities of the free spherical atoms from the total densities in the integrands for the evaluation of the Hamilton matrix elements [149].

6.7 Summary

Apart from the features mentioned in the previous sections many other aspects of the DMol^3 approach are of interest. The forces are calculated according to the Hellmann-Feynman theorem [152, 153]. Due to the localized basis functions a Pulay correction [154] of the forces is required. More precise forces can be obtained by taking into account the imperfect self-consistency of the charge density [152]. Scalar relativistic effects based on the approaches of Koelling and Harmon [155] and of Takeda [156] can be included via local pseudopotentials in all-electron calculations [157]. These additional potentials are localized around the nuclei and include the effects of the mass-velocity and Darwin terms. To improve the convergence of the self-consistent determination of the ground state density a very efficient Pulay charge density mixing scheme is implemented [158–160] that can reduce the number of required iterations drastically. Geometry optimizations can be done with the "eigenvalue follow" (EF) algorithm [161, 162]. Molecular dynamics calculations are available based on the Verlet algorithm [163]. All algorithms have been implemented in DMol^3 in a way to take full advantage of any symmetry of the system under consideration. Apart from the standard all-electron calculations DMol^3 also offers to use pseudopotentials to speed up calculations [164] by approximately one order of magnitude for large systems of heavy elements at the price of a slightly lower accuracy.

All in all, DMol^3 is a very accurate and fast code (cf. Appendix A). The matrix setup, the calculation of the density on the mesh as well as the Pulay orbital derivative terms are scaling linearly with system size [165]. Therefore, the diagonalization of the Hamilton matrix scaling like the cube of the system size soon becomes the dominant term for DMol^3, but the efficient basis set keeps the dimension of the matrix very small.

Chapter 7

Neural Network Interpolation

7.1 Fitting Potential-Energy Surfaces

Even extensive first-principle studies of potential-energy surfaces can only provide a limited number of energy points, typically of the order of 1000, due to the high computational costs of these calculations. On the other hand, for the calculation of a sticking curve the sticking probability has to be calculated for about 20 different kinetic energies. Each of these sticking probabilities must be based at least on a few thousand molecular dynamics trajectories to obtain statistically meaningful results. Finally, each of these trajectories requires the energies and forces for some hundred different configurations. The total number of energy calculations required to determine a sticking curve is therefore of the order of 10^7, which is far beyond what can be obtained from direct *ab initio* calculations. This dilemma can be solved by fitting a continuous potential-energy surface to the *ab initio* energy points provided on a finite grid, to make energies and forces available for arbitrary molecular geometries. In recent years a lot of effort has been spent in the development of corresponding interpolation schemes [86], each of which has particular advantages and disadvantages. Basically, these schemes can be classified into two different categories, "mathematical" approaches and "physical" approaches.

Mathematical methods in general do not require any knowledge about the functional form of the potential-energy surface. They are designed to be very flexible, but typically also require more *ab initio* data points than physical approaches. A simple example for a mathematical method is the interpolation using cubic splines [147]. For two- or three-dimensional potential-energy surfaces splines are very efficient, but the interpolation error using splines increases rapidly with the number of dimensions, and for problems with more than about four degrees of freedom splines become impractical [166]. A method that is applicable also for the interpolation of six-dimensional potential-energy surfaces is the modified Shepard interpolation [167]. In this method the potential close to an *ab initio* point is expanded as a second-order Taylor series. The potential of a new configuration is then constructed as a weighted sum over the

Taylor expansions with respect to many DFT points. The DFT data set does not need to be known completely in the beginning of the fit, but can be extended by running classical molecular dynamics simulations and adding further DFT points in frequently visited regions of the PES or in regions that are not well fitted. The latter can be identified by comparing the predicted energies with respect to the individual Taylor expansions. In this way, the convergence of the fitted potential-energy surface as a function of the number of points can be tested systematically. Another method that has been used recently [26, 27] for the fitting of six-dimensional potential-energy surfaces is the neural network approach [168, 169]. In principle, this very flexible and highly non-linear technique allows to fit any real-valued function to arbitrary accuracy. First applications have shown that the performance of this method is very well suited for molecular dynamics simulations of dissociation events [26, 27]. A detailed description of this technique will be given below. Another mathematical method is genetic programming [170]. In this method the parameters of some analytic functions as well as the functional forms themselves are optimized simultaneously. To find the optimal functional form varying combinations of simple basis functions are used. However, this method so far has not been employed to more than three dimensional potential-energy surfaces. A method, which is at the borderline between pure mathematical fits and physical fits, is to use reasonable analytic functions with several adjustable parameters [17, 86, 171–174]. These functions, which are rather inflexible, have to be selected to represent the symmetry of the system correctly, and the closer they are to the real shape of the potential the more accurate fits can be obtained. Unfortunately, these functions are very hard to find, and if not chosen carefully, analytical functions may easily introduce artefacts into the potential. A variation within the analytical fit approach is the use of the corrugation reduction method [175–179]. The idea of this method is to reduce the corrugation of the potential-energy surface by removing the energies due to the interaction of the individual atoms with the surface. This requires the additional calculation of a three-dimensional potential-energy surface for the atom-surface interaction. The advantage of this method is that the modified potential-energy surface is much easier to fit since most of the surface site dependence, i.e. the corrugation, of the potential is removed. In principle, many techniques could be used to fit this smoothed PES, but so far in most cases a combination of splines and analytic functions has been used. Drawbacks of this method are that it cannot be extended easily to more than six dimensions and its inherent restriction to non-spin-polarized systems. Spin-polarized molecules like O_2 change their spin state upon adsorption, making the spin state to be used in the atomic potential-energy surface ill-defined.

Examples for physical fitting schemes are the tight-binding and the embedded atom method. In the tight-binding method [180–183] the quantum mechanical nature of bonding is taken into account explicitly. The quantities to be parameterized are the elements of the Hamilton and the overlap matrices as a function of the interatomic distances in an atomic basis representation. The resulting secular equation has to be solved by a matrix diagonalization making this method rather time consuming compared to mathematical fits. However, in the tight-binding method the number of required DFT data points is drastically reduced for a given fit accuracy. The basic idea of the embedded atom method (EAM) [184–186] as a semi-empirical potential form is to embed each atom into the electron density of all other atoms of the system. Then, the total energy is the sum of the embedding energy that includes all many-body effects and an electrostatic repulsion term for the interaction between the nuclei. An extension of the embedded atom method is the modified embedded atom method (MEAM) [187], that also includes angular dependent terms to account for covalent bonding. Being developed mainly for bulk materials so far no applications of the embedded atom method to potential-energy surfaces for the dissociation of molecules on surfaces exist, and in general its applicability to these systems has been questioned [188].

In summary, a fitting scheme suitable for all types of problems does not exist. In general, mathematical fitting methods are very fast in the calculation of energies and energy gradients. Their disadvantages are the rather large number of required *ab initio* data points (typically a few thousand), their inability to extrapolate energies beyond the configuration space spanned by the DFT energy points and their rapidly increasing complexity with the dimensionality of the problem. Physical schemes, on the other hand, require less DFT data points (typically a few hundred), possess a reasonable extrapolation capability and allow in principle an easier extension to higher dimensionality. Their drawback is the higher computational effort, for example due to the diagonalization of matrices in case of the tight-binding method, or their inapplicability to the dissociation of molecules at surface in case of EAM, respectively. For these reasons a mathematical fitting method, namely the neural network technique, will be used in this project. Previous work has shown that this method is particularly suitable to be combined with molecular dynamics simulations [26, 27], because the calculation of the energies but also of the forces is very fast and accurate. The following sections introduce the neural network technique as well as its application in molecular dynamics simulations.

7.2 Neural Networks

Inspired by the neural signal processing in biological systems [189], the first artificial neural networks (NN) have been introduced in 1959 [190]. Since then neural network techniques have become a standard tool in many fields of research. They have proven useful in applications like pattern recognition and classification problems (digitizing handwritten text [191], finger print identification [192], heart diseases diagnostics [193] and speech recognition [194]) and analysis of complex data (prediction of stock market performance [195] as well as DNA and protein structure analysis [196–198]). It is also well known that neural networks are well suited for the fitting of non-linear functions of one or more variables [199, 200]. They are very flexible, do not require any assumptions about the functional form of the underlying physical problem and

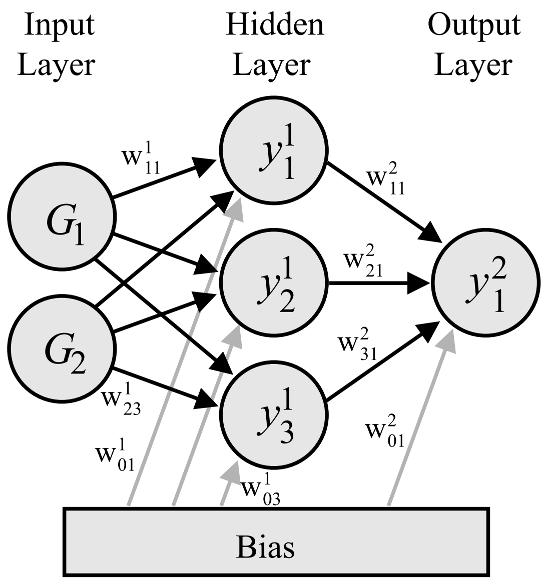

Figure 7.1: Structure of a 2-3-1 feed-forward neural network. The circles represent the nodes, that are connected with the nodes in the adjacent layers by the weights w_{ij}^k. The bias adds a constant to each node in the hidden and output layers to adapt the position of the non-linearity intervals of the activation functions. The function values y_i^k are calculated according to Eq. (7.1).

are in principle able to fit any function to arbitrary accuracy. A few years ago the first applications of neural networks to the interpolation of potential-energy surfaces have been published [166, 201]. Recently, Lorenz, Groß and Scheffler proved the applicability of neural networks in molecular dynamics simulations on high-dimensional potential-energy surfaces [26, 27], which motivated their use in the present work. Since a very detailed description of the relevant aspects of neural networks can be found in [26], only a short summary of the neural network technique and its modifications for the current project will be given here.

Many different types of neural networks exist adapted to the problems they are applied to. For functional fittings the class of multilayer feed-forward neural networks [168, 169] has shown to be particularly useful, and consequently this is the network type that will be applied in this work to fit the six-dimensional potential-energy surface for the oxygen dissociation on the Al(111) surface. The general structure of a feed-forward neural network is shown schematically in Fig. 7.1. It consists of several layers each of which contains one or more nodes represented by the grey circles. In the given example the two nodes in the input layer represent the two variables of the function to be fitted. The function value corresponds to the node in the output layer. Between the input layer and the output layer one hidden layer with three nodes is located. The term hidden layer is used because the numerical values at the nodes of this layer are just auxiliary quantities without a particular meaning. Each node i of a certain layer is connected with the nodes j in the subsequent layer via

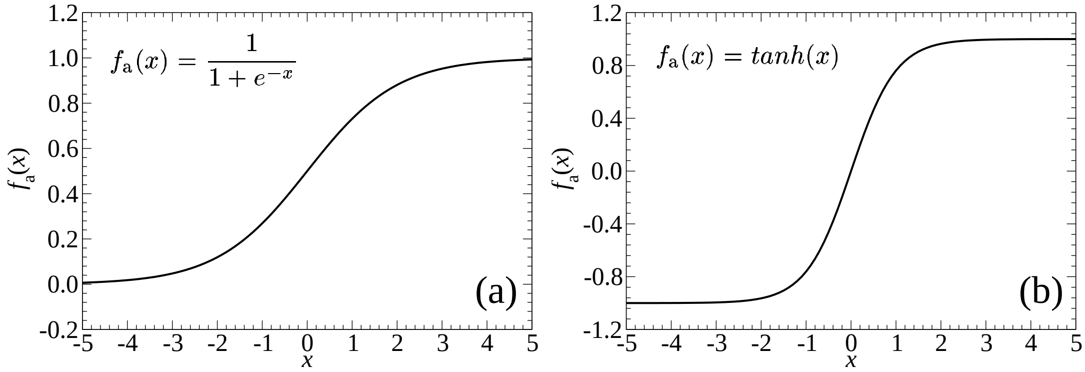

Figure 7.2: Activation functions used in neural network fits. (a) shows the sigmoid function and (b) the hyperbolic tangent function.

weights w_{ij}^k, where k represents the index of the target layer. On each node all the values from the nodes of the preceding layer are summed up after being multiplied by the connecting weights. On the resulting sum a non-linear function f_a is applied. This function is called activation function, transfer function or basis function of the network. Typically, activation functions are sigmoidally shaped functions, but also other types of functions like Gaussians can be used. The sigmoid and the hyperbolic tangent function are exemplified in Fig. 7.2. A requirement for an activation function is its differentiability, because for the weight optimization the derivatives of these functions with respect to the individual weights have to be calculated. The importance of the activation functions lies in that they introduce the non-linearity in the neural network, which allows to fit all types of functions. For very large or very small arguments the activation functions converge to a constant number, but for a certain interval the output changes significantly in a non-linear way. The bias unit shown in Fig. 7.1 acts as an adjustable offset to adjust the position of the non-linearity interval of the activation functions. Then the obtained function value of each node is passed to all the nodes of the subsequent layer and multiplied with the corresponding connecting weights. In a feed-forward neural network the nodes within one layer are not interconnected, but it is possible to add direct links from the nodes in the input layer to the output layer nodes, which can be useful if there are linear dependencies between the input and output data. In the output layer the values are collected and the output value is calculated by applying an activation function, which in this case is typically a linear function to avoid any constraints on the possible range of output values. Another characteristic feature of the feed-forward neural network is that the information is transferred only in one direction through the network, from the input via the hidden layers to the output layer, which is different in other network types. In general, each layer including input and output layers can contain many more nodes than in the simple example shown in Fig. 7.1, and also more than one hidden layer is typically used.

All in all the neural network defines a complicated non-linear function relating the input values to the output values. This function can be given analytically and it depends on many parameters, the weights w_{ij}^k. The value y_j^k of node j in layer k can be obtained from the values y_i^{k-1} of all nodes i in the preceding layer $k-1$ and from the connecting weights by

$$y_j^k = f_{\mathrm{a}}^k \left(w_{0j}^k + \sum_i w_{ij}^k y_i^{k-1} \right) \quad . \tag{7.1}$$

w_{0j}^k is the bias weight for the activation function f_{a}^k acting on node j. In case of y_j^k referring to a node in the first hidden layer ($k=1$) the y_i^{k-1} in Eq. (7.1) are the i input values (coordinates) of one data point, for which in this work the symbol G_i will be used. Using Eq. (7.1) the complete functional form of the full neural network can be constructed. For a given set of weights the output y_1^2 of the three layer neural network shown in Fig. 7.1 is defined by the vector $\mathbf{G} = (G_1, G_2)$ of all input coordinates of one data point.

$$y_1^2\left(\mathbf{G}\right) = f_{\mathrm{a}}^2 \left(w_{01}^2 + \sum_{j=1}^{3} w_{j1}^2 f_{\mathrm{a}}^1 \left(w_{0j}^1 + \sum_{i=1}^{2} w_{ij}^1 G_i \right) \right) \tag{7.2}$$

To label uniquely the structure of a multilayer feed-forward neural network a short hand notation has been established. A "2-3-1 tl" network consists of 2 input nodes, 3 nodes in one hidden layer and one output node. The "t" represents the use of a hyperbolic tangent activation function in the hidden layer and the "l" stands for a linear activation function in the output layer. For the sigmoid function the abbreviation "s" is used.

A priori it is not known which network architecture will be best for a given fitting problem and empirical tests are necessary to find the optimum number of hidden layers and nodes as well as the best activation functions. Too few nodes in the hidden layers will result in underfitting, i.e. important features of the PES will be smoothed out. Too many nodes increase the flexibility of the network and can lead to overfitting, i.e. artificial features appear in the function, which do not have any physical justification [166]. Therefore, one should try to use the smallest possible architecture that yields the desired accuracy. Small networks can also be used to achieve a limited smoothing of the DFT data that might be wanted to reduce the numerical noise in the DFT energies. However, care must be taken that the general shape of the potential-energy surface remains correct. Compared to splines neural networks are less sensitive to noise or outliers, but the latter have to be watched with caution as also real physical extrema might get lost if the PES is not sampled on a dense enough grid. There are no constraints on the coordinates of the input data points. They do not need to be located on a regular grid, but they necessarily have to include all important characteristics of the potential-energy surface, like the positions of energy minima and maxima, energy valleys and reaction barriers.

7.3 Weight Optimization

The intended application of the neural network in this work is to predict energy values for arbitrary input configurations **G**. Therefore, the connecting weights have to be known, and a neural network fit is nothing else but finding the optimal set of weights. The weights are determined in an optimization process based on a set of known output values, i.e. the DFT data points. In the context of neural networks the optimization of the weights is called learning and is done using standard iterative optimization algorithms. The latter require a cost function Γ which is minimized in the learning process. For a given set of weights $\mathbf{w}$ the cost function is the sum of the squared differences between the actual outputs of the neural network $y_j(\mathbf{w}, \mathbf{G}_j)$ and the known correct target values $\mathcal{T}_j(\mathbf{G}_j)$.

$$\Gamma = \sum_j \left| y_j \left(\mathbf{w}, \mathbf{G}_j \right) - \mathcal{T}_j \left(\mathbf{G}_j \right) \right|^2 \tag{7.3}$$

A full optimization cycle in which each data point is presented once to the network is called an epoch. The new updated weight for an epoch μ is calculated from the corresponding weight of the previous epoch $\mu-1$ and the derivative of the cost function with respect to this weight.

$$w_{ij}^k(\mu) = w_{ij}^k(\mu - 1) - \eta \frac{\partial \Gamma}{\partial w_{ij}^k} \quad , \tag{7.4}$$

where $0 < \eta < 1$ is the learning rate. If η is a constant this is basically a steepest descent algorithm, but also more sophisticated schemes like conjugate gradients and quasi-Newton methods [147] can be used. In order to start the optimization procedure an initial guess for the weights is required. Usually random numbers are used for this purpose. In the fitting process care must be taken that neither overfitting nor underfitting occurs. Therefore, several checks have to be done to analyze the quality of a fit.

A very simple but efficient test is to compare parts of the fitted high-dimensional potential-energy surface that can easily be visualized, i.e. two-dimensional cuts, with corresponding images of the original DFT data. Artificial wiggles in between the DFT data points are a clear indication of overfitting. Another method that should be used is to split up the DFT data set into two subsets. The first subset, which typically contains about 90 % of the data points, is used to optimize the weights of the network and is called the training data set. The remaining data points form a test set that is not used to optimize the weights. Since the DFT energies of the test points are known, they can be used to check the accuracy of a fit by comparing the values predicted by the neural network with these exact values, establishing a measure for the interpolation capability of the neural network. In the ideal case the division of the whole data set into the training and the test set is done randomly.

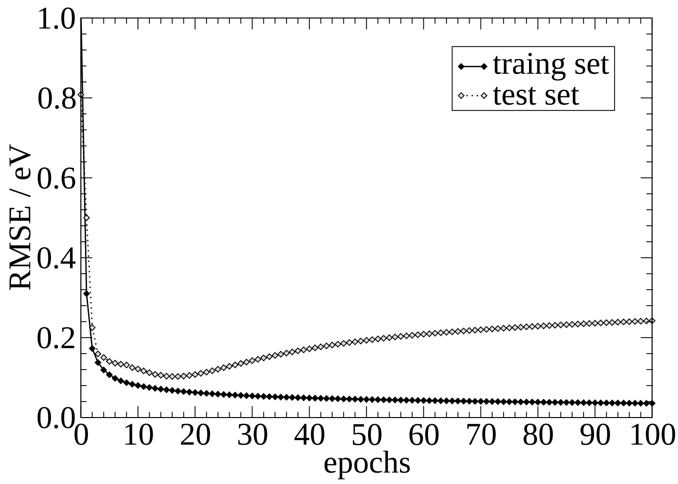

Figure 7.3: Evolution of the root mean squared errors (RMSE) of the training and test data sets in a neural network fit.

However, one has to make sure that all data points which represent extrema of the potential-energy surface are included in the training set. Then in each epoch of the optimization process the root mean squared error (RMSE) can be calculated for both data sets (training and test set).

$$\mathrm{RMSE} = \sqrt{\frac{1}{n}\sum_{i=1}^{n}(y_i - \mathcal{T}_i)^2} \quad , \tag{7.5}$$

where n is the number of data points in the respective data set. A typical evolution of the RMSE of the training and test data as a function of the optimization epochs is shown in Fig. 7.3. In the first epochs the errors of both data sets decrease rapidly with the test error being higher in value. This can be expected as these data points are not included in the training of the network. Then the test error reaches a minimum and afterwards increases slowly, while the training error is reduced continuously. The epoch in which the test error reaches its minimum corresponds to the set of weights with the best prediction accuracy for unknown data points. Afterwards overfitting occurs in that on the one hand the fit of the training points still improves but the regions in between the training points are less accurately reproduced. Another general indication of overfitting is a large discrepancy between the RMSE of the training and test points. To our experience, it is acceptable to have a test RMSE at most twice as high as the training RMSE. A higher ratio is an indication of a poor fit.

While the RMSE of the training set is a good measure for the overall accuracy of a fit, it gives little information on the individual regions of the potential-energy surface, which might be of different importance for the later application of the fit. An example are very high energy regions if the application is to perform molecular dynamics simulations on the interpolated potential-energy surface: Regions with a potential-energy higher than the initial kinetic energy of the molecule will never be reached in the molecular dynamics, and consequently a lower accuracy would be tolerable, while energy barriers and minimum energy paths should be modelled very accurately. To check the fit quality for the different regions individually, the data of the training set can be split up into different groups according to energy and molecular geometry. After the weight optimization the determined optimal set of weights can be used to calculate the mean absolute deviation (MAD) of these groups separately.

$$\mathrm{MAD} = \frac{1}{n}\sum_{i=1}^{n}|y_i - \mathcal{T}_i| \tag{7.6}$$

This allows a detailed insight into the quality of the fitted potential-energy surface. The accuracy of a fit in the individual regions can be controlled by assigning error-weights ω_i to the data points, which must not be confused with the weight parameters w_{ij}^k of the neural network. In the optimization of the neural network the purpose of the ω_i is to modify the errors of the individual training points and therefore the cost function to achieve a more accurate neural network fit in important regions of the potential-energy surface.

7.4 The Kalman Filter

In general, there are two types of learning procedures, on-line learning and off-line learning. In the latter case the whole training data set is presented to the neural network and afterwards the weights are updated, then the next epoch starts. In on-line learning the weights are updated after the presentation of each data point. The advantage of the latter method is a faster convergence in terms of required epochs and a higher probability of not getting trapped in local minima. On the other hand, most standard optimization schemes like conjugate gradient or quasi-Newton schemes can only be used in off-line learning.

An optimization scheme that can be applied to on-line learning is the Kalman filter [202, 203]. It was originally developed for the estimation of parameters from measurements that are generated in real time [204, 205], i.e. when the full data set is not available. Basically, the Kalman filter is a set of mathematical equations that allows to estimate the state of a linear dynamic system. As neural networks constitute non-linear functions, the original Kalman filter cannot be applied directly. Therefore, the extended Kalman filter (EKF) has been developed, which is based on the idea to linearize each new data point around the actual value of the estimate, i.e. the set of weights. These days the Kalman filter is frequently used in neural network fits [26, 205, 206]. Applying the Kalman filter the cost function $\Gamma(k)$ at the presentation of data point k is

$$\Gamma(k) = \sum_{i=1}^{k} e_i^2 \lambda(k)^{k-i} \quad , \tag{7.7}$$

where $e_i = \mathcal{T}_i(\mathbf{G}_i) - y_i(\mathbf{w}, \mathbf{G}_i)$ is the error of data point i, which is the difference between the correct target value $\mathcal{T}_i(\mathbf{G}_i)$ and the output value $y_i(\mathbf{w}, \mathbf{G}_i)$ of the neural network, that in turn depends on the weights and the input values. Equation (7.7) represents a weighted consideration of all previous updates i, the weighting being controlled by a forgetting factor $\lambda(k)$ that increases continuously with k and reaches a saturation value of 1 for very large k. Due to the exponent, $\lambda(k)^{k-i}$ is large for the most recent updates and exponentially decaying for past updates. The value of $\lambda(k)$ itself is given by

$$\lambda(k) = \lambda_0 \lambda(k-1) + 1 - \lambda_0 \quad . \tag{7.8}$$

The starting value $\lambda(0)$ is typically chosen empirically between 0.95 and 0.99 and λ_0 is a constant between 0.9900 and 0.9995 [26]. The rather complicated equations of the extended Kalman filter can be derived from the minimization of Eq. (7.7), details can be found in [26, 207, 208].

The drawback of the Kalman filter is that it is computationally very demanding to adapt the weights after the presentation of each individual data point. However, the computational effort can be reduced by taking into account that data points, which are already fitted rather accurately, will cause only small changes in the weights. Therefore it is possible to reduce the computational demand by setting a threshold value ξ for the error of a data point. Only if the fitting error of a point is higher than this threshold value, which is typically given as a fraction of the root mean squared error of the whole data set, the weights will be adjusted. Otherwise the weights will not be changed and the neural network proceeds to the next training point. If this threshold is applied, the method is called adaptive extended Kalman filter. For all neural network fits in this work the adaptive extended Kalman filter has been applied instead of quasi-Newton methods to enable the more efficient on-line learning. In Fig. 7.4 the course of a neural network fit applying the extended Kalman filter is shown schematically.

Once an accurate set of weights is available, the calculation of the energies using the neural network is about 5 orders of magnitude faster than the original first-principles calculations. The price to be paid is the additional fitting effort, as typically many fits for different network architectures have to be carried out to find the best fit empirically. The total computational effort to find an accurate fit is in the order of a few self-consistent DFT energy calculations.

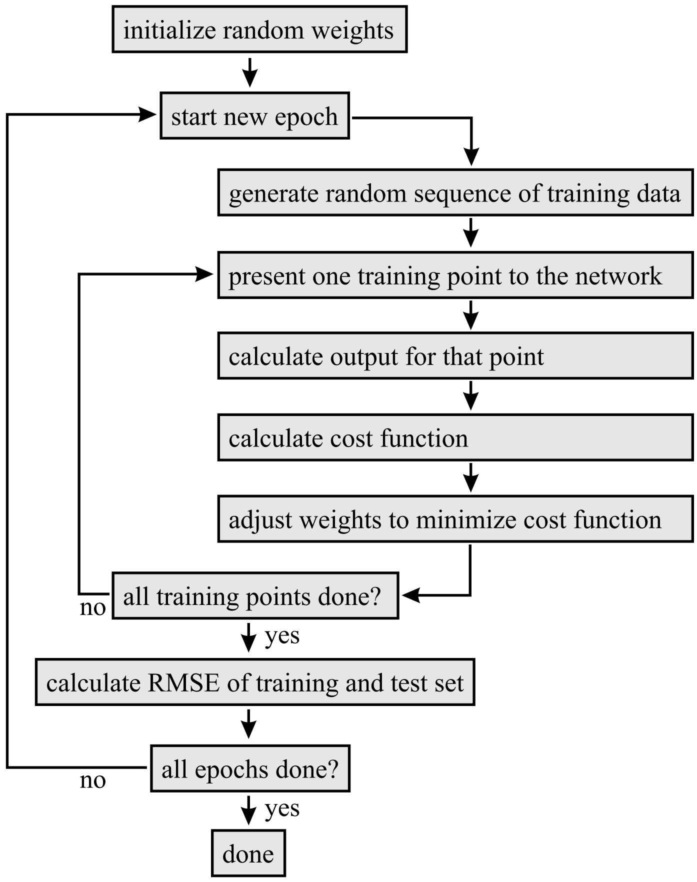

Figure 7.4: Schematic course of a neural network fit for a given number of epochs employing the extended Kalman filter.

Chapter 8

Molecular Dynamics Based on Neural Networks

8.1 Introduction

To perform molecular dynamics simulations, the forces on the nuclei, i.e. the derivatives of the potential-energy surface with respect to the nuclear coordinates, are required. One possibility would be to evaluate the derivatives numerically using finite differences, which is an elaborate task for high dimensional potential-energy surfaces. A more precise method is to calculate the analytic derivatives of the potential-energy surface. This requires not only to have a continuous representation of the potential-energy surface, but it must also be differentiable, which is fulfilled by a neural network interpolation and has been used already in the weight optimization. The derivatives F_{G_i} of the total energy with respect to the input parameters G_i can be obtained from the neural network by

$$F_{G_i}(\mathbf{G}) = -\frac{\partial E(\mathbf{G})}{\partial G_i} \quad , \tag{8.1}$$

where we have used the variable E for the output of the network as it represents the potential-energy. Using analytic derivatives it is guaranteed that the forces are consistent with the energies and in particular that the forces are zero at local minima of the potential-energy surface. If the system of interest would be a molecule in the gas phase this would be all that has to be done, and the forces could be used directly in the classical equations of motion to describe the dynamics of the system. For the dissociation of a molecule on a surface, which has a periodic potential, further steps are required to provide the energies and forces for arbitrary molecular configurations. The necessary extensions of the neural network technique will be described in the next sections.

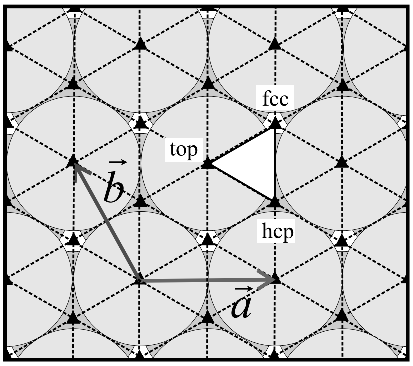

Figure 8.1: Irreducible part of the Al(111) surface. The mirror planes are represented by the dashed lines and the threefold rotational axes by the black triangles. The surface atoms are symbolized by the grey circles.

8.2 The Role of Symmetry

The Al(111) surface is highly symmetric. Apart from the translational symmetry there are three different mirror planes and three 3-fold rotational axes perpendicular to the surface located at the top, fcc and hcp sites. Therefore, the (1×1) unit cell of the Al(111) surface has six times the size of the irreducible wedge, which is spanned by the top, fcc and hcp sites as shown in Fig. 8.1. To avoid redundant calculations, the DFT energies are calculated for molecular positions inside the irreducible wedge only. The coordinate system, which is employed in the mapping of the six-dimensional potential-energy surface is shown in Fig. 8.2. Basically, it is a superposition of a Cartesian coordinate system for the center of mass of the molecule and a spherical coordinate system for the molecular orientation and bond length. θ is the angle between the molecular axis and the surface normal, ϕ is the angle between the positive x-axis and the projection of the molecular axis into the xy-plane, X, Y and Z are the center of mass positions of the molecule and d is the oxygen-oxygen bond length.

The DFT data points cover only a small fraction of the configuration space that is accessible to the molecule in molecular dynamics simulations. As a consequence, training the neural network only with this data set does not provide energies and forces for configurations outside the irreducible wedge. For this reason the coordinates X, Y, Z, θ, ϕ and d cannot be used directly as input for the neural network. Instead, the coordinates can be classified into two types, the “periodic” coordinates X, Y, θ and ϕ which cause periodic oscillations of the energy values when changed continuously, and the “non-periodic” coordinates d and Z. The lateral symmetry represented by X and Y has two different components. The first component is the translational symmetry of the Al(111) surface given by the lattice vectors $\vec{a}$ and $\vec{b}$ (cf. Fig. 8.1). One possibility to include this translational symmetry is to translate an arbitrary molecular

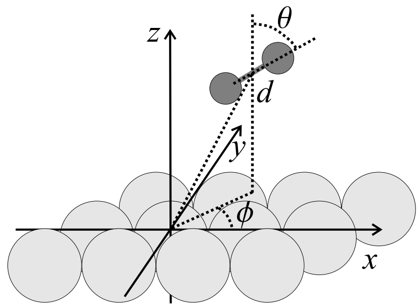

Figure 8.2: Six-dimensional coordinate system employed in the mapping of the potential-energy surface for the oxygen dissociation on the Al(111) surface.

configuration back into the unit cell, which is known to the neural network, before the energies and forces are calculated. This requires that the whole configurational space spanned by the (1×1) unit cell is known to the network. To achieve this, the second component of the lateral symmetry has to be taken into account, which is the symmetry within the unit cell. Here a simple translation is not sufficient, because the incorporation of the symmetry due to the mirror planes and rotational axes is far more involved. A straightforward but not very elegant way would be to unfold the DFT data set calculated for the irreducible wedge into the whole unit cell and train the neural network with this extended data set. This procedure has two clear disadvantages. First, the data set is significantly increased slowing down the optimization of the network weights. More severe is a second problem: Learning the energies for the whole unit cell means that configurations, which are equivalent by symmetry and must have the same energies, are fitted independently. Therefore, the fit accuracy can be different for equivalent points and different energies can emerge. This artificial symmetry breaking has to be avoided. In order to circumvent the problems related to the periodicity of the potential-energy with respect to the four coordinates X, Y, θ and ϕ it has been suggested to use so-called symmetry functions, which automatically map arbitrary molecular configurations into the irreducible wedge of the unit cell [26, 27]. Although a slightly different method has been used in the present work that is introduced in Section 8.4, in the next section a brief summary on molecular dynamics simulations based on symmetry functions will be given to motivate the development of a more general method.

8.3 Molecular Dynamics Based on Symmetry Functions

The basic idea in the application of symmetry functions is that any molecular configuration is mapped into the irreducible wedge of the unit cell before the energy is calculated by the neural network. Then it is sufficient if the training data set for the neural network includes only the DFT data points in the irreducible wedge, and no expansion of the data into the full unit cell needs to be done. A consequence of the mapping is that the coordinates X, Y, θ and ϕ cannot be used as input for the neural network directly. Instead, they are mapped on periodic functions, whose values then are provided as input to the neural network, i.e. $E(X, Y, Z, \theta, \phi, d)$ is replaced by $E(G_1, G_2...)$, the $G_i(X, Y, Z, \theta, \phi, d)$ now being the function values of the symmetry functions which form the input for the neural network. Basically this is a coordinate transformation of the DFT data set. The forces then can be obtained according to

$$F_\alpha = -\frac{\partial G_i}{\partial \alpha}\frac{\partial E}{\partial G_i} \tag{8.2}$$

with α representing one of the original coordinates X, Y, Z, θ, ϕ and d, respectively. It is important to note that the mapping is always done only in one direction, from the original 6 coordinates to the symmetry function values in both cases, in the training of the network and in the request of energies and forces for new configurations. It is not necessary to reconstruct the original set of coordinates belonging to a set of G_i, which allows for a high flexibility in the choice of symmetry functions. Also their number is not constrained to the dimensionality of the potential-energy surface, the reason of which will be given below.

The mapping procedure is similar to an analytic fit in that the symmetry functions have to reproduce the symmetry of the surface correctly. However, in contrast to an analytic fit they do not need to reproduce the DFT energies in value. This is done by the neural network, which is now trained to assign the DFT energies to the symmetry function values G_i. For each molecular configuration outside the irreducible wedge an identical set of symmetry function values for a configuration inside the irreducible wedge does exist. These two configurations are equivalent by symmetry, and are automatically assigned the same energies by the neural network, since the set of input coordinates G_i for the neural network is identical in both cases.

There are some requirements that have to be strictly fulfilled by the symmetry functions in order to be applicable in molecular dynamics. First of all, two inequivalent molecular geometries must not yield the same set of function values, because in case of these two geometries having different potential-energies the neural network would have to fit contradictory data, i.e. two different energies to the same configuration resulting in poor fits. All symmetry functions have to be continuous and differentiable. They have to describe correctly at least the translational symmetry of the surface unit cell, but preferably also the correct symmetry within the unit cell, so that all geometries within the unit cell which are equivalent by symmetry are mapped on the same set of function values $\mathbf{G}$.

A drawback of this method is that the symmetry functions have to be chosen very carefully. Any symmetry included in the analytic symmetry functions inevitably becomes a symmetry property of the interpolated potential-energy surface. This effect can be particularly harmful in molecular dynamics simulations, because symmetry elements like mirror planes strongly affect the rotational motion of the molecules. Therefore, it is desirable to reproduce the symmetry of the molecule surface system as exact as possible. In general, suitable analytic symmetry functions are hard to find and often this is possible only for very simple systems like an atom interacting with a surface. Already for a six-dimensional potential-energy surface constructing appropriate functions is a very tedious task, because complex functions depending on many coordinates arise. As an example we will investigate the angular dependence of these functions for a homonuclear diatomic molecule interacting with the Al(111) surface.

The energies have a periodicity of 180° and 360° concerning the angles θ and ϕ (cf. Fig. 8.2), respectively. Changing the values of the angles by these amounts corresponds to the identity operation. Additionally, both angles are coupled in that rotating ϕ by 180° and replacing θ by $180° - \theta$ (mirroring at a plane parallel to the surface) is also an identity operation. If the center of mass of the molecule is located on a mirror plane or a high symmetry site of the surface, the rotational symmetry is increased in a complex way. At a high symmetry site like the fcc site, the periodicity with respect to ϕ becomes 120° for a tilted molecule and even 60° for a molecular orientation parallel to the surface ($\theta = 90°$). Therefore, the resulting symmetry functions depend simultaneously on θ, ϕ, X and Y in a complex way. So far, it was not possible to derive symmetry functions which exactly match the symmetry of the real system without introducing artefacts.

In the present work an attempt was made to find an alternative method to the use of symmetry functions, which offers the same advantages, but which can be constructed easily for all types of surfaces in a systematic way. This alternative method has been found in using symmetrized and antisymmetrized Fourier terms and is described in the following section.

8.4 The Fourier Method

In the previous section it has been demonstrated that finding appropriate symmetry functions is a difficult task and that it is not always possible even for systems of moderate complexity to construct these functions. Therefore, in the course of this project a general scheme was developed to include the full symmetry of the surface exactly without having to use empirically derived symmetry functions[1]. The aim was to find an approach that is valid for all types of surfaces and that can be systematically derived and is applicable to molecular dynamics simulations. In the Fourier method the analytic symmetry functions depending on the molecular coordinates X, Y, Z, θ, ϕ and d are replaced by Fourier functions, which have extrema at the high symmetry sites defining the irreducible wedge and depend on individual atomic coordinates. In

[1]The original idea to use the individual atomic coordinates and the concept of symmetrizing and anti-symmetrizing was developed by S. Lorenz for atomic distances, but so far this method had not been tested or implemented.

case of a hexagonal surface these are the top, fcc and hcp sites. For a quadratic surface cell the high symmetry sites would be the top, bridge and fourfold hollow site, so the method is general and applicable to other types of surfaces as well. For each of the high symmetry sites a two-dimensional Fourier term depending on the lateral coordinates X and Y is constructed.

To illustrate the procedure it is instructive to have a look at a simpler problem, the potential of a single atom interacting with a surface. No angular dependence exists and the system is fully defined by the three coordinates X, Y and Z of the atom. Functions that have the required symmetry properties are Fourier terms with maxima at the three high symmetry sites of the surface. The Fourier terms are

$$\begin{aligned} f_{\mathrm{top}} &= \left[\cos\left(2\pi\left((X-X_{\mathrm{t}})+\frac{1}{\sqrt{3}}(Y-Y_{\mathrm{t}})\right)\right)+\cos\left(\frac{4\pi}{\sqrt{3}}(Y-Y_{\mathrm{t}})\right)\right. \\ &\quad \left.+\cos\left(2\pi\left((X-X_{\mathrm{t}})-\frac{1}{\sqrt{3}}(Y-Y_{\mathrm{t}})\right)\right)\right]\exp\left(-\frac{1}{2}Z\right) \end{aligned} \tag{8.3a}$$

$$\begin{aligned} f_{\mathrm{fcc}} &= \left[\cos\left(2\pi\left((X-X_{\mathrm{f}})+\frac{1}{\sqrt{3}}(Y-Y_{\mathrm{f}})\right)\right)+\cos\left(\frac{4\pi}{\sqrt{3}}(Y-Y_{\mathrm{f}})\right)\right. \\ &\quad \left.+\cos\left(2\pi\left((X-X_{\mathrm{f}})-\frac{1}{\sqrt{3}}(Y-Y_{\mathrm{f}})\right)\right)\right]\exp\left(-\frac{1}{2}Z\right) \end{aligned} \tag{8.3b}$$

$$\begin{aligned} f_{\mathrm{hcp}} &= \left[\cos\left(2\pi\left((X-X_{\mathrm{h}})+\frac{1}{\sqrt{3}}(Y-Y_{\mathrm{h}})\right)\right)+\cos\left(\frac{4\pi}{\sqrt{3}}(Y-Y_{\mathrm{h}})\right)\right. \\ &\quad \left.+\cos\left(2\pi\left((X-X_{\mathrm{h}})-\frac{1}{\sqrt{3}}(Y-Y_{\mathrm{h}})\right)\right)\right]\exp\left(-\frac{1}{2}Z\right) \end{aligned} \tag{8.3c}$$

Equation (8.3a) has maxima at all top sites, Eq. (8.3b) at all fcc sites and Eq. (8.3c) at all hcp sites. The coordinates X and Y are given in units of the surface in-plane lattice constant. The exponential term depending on the height Z ensures that the function values become independent of the lateral position of the atom for large distances. This is a basic requirement, because for large distances the atom does not interact with the surface and the energy must be independent of the actual X and Y coordinates. X_{t} and Y_{t} define the position of the top site, X_{f} and Y_{f} the position of the fcc site and X_{h} and Y_{h} the position of the hcp site. The three equations are plotted as a function of the X and Y coordinates of the atom in Fig. 8.3.

The position of the atom can now uniquely be defined by the three function values f_{top}, f_{fcc} and f_{hcp} in the same way as it would be defined by giving the three distances to the high symmetry sites. Distances, which have also been tested for their applicability, cannot be used as symmetry functions when forces are needed, because they show discontinuities in the derivatives when the atom leaves the irreducible wedge of the surface and enters a neighboring wedge. This is because for the calculation of the distance always the position with respect to the closest high-symmetry site of each kind has to be used, which is equivalent to a backfolding into the irreducible wedge of the unit cell. This differentiability problem can be avoided when Fourier terms are applied as shown in Eq. (8.3), since the latter are continuous and differentiable

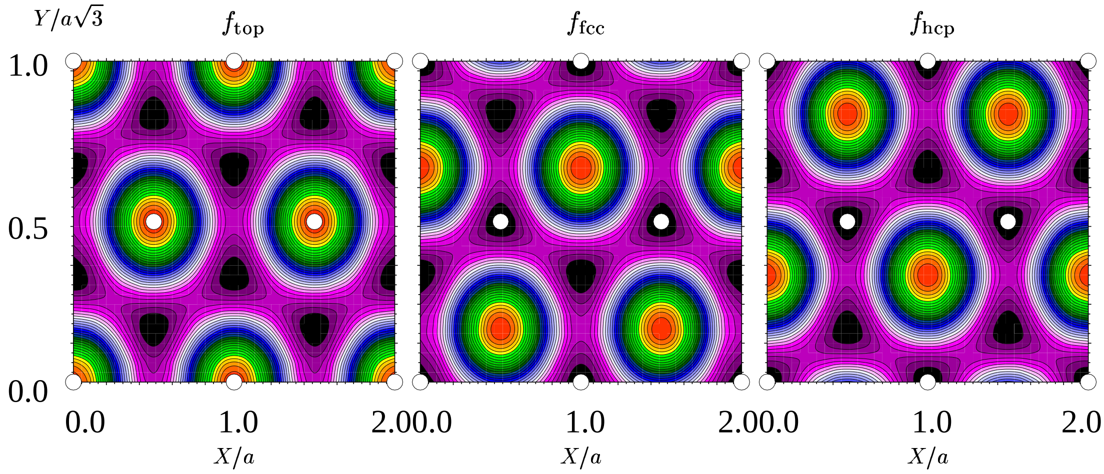

Figure 8.3: Fourier terms for an atomic potential. The three Fourier terms of Eq. (8.3) are plotted as a function of the X and Y coordinates of the atom in units of the lattice constant a. The positions of the top layer surface atoms are marked by the white circles. The absolute function values have no physical meaning, only the correct symmetry is required.

everywhere in space, in particular also at the borders of the irreducible wedge. Consequently, the potential of an atom interacting with a surface can perfectly be described by three Fourier terms defining the position of this atom.

To derive the Fourier method for a six-dimensional potential-energy surface we start with the same approach and define a set of three Fourier terms for each of the two oxygen atoms. The coordinates of the two oxygen atoms X_1, Y_1, Z_1, X_2, Y_2 and Z_2 are:

$$X_1 = \frac{1}{2}d\sin(\theta)\cos(\phi) + X \tag{8.4a}$$

$$Y_1 = \frac{1}{2}d\sin(\theta)\sin(\phi) + Y \tag{8.4b}$$

$$Z_1 = \frac{1}{2}d\cos(\theta) + Z \tag{8.4c}$$

$$X_2 = -\frac{1}{2}d\sin(\theta)\cos(\phi) + X \tag{8.4d}$$

$$Y_2 = -\frac{1}{2}d\sin(\theta)\sin(\phi) + Y \tag{8.4e}$$

$$Z_2 = -\frac{1}{2}d\cos(\theta) + Z \tag{8.4f}$$

Using these atomic coordinates the Fourier terms for both atoms can be constructed.

$$
\begin{aligned}
f_{\mathrm{top1}} &= \left[C_1 - \cos\left(2\pi\left((X_1 - X_{\mathrm{t}}) + \frac{1}{\sqrt{3}}(Y_1 - Y_{\mathrm{t}})\right)\right) - \cos\left(\frac{4\pi}{\sqrt{3}}(Y_1 - Y_{\mathrm{t}})\right)\right. \\
&\quad \left. - \cos\left(2\pi\left((X_1 - X_{\mathrm{t}}) - \frac{1}{\sqrt{3}}(Y_1 - Y_{\mathrm{t}})\right)\right) + Z_1^2\right] \cdot e^{-\frac{1}{2}Z} \qquad (8.5a) \\
f_{\mathrm{fcc1}} &= \left[C_1 - \cos\left(2\pi\left((X_1 - X_{\mathrm{f}}) + \frac{1}{\sqrt{3}}(Y_1 - Y_{\mathrm{f}})\right)\right) - \cos\left(\frac{4\pi}{\sqrt{3}}(Y_1 - Y_{\mathrm{f}})\right)\right. \\
&\quad \left. - \cos\left(2\pi\left((X_1 - X_{\mathrm{f}}) - \frac{1}{\sqrt{3}}(Y_1 - Y_{\mathrm{f}})\right)\right) + Z_1^2\right] \cdot e^{-\frac{1}{2}Z} \qquad (8.5b) \\
f_{\mathrm{hcp1}} &= \left[C_1 - \cos\left(2\pi\left((X_1 - X_{\mathrm{h}}) + \frac{1}{\sqrt{3}}(Y_1 - Y_{\mathrm{h}})\right)\right) - \cos\left(\frac{4\pi}{\sqrt{3}}(Y_1 - Y_{\mathrm{h}})\right)\right. \\
&\quad \left. - \cos\left(2\pi\left((X_1 - X_{\mathrm{h}}) - \frac{1}{\sqrt{3}}(Y_1 - Y_{\mathrm{h}})\right)\right) + Z_1^2\right] \cdot e^{-\frac{1}{2}Z} \qquad (8.5c) \\
f_{\mathrm{top2}} &= \left[C_1 - \cos\left(2\pi\left((X_2 - X_{\mathrm{t}}) + \frac{1}{\sqrt{3}}(Y_2 - Y_{\mathrm{t}})\right)\right) - \cos\left(\frac{4\pi}{\sqrt{3}}(Y_2 - Y_{\mathrm{t}})\right)\right. \\
&\quad \left. - \cos\left(2\pi\left((X_2 - X_{\mathrm{t}}) - \frac{1}{\sqrt{3}}(Y_2 - Y_{\mathrm{t}})\right)\right) + Z_2^2\right] \cdot e^{-\frac{1}{2}Z} \qquad (8.5d) \\
f_{\mathrm{fcc2}} &= \left[C_1 - \cos\left(2\pi\left((X_2 - X_{\mathrm{f}}) + \frac{1}{\sqrt{3}}(Y_2 - Y_{\mathrm{f}})\right)\right) - \cos\left(\frac{4\pi}{\sqrt{3}}(Y_2 - Y_{\mathrm{f}})\right)\right. \\
&\quad \left. - \cos\left(2\pi\left((X_2 - X_{\mathrm{f}}) - \frac{1}{\sqrt{3}}(Y_2 - Y_{\mathrm{f}})\right)\right) + Z_2^2\right] \cdot e^{-\frac{1}{2}Z} \qquad (8.5e) \\
f_{\mathrm{hcp2}} &= \left[C_1 - \cos\left(2\pi\left((X_2 - X_{\mathrm{h}}) + \frac{1}{\sqrt{3}}(Y_2 - Y_{\mathrm{h}})\right)\right) - \cos\left(\frac{4\pi}{\sqrt{3}}(Y_2 - Y_{\mathrm{h}})\right)\right. \\
&\quad \left. - \cos\left(2\pi\left((X_2 - X_{\mathrm{h}}) - \frac{1}{\sqrt{3}}(Y_2 - Y_{\mathrm{h}})\right)\right) + Z_2^2\right] \cdot e^{-\frac{1}{2}Z} \qquad (8.5f)
\end{aligned}
$$

The X and Y coordinates are again given in units of the in-plane surface lattice constant. In contrast to the Fourier terms of the single atom case here a constant C_1 has to be added to the negative cosine functions to shift all function values into the positive range for reasons that will be explained below. Another modification is the addition of the terms Z_1^2 and Z_2^2 that introduce the different heights of the atoms to make a distinction between molecular orientations with different θ values but identical projections into the xy plane possible. Just like in the atomic case the exponential term $e^{-0.5Z}$ has the function to make the site- and angular dependence of the potential vanish for large molecule-surface separations.

As the two oxygen atoms appear individually with their Cartesian coordinates X_1, Y_1 and Z_1 as well as X_2, Y_2 and Z_2, so far the function values depend on which atom is assigned to which number and both atoms are not equivalent (and could thus be applied to heteronuclear molecules like CO). A straightforward solution for homonuclear molecules like O_2 would be to supply each data point twice to the neural network with both possible assignments to cover the full configuration space. This method is not very elegant in that not only the amount of data points is doubled, but also in that two (identical) geometries, which must have the same potential-energy are learned separately and can be assigned different energies by the neural network. A better solution is to modify the functions by symmetrizing and anti-symmetrizing the Fourier terms. With this procedure no information is lost, but the two atoms become indistinguishable. The symmetrization and anti-symmetrization are done by calculating the sums and differences of Fourier terms of both atoms referring to the same symmetry site and squaring the results. Six functions are obtained.

$$G_1 = (f_{\text{top1}} + f_{\text{top2}})^2 \tag{8.6a}$$
$$G_2 = (f_{\text{top1}} - f_{\text{top2}})^2 \tag{8.6b}$$
$$G_3 = (f_{\text{fcc1}} + f_{\text{fcc2}})^2 \tag{8.6c}$$
$$G_4 = (f_{\text{fcc1}} - f_{\text{fcc2}})^2 \tag{8.6d}$$
$$G_5 = (f_{\text{hcp1}} + f_{\text{hcp2}})^2 \tag{8.6e}$$
$$G_6 = (f_{\text{hcp1}} - f_{\text{hcp2}})^2 \tag{8.6f}$$

The square in these equations is the reason for the introduction of the constant C_1 in Eq. (8.5). The function values of the sum of cosine terms in Eq. (8.3) range from -1.5 to +3.0, i.e. the pure Fourier term can be negative. Without adding a constant the information of the sign would be lost upon squaring, and function values which differ only by the sign would be equal afterwards. Therefore, the range of values of the cosine sum is shifted, to make sure that they are positive before being squared. Throughout this work a value of $C_1 = 3.0$ is used. As mentioned above for a heteronuclear diatomic molecule this step is not required making the functions for the neural network simpler for the prize of a higher number of required DFT data points due to the reduced symmetry. The 6 symmetrized and anti-symmetrized functions in Eq. (8.6) are shown in Fig. 8.4 for a molecular orientation of $\theta = 90°$ and $\phi = 30°$ as a function of the center of mass coordinates X and Y. For this plot the bond length is fixed at 1.3 Å and Z is constant at 2.1 Å. The rather complex shape of these functions compared to Fig. 8.3 is a consequence of the superposition of two atomic components.

Using the Fourier terms both atoms are folded back into the irreducible wedge of the surface unit cell individually for arbitrary molecular configurations. The information on the relative position of the atoms is therefore lost. Both atoms originally being located in the same wedge can yield the same set of function values as an interatomic distance of several lattice constants. To include this information another function is added which is nothing but the molecular bond length d.

$$G_7 = d \tag{8.7}$$

Supplying redundant information to the neural network in general does not pose a problem. On the contrary, additional functions of the input variables can assist the learning process, if the functional form is related to the physical problem, i.e. the

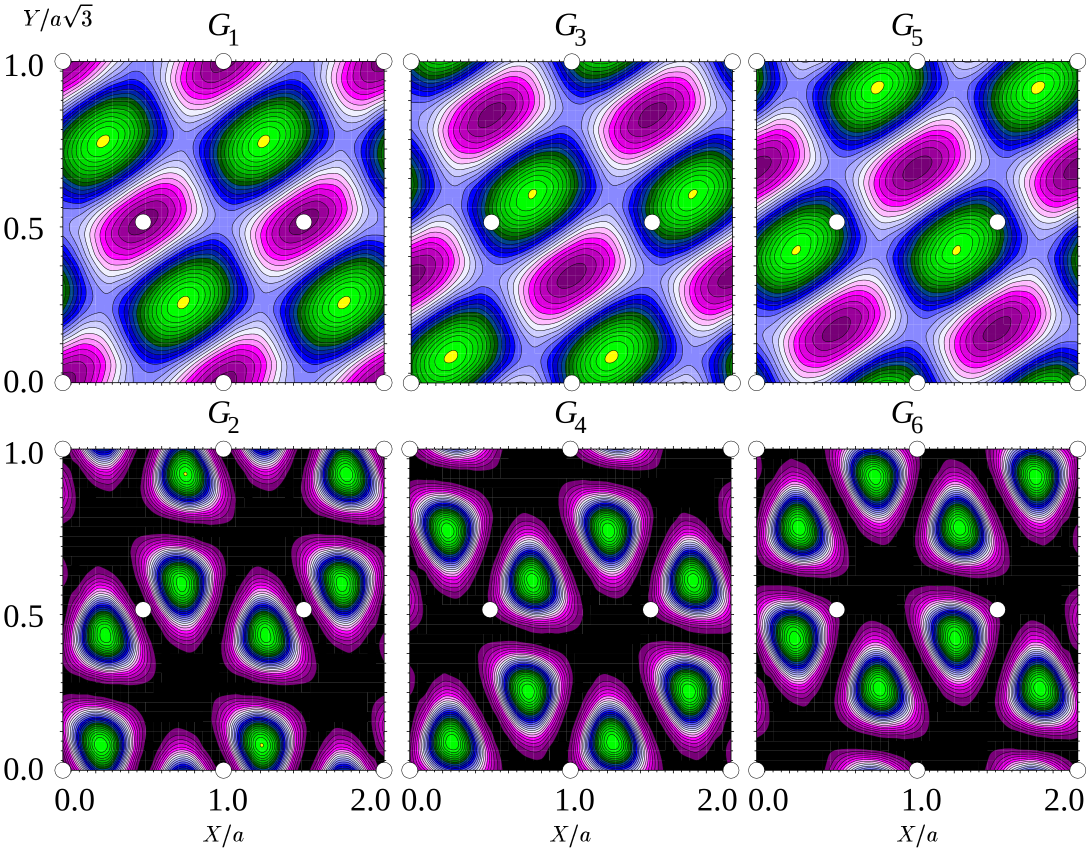

Figure 8.4: Plot of the six symmetrized and anti-symmetrized Fourier terms of Eq. (8.6) as a function of the X and Y center of mass coordinates of the molecule in units of the in-plane lattice constant a. The positions of the top layer surface atoms are marked by the white circles. In all plots the molecule has a distance of 2.1 Å from the surface, a bond length of 1.3 Å and an angular orientation of $\theta = 90°$ and $\phi = 30°$. The absolute function values have no physical meaning, only the correct symmetry is required.

shape of the potential-energy surface. To test this, additional functions are constructed: One term that just depends on the center of mass distance of the molecule from the surface is added (G_8), and three additional Fourier terms with extrema at the top, fcc and hcp sites whose arguments are the center of mass coordinates X and Y are included (G_9 - G_{11}). These functions increase the flexibility of the network while not altering the symmetry.

$$G_8 = e^{-\frac{1}{2}Z} \tag{8.8}$$

$$G_9 = \left[\cos\left(2\pi\left((X - X_t) + \frac{1}{\sqrt{3}}(Y - Y_t)\right)\right) + \cos\left(\frac{4\pi}{\sqrt{3}}(Y - Y_t)\right) + \cos\left(2\pi\left((X - X_t) - \frac{1}{\sqrt{3}}(Y - Y_t)\right)\right)\right] \exp\left(\frac{1}{2}Z\right) \tag{8.9}$$

$$
\begin{aligned}
G_{10} &= \left[\cos\left(2\pi\left((X-X_\mathrm{f})+\frac{1}{\sqrt{3}}(Y-Y_\mathrm{f})\right)\right)+\cos\left(\frac{4\pi}{\sqrt{3}}(Y-Y_\mathrm{f})\right)\right. \\
&\quad \left.+\cos\left(2\pi\left((X-X_\mathrm{f})-\frac{1}{\sqrt{3}}(Y-Y_\mathrm{f})\right)\right)\right]\exp\left(\frac{1}{2}Z\right) \qquad (8.10) \\
G_{11} &= \left[\cos\left(2\pi\left((X-X_\mathrm{h})+\frac{1}{\sqrt{3}}(Y-Y_\mathrm{h})\right)\right)+\cos\left(\frac{4\pi}{\sqrt{3}}(Y-Y_\mathrm{h})\right)\right. \\
&\quad \left.+\cos\left(2\pi\left((X-X_\mathrm{h})-\frac{1}{\sqrt{3}}(Y-Y_\mathrm{h})\right)\right)\right]\exp\left(\frac{1}{2}Z\right) \qquad (8.11)
\end{aligned}
$$

Careful tests have been performed to ensure that the symmetry properties of the surface are exactly reproduced by all 11 functions. In order to determine the symmetry properties, the functions can be considered as an 11-dimensional vector. The molecule is then placed at a certain symmetry site, i.e. parallel to the surface above an fcc site, and rotated around ϕ. If the correct 6-fold symmetry is present, the combination of the 11 vector elements should possess the same periodicity. Exactly this has been found. Additionally, the three-fold rotational symmetry of a tilted molecule at the same site and the two-fold rotational symmetry at the bridge site could be reproduced correctly, as well as that of many other tested configurations.

Finally, we have obtained a method based on functions that can be constructed systematically and that have exactly the symmetry of the system. All functions are continuous and differentiable. In contrast to symmetry functions, which have to be designed for each particular surface individually, the presented Fourier method is independent of the surface and can easily be applied to all types of periodic surfaces by an analogous construction procedure, no matter if the unit cells are hexagonal or rectangular and irrespective of the size of the unit cell.

8.5 The Classical Equations of Motion

To perform molecular dynamics simulations Hamilton's equations of motion have to be solved. They relate the time derivatives of spatial coordinates Q and momentum coordinates P to the partial derivatives of the Hamilton operator of the system with respect to momentum and position.

$$\dot{Q}_i = \frac{\partial H}{\partial P_i} \qquad (8.12a)$$

$$\dot{P}_i = -\frac{\partial H}{\partial Q_i} \qquad (8.12b)$$

The Hamiltonian H for the nuclear coordinates using the coordinate system shown in Fig. 8.2 is given by a kinetic energy term due to the center of mass motion of the molecule, a kinetic energy term due to the internal degrees of freedom of the molecule and the potential-energy term depending on the set of all coordinates $\mathbf{Q}$.

$$H = \frac{1}{2m_{\mathrm{O}_2}} \left(P_{\mathrm{X}}^2 + P_{\mathrm{Y}}^2 + P_{\mathrm{Z}}^2 \right) + \frac{1}{2\mu_{\mathrm{O}_2}} \left(P_d^2 + \frac{P_\theta^2}{d^2} + \frac{P_\phi^2}{d^2 \sin^2 \theta} \right) + V(\mathbf{Q}) \tag{8.13}$$

Here, m_{O_2} is the absolute mass of the oxygen molecule and μ_{O_2} is its reduced mass. The P_i are the momenta with respect to the 6 coordinates that define the molecular configuration.

The equations of motion can be solved by standard techniques like the Verlet algorithm or the more sophisticated Bulirsch-Stoer method. In the Verlet algorithm [163] a constant time step is used, and the configuration at time $t + dt$ is calculated from the configuration at time t and the velocity at time $t + \frac{1}{2}dt$, which can be obtained from the velocity at time t and the forces. The Verlet algorithm will be used in the *ab initio* molecular dynamics simulations in Section 10.5. The more advanced Bulirsch-Stoer method [147] is more efficient, because a variable time step can be used, that can significantly speed up the calculation of the trajectories, but also increases the accuracy in strongly corrugated regions of the potential-energy surface by reducing the time step. The main idea is that the molecular configuration at a time $t+dt$ itself is considered as a function of the step size dt. The step corresponding to the initial step size is successively split up in smaller and smaller intervals, and the predicted new configuration is fitted to a function of the size of these intervals. Then this function is extrapolated to infinitesimally small time intervals. Depending on the convergence of the predicted configuration with decreasing interval size, which is a measure for the complexity of the potential-energy surface, the time step dt is either reduced or increased. The Bulirsch-Stoer method will be used in all classical molecular dynamics simulations, which are based on neural networks, because of its high efficiency and accuracy.

8.6 Summary

The neural network provides an efficient and accurate method to obtain energies and forces for arbitrary molecular configurations, which is required for the intended molecular dynamics applications. The symmetry of the Al(111) surface is considered in the neural network since it speeds up the fitting process and ensures that the full symmetry of the potential-energy surface is taken into account without approximations. The neural network code used in this project has been developed by Lorenz, Groß and Scheffler [26, 27]. Only small modifications have been made in the present work, mainly concerning the implementation of the Fourier method described in the previous section. Based on this interpolation classical molecular dynamics simulations have been performed, which will be presented in Chapters 10 and 13.

Part II

Oxygen Dissociation on Al(111)

Chapter 9

Reference Calculations

Before the sticking properties of oxygen on Al(111) can be addressed, some reference calculations have to be performed to ensure that the system is described reliably by density-functional theory. Calculations on the free oxygen molecule, on bulk aluminium, and on the clean and oxygen-covered Al(111) surface have therefore been carried out. The results are summarized in the following sections.

9.1 The Oxygen Molecule

In its spin triplet ${}^3\Sigma_\mathrm{g}^-$ ground state molecular oxygen is a diradical according to the general definition of diradicals as molecules with two electrons occupying a doubly degenerate orbital [209]. In case of O_2 this is the antibonding $2\pi^*$ state, which forms the highest occupied molecular orbital. In Fig. 9.1 the molecular orbital diagram of the oxygen molecule is shown schematically for the triplet ${}^3\Sigma_\mathrm{g}^-$ ground state, and also for the two most prominent excited ${}^1\Delta_\mathrm{g}$ and ${}^1\Sigma_\mathrm{g}^+$ singlet states. These states differ only in the occupation of the $2\pi^*$ orbitals. There are three energetically degenerate ${}^3\Sigma_\mathrm{g}^-$ triplet states, two degenerate ${}^1\Delta_\mathrm{g}$ singlet states and one ${}^1\Sigma_\mathrm{g}^+$ singlet state. Two of the three ${}^3\Sigma_\mathrm{g}^-$ states can be represented by a single Slater determinant and are called “high-spin” triplets (configurations (e) and (f)). Like the singlet states, the “low-spin” triplet is constructed as a linear combination of two Slater determinants, since the configurations (a), (b), (c) and (d) do not correspond to physical states of the system. This is because open-shell determinants are no eigenfunctions of the total spin operator S^2, unless all open shell electrons have parallel spin [100], which is the case for the triplet configurations (e) and (f) only. By pairwise symmetrizing and anti-symmetrizing the Slater determinants (a) and (b) as well as (c) and (d) and by using the Slater determinants of configurations (e) and (f), six wave-functions can be constructed [117].

$$^1\Delta_\mathrm{g}: \quad \psi_1^\mathrm{s} \quad = \quad \frac{1}{2}\Big[\phi_1(1)\phi_1(2) - \phi_2(1)\phi_2(2)\Big](\alpha(1)\beta(2) - \beta(1)\alpha(2)) \tag{9.1a}$$

$$^1\Delta_\mathrm{g}: \quad \psi_2^\mathrm{s} \quad = \quad \frac{1}{2}\Big[\phi_1(1)\phi_1(2) + \phi_2(1)\phi_2(2)\Big](\alpha(1)\beta(2) - \beta(1)\alpha(2)) \tag{9.1b}$$

$$^1\Sigma_\mathrm{g}^+: \quad \psi_3^\mathrm{s} \quad = \quad \frac{1}{2}\Big[\phi_1(1)\phi_2(2) + \phi_2(1)\phi_1(2)\Big](\alpha(1)\beta(2) - \beta(1)\alpha(2)) \tag{9.1c}$$

$$^3\Sigma_\mathrm{g}^-: \quad \psi_4^\mathrm{t} \quad = \quad \frac{1}{2}\Big[\phi_1(1)\phi_2(2) - \phi_2(1)\phi_1(2)\Big](\alpha(1)\beta(2) + \beta(1)\alpha(2)) \tag{9.1d}$$

$$^3\Sigma_\mathrm{g}^-: \quad \psi_5^\mathrm{t} \quad = \quad \frac{1}{\sqrt{2}}\Big[\phi_1(1)\phi_2(2) - \phi_2(1)\phi_1(2)\Big](\alpha(1)\alpha(2)) \tag{9.1e}$$

$$^3\Sigma_\mathrm{g}^-: \quad \psi_6^\mathrm{t} \quad = \quad \frac{1}{\sqrt{2}}\Big[\phi_1(1)\phi_2(2) - \phi_2(1)\phi_1(2)\Big](\beta(1)\beta(2)) \tag{9.1f}$$

ϕ_1 and ϕ_2 refer to the spatial functions and α and β to the spin functions. According to the Pauli principle, each wave-function has to be antisymmetric with respect to interchange of two electrons. The three singlet states ψ_1^s, ψ_2^s and ψ_3^s have antisymmetric spin functions and symmetric spatial functions, while the three triplet states ψ_4^t, ψ_5^t and ψ_6^t have symmetric spin functions and antisymmetric spatial functions. As mentioned above, all three singlet states ψ_1^s, ψ_2^s and ψ_3^s as well as the triplet state ψ_4^t are combinations of two Slater determinants. ψ_5^t and ψ_6^t are single-determinant wave-functions.

First, the $^3\Sigma_\mathrm{g}^-$ triplet ground state will be investigated. Formally, Kohn-Sham DFT based on LDA and GGA functionals is a single-determinant method [211, 212], i.e. the Kohn-Sham orbitals used to construct the density form one Slater determinant. However, no reference to this "wave-function" is made and states corresponding to wave-functions being linear combinations of two or more Slater determinants have to be treated with great care [213–216] when using the LDA or GGA. This aspect will be discussed below in the context of the singlet states of the oxygen molecule. In case of the triplet state, two of the three configurations, the high-spin triplets, are described by single Slater determinants and do not pose a problem in Kohn-Sham DFT. However, for the low-spin triplet this is different, and the question arises, if the three degenerate $^3\Sigma_\mathrm{g}^-$ states will have the same energy in DFT. In general, DFT applying LDA and GGA functionals yields the same total energy for different configurations only if the charge and spin densities are identical. This is the case for the high-spin triplets ψ_5^t and ψ_6^t corresponding to configurations (e) and (f) in Fig. 9.1, which can be directly obtained from standard spin-polarized DFT calculations. They form the ground state of O_2. On the other hand, the low-spin triplet ψ_4^t has another spin symmetry ($M_\mathrm{s} = 0$) and spin-density and is therefore not necessarily degenerate with the high-spin triplets [215]. Before investigating the two-determinant low-spin triplet ψ_4^t in more detail, we will first have a closer look at the properties of the high-spin triplet state.

It is well known that the binding energy of the $^3\Sigma_\mathrm{g}^-$ ground state of O_2 is not accu-

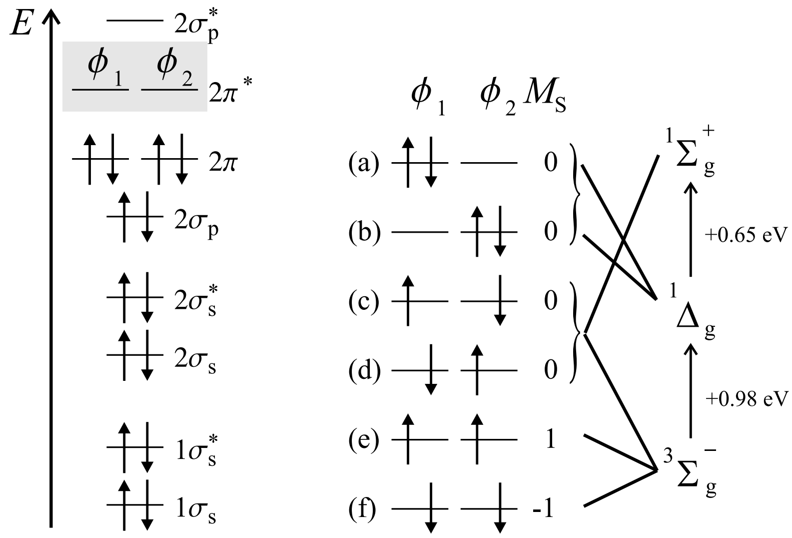

Figure 9.1: Schematic molecular orbital diagram of the oxygen molecule in its triplet $^3\Sigma_g^-$ ground state and the two excited singlet states $^1\Delta_g$ and $^1\Sigma_g^+$. These states differ only in the occupation of the $2\pi^*$ state shown in grey. By occupying this state with two electrons 6 configurations can be constructed as shown on the right side. There are three energetically degenerate $^3\Sigma_g^-$ states, two degenerate $^1\Delta_g$ states and one $^1\Sigma_g^+$ state. Two of the three $^3\Sigma_g^-$ states, (e) and (f), can be represented by a single Slater determinant and are called "high-spin" triplets. Like all singlet states, the "low-spin" triplet is constructed as a linear combination of two Slater determinants (cf. Eq. (9.1)). The energy differences have been taken from experiment [210]. The mixing of s and p character in the 2σ and $2\sigma^*$ orbitals has been neglected in this scheme.

rately described by current exchange-correlation functionals [75]. However, there are encouraging studies on the dissociation of oxygen molecules at transition metal surfaces [181, 217–219] using density-functional theory, which suggests that some of the errors in the description of gas phase oxygen molecule cancel in the PES describing its interaction with a surface. It is therefore crucial to understand the exact reasons behind the errors in the gas phase description and to assess to which extent they affect the potential-energy surface we aspire to compute, or where we correspondingly have to critically check the obtained results. For the discussion of the free O_2 molecule fundamental physical properties like the binding energy, the equilibrium bond length and the vibrational frequency in the spin triplet $^3\Sigma_g^-$ ground state have been calculated. Five different functionals have been used (LDA [113], PBE [114], PW91 [116], BLYP [220] and RPBE [74]) to estimate the functional dependence of these quantities. The calculations have been carried out without periodic boundary conditions employing a basis function cutoff of 9 bohr, an *all* basis and the default integration grid (*iomin*=1, *iomax*=5, *thres*=0.0001, *rmaxp*=9 bohr, *s*=1.0), which is identical to the basis set that will be used in the calculation of the potential-energy surface. To obtain converged vibrational frequencies a higher cutoff of 14 bohr had to be employed. The also required calculations of the free oxygen atom have been done using a large cutoff of 18 bohr and a denser integration mesh (*iomin*=1, *iomax*=7, *thres*=0.000001, *rmaxp*=18 bohr, *s*=1.5, cf. Appendix B) to obtain fully converged total energies eliminating the convergence of the atomic calculations as possible source of error.

In all calculations the correct high-spin triplet ground state of the oxygen molecule has been found, i.e the spins of the two electrons are aligned and the integrated spin density corresponds to a triplet state. The obtained binding energies are listed in Table 9.1, the bond lengths are given in Table 9.2, and the vibrational frequencies are summarized in Table 9.3. In all tables also experimental and theoretical values from the literature are included. The zero point energy (ZPE) of the oxygen molecule, which is about 0.1 eV [210, 221–223], has not been taken into account in the calculation of the binding energies. It is also not considered in the calculation of the bond length, which is taken to be the minimum-energy bond length of the molecule, and in the vibrational energy.

The comparison of the binding energies shows that all tested exchange-correlation functionals yield a remarkably overestimated bond strength ("overbinding"). The worst description is provided by the LDA with an overbinding of more than 2 eV compared to the experimental value of 5.1 eV [224], but also all GGAs show errors of more than 0.5 eV. In contrast to the binding energy, the deviations of the DFT bond lengths from experiment (1.207 Å [210]) shown in Table 9.2 are rather small for all tested functionals. The shortest bond is found for the LDA as a consequence of the strongest overbinding. The vibrational frequencies do not show a clear trend, but DFT with LDA or GGA functionals is known for deviations in the frequencies in the order of 10 % [104].

The reason for the exceptionally large error in the binding energy obtained from approximate exchange-correlation functionals has been investigated in detail by Gunnarsson and Jones [75]. They argue that the exchange energy in the LDA (cf. Eq. (5.17)), which is also an important contribution to the exchange energy in all GGAs, is a rather bad approximation for the exchange energy. However, in the calculation of binding energies, which are differences of DFT energies, the errors usually cancel to a large extent yielding rather reliable binding energies. Nevertheless, for O_2 and a few other molecules this is not true, and large errors can result. To understand this phenomenon, Gunnarsson and Jones refer to the "exact"[1] exchange energy $E_{\mathrm{X}}^{\mathrm{HF}}$ in Hartree-Fock theory.

$$E_{\mathrm{X}}^{\mathrm{HF}} = \sum_i \sum_j \int \int \frac{\phi_i(\mathbf{x}_1)\phi_j^*(\mathbf{x}_1)\phi_j(\mathbf{x}_2)\phi_i^*(\mathbf{x}_2)}{|\mathbf{r}_1 - \mathbf{r}_2|} d\mathbf{x}_1 d\mathbf{x}_2 \tag{9.2}$$

The integrand is a product of four single-particle wave-functions and has therefore a complex nodal structure. By using this equation, in Hartree-Fock theory the nodal

[1]The description of exchange in Hartree-Fock is exact under the assumption that the wave-function of the system can be represented by a single Slater determinant.

E_b (eV)	Reference	
7.428	DFT, LDA, noZPE	this work
6.099	DFT, PBE, noZPE	this work
6.074	DFT, PW91, noZPE	this work
5.750	DFT, BLYP, noZPE	this work
5.646	DFT, RPBE, noZPE	this work
5.116	experiment	[224]
5.123	experiment	[225]
7.10-7.30	DFT, LDA, noZPE	[74]
7.577	DFT, LDA, ZPE	[226]
7.590	DFT, LDA, ZPE	[114]
7.572	DFT, LDA	[227]
6.202	DFT, PW91, ZPE	[114]
5.864	DFT, PW91, ZPE	[226]
5.966	DFT, PW91	[228]
5.84-6.06	DFT, PW91, noZPE	[74]
5.81-5.99	DFT, PBE, noZPE	[74]
6.149	DFT, PBE, noZPE	[229]
6.245	DFT, PBE, ZPE	[114]
5.51-5.59	DFT, RPBE, noZPE	[74]
5.754	DFT, revPBE, noZPE	[229]
5.53-5.63	DFT, revPBE, noZPE	[74]
5.782	DFT, BLYP, ZPE	[226]
5.933	DFT, BLYP	[227]
5.205	DFT, B3LYP, ZPE	[226]
1.253	Hartree-Fock	[227]
1.431	Hartree-Fock, ZPE	[114]
5.100	Møller Plesset order 2	[227]
4.294	Quadratic Configuration Interaction	
	Single and Double Excitations	[227]
5.200	Coupled Cluster Single	
	and Double Excitations, noZPE	[221]
4.710	Quantum Monte Carlo, noZPE	[230]
4.844	Quantum Monte Carlo, ZPE	[231]

Table 9.1: Molecular binding energies of O_2 in its $^3\Sigma_g^-$ ground state. The binding energy ranges of Ref. [74] indicate the dependence on the chosen pseudopotential. The zero point energy is approximately 0.1 eV (included=ZPE, not included=noZPE, otherwise no information on the zero point vibration is given).

d (Å)	Reference	
1.210	DFT, LDA)	this work
1.224	DFT, PBE	this work
1.224	DFT, PW91	this work
1.236	DFT, BLYP	this work
1.229	DFT, RPBE	this work
1.207	experiment	[210]
1.211	DFT, LDA	[152]
1.223	DFT, LDA	[232]
1.215	DFT, LDA	[227]
1.218	DFT, PW91	[228]
1.239	DFT, BP86	[233]
1.240	DFT, BLYP	[227]
1.168	Hartree-Fock	[234]
1.168	Hartree-Fock	[227]
1.163	Hartree-Fock	[234]
1.246	Møller Plesset order 2	[227]
1.242	Møller Plesset order 2	[234]
1.211	Møller Plesset order 3	[234]
1.206	Configuration Interaction	
	Double Excitations	[234]
1.221	Quadratic Configuration Interaction	
	Single and Double Excitations	[227]
1.193	Dynamic Monte Carlo	[230]

Table 9.2: Molecular bond length of O_2 in its $^3\Sigma_g^-$ ground state obtained from the minimum energy configuration. The zero point vibrations have not been taken into account.

ν (cm^{-1})	Reference	
1592	DFT, LDA	this work
1527	DFT, PBE	this work
1502	DFT, PW91	this work
1464	DFT, BLYP	this work
1597	DFT, RPBE	this work
1580	experiment	[210]
1642	DFT, LDA	[227]
1518	DFT, BLYP	[227]
1998	Hartree-Fock	[227]
1413	Møller Plesset 2	[227]
1639	Quadratic Configuration Interaction	
	Single and Double Excitations	[227]
1665	Dynamic Monte Carlo	[230]

Table 9.3: Vibration frequencies of O_2 in its $^3\Sigma_g^-$ ground state. The zero point vibrations have not been taken into account.

structure is explicitly taken into account in the calculation of the exchange energy in that parts of the integrand with different sign cancel each other in the integration reducing the Hartree-Fock exchange energy.

Formally, Hartree-Fock theory and DFT can be expressed by very similar equations, with a few, but very important, differences. The most important difference for the present discussion is that in Hartree-Fock calculations only the exchange is taken into account and correlation is completely neglected, while in DFT both are included in the exchange-correlation functional [104]. If the latter were known exactly, the correct oxygen binding energy would be obtained. However, the very simple approximation to the functional form of the exchange energy employed in the LDA does not take into account the nodal structure of the single-particle states. Therefore, in DFT no partial cancellation of the integrands occurs (cf. Eq. (5.17)), and the exchange energy can be significantly overestimated in some cases. Usually, this is not critical in the calculation of binding energies, i.e. energy differences, if both species, the molecule and the free atoms, have a similar nodal structure. Then, the errors would be comparable in both cases and cancel each other, but this is not true for the oxygen molecule. The highest occupied orbital of an oxygen atom has p-character ($l = 1$), while the $2\pi^*$ orbitals of the oxygen molecule can be characterized as d-like ($l = 2$) [75] due to the two nodal planes along and perpendicular to the molecular axis. Consequently, the cancellation of errors in the exchange energy does not work in case of the oxygen molecule. Another prominent failure of DFT for the same reason is the F_2 molecule with a binding energy error of 1.7 eV for the LDA [75]. In general, this applies to all first row dimers with more than half-filled p-shells. On the other hand, if the latter are only up to half-filled, the highest occupied molecular orbital is the bonding π orbital, which has p-character like the constituent atoms giving rise to a much better binding energy due to an efficient error cancellation.

The dominant role of an overestimated exchange energy in the overbinding of O_2 in DFT is also supported by the absence of overbinding in Hartree-Fock theory (cf. Table 9.1), but due to the neglect of correlation in HF the absolute deviation from experiment is much worse (4 eV) than in DFT. Further, an almost perfect binding energy is obtained with the B3LYP hybrid functional [226], which uses a mixture of Hartree-Fock exchange and LDA exchange, as well as Becke's B88 [235] exchange[2]. The overbinding of the oxygen molecule is also reduced when GGA functionals are used instead of the LDA. This is because these functionals explicitly take into account the gradient of the electron density in form of a reduced density gradient. The more inhomogeneous system, i.e. the isolated atom, has a higher average reduced density gradient and experiences a decrease of the exchange-correlation energy relative to the less inhomogeneous molecule [115]. Consequently the binding energy is reduced, but still a significant overbinding is present for the oxygen molecule even within the

[2]While this underlines the importance of the exchange energy, the numerical agreement is not surprising since the mixing ratio of the different exchange terms has been obtained by fitting to a set of molecules including O_2.

GGAs.

Apart from the triplet ground state also the excited singlet states of the oxygen molecule are of interest, because the $^1\Delta_\mathrm{g}$ singlet potential-energy surface is one of the diabatic energy surfaces possibly being involved in the adsorption process. A suitable quantity to assess the accuracy of this singlet surface is the singlet-triplet gap ΔE_ST, which is defined as the energy difference between the $^3\Sigma_\mathrm{g}^-$ triplet ground state and the $^1\Delta_\mathrm{g}$ singlet state of the free O_2. This quantity is known from experiment to be about 0.98 eV [210].

In Kohn-Sham DFT there are in principle two possibilities to calculate an oxygen molecule in a singlet state, based on restricted and unrestricted DFT, respectively. It should be noted that while DFT in principle is exact and allows to calculate the total energy as a functional of the density only, in practical calculations spin-densities are introduced to increase the flexibility, which is necessary to compensate for some deficiencies in current functionals. In case of a spin-restricted, i.e. non-spin-polarized, DFT calculation the spin-up and the spin-down densities are the same, and consequently the magnetization-density is zero at each point in space. This corresponds to an occupation of 0.5 electrons for each spin in each of the $2\pi^*$ orbitals under the constraint of equal spatial functions for both spins in unrestricted DFT, which yields the same energy as a restricted calculation under these conditions. For the PBE and the RPBE functionals the obtained singlet-triplet gaps are listed in Table 9.4 ("restricted"). They are clearly higher than the experimental splitting, and the reason is that in non-spin-polarized DFT there is no way to distinguish between the $^1\Delta_\mathrm{g}$ singlet states ψ_1^s and ψ_2^s, the $^1\Sigma_\mathrm{g}^+$ singlet state ψ_3^s and the low-spin $^3\Sigma_\mathrm{g}^-$ triplet state ψ_4^t, because the densities of these states are identical. Since the energy depends only on the density, in DFT these states are artificially degenerate. It is somewhat surprising that even a triplet state is included in this "singlet" calculation, but this has been found also for many other systems [214, 215]. In summary, only a crude approximation to the singlet state can be obtained from spin-restricted DFT, yielding a singlet-triplet gap being about 0.2 eV larger than the experimental value with respect to the $^1\Delta_\mathrm{g}$ state due to the admixture of other states.

The second approach to the singlet O_2 is to use spin-unrestricted, i.e. spin-polarized, DFT calculations. As unrestricted DFT per default yields the high-spin triplet ground state of the oxygen molecule, the occupation numbers have to be constrained to calculate a singlet state. The correct occupations referring to the two $^1\Delta_\mathrm{g}$ states ψ_1^s and ψ_2^s would correspond to 0.5 electrons in each $2\pi^*$ orbital of each spin. However, these occupation numbers yield the same total density and spin-density as the $^1\Sigma_\mathrm{g}^+$ state, which in turn is indistinguishable from the low-spin triplet state [215], and correspond to the spin-restricted calculation. Consequently, we are facing again the dilemma that current exchange-correlation functionals do not take into account the symmetry of the states. Actual calculations using these occupations reduce to the spin-restricted result. To overcome the mixing of the $^1\Delta_\mathrm{g}$ and the $^1\Sigma_\mathrm{g}^+$ states it has been suggested to approximate the wave-function by a single determinant to obtain different charge and spin-densities for both singlets [214]. This could be justified when assuming that

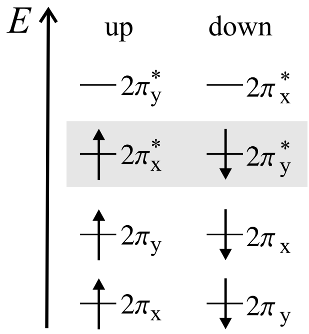

Figure 9.2: Molecular orbital diagram of the "singlet" oxygen molecule calculated using spin-unrestricted DFT. Due to the single-determinant form an unphysical symmetry-broken spin-density is obtained, since the spin-up and spin-down orbitals are degenerate, but have different spatial parts.

spatially separated orbitals are only weakly interacting systems [215]. Basically each of the determinants (a), (b), (c) and (d) in Fig. 9.1 could be used to initialize the DFT calculations, and we found that in a self-consistent calculation only the determinants (c) and (d) can be obtained. This is because doubly occupying an orbital increases the energy of this orbital, which in turn has the consequence that the spatial parts of the spin-up and spin-down orbitals become very different in order to lower the energy, which in the end yields the same configuration as starting directly from determinants (c) or (d). The molecular orbital diagram of the obtained unrestricted "singlet" molecule is shown in Fig. 9.2, and the corresponding singlet-triplet gaps are listed in Table 9.4 for the PBE and the RPBE functional ("unrestricted"). Independent of the functional[3] they are about 0.4 eV in agreement with gaps reported in the literature [233, 236], which is significantly smaller than the experimental value of 0.98 eV with respect to the $^1\Delta_g$ state. To understand this discrepancy it is instructive to analyze the single-particle states and occupations of the unrestricted singlet calculation. It is immediately clear that this configuration based on a single Slater determinant cannot be a correct singlet state, since both orbitals describe regions in space with net spin-densities of opposite spin breaking the molecular symmetry, which is not allowed for a pure singlet state. An analysis of the Slater determinant (c) in Fig. 9.1 corresponding to the unrestricted calculation shows that it can be obtained as a linear combination of the states ψ_3^s and ψ_4^t, i.e. it is a mixture[4] of a singlet and a triplet state [213].

[3] The independence of the functional clearly shows that the poor description of ΔE_{ST} is not related to the overbinding in the high-spin triplet O_2. Since the nodal structure of the orbitals for the triplet and the singlets are identical, the errors in the exchange energies cancel in the calculation of ΔE_{ST}.

[4] It should be noted that although the single Slater determinant is a mixture of two wave-functions, this is not true for the spin density, which is different from the spin densities of the $^1\Sigma_g^+$ state and the low-spin triplet.

ΔE_{ST} (eV)	Reference	
0.392	PBE, spin-unrestricted	this work
1.138	PBE, spin-restricted	this work
0.393	RPBE, spin-unrestricted	this work
1.171	RPBE, spin-restricted	this work
0.98	experiment	[210]
0.40	DFT, BP86, spin-unrestricted	[233]
0.43	DFT, PW91, spin-unrestricted	[236]
1.1	DFT, PW91, spin-restricted	[237]
0.495	Møller Plesset order 4, spin-unrestricted	[238]
1.134	Multi-configuration self-consistent field	[239]

Table 9.4: Singlet-triplet gaps of O_2.

$$\frac{1}{\sqrt{2}}\left(\phi_1(1)\phi_2(2)\alpha(1)\beta(2) - \phi_2(1)\phi_1(2)\beta(1)\alpha(2)\right) = \frac{1}{\sqrt{2}}\left(\psi_3^{\mathrm{s}} + \psi_4^{\mathrm{t}}\right) \tag{9.3}$$

This phenomenon is called "spin-contamination" in the quantum chemistry community [234], and often the triplet contribution to the singlet state is quantified by calculating the expectation value of the total spin operator $< S^2 >$ [120, 233, 238]. Typically, values close to 1 are found, which correspond to an equal mixture of a singlet ($< S^2 >$=0) and a triplet ($< S^2 >$=2) in qualitative agreement with Eq. (9.3). The singlet-triplet gaps obtained from a single determinant are significantly underestimated, and it has been suggested to extrapolate the energy of the singlet state by removing the triplet energy, which is called "spin-projection" [238]. The triplet energy is assumed to be equal to the high-spin triplet energy, which is somewhat inconsistent since the triplet contribution originates from the low-spin triplet, whose DFT energy is not known. The spin-projected singlet-triplet gap calculated using the high-spin triplet is typically similar to the experimental gap with respect to the $^1\Delta_{\mathrm{g}}$ state, but usually no clear statement is made, if this gap refers to the $^1\Delta_{\mathrm{g}}$ or the $^1\Sigma_{\mathrm{g}}^+$ state [120, 233]. As the determinant in Eq. (9.3) cannot be constructed as a linear combination of the $^1\Delta_{\mathrm{g}}$ states ψ_1^{s} and ψ_2^{s} the similarity to the $^1\Delta_{\mathrm{g}}$ state seems to be coincidental. Besides, the applicability of the spin-projection technique has been questioned. It has been shown that spin-projection can lead to wrong potential-energy surfaces having discontinuities in the first derivative [240]. This is because e.g. for the dissociation of a closed shell molecule the singlet ground state is well described by a restricted calculation close to the equilibrium geometry, while beyond a certain bond length higher multiplets contribute to the total energy.

The failure of density-functional theory in the description of states being composed of several Slater determinants, like the $^1\Delta_{\mathrm{g}}$ state of the oxygen molecule, has been attributed to a deficiency of current exchange-correlation functionals [214]. While in wave-function based methods the system is characterized by the quantum numbers L, M_{L}, S and M_{S}, in density-functional theory the present approximate exchange-correlation functionals do not contain the dependence on these symmetry properties. In the literature this is known as the "multiplet problem" of density-functional theory [104]. While each charge and spin density can be constructed from a single Slater determinant, for the wave-function this is not true. It has been shown in detail by Ziegler and Baerends [213, 241] and by von Barth [214] that the exchange energy expression employed in the LDA suggested by Slater [242], which is also an integral part of all GGA functionals, is only correct for states, i.e. wave-functions, that can be represented by a single Slater determinant. This would e.g. be the case for the high-spin $^3\Sigma_g^-$ ground state of the oxygen molecule. A strict derivation of the exchange term starting from the Schrödinger equation yields four components, two of which correspond to the spin-up and spin-down exchange terms of the homogeneous electron gas used in density-functional theory. The remaining two terms are not included in the LDA, which is a good approximation only for systems that can be represented by a single Slater determinant, since in this case these terms vanish. In all other cases significant errors can be introduced by neglecting these terms. Consequently, Ziegler and Baerends recommend not to use exchange-correlation functionals based on the exchange of the homogeneous electron gas for multi-determinant states.

Apart from density-functional theory also other single-determinant methods, like Hartree-Fock theory or Møller Plesset perturbation theory, are not able to correctly reproduce the singlet states of O_2, because the Hartree-Fock exchange energy expression is derived assuming explicitly a single-determinant wave-function [100]. However, the singlet-triplet splitting can be calculated accurately [117] by multi-reference methods like MCSCF [103] augmented by dynamical correlation using configuration interaction (MCCI) or perturbative approaches (MCPT).

Finally, the binding energies, equilibrium bond lengths and vibrational frequencies of the singlet state have been calculated from spin-restricted and spin-unrestricted calculations as described above. The results are summarized in Table 9.5. Although these calculations do not properly describe the singlet states, they can provide an estimate for the dependence of these quantities on the actually chosen approximation to the singlet state. The differences between the restricted and the unrestricted calculations concerning the bond length and the vibrational frequencies are very small. The binding energies reflect the differences in the singlet-triplet splitting (cf. Table 9.4) and the functional dependence of the overbinding (cf. Table 9.1). A direct comparison to experiment is not possible since no well defined states can be calculated in DFT.

In summary, there are two major deficiencies in the description of the oxygen molecule caused by using only an approximation to the unknown correct exchange-correlation functional. First, the oxygen binding energy in the $^3\Sigma_g^-$ state is significantly overestimated. From the results obtained using different functionals we conclude that at least gradient-corrected functionals are necessary to investigate the dissociation of O_2 on Al(111), although also the binding energies obtained with the different GGAs are still remarkably off from the experimental value by more than about 0.5 eV. Particularly the PBE and the RPBE functionals seem to form two extrema within the tested GGA functionals, the deviations from experiment being about 1 eV

E_{bind} (eV)	ν (cm^{-1})	d (Å)	Reference	
6.402	1584	1.210	restricted (LDA)	this work
4.945	1513	1.226	restricted (PBE)	this work
4.920	1512	1.225	restricted (PW91)	this work
4.605	1449	1.237	restricted (BLYP)	this work
4.463	1486	1.231	restricted (RPBE)	this work
6.909	1589	1.210	unrestricted (LDA)	this work
5.691	1521	1.225	unrestricted (PBE)	this work
5.675	1520	1.225	unrestricted (PW91)	this work
5.356	1458	1.236	unrestricted (BLYP)	this work
5.242	1495	1.231	unrestricted (RPBE)	this work
4.139	1509	1.216	$^1\Delta_\mathrm{g}$ experiment	[210]
3.480	1433	1.227	$^1\Sigma_\mathrm{g}^+$ experiment	[210]

Table 9.5: Binding energies, frequencies and bond lengths of “singlet” O_2. The zero point vibrations have not been taken into account.

and 0.6 eV, respectively. Those two functionals have therefore been chosen to map the potential-energy surfaces for the oxygen dissociation on Al(111), to obtain an estimate for the uncertainties due to the exchange-correlation functional. Nevertheless, the overbinding will not strongly affect the shape of the potential-energy surface for the oxygen dissociation on Al(111), because the latter represents energy differences of similar configurations of the O_2 molecule, and the errors due to the poor description of the oxygen binding energy are expected to cancel each other to a large extent, at least far away from the surface. Closer to the surface a strong interaction with the aluminium atoms, i.e. hybridization, sets in, and in this situation the electronic structure becomes completely different from the free O_2 molecule. Consequently, the above mentioned reasons for the overbinding in O_2 do not apply anymore.

The second problem, the significantly underestimated singlet-triplet splitting in unrestricted DFT due to the poor description of the singlet state by current approximate exchange-correlation functionals, does not affect the diabatic triplet potential-energy surface due to the single-determinant nature of the high-spin triplet state. The triplet PES is most important for the present work, as non-adiabatic effects can only account for the low sticking probability of oxygen molecules, if energy barriers exist on this energy surface. However, a full consideration of non-adiabatic effects will also have to include transitions to other diabatic energy surface, an important example being the singlet energy surface. From our calculations of the free oxygen molecule we conclude that an “accurate” description of the singlet states is available neither from spin-restricted nor from spin-unrestricted calculations. A wrong energetic position of the singlet surface with respect to the triplet state is obtained, i.e. the singlet-triplet splitting is overestimated in restricted DFT and underestimated in unrestricted DFT. Therefore, only the qualitative shape of the singlet PES can be obtained.

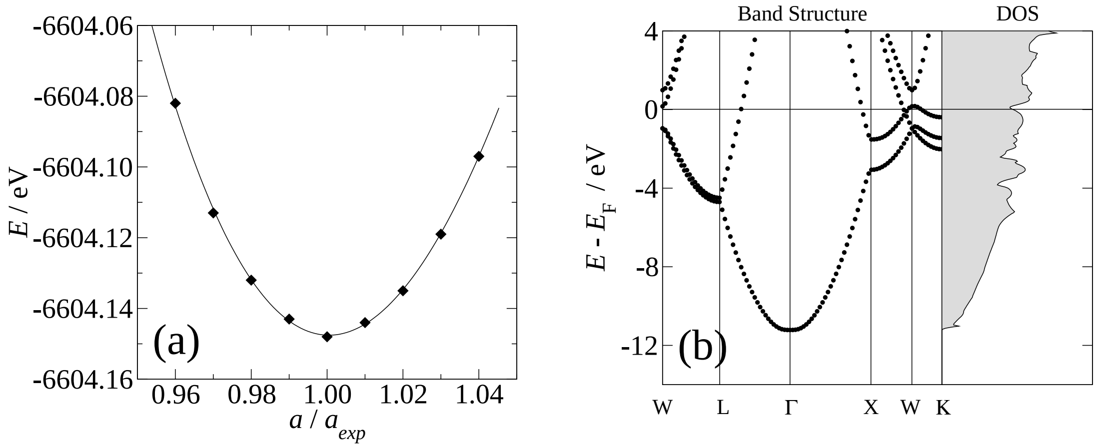

Figure 9.3: Properties of bulk aluminium obtained using the PBE functional. (a) shows the total energy of bulk aluminium as a function of the lattice constant (in units of the experimental lattice constant), the line indicates the energy curve obtained from a fit according to Eq. (9.4). (b) shows the band structure and the density of states of bulk aluminium (spurious peaks are caused by the tetrahedron method [122]).

9.2 Aluminium

9.2.1 Bulk Aluminium

Bulk aluminium has a face centered cubic (fcc) structure, in which each atom is coordinated by 12 nearest neighbors. A fundamental property of bulk aluminium is its equilibrium lattice constant, which has to be known accurately to construct the slabs representing the Al(111) surface. To determine the lattice constant, the total energy of bulk aluminium has been calculated for 9 different lattice constants, i.e. the experimental lattice constant of 4.05 Å [121], as well as lattice constants increased and decreased by up to ±4 % in 1 % steps. The calculations have been done using a basis function cutoff of 9 bohr, a *dnd* basis, a mesh of 12×12×12 k-points (72 k-points in the irreducible wedge of the Brillouin zone) and a Fermi broadening of 0.1 eV employing the LDA, PBE and RPBE functionals. The bulk properties are converged with respect to these parameters, which has been confirmed by the convergence test calculations summarized in Appendix B. The obtained energy curve as a function of the lattice constant is shown in Fig. 9.3(a) for the PBE functional. From these energies the minimum energy lattice constant can be determined using Murnaghan's equation of state [243, 244].

$$E(V) = E(V_0) + \frac{B_0 V}{B_0'(B_0'-1)}\left[B_0'(1-\frac{V_0}{V})(\frac{V_0}{V})^{B_0'} - 1\right] \tag{9.4}$$

V is the volume of the unit cell, V_0 is the equilibrium volume, B_0 is the bulk modulus and B_0' the derivative of the bulk modulus with respect to pressure p. The bulk modulus is defined as the second derivative of the energy with respect to the volume and can also be obtained from Eq. (9.4).

$$B_0(T,V) = -V\left(\frac{\partial p}{\partial V}\right)_T = V\left(\frac{\partial^2 E}{\partial V^2}\right) \tag{9.5}$$

The lattice constants and bulk moduli defined this way are listed in Table 9.6 for each functional and compared to experimental and theoretical data available in the literature. Additionally, the cohesive energy E_{coh} has been calculated, which is defined as

$$E_{\mathrm{coh}} = \frac{1}{N}(E_{\mathrm{bulk}} - N \cdot E_{\mathrm{atom}}) \quad . \tag{9.6}$$

N is the number of aluminium atoms in the unit cell, and E_{bulk} and E_{atom} are the total energies of a bulk atom and a free atom respectively[5]. Finally, also the density of states and the band structure or bulk aluminium have been calculated using the PBE functional. They are shown in Fig. 9.3(b).

The calculated lattice constants, bulk moduli and cohesive energies are in excellent agreement with data reported in the literature. The LDA tends to overbind and yields a significantly too high cohesive energy, and a too small lattice constant. The overbinding is not present using the PBE functional, which yields very similar results to the PW91 functional [114]. DFT data on aluminium using the RPBE functional are not available in the literature, but the characteristic weaker binding [74] compared to the PBE functional is also found here, which manifests mainly in the lower cohesive energy, while the lattice constant is only about 1% larger than the PBE value.

9.2.2 The Al(111) Surface

The lowest energy surface of aluminium is the close packed, unreconstructed Al(111) surface [36, 37], although the Al(100) and Al(110) are only slightly less stable. It can be characterized by physical quantities like the work function, the geometry changes due to relaxation and the surface energy. To test the accuracy of the description of the Al(111) surface using DMol^3 these quantities have been calculated for a 7 layer Al(111) slab geometry with a vacuum size of 30 Å. Tests have been done to ensure that the slab is thick enough to provide a reliable model for the surface. The two outermost aluminium layers have been fully relaxed while the atoms of the 3 central layers have been kept fixed at bulk positions. The calculations have been done using

[5]The atomic calculation has been done employing a *dnp* basis and a basis function cutoff of 18 bohr to obtain a completely converged total energy of the atom. A cutoff of 9-bohr yields an approximately 0.13 eV higher total energy. No periodic boundary conditions have been used in the atomic calculation.

Reference	a_0 (Å)	B_0 (GPa)	E_{coh} (eV)
this work (AE, LDA)	3.994	84.5	4.025
this work (AE, PBE)	4.051	76.1	3.447
this work (AE, RPBE)	4.082	72.9	3.161
[225] (experiment)	4.041	—	3.36
[121] (experiment)	4.05	72.2	3.39
[67] (PP, LDA)	3.96	—	—
[245] (PP, LDA)	3.97	83	4.09
[246] (PP, LDA)	3.96	80.8	4.06
[245] (PP, PW91)	4.05	79	3.52
[4] (PP, PW91)	4.042	70.5	—
[246] (PP, PW91)	4.032	72.0	3.51

Table 9.6: Bulk properties of aluminium. PP indicates the use of pseudopotentials, while AE refers to all-electron calculations.

the same basis parameters as for bulk-aluminium and a k-point mesh of 12×12×1 k-points (19 k-points in the irreducible wedge of the Brillouin zone). The changes in the layer spacings due to the relaxation between the first and the second layer, Δ_{12}, and between the second and the third layer, Δ_{23}, with respect to the bulk layer distance are given in Table 9.7. We find a slight outward relaxation of about 1 % of the first metal layer for all functionals tested in this work, which is in good agreement with experimental and theoretical values from the literature.

The surface energy γ can be calculated from the total energy of the relaxed aluminium slab E_{slab}, the bulk energy per atom E_{bulk} and the surface area A per surface unit cell,

$$\gamma = \frac{1}{2A}(E_{\mathrm{slab}} - N \cdot E_{\mathrm{bulk}}) \quad . \tag{9.7}$$

The values obtained for the LDA, PBE and RPBE functionals are given in Table 9.8 and compared to experimental and theoretical values. The trend of the surface energies with respect to the functional reflects the generally anticipated binding properties of the functionals, in that the LDA yields the highest and the RPBE functional the lowest value.

The work function ϕ_{e}, which is the energy required to remove an electron from the surface, is determined from the electrostatic potential in the center of the vacuum region ϕ_∞ and the Fermi energy ϵ_{F} of the slab.

$$\phi_{\mathrm{e}} = \phi_\infty - \epsilon_{\mathrm{F}} \tag{9.8}$$

The calculated work functions for the three functionals are listed in Table 9.9. The experimental work function is best reproduced by the LDA, while the PBE and RPBE values differ from experiment by about 0.2 and 0.3 eV respectively.

Reference	Δ_{12} (%)	Δ_{23} (%)
this work (LDA)	+1.4	-0.4
this work (PBE)	+2.0	-0.1
this work (RPBE)	+1.2	-0.8
[247] (LEED)	+0.9 ± 0.5	—
[248] (LEED)	+1.7 ± 0.3	+0.5 ± 0.7
[249] (LEED)	+2.2	—
[67] (LDA)	+1	-2
[250] (LDA)	+0.8	+0.5
[4] (PW91)	+1.06	-1.53
[24] (PW91)	+1.08	-0.10

Table 9.7: Relaxation of the clean Al(111) surface.

Reference	γ (meV/Å^2)
this work DFT, LDA	83
this work DFT, PBE	70
this work, DFT, RPBE	61
[251] experiment	71.3
[252] experiment	73
[253] experiment	72
[254] DFT, LDA	79.3
[255] DFT, LDA	52
[37] DFT, LDA	70
[36] DFT, PBE	74.8

Table 9.8: Surface energy of the Al(111) surface.

Reference	ϕ_e (eV)
this work, DFT, LDA	4.139
this work, DFT, PBE	3.998
this work, DFT, RPBE	3.944
[256] experiment	4.24
[250] (LDA)	4.25
[257] (LDA)	4.275
[255] (LDA)	4.17
[60] (LDA)	4.7
[254] (LDA)	4.54
[4] (PW91)	4.085

Table 9.9: Work function of the Al(111) surface.

9.3 The Oxygen-Covered Al(111) Surface

The last system we have to investigate before we can proceed to the dissociation of O_2 at Al(111) is the oxygen-covered Al(111) surface. The purpose of this chapter is two-fold. First, it is a good test to show that DMol^3 provides an accurate description of the stable adsorption sites, i.e. the local minima of the PES we want to study later on. Therefore, the equilibrium structures of (1×1) and (2×2) slabs with oxygen atoms adsorbed at the fcc, hcp, top and bridge sites have been calculated and compared to earlier published results. Second, the variations in the obtained results when using different exchange-correlation functionals are of interest, because this gives a first feeling of functional dependencies of the potential-energy surface for the oxygen dissociation on Al(111).

The most stable adsorption site for oxygen atoms on the Al(111) surface is the threefold fcc hollow site [4, 5, 35, 55, 67]. This site is shown in Fig. 9.4, together with other on-surface sites, like the hcp, top and bridge sites. The oxygen binding energies and equilibrium structures have been calculated employing a 7 layer aluminium slab

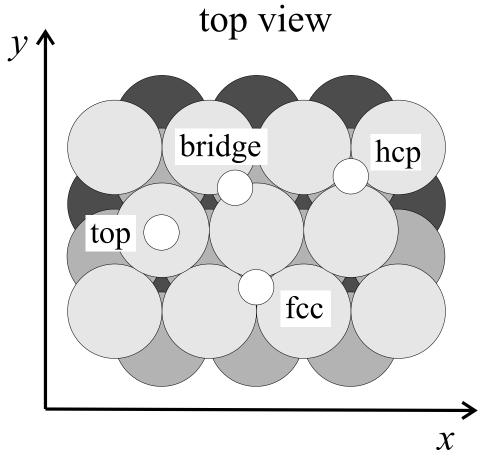

Figure 9.4: On-surface adsorption sites of oxygen on the Al(111) surface.

and a vacuum size of 30 Å. The oxygen binding energy E_{bind} at a given coverage θ is defined as the difference of the energy of the oxygen-covered slab $E_{\mathrm{Al,O}}$ and the energies of the clean aluminium slab E_{Al} as well as the binding energy of the free oxygen molecule $E_{\mathrm{bind,O_2}}$. Due to the inversion symmetry of the slab oxygen is adsorbed on both sides. Consequently the number of oxygen atoms N has to be taken into account.

$$E_{\mathrm{bind}} = -\frac{1}{N}\left(E_{\mathrm{Al,O}} - E_{\mathrm{Al}} - \frac{N}{2}\cdot E_{\mathrm{bind,O_2}}\right) \tag{9.9}$$

For an oxygen coverage of $\theta_{\mathrm{O}} = 1$ monolayer (ML, defined as the fraction of oxygen atoms to the number of first layer metal atoms) a (1×1) slab and for a coverage of $\theta_{\mathrm{O}} = 0.25$ ML a (2×2) slab has been used. All calculations have been done employing the same basis set applied in Section 9.1 and a 12×12×1 k-point mesh in case of the (1×1) and a 6×6×1 k-point mesh in case of the (2×2) supercells (19 and 13 k-points in the irreducible wedge of the Brillouin zone, respectively). In all cases the positions of the oxygen atoms and the outermost two aluminium layers were allowed to relax. All energies have been extrapolated to 0 K [258] and the atomic positions have been optimized using the *gdiis* (geometry optimization by direct inversion in the iterative subspace) algorithm [158] until the forces were below 5 mRy bohr^{-1}. The obtained oxygen binding energies are listed in Table 9.10 for the (1×1) slabs and in Table 9.11 for the (2×2) slabs. The layer separations between the first and the second aluminium layer, Δ_{12}, and between the second and the third layer, Δ_{23}, as well as the distance of the oxygen layer from the first aluminium layer $\Delta_{\mathrm{O,Al}}$ and the oxygen-aluminium bond length $d_{\mathrm{O,Al}}$ are summarized in Tables 9.12 and 9.13. In case of the (2×2) slabs the layer separations have been calculated by averaging over all 4 aluminium atoms within one layer. All data show, that the LDA yields the strongest and the RPBE

site	E_{bind} (eV) this work LDA	this work PBE	this work RPBE	Kiejna and Lundqvist [4, 56] PW91
fcc	-5.312 (0.000)	-4.681 (0.000)	-4.437 (0.000)	-4.782 (0.000)
hcp	-5.101 (0.211)	-4.474 (0.208)	-4.223 (0.214)	-4.612 (0.170)
bridge	-4.098 (1.214)	-3.544 (1.138)	-3.350 (1.087)	—
top	-0.463 (4.850)	-0.165 (4.517)	-0.033 (4.404)	—

Table 9.10: Oxygen binding energies at different adsorption sites of a (1×1) Al(111) slab obtained from Eq. (9.9). The values in brackets are the binding energies with respect to the binding energy at the fcc site.

functional the weakest binding, which is also reflected by the bond lengths. The same trend in the oxygen binding energy with respect to these functionals has also been found by Hammer *et al.* [74] on several transition metal surfaces. In agreement with experiment the fcc site is most stable, and the oxygen atom has a vertical distance of about 0.7 Å from the first metal layer [35, 44, 57–59]. The only qualitative difference to previously published data concerns the binding energy in the fcc site of a (2×2) slab. In Ref. [67] the PW91 functional is found to give a stronger binding than the LDA. This is in contrast to our PBE data, which should perform very similar to PW91 [114], and also their absolute value of the binding energy is much too large compared to other calculations using the same functional [4, 24, 71]. Other calculations using the PW91 functional [4, 24, 71] yielded binding energies very similar to our PBE value. The reason for this discrepancy might either be due to the pseudopotential employed in [67], or more probably due to the non-selfconsistent post-GGA procedure that was applied, i.e. the PW91 binding energy was calculated using a slab geometry relaxed within the LDA, and the gradient correction to the binding energy was obtained from a non-selfconsistent calculation using the LDA density. The latter possibility is also supported by an excellent agreement between the absolute values of the LDA binding energies determined in Ref. [67] and in the present work.

Finally, also calculations of oxygen atoms adsorbed in the fcc site of a (3×3) aluminium slab have been carried out corresponding to a coverage of $\frac{1}{9}$ ML. The results are given in Table 9.14. The oxygen binding energies for all functionals are shown in Fig. 9.5 as a function of the supercell size. It can clearly be seen that the absolute value of the binding energy decreases with increasing cell size indicating an attractive interaction between the oxygen atoms. This is in excellent agreement with the STM experiments of Brune *et al.* [5, 8] showing islands of chemisorbed oxygen atoms and also with previous DFT studies [4].

	E_{bind} (eV)			
site	this work LDA	this work PBE	this work RPBE	Ref. [4, 56] PW91
fcc	-4.840 (0.000)	-4.215 (0.000)	-3.932 (0.000)	-4.312 (0.000)
hcp	-4.397 (0.443)	-3.785 (0.430)	-3.505 (0.427)	-3.992 (0.320)
bridge	-3.986 (0.854)	-3.432 (0.783)	-3.190 (0.742)	—
top	-1.558 (3.282)	-1.222 (2.993)	-1.066 (2.866)	—
site	Ref. [67] LDA	Ref. [67] PW91	Ref. [24] PW91	Ref. [71] PW91
fcc	-4.76 (0.00)	-5.00 (0.00)	-4.527 (0.000)	-4.3 (0.000)
hcp	-4.41 (0.35)	-4.63 (0.37)	—	—
bridge	-3.97 (0.79)	-4.25 (0.75)	—	—
top	-1.70 (3.06)	-2.06 (2.94)	—	—

Table 9.11: Oxygen binding energies at different adsorption sites of a (2×2) Al(111) slab obtained from Eq. (9.9). The values in brackets are the binding energies with respect to the binding energy at the fcc site.

	this work, LDA			
site	Δ_{12} (%)	Δ_{23} (%)	$\Delta_{\mathrm{O,Al}}$ (Å)	$d_{\mathrm{O,Al}}$ (Å)
fcc	+1.0	-2.1	0.725	1.785
hcp	+2.2	-1.8	0.739	1.790
bridge	+1.1	-1.8	0.902	1.676
top	-2.0	+0.1	1.672	1.672
	this work, PBE			
site	Δ_{12} (%)	Δ_{23} (%)	$\Delta_{\mathrm{O,Al}}$ (Å)	$d_{\mathrm{O,Al}}$ (Å)
fcc	+1.5	-2.1	0.743	1.807
hcp	+3.0	-1.3	0.757	1.812
bridge	+1.8	-1.3	0.919	1.697
top	-1.3	+0.1	1.694	1.694
	this work, RPBE			
site	Δ_{12} (%)	Δ_{23} (%)	$\Delta_{\mathrm{O,Al}}$ (Å)	$d_{\mathrm{O,Al}}$ (Å)
fcc	+0.9	-3.0	0.742	1.824
hcp	+2.2	-2.2	0.757	1.830
bridge	+1.0	-2.2	0.916	1.709
top	-2.0	-0.6	1.701	1.701
	Kiejna and Lundqvist [4], PW91			
site	Δ_{12} (%)	Δ_{23} (%)	$\Delta_{\mathrm{O,Al}}$ (Å)	$d_{\mathrm{O,Al}}$ (Å)
fcc	+3.93	-1.36	0.709	1.796

Table 9.12: Equilibrium structures for oxygen adsorbed at different adsorption sites of a (1×1) Al(111) slab.

	this work, LDA			
site	Δ_{12} (%)	Δ_{23} (%)	$\Delta_{O,Al}$ (Å)	$d_{O,Al}$ (Å)
fcc	+0.5	-1.3	0.803	1.842
hcp	+1.6	-1.3	0.817	1.852
bridge	+0.8	-1.4	0.950	1.759
top	+1.1	-0.8	1.461	1.670
	this work, PBE			
site	Δ_{12} (%)	Δ_{23} (%)	$\Delta_{O,Al}$ (Å)	$d_{O,Al}$ (Å)
fcc	+1.3	-0.8	0.837	1.870
hcp	+2.5	-0.7	0.871	1.882
bridge	+1.4	-0.7	1.019	1.781
top	+2.0	+0.0	1.514	1.693
	this work, RPBE			
site	Δ_{12} (%)	Δ_{23} (%)	$\Delta_{O,Al}$ (Å)	$d_{O,Al}$ (Å)
fcc	+0.5	-1.6	0.840	1.884
hcp	+1.8	-1.5	0.883	1.899
bridge	+0.8	-1.5	1.050	1.787
top	+1.0	-0.6	1.576	1.699
	Kiejna and Lundqvist [4], PW91			
site	Δ_{12} (%)	Δ_{23} (%)	$\Delta_{O,Al}$ (Å)	$d_{O,Al}$ (Å)
fcc	+2.47	-1.16	0.772	—

Table 9.13: Equilibrium structures for a quarter monolayer of oxygen adsorbed at different adsorption sites of a (2×2) Al(111) slab.

	this work LDA	this work PBE	this work RPBE
E_{bind}(fcc) (eV)	-4.692	-4.076	-3.777
$\Delta_{O,Al}$ (Å)	0.763	0.816	0.846
$d_{O,Al}$ (Å)	1.846	1.867	1.881
Δ_{12} (%)	+0.2	+1.3	+1.3
Δ_{23} (%)	-1.8	-0.6	-0.6

Table 9.14: Oxygen binding energies, oxygen-aluminium bond lengths $d_{O,Al}$ and layer distances Δ for $\theta_O = \frac{1}{9}$ adsorbed in the fcc hollow site of a (3×3) slab.

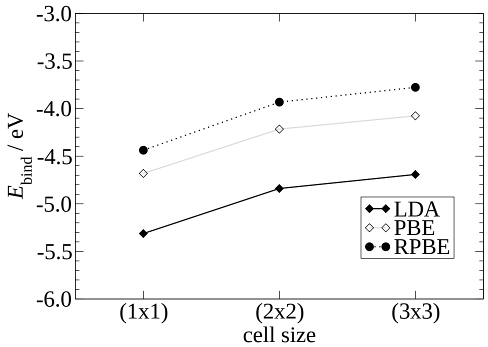

Figure 9.5: Oxygen binding energy as a function of the supercell size using different functionals.

Chapter 10

The Adiabatic Potential-Energy Surface

10.1 Calculation of the Adiabatic Potential-Energy Surface

The calculation of the adiabatic potential-energy surface for the dissociation of oxygen molecules on the Al(111) surface is one of the most important parts of this project. An accurate mapping of this energy surface combined with a reliable fit allows to perform molecular dynamics simulations to obtain the sticking curve for oxygen molecules on the Al(111) surface from first-principles for the first time. Due to the almost complete absence of energy barriers reported for the parts of the potential-energy surface investigated so far [22, 24, 70–73], a high sticking probability is very likely to be found. Nevertheless, it is not possible to estimate the steering effect by the surface potential on the molecular trajectories without performing multi-dimensional dynamical studies. Slow molecules might be steered systematically to certain surface sites and angular orientations which can have a strong effect on the sticking properties [15–17]. To account for the possibility of such steering effects, performing a statistically significant number of molecular dynamics runs is the only available tool. The finally obtained adiabatic sticking curve will be an important reference when going beyond the adiabatic approach to investigate the possible role of non-adiabatic effects.

A (3×3) slab geometry has been chosen to map the adiabatic potential-energy surface. Tests have shown (cf. Appendix B) that in a (2×2) slab, which has hitherto been used exclusively in the literature, the lateral interactions between oxygen molecules in neighbored cells can still be significant. For some geometries they can be of the order of 0.2 eV, which is the same order of magnitude as the expected energy barriers. This becomes obvious when looking at the lattice constant of a (2×2) unit cell, which is about 5.7 Å. The criterion for dissociative adsorption employed in this work is a doubling of the O_2 bond length compared to the value 1.2 Å of the free molecule. In case of a molecule oriented parallel to the surface the oxygen atoms are at this bond length already rather close to their periodic images. By testing several supercells of different sizes we found that only a (3×3) supercell is large enough to allow for an accurate mapping of the potential up to a bond length of 2.4 Å for arbitrary molecular orientations with negligible lateral interactions (cf. Appendix B). Therefore, this cell size has been used in all calculations. Since the aluminium lattice constants obtained for the PBE and the RPBE functional are very similar (cf. Section 9.2), the PBE lattice constant has been used for all calculations. The adsorption of oxygen molecules on Al(111) gives rise to large surface dipole moments which are rather long ranged. As in $DMol^3$ no dipole correction [259] is yet implemented, oxygen has to be adsorbed on both sides of the slab to neutralize the dipole field by inversion symmetry. However, adsorbing oxygen molecules on both sides of the slab requires a rather thick slab of 7 aluminium layers to avoid interactions between the oxygen atoms through the slab (cf. Appendix B). Consequently, in total the supercell employed here consists of 63 aluminium atoms and 4 oxygen atoms. It is shown in Fig. 10.1. Interactions between the oxygen molecules through the vacuum can easily be avoided by choosing a large vacuum, which does not cause additional computational costs employing atomic orbital basis functions of finite range. The potential-energy surface is mapped up to a molecule-surface distance of 10 Å. Taking into account both surfaces and an additional vacuum of 10 Å between the image oxygen molecules when they have the maximum distance from the surface, a total vacuum thickness of 30 Å is sufficient. In the calculation of potential-energy surfaces for molecule-surface interactions a standard procedure is to employ the frozen surface approximation [17], i.e. only the degrees of freedom of the molecule are taken into account and the substrate is fixed reducing the dimensionality of the potential-energy surface to six, which allows for a systematic mapping. This is a rather drastic approximation and its validity has to be checked carefully for each system. In order to investigate its applicability to the dissociation of oxygen on Al(111) we have performed detailed studies of the effects of substrate mobility, which are summarized in Section 10.5. We found that in the typical barrier region, i.e. for $Z > 2$ Å, the motion of the aluminium atoms due to the approaching oxygen molecule is negligible. Only for smaller molecule-surface separations large forces are acting on the substrate atoms making this approximation questionable. At this late stage of the dissociation process the mobility of substrate atoms will have a clear effect on the dissociation mechanism and on the dissipation of the adsorption energy. Consequently, for the calculation of the sticking curve the frozen surface approximation is not critical, and in this project the surface atoms have been fixed at their bulk position, because the clean Al(111) surface only shows a marginal outward relaxation of about 1 % of the bulk layer separation (cf. Section 9.2 and Ref. [4] and [56]).

Apart from the supercell setup well converged basis set parameters for the DFT calculation are equally important. Corresponding tests have been performed very carefully, since on the one hand the obtained energies should be sufficiently accurate to find barriers of about 0.1 eV, while on the other hand thousands of calculations have to be performed. The efficiency of the calculations is therefore also very important.

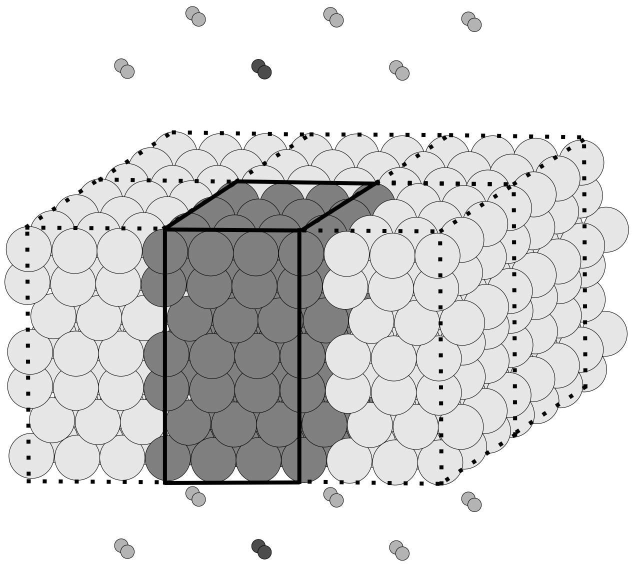

Figure 10.1: Structure of the (3×3) supercell employed in the mapping of the adiabatic potential-energy surface.

For all calculations a basis function cutoff of 9 bohr has been used together with an *all* basis for the oxygen atoms and a *dnd* basis for the aluminium atoms. For this cutoff the default integration mesh (*iomin*=1, *iomax*=5, *thres*=0.0001, *rmaxp*=9 and *s*=1) is of sufficient accuracy. To improve the convergence of the calculations a Fermi broadening with an electronic temperature of 0.1 eV has been employed[1], and the energies have been extrapolated to zero temperature [258]. A k-point mesh of 4×4×1 k-points has been used. This corresponds to 10 k-points in the irreducible wedge of the first Brillouin zone for the lowest possible symmetry of the system. This set of k-points has been used for all calculations, irrespective of a possibly higher symmetry due to the molecular configuration, to obtain directly comparable energies. Test calculations showing the convergence of the system with respect to the k-point mesh, the basis set and the basis function cutoff are given in Appendix B. To check the functional dependence, the potential-energy surface has been calculated using the RPBE [74] and the PBE [114] functionals. Even though both functionals belong to the class of GGA functionals and perform much better than the LDA in case of the oxygen molecule, they have been shown to yield rather different binding energies of the oxygen molecule [74] (cf. Section 9.1), which allows to estimate the uncertainties in our results due to the treatment of exchange and correlation.

The six-dimensional potential-energy surface has been mapped by calculating many

[1]Some geometries are extremely hard to converge, in particular when nearly-free oxygen atoms far away from the surface emerge. In an attempt to improve the convergence, a Broyden charge density mixing scheme [260–263] has been implemented in $DMol^3$ in this project, but it has shown to be slightly inferior to the already included Pulay mixing scheme [159, 160].

two-dimensional cuts, in which the energy is given as a function of the bond length d and the center of mass distance of the molecule from the surface Z. Due to their shape these cuts are commonly called "elbow plots". All other degrees of freedom, i.e. the angles θ and ϕ and the lateral coordinates X and Y, remain fixed in the elbow plots. The configuration space referring to these four dimensions is mapped by calculating elbow plots for many different surface sites and many different molecular orientations. The employed coordinate system is shown in Fig. 8.2. This way the six-dimensional adiabatic potential-energy surface has been mapped by calculating 38 elbow plots at the high symmetry fcc, hcp, top and bridge sites for perpendicular, parallel and several tilted molecular orientations. The 38 molecular orientations of the calculated elbow plots are listed in Appendix C. The symmetry of the surface has been fully exploited in that only energies for points within the irreducible wedge of the unit cell have been calculated, which is shown in Fig. 8.1. The points to construct the elbow plots have been selected manually on an irregular grid to avoid calculations of energetically irrelevant geometries. This also allows for a denser sampling of very important parts of the energy surface, i.e. barrier regions and minimum energy pathways. The zero point of the potential-energy is defined as the total energy for an infinite molecular distance from the surface, the molecule having its equilibrium bond length of 1.224 Å.

10.2 Properties of the Adiabatic Potential-Energy Surface

Some of the obtained elbow plots are shown in Fig. 10.2 and 10.3 for the RPBE and the PBE functional, respectively. In case of the RPBE functional we find several elbow plots with shallow energy barriers of up to 0.1 eV, while in case of the PBE functional none of the calculated elbow plots shows a barrier towards adsorption. Apart from one elbow plot discussed below this is in excellent agreement with all previous studies [22, 24, 73]. Direct comparison of the elbow plots obtained with the PBE and the RPBE functionals shows that the RPBE potential-energy surface is less attractive. This is a general feature of the RPBE functional [74] and is consistent with the calculations on the free oxygen molecule and on the oxygen-covered Al(111) surface in Section 9.3. The energy difference between the PBE and the RPBE PES is far smaller than the binding energy difference of the free O_2 obtained for these functionals (cf. Section 9.1), which is about 0.5 eV, as long as the bond length is close to the value of the free molecule. It can therefore be concluded that the strong overbinding of the O_2 molecule does not play a significant role in case of the adiabatic PES due to an efficient error cancellation that occurs, since the PES represents only energy differences of very similar molecular configurations.

The elbow plots shown in Fig. 10.2(a) and 10.3(a) correspond to a molecule oriented perpendicular to the surface above an fcc site. A stretching of the bond length in this orientation with a slightly increasing center of mass height Z would correspond to an abstraction mechanism, because in this case an elongation of the bond length can only be realized when one atom approaches the surface while the other atom is reflected into the gas phase. A small local minimum at $d = 1.4$ Å and $Z = 1.7$ Å has been found in agreement with previous studies of this elbow plot [24, 73]. The parallel orientations shown in Fig. 10.2 and 10.3 (b), (d), (e) and (f) all give rise to a dissociation with both atoms adsorbing on the surface. The elbow plot shown in Fig. 10.2(f) for a molecule above the bridge site shows an energy barrier, which has also been reported in independent studies [22, 24, 73]. In [22] the barrier has been found only in case of the RPBE functional ($E_\mathrm{b} = 0.14$ eV), while the BP86 functional [235, 264] did not yield a barrier. In [24, 73] the barrier has been found for all four tested functionals, PW91 [116], PBE [123], revPBE [229] and RPBE [74], but only one barrier height of $E_\mathrm{b} = 0.2$ eV is given without referring to one of the functionals. As shown in Fig. 10.2(f) in the present work a barrier of 0.08 eV has been found for this molecular orientation using the RPBE functional, while in case of the PBE functional no barrier exists (Fig. 10.3(f)). The reason for this difference between our study and the work of Yourdshahyan *et al.* in case of the PBE functional might be the pseudopotential approach or the smaller (2×2) unit cell employed in [24, 73]. The only molecular orientation which does not permit the dissociation of the oxygen molecule is shown in Fig. 10.3(c) and 10.2(c). In this configuration the molecule is oriented perpendicular to the surface above a top site. Due to the comparably small adsorption energy of an oxygen atom at a top site (about 4 eV with respect to the free atom) and the rather high binding energy of the oxygen molecule (5.1 eV [224]), a dissociation is not possible for energetic reasons in this orientation. However, none of these elbow plots is able to describe a real dissociation event, because the molecule is not constrained to move in two dimensions. When the molecule approaches the surface, its angular orientation and lateral positions will change making predictions based on the inspection of two-dimensional cuts of the potential-energy surface very difficult.

A problem when calculating the adiabatic potential-energy surface for the dissociation of oxygen on Al(111) with standard DFT implementations is the charge transfer from the metal to the oxygen molecule that occurs even for very large molecule-surface separations. This is because the antibonding $2\pi^{*\downarrow}$ orbitals, which are unoccupied in the free molecule, are lower in energy than the Fermi energy of the metal. As the states in a DFT calculation are filled in energetic order, electron density is transferred from the aluminium to the oxygen molecule, which shifts up the energy level of the $2\pi^{*\downarrow}$ orbitals until they are aligned with the Fermi level. For separations between 5 and 10 Å the charge transfer to the molecule is of the order of a few percent of an electron as shown in Fig. 10.4(a). This charge transfer into the $2\pi^{*\downarrow}$ orbitals affects the convergence of the total energy with increasing separation from the surface and also the spin state of the molecule, because due to the charge transfer the spin triplet of the oxygen molecule is slightly reduced. Both effects are shown in Fig. 10.4 (b) and (c), respectively. The charge and the spin of the oxygen molecule have been determined using two different methods, the Mulliken population analysis [265] and the

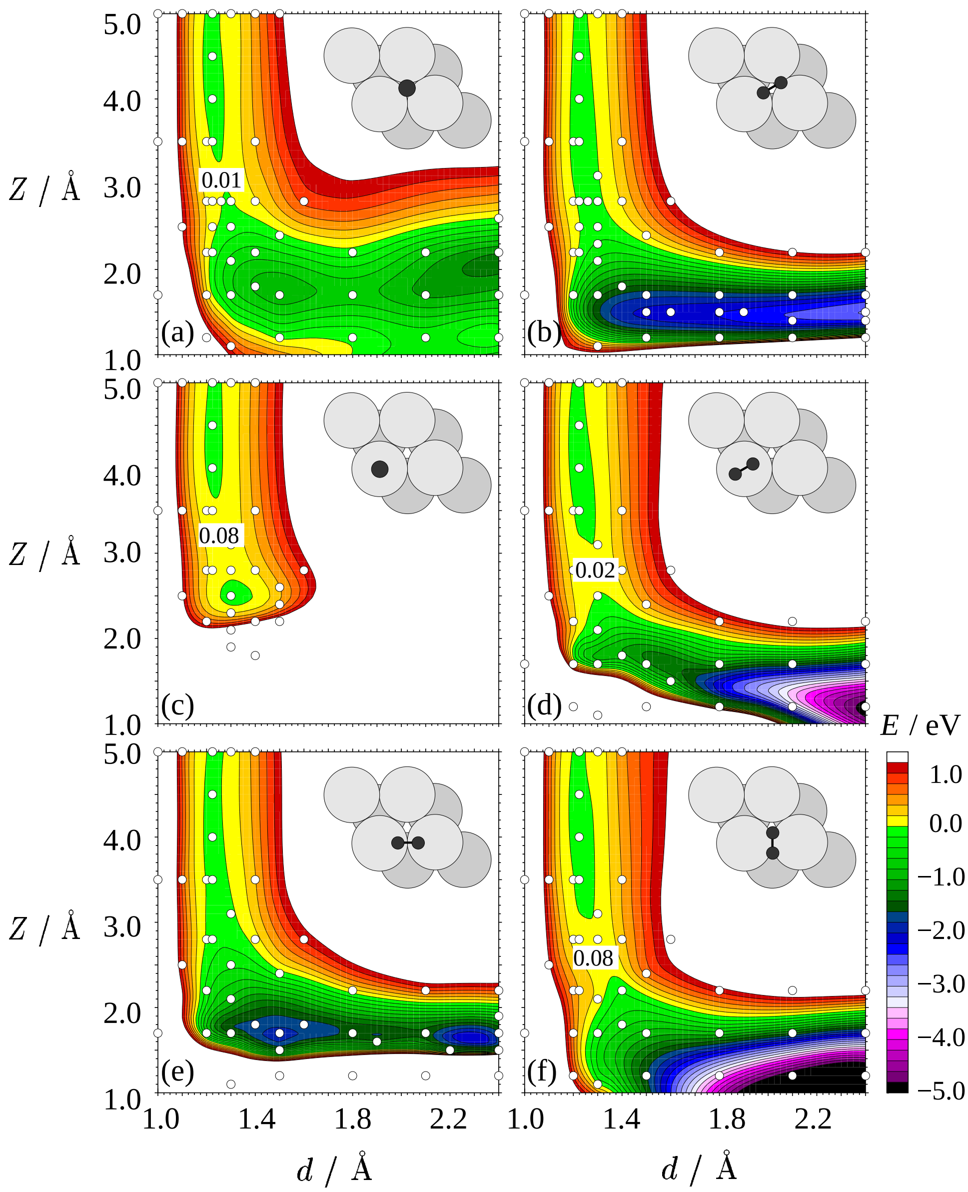

Figure 10.2: Two-dimensional cuts through the six-dimensional adiabatic potential-energy surface calculated using the RPBE functional. For some molecular orientations shallow energy barriers exist. The white circles represent the calculated DFT energy points. The substrate has been frozen in the geometry of the bulk-truncated surface. The energy zero point corresponds to an oxygen molecule in the triplet ground state at an infinite distance from the surface without any charge transfer.

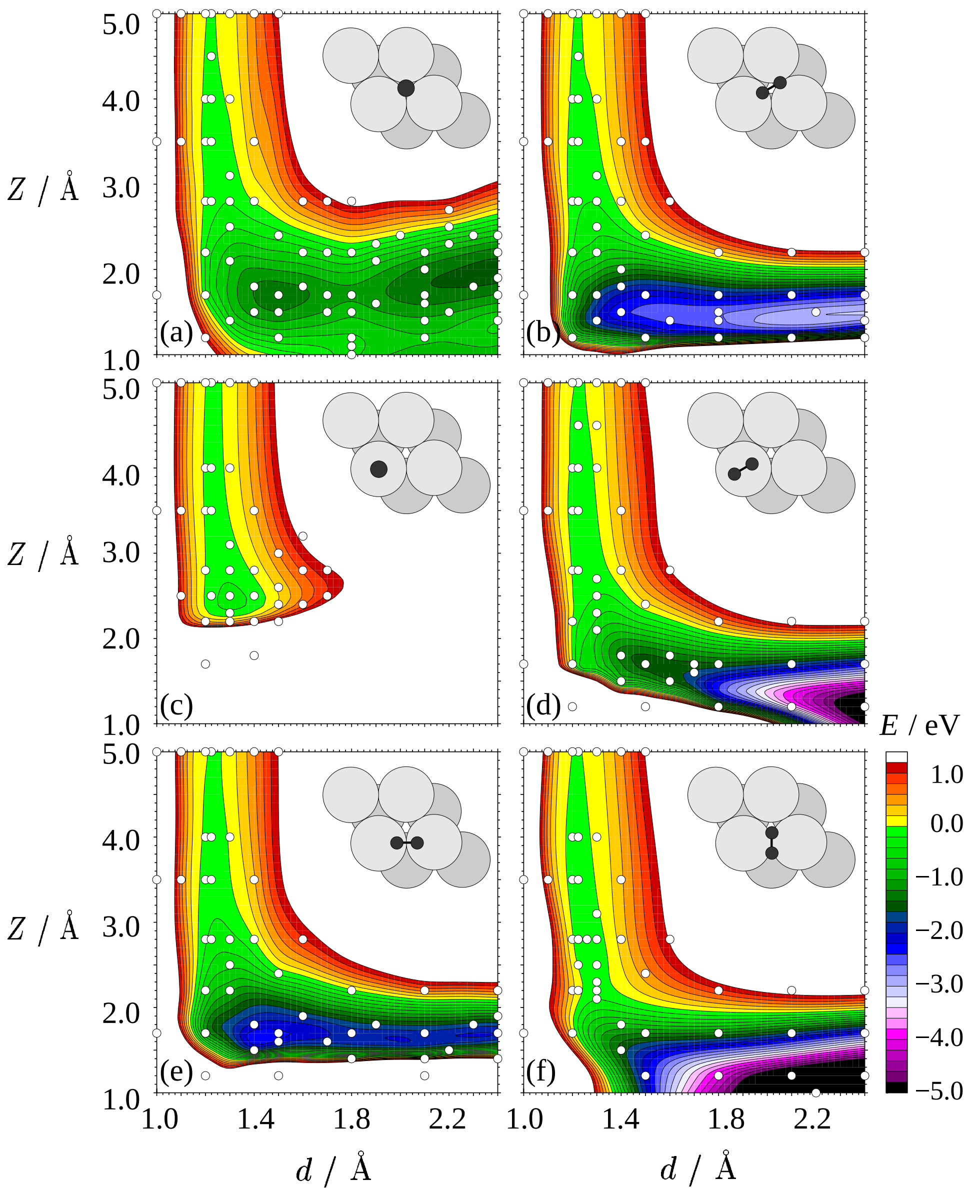

Figure 10.3: Two-dimensional cuts through the six-dimensional adiabatic potential-energy surface calculated using the PBE functional. None of the calculated elbow plots shows energy barriers. The white circles represent the calculated DFT energy points. The substrate has been frozen in the geometry of the bulk-truncated surface. The energy zero point corresponds to an oxygen molecule in the triplet ground state at an infinite distance from the surface without any charge transfer.

Hirshfeld analysis [139] to estimate the uncertainties inherent to such charge analysis methods. For large separations of the molecule from the surface both methods become exact and yield the same results. The obtained molecular charges start to differ for distances smaller than 5 Å and become very large in the interaction region closer to the surface, but the determined spin states seem to be rather consistent in both methods in the plotted range. To understand the charge transfer from the surface to the molecule, calculations of a charged free oxygen molecule have been carried out. The energetic position of the $2\pi^{*\downarrow}$ orbital is shown as a function of the charge of the molecule in Fig. 10.5. The Fermi energy obtained from a calculation on the clean aluminium slab is -4.522 eV and also shown in this figure. From these data it can be concluded that in the limit of an infinite molecular distance from the surface still a charge $q \approx -0.014$ e is transferred to the molecule. In Chapter 13 it will be shown how this charge transfer can be avoided and what the consequences for the total energy are.

When the oxygen molecule approaches the surface, the energetically more favorable orientation is initially perpendicular to the surface. This is in agreement with previous studies [24]. Closer to the surface a parallel orientation is preferred. The approach is accompanied by a continuous charge transfer from the surface to the molecule and a reduction of the triplet spin until finally the singlet state of the adsorbed atoms is reached. For a molecule oriented perpendicular to the surface above an fcc site the partial density of states (DOS) of the oxygen $2p$ states is shown in Fig. 10.6 for several molecular distances from the surface. 6 Å above the surface the 2π and $2\pi^*$ states of the oxygen molecule are very localized sharp peaks. Due to the slight charge transfer mentioned above, the $2\pi^{*\downarrow}$ state is just above the Fermi level and filled only by a small fraction of an electron. When the molecule approaches the surface, the states broaden and up and down spin-densities become more similar, which is the reason for the reduction of the spin of the molecule. At $Z = 2.2$ Å both spin-densities have become almost identical. The evolution of the total spin of the system can be monitored by integrating the spin-density of the whole system. This has been done and the spin has been found to decrease from 90 % of the spin of the free molecule at $Z = 3.5$ Å continuously to 10 % at $Z = 1.9$ Å. To a good approximation this is independent of the molecular orientation. Below $Z = 1.8$ Å the spin vanishes completely.

10.3 Interpolation of the Adiabatic Potential-Energy Surface

Having calculated the adiabatic potential-energy surface for two different functionals on a grid, the next step is to find a reliable fit to obtain the adiabatic energies for all possible molecular geometries as required for the molecular dynamics simulations of the sticking process. This has been done using the neural network technique and

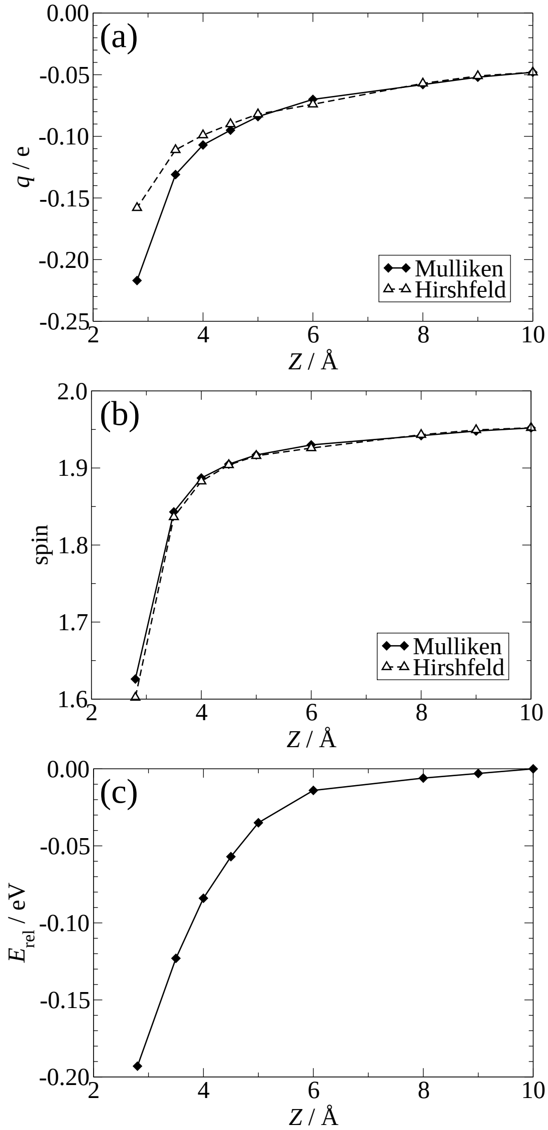

Figure 10.4: Charge, spin and energy as a function of the molecular distance Z from the surface. (a) shows the total charge q on the oxygen molecule obtained from a Mulliken population analysis [265] (black line) and from a Hirshfeld analysis [139] (dashed line). In (b) the total spin of the oxygen molecule is shown for these two methods. In (c) the energy of the system is plotted with respect to an arbitrary zero point at $Z = 10$ Å. The values have been obtained with the PBE functional for a molecule oriented parallel to the surface above an fcc site (geometry 2 in Appendix C).

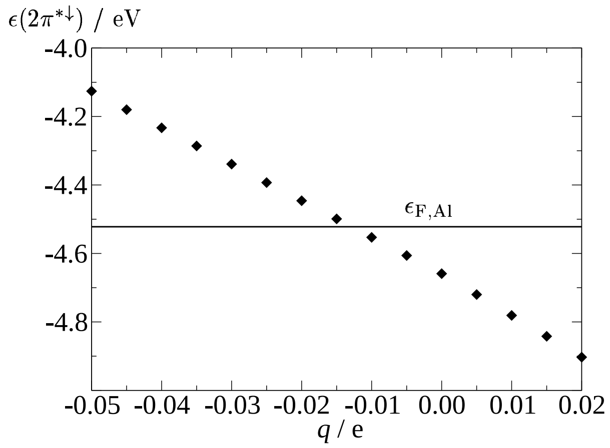

Figure 10.5: Energetic position of the $2\pi^{*\downarrow}$ orbital of a free oxygen molecule as a function of the molecular charge q. The black line indicates the Fermi level $\epsilon_{\mathrm{F,Al}}$ of a clean Al(111) slab. The zero point of the energy corresponds to the vacuum level in the calculation of the free molecule, which is very close to the vacuum level of the potential in the Al(111) slab calculation.

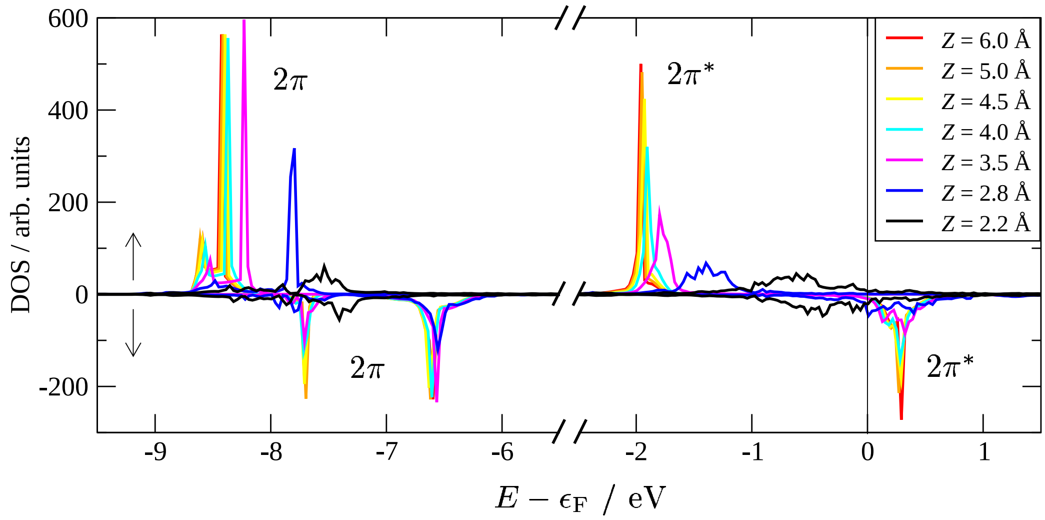

Figure 10.6: Partial density of states (DOS) of the oxygen $2p$ states for several molecular distances Z from the surface calculated with the RPBE functional. The oxygen molecule is oriented perpendicular to the surface above an fcc site and the bond length is fixed to 1.224 Å (geometry 1 in Appendix C).

the Fourier method described in Chapters 7 and 8. Our intention is to perform molecular dynamics simulations up to a kinetic energy of 1 eV with a potential-energy of zero corresponding to an infinite separation between the molecule and the surface. Consequently, our primary aim is to fit the potential-energy surfaces as accurately as possible up to potential-energies of about +1 eV. For higher potential-energies a less accurate fitting is acceptable as this region of the PES is not accessible in the molecular dynamics runs.

First, the DFT data set has to be prepared for the fitting. In case of the PBE functional a total of 1723 *ab initio* data points has been calculated. To focus the fit on the most important part of the potential-energy surface all points with a bond length larger than 2.4 Å or a center of mass distance from the surface of more than 6.0 Å have been removed from the data set. The remaining number of points is 1649. For 46 different molecular orientations 4 (d,Z)-points with an energy of +5.0 eV and the coordinates (d=1.2 Å, Z=0.0 Å), (d=1.0 Å, Z=0.8 Å), (d=1.2 Å, Z=0.5 Å) and (d=1.0 Å, Z=0.0 Å) have been added to the data set[2]. These 184 high energy points are not necessary, but help the neural network to fit the very repulsive energy region close to the surface. These points could have been calculated also by density-functional theory, but this region is not accessible in the molecular dynamics due to the high potential-energy, and therefore precise energies are not required. These points do not reduce the quality of the fitted potential-energy surface at all, as can be seen in the comparison of the calculated and the fitted elbow plots in Fig. 10.9. Another modification of the data set has to be done to define a common zero point for the potential-energy surface. The goal is to get a potential that just depends on the bond length of the molecule at large distances from the surface when there is no interaction between the molecule and the surface present. The DFT data points are available for distances up to 6.0 Å from the surface for all calculated elbow plots, but due to numerical noise in the DFT data at this distance, differences of the total energies between different molecular orientations of the order of a few meV are still present. Considering that the neural network fit will produce an additional fitting error for these energies, it cannot be taken for granted that the potential-energy in the molecular dynamics runs will be independent of the molecular orientation at this distance. To make sure that all molecular dynamics trajectories start with the same potential-energy, the data set has to be modified in two steps. First, the numerical noise in the DFT data has been removed by defining the energy of the point (d=1.224 Å, Z=6.0 Å) as the zero point for each molecular orientation, i.e. the energies for each elbow plot have been shifted individually by typically 1 or 2 meV to obtain a common reference zero point. However, this does still not guarantee that the neural network will yield exactly this energy in the fit. Without changing the shape of the potential-energy surface, the zero points (d=1.224 Å, Z=6.0 Å) for each molecular orientation have therefore been copied to points (d=1.224 Å, Z=D Å) in the vacuum with zero energy,

[2]It has been tested that the actual choice of this energy has no effect on the fit quality as long as it is large compared to the kinetic energy of the molecule.

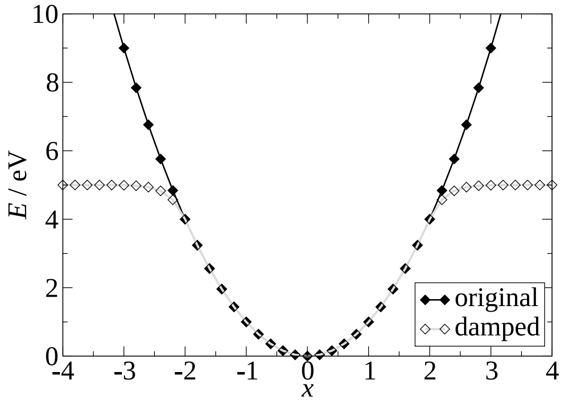

Figure 10.7: Damping of high potential-energies to a maximum value E_t=5 eV in order to reduce the range of values (example of a parabolic potential) for the neural network fit. For the molecular dynamics only energies up to +1.0 eV are of interest, which are not affected by the damping.

D having values of 7.0, 8.0, 9.0 and 10.0 Å. These additional points are sufficient for the training of the neural network to obtain a very low fitting error for the zero point of the potential-energy, which is typically well below 1 meV. These points could have been obtained also by density-functional theory, but because of the artificial charge transfer due to the relative position of the Fermi energy of the metal and the oxygen $2\pi^{*\downarrow}$ states described in the previous section, the total energy would converge only very slowly without adding relevant physics. Finally, the potential-energy of all points with an energy being higher than a threshold energy E_t has been scaled down to a value between ($E_\mathrm{t} - 1$ eV) and E_t as shown exemplary in Fig. 10.7 for a parabolic potential using an equation that ensures continuous derivatives.

$$E \;=\; \begin{cases} E & \text{for} \quad E \le E_\mathrm{t} \\ E_\mathrm{t} - \exp\left(E_\mathrm{t} - 1\mathrm{eV} - E\right) & \text{for} \quad E > E_\mathrm{t} \end{cases} \tag{10.1}$$

The actually chosen value for E_t is 5 eV. The resulting reduced range of values increases the accuracy of the neural network for small energy differences. After these extensions the full data set consists of 2236 energy points, 2157 are used to train the network weights and 79 randomly chosen points are used in the test set.

Apart from the network architecture and the parameters of the Kalman filter, the quality of the fit in certain regions of the potential-energy surface can be controlled by assigning weights ω to the fitting errors of the data points. Points that should be accurately fitted will be assigned high weights, but points which are not very important, for example due to a very high potential-energy, will be assigned low weights. Unfortunately there is no general prescription how the actual weights should be selected to obtain a suitable fit. Therefore, several sets of weights have been tested empirically. Certainly, a good fit of the minimum energy path in the entrance channel will be of crucial importance. Such points are correspondingly given the highest

Points	ω
E <1 eV	2.0
$d = 1.224$ Å $\wedge$ (2.8 Å $\leq Z <$ 4.8 Å)	1000.0
$d = 1.224$ Å $\wedge$ $Z >$ 4.8 Å	5000.0
(1.21 Å $< d <$ 1.49 Å) $\wedge$ (1.5 Å $\leq Z <$ 2.6 Å) $\wedge$ (-1.0 eV $< E <$ +1.0 eV)	11.0
$d = 1.3$ Å $\wedge$ $Z = 2.1$ Å	1067.0

Table 10.1: Set of weights assigned to the data points for fitting the adiabatic potential-energy surface.

weights. The best set of weights found for fitting the adiabatic potential-energy surface obtained with the PBE functional is defined in Table 10.1.

All in all 54 different fits have been performed to interpolate the PBE potential-energy surface using different network architectures, parameters and weights. Finally, the best fit found employs a 11-38-38-1-tl architecture with $\lambda_0 = 0.99770$ and $\lambda(0) = 0.98000$ having 1977 connecting weights to be optimized. The adaptive filter has not been used. The obtained average errors of the training and test data are 0.038 eV and 0.062 eV, respectively. Two PBE-DFT elbow plots are shown in Fig. 10.9 and compared to the corresponding plots based on the full six-dimensional neural network interpolation. Like for all other calculated elbow plots the agreement is excellent.

Apart from the overall fitting error the quality of the fit in certain regions of the potential-energy surface is of interest. 14 groups of points have therefore been defined using energetic and geometric criteria, and the mean absolute deviations (MAD) have been calculated individually for these groups. The results are given in Table 10.2. The points with a potential energy lower than 1 eV (group 1), which are most relevant for the molecular dynamics, are fitted significantly better than the points with $E > 1$ eV (group 2). The points along the minimum energy path in the physisorption region have a very high accuracy, the MAD being less than 1 meV (group 3). In Fig. 10.8, the fitted neural network energies are plotted against the original PBE DFT energies in two different scales. An error-free fit would correspond to a line with a slope of one. As can be seen the number of points with significant fitting errors is very small.

The adiabatic potential-energy surface obtained with the RPBE functional consists of 1369 DFT energy points. The same steps as described for the PBE functional have been done to prepare the data for the neural network fit yielding all in all 2136 energy points, 2067 of which are used in the training set and 69 randomly chosen DFT points form the test set. 80 different fits have been carried out employing many different network architectures, neural network parameters and weights. The best fit results from a 11-40-40-1-tl network with the parameters $\lambda_0 = 0.99770$ and $\lambda(0) = 0.98000$ of the adaptive Kalman filter. The same set of fitting weights ω as for the PBE data set has shown to yield the best fit (Table 10.1). The mean absolute errors of the training data points and the test data points are 0.022 eV and 0.050 eV respectively. The errors of the individual point groups are listed in Table 10.2 and show that the quality of this fit is excellent, which is also confirmed by the agreement of the elbow plots based on

		RPBE		PBE	
Group	Points	Points	MAD (eV)	Points	MAD (eV)
1	E <1 eV	1563	0.0147	1693	0.0281
2	E >1 eV	573	0.0449	543	0.0704
3	$d = 1.224$ Å $\wedge$ $Z > 2.8$ Å	763	0.0006	391	0.0007
4	$d = 1.300$ Å $\wedge$ $Z = 2.1$ Å	46	0.0031	11	0.0016
5	$d = 1.500$ Å $\wedge$ $Z = 2.4$ Å	46	0.0408	40	0.0388
6	$d = 1.200$ Å $\wedge$ $Z = 2.2$ Å	45	0.0347	39	0.0489
7	$d = 1.200$ Å $\wedge$ $Z = 2.8$ Å	11	0.0118	40	0.0198
8	$d = 1.400$ Å $\wedge$ $Z = 2.8$ Å	45	0.0283	39	0.0228
9	$d = 1.200$ Å $\wedge$ $Z = 1.7$ Å	45	0.0444	40	0.0490
10	$d = 1.500$ Å $\wedge$ $Z = 1.7$ Å	45	0.0321	39	0.0509
11	$d = 1.400$ Å $\wedge$ $Z = 1.8$ Å	46	0.0351	52	0.0676
12	$d = 1.300$ Å $\wedge$ $Z = 2.5$ Å	46	0.0200	40	0.0240
13	$d = 1.224$ Å $\wedge$ $Z = 3.5$ Å	46	0.0015	17	0.0022
14	$d = 1.224$ Å $\wedge$ $Z = 2.8$ Å	44	0.0018	14	0.0033

Table 10.2: Mean absolute deviations (MAD) of different groups of points for the best fits of the adiabatic potential-energy surface calculated with the RPBE and the PBE functional.

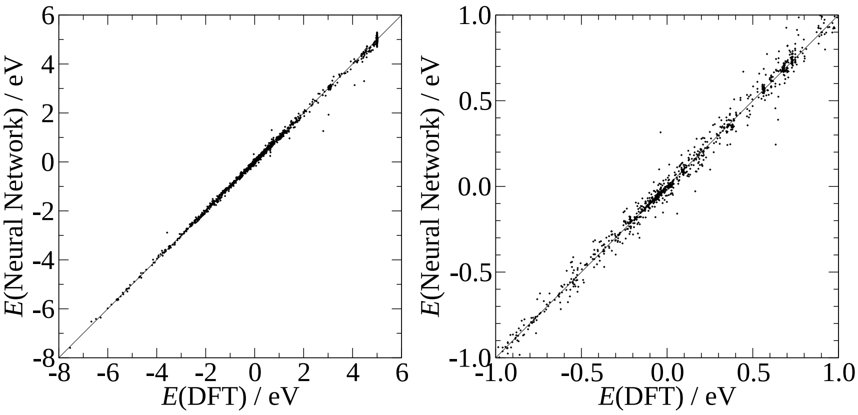

Figure 10.8: Plot of the fitted energies of the training set as a function of the original PBE-DFT energies in two different scales. The line represents a perfect, error-free fit.

the DFT data with the elbow plots obtained from the six-dimensional neural network fit. Based on these fits, a large number of molecular dynamics trajectories can now be calculated to obtain the sticking probability for different initial kinetic energies.

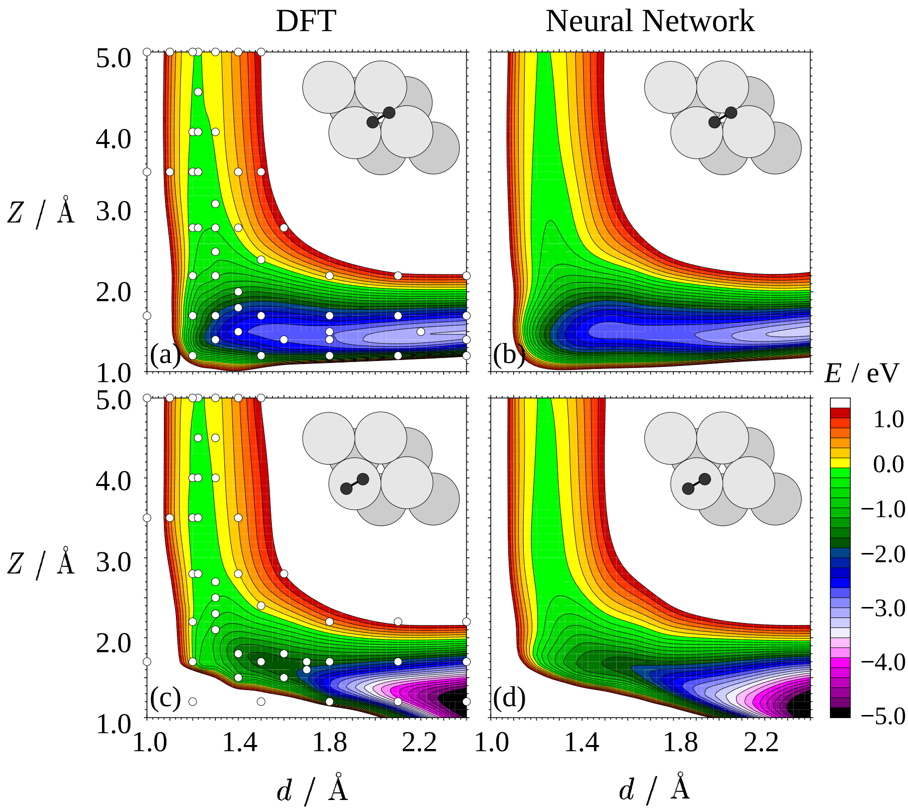

Figure 10.9: Comparison of two elbow plots obtained from the six-dimensional neural network interpolation ((b) and (d)) with the corresponding two-dimensional plots of the original DFT data ((a) and (c)) for the PBE functional.

10.4 Molecular Dynamics on the Adiabatic Potential-Energy Surface

The sticking curve obtained for the RPBE and the PBE functional is shown in Fig. 10.10 and compared to the experimental sticking data [9]. For each kinetic energy 2000 trajectories have been calculated starting at 9.5 Å above the surface with random initial orientations and lateral positions to get statistically meaningful results. Like in the experiment [9] the molecules hit the surface at normal incidence. A trajectory is terminated when the molecular bond length increases to 2.4 Å (dissociation), or when the molecule-surface separation increases beyond 6.0 Å after a preceding closer approach (reflection). For both functionals, the sticking probability is almost unity independent of the kinetic energy, which is in strong disagreement with experiment. In case of the PBE functional this is immediately obvious due to the absence of energy barriers towards dissociation. Yet, also the shallow energy barriers found for some elbow plots calculated with the RPBE functional do not reduce the sticking probability. This has two reasons: First, the height of these barriers is very small and can be over-

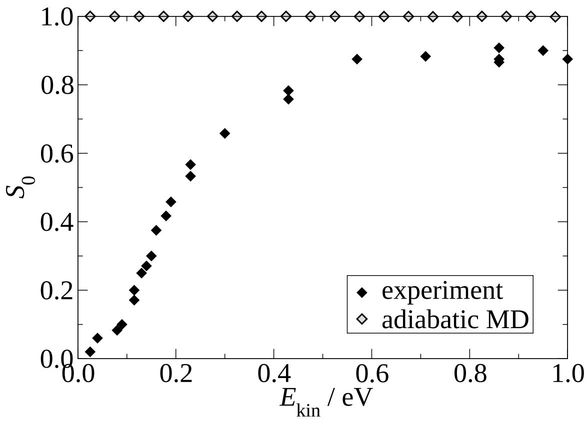

Figure 10.10: Adiabatic sticking curve. The black diamonds represent the experimental data, the empty diamonds represent the sticking probabilities obtained from the adiabatic molecular dynamics simulations. Both functionals, PBE and RPBE, yield the same adiabatic sticking curve.

come even by thermal molecules in most cases. Second, slow thermal molecules can easily be steered towards the energetically most favorable entrance channels, which do not have energy barriers. At this point careful tests to determine the dependence of the sticking curves on the actual fit, the number of trajectories, the initial height of the molecules at the beginning of the trajectories and many more parameters have been carried out. We found that all fits, independent of the quality of the fit, yield basically the same adiabatic sticking curves since the most prominent feature of the potential-energy surface, the absence or small height of energy barriers is generally well reproduced by the neural network. Giving details of the sticking probabilities obtained using different parameters is accordingly not very instructive for the adiabatic potential-energy surface. A detailed investigation of these effects will therefore be given in Chapter 13 for the sticking curves based on the spin-constrained triplet potential-energy surface, for which equivalent tests have been carried out.

Finally, it can be concluded that the low sticking probability of thermal oxygen molecules impinging on the Al(111) surface cannot be explained by calculations based on the adiabatic potential-energy surface obtained from state-of-the-art density-functional theory. Consequently, dynamical steering effects can be excluded as source for the discrepancy between experiment and theory. There are two remaining explanations for this result. Either current GGA functionals are not sufficiently accurate to describe the dissociation of the oxygen molecule, which is not very likely due to the error cancellation in the oxygen binding energy in the PES, or the adiabatic description of the dissociation process is not appropriate. In the remainder of this work we will focus on the latter aspect, but before we can proceed to the investigation of the role of non-adiabatic effects, the validity of the applied frozen surface approximation will be demonstrated by a study of the effects of mobile substrate atoms.

10.5 *Ab initio* Molecular Dynamics

Due to the large mass of the oxygen molecule and the high adsorption energy set free in the dissociative adsorption event of an oxygen molecule on Al(111) it is *a priori* not clear whether the frozen surface approximation employed in the calculation of the six-dimensional potential-energy surface is justified. Motion of the substrate atoms under the influence of the approaching oxygen could affect barrier heights and molecular steering, and will certainly also have an effect on the final adsorption mechanism. To investigate the effect of the mobility of the substrate atoms, "on-the-fly" *ab initio* molecular dynamics simulations based on the adiabatic potential-energy surface have been carried out using the DMol^3 code. For each geometry step the energy and forces are obtained from a fully self-consistent density-functional calculation.

Direct *ab initio* molecular dynamics runs are computationally extremely demanding. A typical simulation of one single trajectory consisting of 200 geometry steps costs as much as calculating 4 elbow plots. Since only a semi-quantitative assessment of the effects of substrate mobility is aspired by these simulations, the employed slab geometry and the calculational parameters have been modified compared to the ones employed in the mapping of the six-dimensional potential-energy surface. The slab thickness of the (3×3) supercell has been reduced to 5 layers. A 3×3×1 k-point mesh yielding 9 k-points in the irreducible wedge of the Brillouin zone has been employed together with a *dnd* basis for oxygen and aluminium. The effects of these reductions are comparably small, as can be seen in the convergence tests in Appendix B. The PBE functional has been used to represent exchange and correlation, because this functional yields a more attractive potential-energy surface than the RPBE functional giving rise to a stronger molecule-surface interaction. All other parameters are identical to those described in Section 10.1.

Trajectories have been calculated for 12 different initial molecular orientations (geometries 1-12 in Appendix C) starting at Z=3.5 Å above the surface to minimize the number of DFT calculations in the region of weak interactions. Two different initial kinetic energies have been used, namely E = 0.05 eV and E = 1.00 eV, to cover the low and high energy limit. The lower energy is slightly higher than thermal energy for two reasons: First, a slightly higher initial velocity of the molecule reduces the number of calculations for separations with weak interactions while on the other hand according to experiment the sticking probability should still be very small [9]. Second, the slightly higher kinetic energy accounts for the reduction of the potential-energy that is present already at 3.5 Å above the surface. Therefore, starting the molecular dynamics runs at 3.5 Å with a slightly higher kinetic energy has the same effect as starting very far from the surface at zero potential-energy and thermal kinetic energy (0.025 eV) and subsequently converting the potential-energy gain in kinetic energy during the run. As the slab consists only of 5 metal layers, only the outermost surface layer atoms are allowed to move in all three dimensions in the molecular dynamics runs. The initial position of all metal atoms is like in bulk aluminium.

Employing a Verlet algorithm [163], a constant time step of 2.5 fs has been chosen.

This should be sufficiently small to account for the fastest vibrations occurring in the system. This has been tested by comparison with the vibrational frequency obtained for a free oxygen molecule. The frequency was found to be $\nu = 4.57 \cdot 10^{13}\mathrm{s}^{-1}$ from a Fourier transform of the vibrations in a molecular dynamics run on the free oxygen molecule under the same conditions, but with a smaller time step of 0.05 fs and a run time of 200 fs. The obtained frequency is in very good agreement with the experimental value of $\nu = 4.737 \cdot 10^{13}\mathrm{s}^{-1}$ [266]. This frequency corresponds to a vibration period of about 22 fs, thus being ten times larger than the time step of the molecular dynamics simulations of oxygen dissociation on Al(111). Each trajectory consists of 200 time steps covering a total time of 500 fs which is long enough to model the first impact of the molecule and the resulting motion of the oxygen and aluminium atoms. Longer runs would not provide a more realistic picture since no mechanism for energy dissipation is included in the dynamics. In order to conserve the energy, a *NVE* ensemble, i.e. constant particle number, volume and energy, has been applied.

The motion of the aluminium atoms in all calculated trajectories at both initial kinetic energies clearly shows that a significant mobility sets in only when the molecule is getting closer than 2.5 Å to the first aluminium layer, which has to be compared to the position of the energy barriers. If the oxygen-induced motion of the aluminium atoms is significant already at the onset of the barriers, the system will be able to respond to the approaching oxygen molecule by a rearrangement of atomic positions effectively changing the barrier heights. While the adiabatic potential-energy surface does not show energy barriers giving rise to a low sticking probability, the onset of the sizeable barriers on the diabatic spin-triplet energy surface, that will be introduced in Chapter 13, is typically about 3 Å above the surface making the region of strong interaction with the surface atoms at distances smaller than 2.5 Å inaccessible for thermal molecules. We therefore conclude that the sticking of low energy molecules will not be appreciably affected by the mobility of the substrate atoms. This is in agreement with the experiments of Österlund *et al.* [9], in which at most a very weak dependence of the sticking probability on the surface temperature has been found. Only for molecules, which can overcome the barriers and get very close to the surface, the motion of the aluminium atoms will play a significant role. Yet, these molecules stick on the surface even in case of the frozen surface approximation. For the specific task of calculating the sticking curve, the mobility of the substrate atoms will be essentially negligible. Nevertheless, closer to the surface the motion becomes extremely large demonstrating that without consideration of this mobility the investigation of the final dissociation mechanism is not possible.

For all but one of the investigated trajectories we find a dissociation of the oxygen molecule. The only exception is an oxygen molecule oriented perpendicular to the surface above the top site (geometry 7 in Appendix C). Due to symmetry reasons the molecule in this case is confined to this orientation, and as shown in Fig. 10.2(c) a dissociation in this particular geometry is energetically not possible. However, statistically this case is of negligible importance. In Fig. 10.11 the heights of the

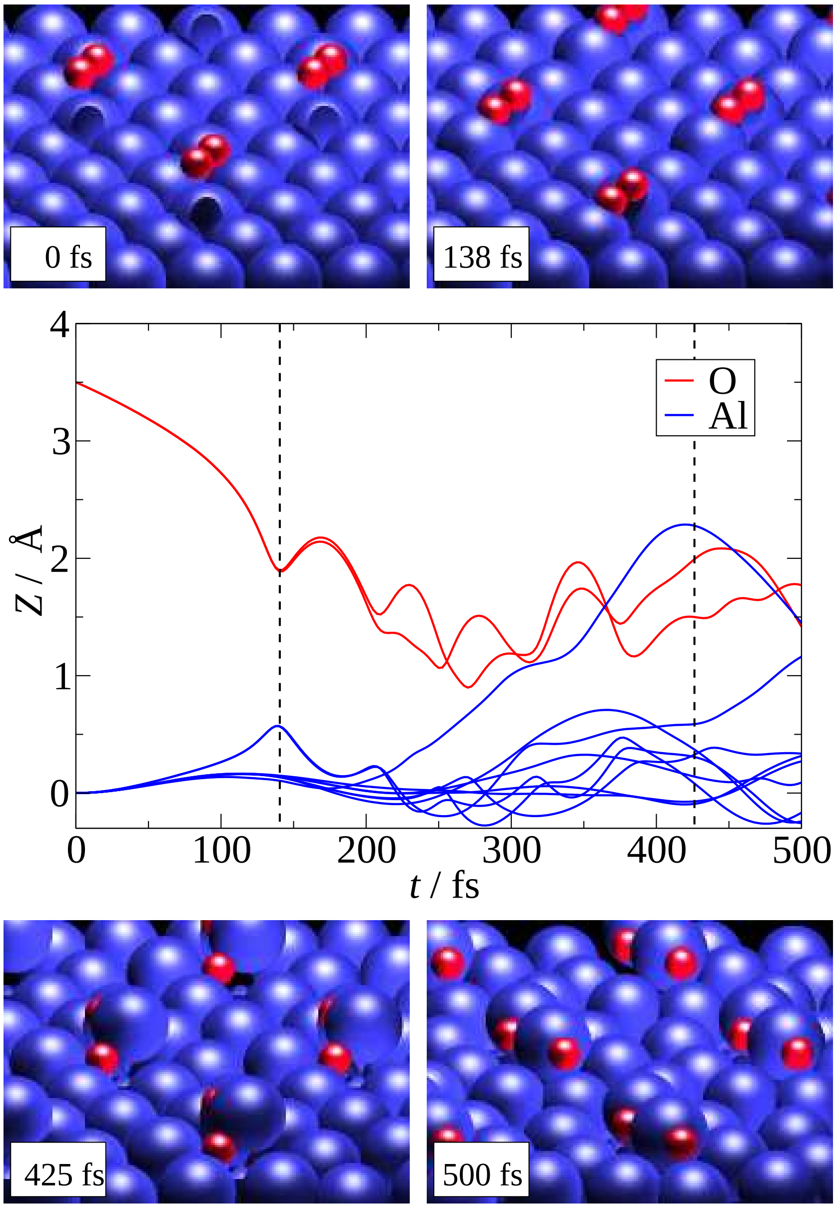

Figure 10.11: Vertical positions of the two oxygen atoms (red) and the 9 top layer aluminium atoms (blue) in a molecular dynamics trajectory as a function of the simulation time. Initially the molecule is located parallel to the surface at a height of 3.5 Å above a fcc hollow site ($\theta = 90°$, $\phi = 60°$, geometry 3 in Appendix C). The initial kinetic energy towards the surface is 0.05 eV. Due to the initial bulk-like positions the aluminium atoms start to relax slightly outwards. A strong interaction sets in after 100 fs when the oxygen atoms are closer than 2.5 Å to the surface resulting in several collisions, the first of which occurs at 140 fs. The aluminium atoms start to move strongly with vertical elongations of up to 2 Å.

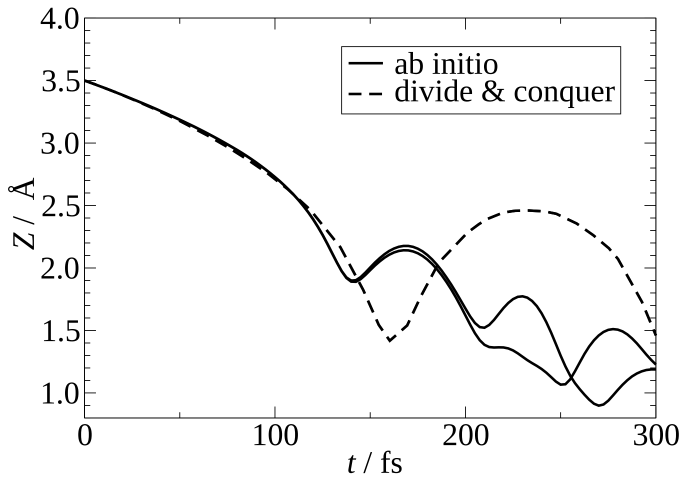

Figure 10.12: Comparison of the vertical positions of the two oxygen atoms as a function of the simulation time obtained from an on-the-fly *ab initio* molecular dynamics simulation (black lines) and from the divide and conquer approach employing the frozen surface approximation (dashed line). In both cases the molecule is initially located parallel to the surface at a height of 3.5 Å above an fcc hollow site ($\theta = 90°$, $\phi = 60°$, geometry 3 in Appendix C). The initial kinetic energy towards the surface is 0.05 eV. Up to 140 fs the trajetories are essentially identical, which corresponds to a molecule-surface separation of less than 2.0 Å. Then due to collisions with mobile substrate atoms in case of the *ab initio* molecular dynamics the two trajectories start to differ. In case of the frozen surface in the neural network based molecular dynamics the molecule stays parallel to the surface all the time, while in case of the mobile substrate atoms the motion is more complex and the molecule changes its angular orientation.

oxygen and first layer metal atoms are shown as a function of the simulation time for one trajectory. Initially, the molecule is oriented parallel to the surface above an fcc site and has a kinetic energy of 0.05 eV. In the first 100 fs there is no significant interaction between the molecule and the surface, and the constant molecular velocity towards the surface is determined by the initial kinetic energy. Then, when the molecule is getting closer than 2.5 Å to the surface, a strong interaction sets in, and the molecule is accelerated towards the surface while at the same time aluminium atoms are pulled out of the surface. The first collision, which can be identified by the change in the direction of motion, occurs at 140 fs. In the further course of the dissociation almost all surface atoms start to move strongly, the most prominent elongation being about 2 Å.

Another interesting possibility to test the validity of the frozen surface approximation is to compare a trajectory obtained from an on-the-fly *ab initio* molecular dynamics run with a trajectory from the six-dimensional divide and conquer approach calculated under the same conditions within the frozen surface approximation, i.e. the same initial position and kinetic energy, but based on the neural network fit. The vertical positions of the oxygen atoms for both cases are shown in Fig. 10.12 as a function of the simulation time. In both cases the molecule follows the same trajectory for the first 140 fs, which would also be the case if the substrate had been fully relaxed for the mapping of the six-dimensional PES. Only then, when the molecule is closer than 2.0 Å to the surface, the trajectories start to differ due to the influence of the mobile substrate atoms. This is much closer to the surface than the onset of the energy barriers in case of the spin-constrained triplet potential-energy surface in Chapter 13. This proves both, the validity of the frozen surface approximation in the region of the potential-energy surface being relevant for the sticking of thermal molecules and also the high quality of the neural network interpolation, because the direct *ab initio* molecular dynamics can be regarded as an error-free, perfect fitting scheme. Identical trajectories therefore underline the high accuracy of the neural network fit.

Recently, a paper was published by Ciacchi and Payne [267]. They performed *ab initio* molecular dynamics simulation based on the Car-Parrinello scheme [96] to study the dissociative adsorption of oxygen on Al(111) as well as the early stages of oxide formation. In agreement with our studies they find a strong mobility of substrate atoms and oxygen atoms temporary being in subsurface positions. However, like our *ab initio* trajectories, their simulations are based on the adiabatic potential-energy surface, which at least with the currently available functionals leads obviously to a description of the dissociation process which is in contrast to experiment.

Having shown that the frozen surface approximation is applicable to the calculation of the sticking curve for the oxygen dissociation on Al(111) without introducing errors in the obtained sticking probabilities, we are now able to proceed to the investigation of the role of non-adiabatic effects in the adsorption process.

Chapter 11

Non-Adiabatic Effects: The Model

It has been speculated for a few years now [9, 22, 73] that non-adiabatic effects could be the reason for the experimentally found low sticking probability of thermal oxygen molecules impinging on the Al(111) surface. The basic idea behind this assumption is that the electrons do not have enough time to relax to the ground state during the approach of the oxygen molecule to the surface. This is supported by the molecular dynamics simulations reported in the previous chapter showing that the approach and the dissociation are very fast processes taking only about 0.5 ps in the adiabatic approximation. Correspondingly, the oxygen molecule will continue moving on the initial diabatic neutral spin-triplet potential-energy surface for some time, instead of switching to the energetically more favorable adiabatic ground state potential-energy surface through spin relaxation and charge transfer. The low probability of such transitions is of course crucial for the model and has to be verified at a later stage. A detailed discussion of this aspect will be given in Chapter 15. However, first of all the qualitative shape of the possibly involved diabatic PESs has to be investigated. If no energy barriers towards dissociation exist on the initial neutral triplet diabatic PES, non-adiabatic effects cannot account for the low sticking probability of thermal oxygen molecules and an investigation of the transition probability is obsolete.

Therefore, to investigate the possible role of non-adiabatic effects in the dissociation of oxygen molecules on the Al(111) surface, the relevant diabatic PESs have to be calculated. Due to the large charge transfer from the metal to the oxygen upon adsorption and due to the different spin states of the free O_2 molecule and adsorbed oxygen atoms, the definition of the diabatic potential-energy surfaces is not a trivial task. So far there have been several attempts to obtain the diabatic potential-energy surfaces qualitatively from empirical potentials [21, 29, 68] or from very simple one-dimensional models [28]. Both approaches are not very satisfying and there is a clear need for a multi-dimensional calculation of the diabatic PESs from first-principles.

For the dynamic adsorption process two possible models for the diabatic PESs emerge, one is based on charge transfer and the other one focusses on the spin change in the molecule upon dissociation. Both models have in common that the first diabatic potential-energy surface is that of a neutral oxygen molecule in a spin-triplet state. A finite lifetime of the O_2 molecule on this triplet potential-energy surface exists, and transitions are induced by a coupling with other energetically close lying diabatic PESs at some distance to the surface. And this is, where the two models differ.

The suggested charge transfer model [28, 268] is based on an electron-hole pair excitation. When the O_2 molecule approaches the surface, an electron from the metal is transferred into an unoccupied $2\pi^{*\downarrow}$ orbital of the molecule establishing the second, ionic diabatic PES. Further ionic energy surfaces can be constructed by additional electron transfers. This process is well defined for large molecule-surface separations, but then the probability of this process will be very small. However, when the interaction with the surface sets in, the $2\pi^{*\downarrow}$ orbitals cannot be clearly identified any more due to hybridization and the atomic charges are not well defined. The molecular charges obtained from different partitioning methods like the Mulliken analysis [265] or the Hirshfeld analysis [139] can be significantly different, which is a problem for both, the neutral and the ionic potential-energy surface. To circumvent this general problem, Lundqvist and coworkers used unmodified hybrid orbitals to obtain an approximation of the ionic potential-energy surface by means of an extended ΔSCF method [268, 269]. The aluminium contribution to these states is completely neglected. This leads to uncertainties in the total energies and so far no energy barriers could be found with this approach [270]. A high-dimensional mapping of the diabatic potential-energy surfaces using this method has not been done so far.

The model employed in this work focusses on the spin of the oxygen molecule. That spin effects can indeed be important has been shown for the oxygen adsorption on silicon [92, 93], and a possible role for the oxygen-aluminium system has also been suggested [22]. From the initial neutral spin-triplet energy surface the molecule could change its spin for example by a spin-flip of an electron in the $2\pi^*$ orbital or by exchange of electrons with the metal surface. In both cases the second diabatic potential-energy surface to be calculated is a spin singlet potential-energy surface and the reduction of the spin from triplet to singlet happens in one step. Using the spin as the central quantity causes similar difficulties as in the case of the charge, because also the spin cannot be assigned uniquely to individual atoms in interacting systems. This is mainly a problem for the triplet potential-energy surface, because in case of the spin-singlet PES the spin is zero for every atom and no assignment has to be made, which is one advantage of this model. The investigations concerning the charge transfer in Chapter 10 have shown that for medium molecule-surface separations around 3 Å the spins are less sensitive to the partitioning method than the atomic charges. If the expected energy barriers will be located at this distance, which has to be confirmed, the spin state of the molecule can be determined rather reliably and is independent of the method. If necessary, based on the actual spin a projection method could be developed to obtain a pure triplet oxygen state reducing the problem of hybridization.

Of course the real adsorption process can involve charge transfer *and* a spin change,

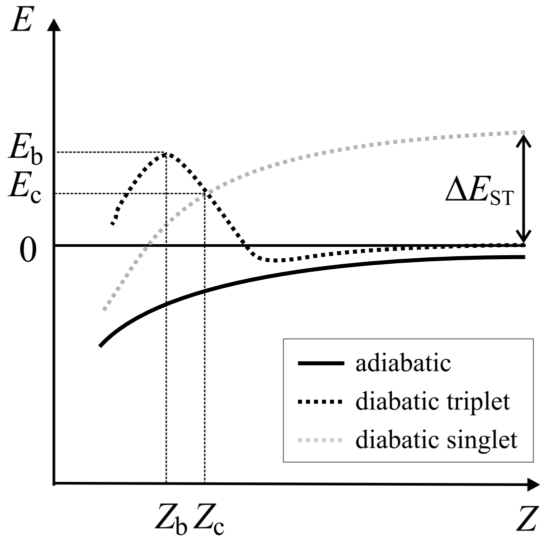

Figure 11.1: Schematic one-dimensional energy diagram of the potential-energy surfaces in the spin model as a function of the molecular distance Z from the surface. The adiabatic ground state (black line) has the lowest energy for all distances and does not show an energy barrier. For large distances the diabatic triplet potential-energy surface (black dotted line) of the neutral molecule is close to the adiabatic PES, but they are not identical due to the artificial charge transfer at all distances in the adiabatic case. When the molecule is approaching the surface on the triplet PES there might be a shallow physisorption well and possibly there might be an energy barrier E_{b} towards dissociation at a distance Z_{b}. The singlet diabatic potential-energy surface (grey dotted line) is lower in energy than the triplet PES close to the surface, while far away the singlet PES is higher in energy by an amount equal to the triplet-singlet gap ΔE_{ST} of the free molecule. The triplet and singlet PES cross at a distance Z_{c} and an energy E_{c}.

and therefore no strict separation of both models is possible. Constructing the ionic potential-energy surface by transferring one electron from the surface to the molecule necessarily reduces the molecular spin to a doublet. On the other hand, the singlet potential-energy surface of the finally adsorbed molecule will have to account for charge transfer. How this may be achieved in the spin model will be described in Chapter 14. Finally, in both models the initial diabatic potential-energy surface corresponds to a neutral oxygen molecule in a triplet spin state and the difference between both methods is in the approximations made in the calculation of the triplet energy surface. A transition to the second diabatic PES, which is different in the two models, will result in sticking in both cases.

In the spin model applied here the two involved diabatic potential-energy surfaces need to fulfil some requirements. The triplet PES should be identical to the adiabatic energy surface in the asymptotic limit of a very large molecule-surface separation. However, this is not true since due to the artificial charge transfer from the metal to the molecule the energy of the adiabatic PES is too low. Consequently, the neutral triplet PES would be a more suitable starting point for molecular dynamics simulations. On the other hand the singlet PES should be identical to the adiabatic PES of an adsorbed molecule for small separations. While for the neutral triplet PES the molecule is in a triplet and the surface in a singlet state without any charge transfer between the two subsystems, in the latter case both subsystems are in an overall singlet state and the charge transfer corresponds to the adiabatic electronic ground state. A correct description of these two boundary conditions is a basic requirement for the diabatic potential-energy surfaces is this simple two-state model, which is shown schematically in Fig. 11.1. The adiabatic potential-energy surface has the lowest energy for all molecule-surface separations. At large separations Z the triplet PES is somewhat higher than the adiabatic PES since the lowering of the energy due to the artificial charge transfer is prevented. Closer to the surface there might be a physisorption well, possibly followed by an energy barrier E_{b}. Showing the existence of this barrier is essential to prove the importance of non-adiabatic effects. Once the barrier is overcome, the molecule might adsorb on the surface although being in a triplet state, but less strongly bound than in the singlet state. Still, the lifetime on the triplet PES will be very short close to the surface due to the coupling to other diabatic PESs. With increasing separation from the surface the singlet state quickly rises in energy and crosses the triplet PES at a distance Z_{c} from the surface. For very large separations from the surface the singlet curve is higher in energy than the triplet state by an energy equal to the experimental singlet-triplet gap ΔE_{ST} of the free oxygen molecule, which is about 0.98 eV [210].

Based on this concept, the first step towards a quantitative verification of the importance of non-adiabatic effects in the oxygen dissociation is an accurate calculation of the spin-triplet potential-energy surface in six dimensions, combined with the identification of eventual energy barriers towards dissociation. The method developed for this task is explained in the following chapters. Then the possible role of other diabatic energy surfaces like the spin-singlet PES or an ionic PES as suggested in the charge transfer model [268] and the effect of transitions between the diabatic energy surfaces are discussed in Chapters 14 and 15.

Chapter 12

Spin-Constrained Density-Functional Theory

12.1 The Fixed-Spin-Moment Approach

To investigate the possible role of non-adiabatic effects in the dissociation of oxygen molecules on the Al(111) surface it is necessary to go beyond the standard adiabatic DFT ground state formalism. We need to calculate the diabatic potential-energy surfaces of the triplet and the singlet oxygen molecule interacting with the aluminium surface as accurately as possible.

First attempts to use density-functional theory to calculate total energies for other states than the global ground state have been started shortly after the introduction of spin-polarized density-functional theory in the 1970's. Gunnarsson and Lundqvist [118] extended DFT to calculate the lowest excited state of each symmetry establishing the so-called ΔSCF method. A few years later very general constraints have been proposed by Dederichs *et al.* [34] to investigate problems connected with general charge and magnetization fluctuations in solids. They suggested to extend standard ground state density-functional theory to include arbitrary constraints by a Lagrange multiplier that can be interpreted as an additional potential in the Hamiltonian. Adjusting this potential allows to define the constraint and to calculate the ground state of the constrained system, while a potential of zero would correspond to the unconstrained global ground state. An application of this method is to constrain the occupation of certain atomic orbitals by a projection potential which acts only on some angular momentum while the other electrons in the system are allowed to relax. They recognized that these constrained ground state calculations could be important for magnetism, and in case that the magnetization in a cell is constrained, the additional potential can be interpreted as a magnetic field. However, this promising method has so far rarely been applied in full generality, the most important applications being studies on non-collinear magnetism and spin dynamics [271].

A simplified version of this very general approach that has become a standard tool in density-functional theory [30–33] is the fixed-spin-moment (FSM) method. It allows to calculate the total energy as a function of the overall magnetization of the system and has been introduced in 1984 [272]. In contrast to standard DFT calculations, in which the total number of electrons N is fixed and the electron numbers of each spin $N^{\uparrow}$ and $N^{\downarrow}$ are varied to minimize the total energy, the constraint of fixed $N^{\uparrow}$ and $N^{\downarrow}$ is introduced in the fixed-spin-moment approach. Consequently, two Fermi energies $\epsilon_{\mathrm{F}}^{\uparrow}$ and $\epsilon_{\mathrm{F}}^{\downarrow}$ are obtained [31]. This procedure can be interpreted as applying an external magnetic field that enforces a net overall magnetic moment M on the system given by $M = N^{\uparrow} - N^{\downarrow}$.

A frequent application of the fixed-spin-moment method is the investigation of phase diagrams of magnetic bulk materials [30], as it allows to vary the magnetic moment arbitrarily and thus to get total energies as a function of the magnetization. A severe limitation of the fixed-spin-moment approach is that no control over the location of the spin-density in the system is possible. Nevertheless, due to its simplicity the fixed-spin-moment approach is the only method that is routinely available in most density-functional codes. As a first step towards the calculation of the spin-triplet potential-energy surface we therefore explored, if the fixed-spin-moment approach can be used to obtain a reliable description of this diabatic energy surface.

12.2 Application of the Fixed-Spin-Moment Approach

By definition the fixed-spin-moment approach yields an overall triplet state of the system. However, *a priori* it is not clear if the spin will be located on the oxygen molecule when the molecule-surface interaction sets in at smaller separations. In order to investigate the location of the spin and the effect of the overall triplet on the potential-energy surface, a series of fixed-spin-moment calculations has been performed. For 12 molecular orientations (geometries 1-12 in Appendix C) elbow plots have been calculated using the PBE functional. None of the elbow plots shows any energy barrier. Additionally, two elbow plots have been recalculated using the RPBE functional to check the functional dependence yielding the same result. The employed supercells and calculational parameters are identical to those of the adiabatic potential-energy surface (cf. Chapter 10). The two elbow plots obtained with the RPBE functional are shown in Fig. 12.1.

The investigation of the spin distribution between the oxygen molecule and the surface cannot be done unambiguously, because no method is available to uniquely assign charges and spins to certain atoms. To get a qualitative picture a Mulliken population analysis has been done. It shows that for a molecule-surface separation of 3.5 Å about 10 % of the spin is centered at aluminium atoms and for a molecule-surface distance of 2.1 Å even about 60 % of the spin are on the aluminium atoms. This will be illustrated by a spin-density plot in Chapter 13 (Fig. 13.6). The delocalization of the

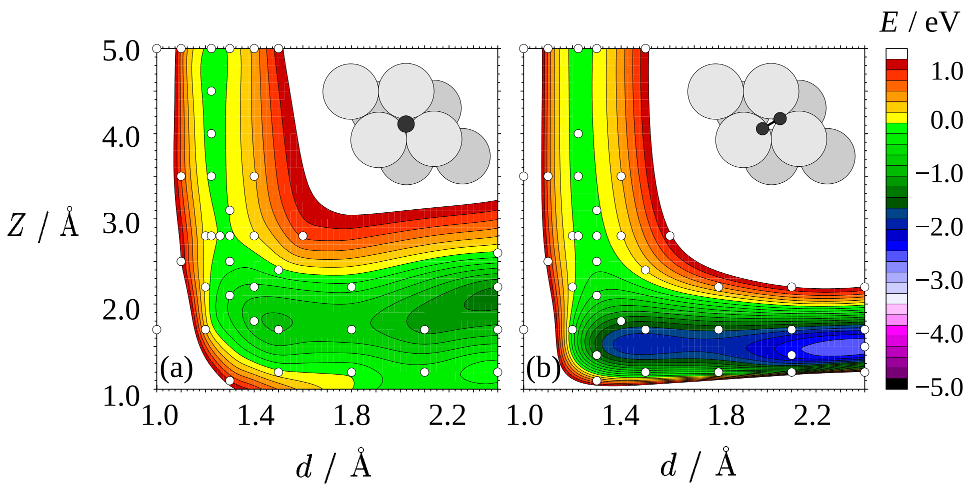

Figure 12.1: Elbow plots for the oxygen molecule oriented perpendicular (a) and parallel (b) to the surface above an fcc site. The calculations have been done using the fixed-spin-moment method for an overall spin-triplet state employing the RPBE functional. The white dots represent the DFT calculations, in which the surface atoms have been fixed at bulk positions. No energy barriers exist on this PES. The energy zero point corresponds to an oxygen molecule in the triplet ground state at an infinite distance from the surface without any charge transfer.

spin might be a reason for the absence of energy barriers. To verify this assumption a method has to be found to calculate a more precise triplet potential-energy surface, i.e. the spin-triplet should be as localized as possible on the oxygen atoms and the aluminium surface should stay in an overall singlet state. This is a much stronger constraint than the fixed-spin-moment approach and more in the spirit of Dederichs *et al.* [34]. However, such a spin-constraint was not implemented in DMol^3, nor in any other available DFT code. We therefore further developed and implemented a spin-constraint, as will be described in more detail in the next sections.

12.3 Spin-Constrained Density-Functional Theory

To confine the triplet spin on the oxygen molecule for arbitrary molecular geometries, in particular for small separations from the surface, and to maintain the singlet state of the aluminium surface, we first need to find a way to measure the spin of these two subsystems. For this purpose we are making use of the atomic orbital basis set used in DMol^3 [133]. Each basis function can be assigned either to an oxygen atom or to an aluminium atom, depending on the atom it is centered at. This is the same procedure as in a Mulliken population analysis [265]. In contrast to a Mulliken population analysis here we are not interested in calculating atomic charges and spins but we want to find total occupations and spins for defined subsystems. We are doing this by a projection of each single-particle state onto the subspace spanned by the oxygen and aluminium basis functions, respectively. All basis functions centered at oxygen atoms form the oxygen subsystem and all basis functions centered at aluminium atoms form the aluminium subsystem. Every single-particle eigenstate $\phi_i^{\mathbf{k}\sigma}$ of the system is a linear combination of oxygen and aluminium basis functions χ_j, which for calculations using periodic boundary conditions are replaced by **k**-dependent Bloch basis functions $\varphi_j^{\mathbf{k}}$ [121] (cf. Eq. (6.2)). σ represents either spin-up or spin-down and **k** is referring to the k-point.

$$\phi_i^{\mathbf{k}\sigma} = \sum_{j=1}^{n} c_{ij}^{\mathbf{k}\sigma} \varphi_j^{\mathbf{k}} \tag{12.1}$$

Now, each state i can be split up into an oxygen part $p_{\mathrm{O}_2,i}^{\mathbf{k}\sigma}$ and an aluminium part $p_{\mathrm{Al},i}^{\mathbf{k}\sigma}$. This is done taking into account the non-orthogonality of the atomic orbitals by the overlap matrix elements $S_{jk}^{\mathbf{k}}$.

$$p_{\mathrm{O}_2,i}^{\mathbf{k}\sigma} = <\phi_i^{\mathbf{k}\sigma}|\phi_{i,\mathrm{O}_2}^{\mathbf{k}\sigma}> = \sum_{j=1}^{n}\sum_{k=1}^{m} c_{ij}^{\mathbf{k}\sigma} S_{jk}^{\mathbf{k}} c_{ik}^{\mathbf{k}\sigma} \tag{12.2a}$$

$$p_{\mathrm{Al},i}^{\mathbf{k}\sigma} = <\phi_i^{\mathbf{k}\sigma}|\phi_{i,\mathrm{Al}}^{\mathbf{k}\sigma}> = \sum_{j=1}^{n}\sum_{k=m+1}^{n} c_{ij}^{\mathbf{k}\sigma} S_{jk}^{\mathbf{k}} c_{ik}^{\mathbf{k}\sigma} \quad , \tag{12.2b}$$

where n is the total number of basis functions and m the number of oxygen basis functions. $c_{ij}^{\mathbf{k}\sigma}$ is the j-th element of the eigenvector of state i, spin σ and k-point **k**. $\phi_{i,\mathrm{O}_2}^{\mathbf{k}\sigma}$ is the oxygen component of $\phi_i^{\mathbf{k}\sigma}$, i.e. all coefficients referring to aluminium basis functions have been set to zero. Correspondingly $\phi_{i,\mathrm{Al}}^{\mathbf{k}\sigma}$ is the aluminium component of $\phi_i^{\mathbf{k}\sigma}$ with the oxygen coefficients being zero. The normalization condition $p_{O_2,i}^{\mathbf{k}\sigma} + p_{Al,i}^{\mathbf{k}\sigma} = 1$ holds for each state by construction, because $\phi_{i,\mathrm{O}_2}^{\mathbf{k}\sigma} + \phi_{i,\mathrm{Al}}^{\mathbf{k}\sigma} = \phi_i^{\mathbf{k}\sigma}$, and can be used to reduce the computational effort in that just one of the double sums in Eq. (12.2) needs to be calculated and the other can be obtained via the normalization condition.

Having split up each single-particle state into an oxygen part and an aluminium part, now the partial densities of states (pDOS) can be constructed for oxygen and aluminium and for both spin orientations so that all in all four partial densities of states result. In Fig. 12.2 the oxygen parts of the single-particle states up to the Fermi level are shown for two different molecular positions as a function of the eigenstate number.

Summing up separately the oxygen parts and aluminium parts of each state over all occupied states i for each subsystem yields the electron numbers $N_{\mathrm{O}_2}^{\uparrow}$, $N_{\mathrm{O}_2}^{\downarrow}$, $N_{\mathrm{Al}}^{\uparrow}$ and $N_{\mathrm{Al}}^{\downarrow}$ for each subsystem and each spin.

$$N_{\mathrm{O}_2}^{\sigma} = \sum_{\mathbf{k}}\sum_{i}\sum_{j=1}^{n}\sum_{k=1}^{m} f_i^{\mathbf{k}\sigma} c_{ij}^{\mathbf{k}\sigma} S_{jk}^{\mathbf{k}} c_{ik}^{\mathbf{k}\sigma} \tag{12.3a}$$

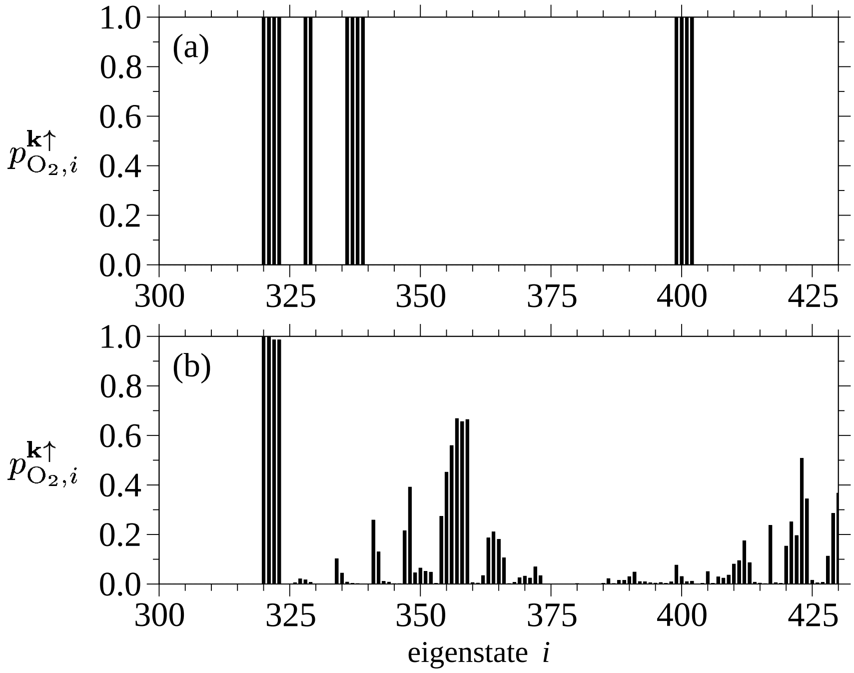

Figure 12.2: Decomposition of the spin-up single-particle state for an oxygen molecule parallel to the surface above an fcc site ($\theta = 90°$, $\phi = 30°$) in a (3×3) supercell. In (a) the molecule is 6 Å above the surface with a bond length of 1.224 Å and the states are either pure oxygen ($p^{\mathbf{k}\sigma}_{\mathrm{O}_2,i} = 1$) or aluminium states ($p^{\mathbf{k}\sigma}_{\mathrm{O}_2,i} = 0$) due to the weak interaction at this separation. In (b) the molecule is 2.1 Å above the surface with a bond length of 1.3 Å. In this case hybridization with the aluminium states of the surface sets in and many valence states have oxygen and aluminium contributions. The data have been obtained for the Γ point in a calculation using 10 k-points in total.

$$N^{\sigma}_{\mathrm{Al}} = \sum_{\mathbf{k}} \sum_{i} \sum_{j=1}^{n} \sum_{k=m+1}^{n} f_i^{\mathbf{k}\sigma} c_{ij}^{\mathbf{k}\sigma} S_{jk}^{\mathbf{k}} c_{ik}^{\mathbf{k}\sigma} \qquad (12.3\text{b})$$

$f_i^{\mathbf{k}\sigma}$ is the occupation number of state i. The spin $\mathcal{S}$ of each of the two subsystems is then the difference between the electron numbers of both spin orientations of each subsystem.

$$\mathcal{S}_{\mathrm{O}_2} = N^{\uparrow}_{\mathrm{O}_2} - N^{\downarrow}_{\mathrm{O}_2} \qquad (12.4\text{a})$$

$$\mathcal{S}_{\mathrm{Al}} = N^{\uparrow}_{\mathrm{Al}} - N^{\downarrow}_{\mathrm{Al}} \qquad (12.4\text{b})$$

Having established a method to quantify the spin we can now start to modify the spins by changing the occupations of the subsystems. Therefore, the N electrons of the system are distributed in the four partial densities of states in a way that yields exactly the spin and charge in the two subsystems that we want to obtain. For the (3×3) supercell (containing 2 oxygen molecules and 63 Al atoms, $N = 851$) used here, the electron numbers are $N^{\uparrow}_{\mathrm{O}_2} = 18$, $N^{\downarrow}_{\mathrm{O}_2} = 14$, and $N^{\uparrow}_{\mathrm{Al}} = N^{\downarrow}_{\mathrm{Al}} = 409.5$. This corresponds to an overall singlet of the aluminium surface and a triplet on each of the two oxygen molecules. To guarantee the correct occupations in both oxygen molecules they have to be equivalent, which is automatically true due to the applied inversion symmetry[1]. We obtain four Fermi energies $\epsilon^{\uparrow}_{\mathrm{F,O_2}}$, $\epsilon^{\downarrow}_{\mathrm{F,O_2}}$, $\epsilon^{\uparrow}_{\mathrm{F,Al}}$ and $\epsilon^{\downarrow}_{\mathrm{F,Al}}$, which are in general all different. If the Fermi energies were degenerate at this stage the ground state spin of the system would be exactly what we need and nothing else would have to be done. However, if the Fermi energies are different they have to be modified to conserve the spin configuration, because in the course of a standard DFT calculation the states are filled in energetic order and only one averaged Fermi energy would be obtained corresponding to the adiabatic spin configuration.

To conserve the spin, the Fermi energies have instead to be equal in value when the single-particle states are filled according to their energetic order. There are several possibilities to implement this. The oxygen Fermi energies could be shifted to the aluminium Fermi energies and vice versa and also all Fermi energies could be shifted to their average value. However, these shifts have to be done under the constraint that the electron numbers that can be filled in the subsystems up to the Fermi level remain constant. We have chosen to shift the oxygen Fermi energies to the aluminium Fermi energies as shown schematically in Fig. 12.3 for one of the two spin orientations. In order to shift only the oxygen subsystem, we need a method that affects only the oxygen part of each single-particle state, because the method has to be general to be able to deal with hybridization. In case of hybridization shifting the complete state would not change the relative positions of the oxygen and aluminium Fermi energies. Affecting only a part of each state will in the end result in different compositions of the single-particle states with respect to oxygen and aluminium basis functions, which is the flexibility we need.

In a first step the Fermi energies are therefore aligned separately for each spin, i.e. $\epsilon^{\sigma}_{\mathrm{F,O_2}} = \epsilon^{\sigma}_{\mathrm{F,Al}}$. This is done by applying an additional auxiliary field $H^{\mathbf{k}\sigma}_{\mathrm{B}}$ on the oxygen part of each eigenstate. The auxiliary field is added to the standard DFT Hamiltonian $H^{\mathbf{k}\sigma}_0$ to form a new effective Hamiltonian $H^{\mathbf{k}\sigma}$. Like $H^{\mathbf{k}\sigma}_0$ the auxiliary field depends on the spin and on the actual k-point. This can be written in terms of the corresponding matrices.

$$\mathbf{H}^{\mathbf{k}\sigma} = \mathbf{H}^{\mathbf{k}\sigma}_0 + \mathbf{H}^{\mathbf{k}\sigma}_{\mathrm{B}} = \mathbf{H}^{\mathbf{k}\sigma}_0 + \Delta\epsilon^{\sigma}_{\mathrm{F}} \cdot \mathbf{P}^{\mathbf{k}}_{\mathrm{O_2}} \tag{12.5}$$

The auxiliary field consists of a “strength” $\Delta\epsilon^{\sigma}_{\mathrm{F}} = \epsilon^{\sigma}_{\mathrm{F,Al}} - \epsilon^{\sigma}_{\mathrm{F,O_2}}$, which is the difference in Fermi energies that has to be overcome, and a projection matrix $\mathbf{P}^{\mathbf{k}}_{\mathrm{O_2}}$ into the oxygen subspace that ensures that the aluminium part of each state is not affected. The form of the projection operator $P^{\mathbf{k}}_{\mathrm{O_2}}$ into the oxygen subspace is given by

[1]The extension of the method presented here to more than two subsystems should be straightforward, i.e. each oxygen molecule could also be occupied individually.

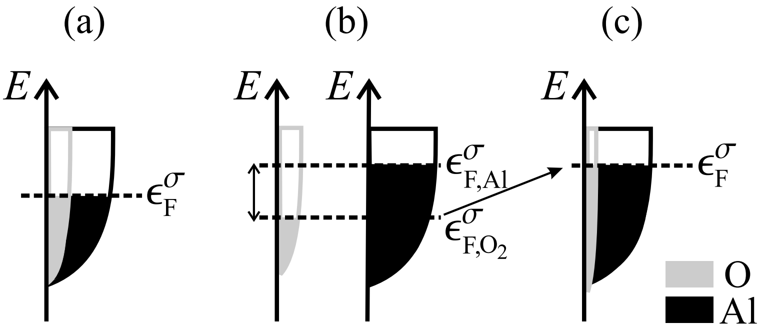

Figure 12.3: Schematic procedure to align the Fermi energies for one spin orientation σ. In (a) the total density of states for an arbitrary molecular orientation is shown. Using Eq. (12.2) the total density of states can be split up into the partial densities of states of the oxygen and aluminium subsystems as shown in (b). Filling these partial densities of states with an arbitrary number of electrons yields Fermi energies $\epsilon^{\sigma}_{\mathrm{F,O_2}}$ and $\epsilon^{\sigma}_{\mathrm{F,Al}}$ that are different in the general case. Therefore these Fermi energies have to be aligned under the constraint of constant electron numbers as shown in (c).

$$P^{\mathbf{k}}_{\mathrm{O}_2} \;=\; \frac{1}{2}\cdot\left(\sum_{i=1}^{m}|\varphi_i^{\mathbf{k}}\rangle\langle\varphi^{i\mathbf{k}}| + \sum_{i=1}^{m}|\varphi^{i\mathbf{k}}\rangle\langle\varphi_i^{\mathbf{k}}|\right) \quad . \tag{12.6}$$

The summation is done only over the m oxygen basis functions, while a summation over all n basis functions would yield the identity operator. Due to the non-orthogonality of the atomic orbital basis functions χ_i and the derived Bloch basis functions $\varphi_i^{\mathbf{k}}$, the formalism of a dual basis employing covariant and contravariant basis functions has to be used [273, 274]. The definitions of the covariant Bloch basis functions $\varphi_i^{\mathbf{k}}$ and the contravariant Bloch basis functions $\varphi^{i\mathbf{k}}$ are

$$\langle\varphi^{i\mathbf{k}}| \;=\; \sum_{\nu=1}^{n}(S^{\mathbf{k}}_{\nu i})^{-1}\langle\varphi_\nu^{\mathbf{k}}| \quad , \tag{12.7a}$$

$$|\varphi^{i\mathbf{k}}\rangle \;=\; \sum_{\nu=1}^{n}|\varphi_\nu^{\mathbf{k}}\rangle(S^{\mathbf{k}}_{\nu i})^{-1} \quad , \tag{12.7b}$$

$$\langle\varphi_i^{\mathbf{k}}| \;=\; \sum_{\nu=1}^{n}S^{\mathbf{k}}_{\nu i}\langle\varphi^{\nu\mathbf{k}}| \quad , \tag{12.7c}$$

$$\text{and} \quad |\varphi_i^{\mathbf{k}}\rangle \;=\; \sum_{\nu=1}^{n}|\varphi^{\nu\mathbf{k}}\rangle S^{\mathbf{k}}_{\nu i} \quad , \tag{12.7d}$$

with $(\mathbf{S}^{\mathbf{k}})^{-1}$ being the inverse overlap matrix. For covariant and contravariant basis functions the following orthonormality relation holds,

$$<\varphi^{i\mathbf{k}}|\varphi_j^{\mathbf{k}}> \;=\; <\varphi_i^{\mathbf{k}}|\varphi^{j\mathbf{k}}>=\delta_{ij} \quad , \tag{12.8}$$

where δ_{ij} is the usual Kronecker Delta.

Consequently, there are two equivalent formulations[2] of the projection operator that could be used.

$$P^{\mathbf{k}}_{\mathrm{O_2}} = \sum_{i=1}^{m} |\varphi^{\mathbf{k}}_i >< \varphi^{i\mathbf{k}}| \tag{12.9a}$$
$$P^{\mathbf{k}}_{\mathrm{O_2}} = \sum_{i=1}^{m} |\varphi^{i\mathbf{k}} >< \varphi_i \mathbf{k}| \tag{12.9b}$$

Both formulations yield non-Hermitian matrices. This is why an equally weighted linear combination of the two possible projection operators has been used in Eq. (12.6) to obtain Hermitian matrices.

The method can be significantly simplified since it can be shown that the element $P^{\mathbf{k}}_{\mathrm{O_2,ij}}$ of the projection operator is equal to the overlap matrix element $S^{\mathbf{k}}_{ij}$ if i and j both refer to oxygen basis functions. In case of either i or j being an oxygen basis function and the other index referring to an aluminium basis function, $P^{\mathbf{k}}_{O_2,ij}$ is equal to $\frac{1}{2} \cdot S^{\mathbf{k}}_{ij}$. Finally, for i and j both pointing to aluminium basis functions $P^{\mathbf{k}}_{O_2,ij}$ is zero, because the aluminium pDOS must not be affected by the auxiliary field. To show this we use the definitions of the covariant and contravariant basis functions in Eq. (12.7). Inserting these expressions in (12.6) yields for the projection operator

$$P^{\mathbf{k}}_{\mathrm{O_2}} = \frac{1}{2} \cdot \left(\sum_{\mu=1}^{m} \sum_{\tau=1}^{n} |\varphi^{\mathbf{k}}_{\mu}\rangle (S^{\mathbf{k}}_{\tau\mu})^{-1} \langle \varphi^{\mathbf{k}}_{\tau}| + \sum_{\nu=1}^{m} \sum_{\lambda=1}^{n} |\varphi^{\mathbf{k}}_{\lambda}\rangle (S^{\mathbf{k}}_{\lambda\nu})^{-1} \langle \varphi^{\mathbf{k}}_{\nu}| \right) \quad . \tag{12.10}$$

Then the matrix elements $P^{\mathbf{k}}_{\mathrm{O_2,ij}}$ are given by

$$\begin{aligned} P^{\mathbf{k}}_{\mathrm{O_2,ij}} &= \langle \varphi^{\mathbf{k}}_i | P^{\mathbf{k}}_{\mathrm{O_2}} | \varphi^{\mathbf{k}}_j \rangle && (12.11a) \\ &= \frac{1}{2} \langle \varphi^{\mathbf{k}}_i | \Bigg(\sum_{\mu=1}^{m} \sum_{\tau=1}^{n} |\varphi^{\mathbf{k}}_{\mu}\rangle (S^{\mathbf{k}}_{\tau\mu})^{-1} \langle \varphi^{\mathbf{k}}_{\tau}| \\ &\quad + \sum_{\nu=1}^{m} \sum_{\lambda=1}^{n} |\varphi^{\mathbf{k}}_{\lambda}\rangle (S^{\mathbf{k}}_{\lambda\nu})^{-1} \langle \varphi^{\mathbf{k}}_{\nu}| \Bigg) | \varphi^{\mathbf{k}}_j \rangle && (12.11b) \\ &= \frac{1}{2} \Bigg(\sum_{\mu=1}^{m} \sum_{\tau=1}^{n} \langle \varphi^{\mathbf{k}}_i | \varphi^{\mathbf{k}}_{\mu}\rangle (S^{\mathbf{k}}_{\tau\mu})^{-1} \langle \varphi^{\mathbf{k}}_{\tau} | \varphi^{\mathbf{k}}_j \rangle \end{aligned}$$

[2]The equivalence can be proven using the definitions of the covariant and contravariant basis functions (Eq. (12.7)):

$$\begin{aligned} \sum_i |\varphi_i >< \varphi^i| &= \sum_i \sum_{\mu} |\varphi^{\mu} > S_{\mu i} \sum_{\nu} (S_{\nu i})^{-1} < \varphi_{\nu}| = \sum_i \sum_{\mu} \sum_{\nu} |\varphi^{\mu} > S_{\mu i} (S_{\nu i})^{-1} < \varphi_{\nu}| \\ &= \sum_{\mu} \sum_{\nu} |\varphi^{\mu} > \delta_{\mu\nu} < \varphi_{\nu}| = \sum_{\mu} |\varphi^{\mu} >< \varphi_{\mu}| \end{aligned}$$

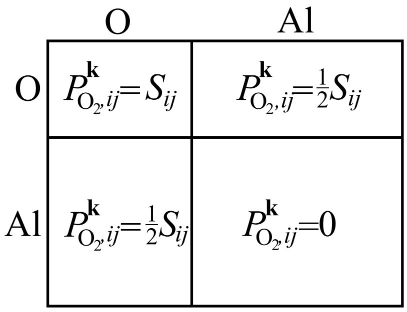

Figure 12.4: Structure of the projection matrix into the oxygen subspace $\mathbf{P}^{\mathbf{k}}_{\mathrm{O_2}}$ and its relation to the overlap matrix $\mathbf{S}^{\mathbf{k}}$.

$$
\begin{aligned}
&\quad + \sum_{\nu=1}^{m}\sum_{\lambda=1}^{n} \langle \varphi^{\mathbf{k}}_i | \varphi^{\mathbf{k}}_\lambda \rangle (S^{\mathbf{k}}_{\lambda\nu})^{-1} \langle \varphi^{\mathbf{k}}_\nu | \varphi^{\mathbf{k}}_j \rangle \Bigg) && (12.11c)\\
&= \frac{1}{2}\left(\sum_{\mu=1}^{m}\sum_{\tau=1}^{n} S^{\mathbf{k}}_{i\mu}(S^{\mathbf{k}}_{\tau\mu})^{-1} S^{\mathbf{k}}_{\tau j} + \sum_{\nu=1}^{m}\sum_{\lambda=1}^{n} S^{\mathbf{k}}_{i\lambda}(S^{\mathbf{k}}_{\lambda\nu})^{-1} S^{\mathbf{k}}_{\nu j} \right) && (12.11d)\\
&= \frac{1}{2}\left(\sum_{\mu=1}^{m} S^{\mathbf{k}}_{i\mu}\delta_{\mu j} + \sum_{\nu=1}^{m} \delta_{i\nu} S^{\mathbf{k}}_{\nu j} \right) && (12.11e)\\
&= \begin{cases} S^{\mathbf{k}}_{ij} & \text{for} \quad i \le m \wedge j \le m \\ \frac{1}{2} S^{\mathbf{k}}_{ij} & \text{for} \quad i \le m \vee j \le m \\ 0 & \text{for} \quad i > m \wedge j > m \quad . \end{cases} && (12.11f)
\end{aligned}
$$

The structure of the projection operator is shown schematically in Fig. 12.4.

The new modified Hamiltonians obtained from Eq. (12.5) are diagonalized and the resulting eigenvectors are used to construct new partial densities of states having Fermi energies $\epsilon^{\sigma}_{\mathrm{F,Al}}$ and $\epsilon^{\sigma}_{\mathrm{F,O_2}}$ closer to each other. Self-consistency is reached for each σ in an internal self-consistency-loop for each electronic DFT iteration until the Fermi energies are aligned to an arbitrary precision. In practical calculations it was found that converging the Fermi energies is very difficult, if the oxygen molecules are far away from the surface. In this case no hybridization occurs and the pure oxygen states start to oscillate around the Fermi level. However, it is not necessary to perfectly align the Fermi energies in this particular case, because our final interest is in the spins and occupations of the subsystems. In the absence of hybridization, $\epsilon^{\sigma}_{\mathrm{F,O_2}}$ can be anywhere in between a state that has to be occupied and a state that has to be unoccupied without changing the spin state, i.e. the physics of the system. In practical calculations not the Fermi energies, but the spins or the occupations of the subsystems can therefore be used as convergence criterion, which strongly reduces the computational costs. The convergence criterion used in this work is a maximum deviation of ± 0.005 electrons in each subsystem which causes uncertainties in the total energies of less than 10 meV. Additionally, the convergence of the strength of the auxiliary field, i.e. the difference in Fermi energies, can be significantly improved by using sophisticated algorithms like the Pulay mixer [159, 160], which has been implemented for this purpose in the inner self-consistency cycle. In the first few DFT iterations typically about 5 to 10 inner iterations are required, but often close to electronic self-consistency of the DFT calculation no further changes in the strength of the field are necessary, reducing the computational effort close to that of a standard DFT calculation in the last iterations. In the end, we then have obtained equal Fermi energies for each spin.

$$\epsilon_{\mathrm{F}}^{\uparrow} = \epsilon_{\mathrm{F,O_2}}^{\uparrow} = \epsilon_{\mathrm{F,Al}}^{\uparrow} \tag{12.12a}$$
$$\epsilon_{\mathrm{F}}^{\downarrow} = \epsilon_{\mathrm{F,O_2}}^{\downarrow} = \epsilon_{\mathrm{F,Al}}^{\downarrow} \tag{12.12b}$$

To align also the Fermi energies $\epsilon_{\mathrm{F}}^{\uparrow}$ and $\epsilon_{\mathrm{F}}^{\downarrow}$, the densities of states for spin-up and spin-down, i.e. the eigenvalues ϵ_i^{σ}, are in a second step shifted against each other by $\Delta\epsilon = \frac{1}{2}(\epsilon_F^{\uparrow} - \epsilon_F^{\downarrow})$ to their average Fermi energy ϵ_F.

$$\epsilon_i^{\mathbf{k}\uparrow\prime} = \epsilon_i^{\mathbf{k}\uparrow} - \Delta\epsilon_{\mathrm{F}} \tag{12.13a}$$
$$\epsilon_i^{\mathbf{k}\downarrow\prime} = \epsilon_i^{\mathbf{k}\downarrow} + \Delta\epsilon_{\mathrm{F}} \tag{12.13b}$$

This step fixes the total spin of the system, which is necessary, since so far only the electron distribution between the oxygen and aluminium subsystem has been modified still allowing for a redistribution of electrons between the two spin orientations. In principle, this last step is an alternative formulation of the fixed-spin-moment approach working with only one Fermi energy instead of the usual two Fermi energies $\epsilon_{\mathrm{F}}^{\uparrow}$ and $\epsilon_{\mathrm{F}}^{\downarrow}$, because in this step only $N^{\uparrow}$ and $N^{\downarrow}$ are fixed. Having now set the total spin of the system as well as the occupations of the subsystems, the final self-consistent DFT-solution has the spin-triplet located on the oxygen molecule while the metal surface is still in a singlet state. However, it should be noted that this method is far more general, and by changing the occupation numbers of the subsystems in principle arbitrary diabatic potential-energy surfaces can be calculated including other spin and charge states.

The eigenvectors and eigenvalues of the modified Hamiltonians can directly be used in the standard routines of the DMol^3 code, but still a correction term for the total energy is required because of the applied auxiliary field and the shift of the eigenvalues. This can be derived from the auxiliary field and the energy shift, which are both known. The contribution due to the shift of the eigenvalues is

$$\Delta E_{\mathrm{shift}} = \Delta\epsilon \sum_{\mathbf{k}} \sum_{i=1}^{n} (f_i^{\mathbf{k}\uparrow} - f_i^{\mathbf{k}\downarrow}) \quad , \tag{12.14}$$

with $f_i^{\mathbf{k}\sigma}$ being the occupation numbers of state i. The correction term due to the auxiliary field can be derived from the total energy expression (6.17), because the auxiliary field is known. Only the sum over all eigenvalues $\epsilon_i^{\mathbf{k}\sigma}$ has to be corrected due to the modified Hamiltonian, and all remaining terms in Eq. (6.17), which depend only on the electron density, have been summarized as E_{R}.

$$\begin{aligned}
E_{\mathrm{tot}} &= \sum_{\mathbf{k}} \sum_{\sigma} \sum_{i} \epsilon_i^{\mathbf{k}\sigma} f_i^{\mathbf{k}\sigma} + E_{\mathrm{R}} && (12.15a)\\
&= \sum_{\mathbf{k}} \sum_{\sigma} \sum_{i} < \phi_i^{\mathbf{k}\sigma} | H^{\mathbf{k}\sigma} | \phi_i^{\mathbf{k}\sigma} > f_i^{\mathbf{k}\sigma} + E_{\mathrm{R}} && (12.15b)\\
&= \sum_{\mathbf{k}} \sum_{\sigma} \sum_{i} < \phi_i^{\mathbf{k}\sigma} | H_0^{\mathbf{k}\sigma} + H_{\mathrm{B}}^{\mathbf{k}\sigma} | \phi_i^{\mathbf{k}\sigma} > f_i^{\mathbf{k}\sigma} + E_{\mathrm{R}} && (12.15c)\\
&= \sum_{\mathbf{k}} \sum_{\sigma} \sum_{i} \Big(< \phi_i^{\mathbf{k}\sigma} | H_0^{\mathbf{k}\sigma} | \phi_i^{\mathbf{k}\sigma} > f_i^{\mathbf{k}\sigma} \\
&\quad + < \phi_i^{\mathbf{k}\sigma} | H_{\mathrm{B}}^{\mathbf{k}\sigma} | \phi_i^{\mathbf{k}\sigma} > f_i^{\mathbf{k}\sigma} \Big) + E_{\mathrm{R}} && (12.15d)\\
&= E_{\mathrm{SC}} + E_{\mathrm{B}} + E_{\mathrm{R}} && (12.15e)
\end{aligned}$$

E_{tot} is the uncorrected total DFT energy including the energy of the auxiliary field, E_{B} is the energy due to the auxiliary field and E_{SC} is the sum of all eigenvalues calculated from the standard DFT Hamiltonian but employing the single-particle states obtained using the spin-constraint. Inserting Eq. (12.1) and the auxiliary field matrix in the expression for E_{B} yields the explicit form of E_{B}.

$$E_{\mathrm{B}} = \sum_{\mathbf{k}} \sum_{\sigma} \sum_{i=1}^{n} \sum_{j=1}^{n} \sum_{l=1}^{n} c_{ij}^{\mathbf{k}\sigma} \cdot c_{il}^{\mathbf{k}\sigma} \cdot H_{\mathrm{B,jl}}^{\mathbf{k}\sigma} \cdot f_i^{\mathbf{k}\sigma} \tag{12.16}$$

The triple summation over all single-particle states and basis functions makes the calculation of E_{B} rather time consuming. Therefore, the energy correction term is calculated only once after self-consistency of the DFT calculation has been reached. Finally, the corrected energy E of the spin-constrained calculation is

$$E = E_{\mathrm{SC}} + E_{\mathrm{R}} + \Delta E_{\mathrm{shift}} = E_{\mathrm{tot}} + \Delta E_{\mathrm{shift}} - E_{\mathrm{B}}. \tag{12.17}$$

It is important to note that this method is completely parameter free and forms a fully self-consistent DFT method. The auxiliary field is a self-adjusting field that has a configuration-dependent strength which is determined self-consistently without any additional input except for the chosen occupations of the subsystems. The latter of course are based on a scheme that assigns electrons to certain atoms of the system and therefore, like other partitioning schemes, it is problematic for small molecule-surface separations. However, the separation of the system into two subsystems using projections onto atomic orbitals is an obvious and natural choice in this context and becomes exact for large Z where no hybridization is present. Furthermore, it is important to note that with this procedure the partial densities of states are not frozen and shifted statically, but in each interaction the single-particle states are flexible to vary the contribution of each basis function freely while the auxiliary field is determined self-consistently. Therefore, both, the molecule and the surface, have a completely relaxed electronic structure under the given constraint. In particular this allows for a local spin-polarization of the surface aluminium atoms close to the oxygen molecule. This is not a real absolute magnetization but a local decrease of spin-up-density and an increase of spin-down-density. The overall spin of the surface remains a singlet. This effect will be shown in Fig. 13.6 for the triplet PES.

From the computational side the determination of the strength of the auxiliary field forms an additional internal self-consistency cycle within each DFT iteration that requires the calculation of the eigenvalues and eigenvectors for each k-point and therefore is rather time consuming. However, for the tested systems only the very first DFT iterations require several inner iterations and also the overall DFT-convergence is generally much improved speeding up calculations, because the oscillation of states around the Fermi level is reduced. All in all, the costs of calculations using the spin-constraint are therefore about the same as the costs of standard adiabatic calculations.

An advantage of the spin-constraint presented here is that with this method all other parts of the DFT code can be used without further modification, and formally the full ground state machinery of DFT can be applied. In Fig. 12.5 the course of a DFT calculation employing the spin-constraint is shown schematically. Care must be taken that the modification of the Hamiltonian and the analysis of the eigenvectors are done in the representation of the atom-centered basis functions and not in the orthogonal basis that is used for the diagonalization of the Hamiltonian as described in Chapter 6. The whole formalism can also be used for calculations without periodic boundary conditions. In this case all indices $\mathbf{k}$ referring to the k-point are omitted and all Bloch basis functions $\varphi_i^{\mathbf{k}}$ are replaced by the non-periodic basis functions χ_i.

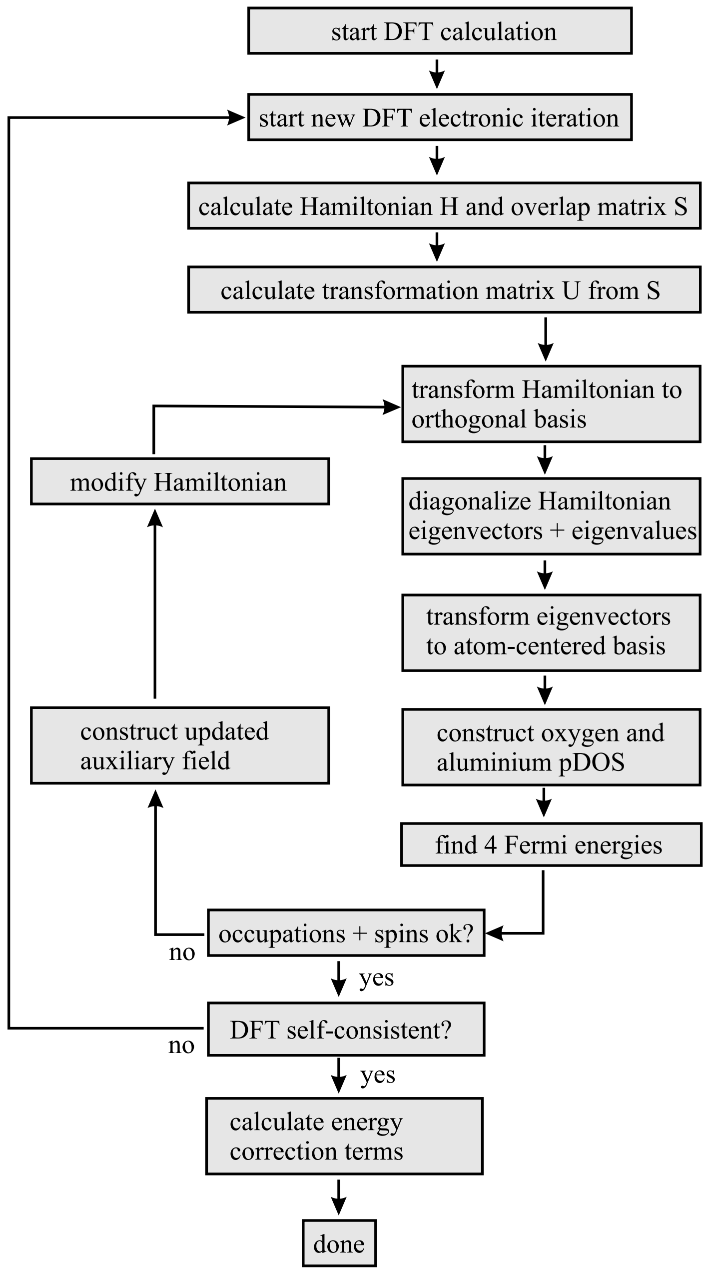

Figure 12.5: Flow chart of a DFT calculation employing a spin-constraint.

Spin	E (eV)	$N^{\uparrow}$	$N^{\downarrow}$
restricted	-31.744 = E_{S}	1	1
unrestricted	-31.744 = E_{S}	1	1
FSM 0.0	-31.744 = E_{S}	1	1
FSM 2.0	-21.478 = E_{T}	2	0

Table 12.1: Total energies of a free hydrogen molecule in different spin states. A fixed-spin-moment calculation (FSM) of spin 2 yields the triplet energy E_{T}, while a standard DFT calculation provides the singlet ground state energy E_{S}.

12.4 A Simple Test System

Once the spin-constraint has been implemented in DMol^3, a simple test system has to be found that allows fast calculations and that can easily be compared with known correct results. A requirement for this system is that it can be divided into two subsystems and at least one of the two subsystems should be able to switch from one state to another, e.g. from a singlet to a triplet state and vice versa. The most simple system consists of two hydrogen molecules. One hydrogen molecule mimics the oxygen molecule and the other the aluminium surface. Depending on the relative spin orientations of the electrons in the hydrogen molecule it can be either in a triplet state ($1\sigma_s^{\uparrow 1}$,$1\sigma_s^{*\uparrow 1}$) or in the singlet ($1\sigma_s^{\uparrow 1}$,$1\sigma_s^{\downarrow 1}$) ground state. Using the spin-constraint DFT formalism one hydrogen molecule can now be switched from singlet to triplet while the other is not affected by the auxiliary field and stays in the singlet state.

In order to establish a firm reference, first the total energies of a free hydrogen molecule in different spin states are calculated using standard density-functional theory. For this simple system a fixed-spin-moment approach is sufficient to calculate the triplet state of the hydrogen molecule providing an exact reference. All calculations are performed using a cutoff of 9 bohr for the basis functions, an *all* basis set and the PBE functional. A bond length of 0.752 Å is used for the molecule. For these calculations it is not relevant whether the total energies are absolutely converged. It is only important to obtain comparable energies, i.e. the parameters must be the same in all calculations. In Table 12.1 the obtained total energies for the free hydrogen molecule are listed. The triplet spin molecule is unstable with respect to the dissociated atoms, but this is not of interest here as we compare fixed configurations without relaxing the system.

The calculations on the extended system consisting of two hydrogen molecules are carried out in a large cubic box with a side length of 20 Å with periodic boundary conditions. Only the Γ point is used. The molecules are oriented parallel to each other with a distance of 7 Å to avoid any interaction between the molecules. A spin-unrestricted calculation yields a total energy of -63.489 eV, which is exactly twice the energy of the afore calculated isolated free singlet molecule proving the absence of interactions between the two molecules. The same we also find for all other spin states listed in Table 12.1.

Spin	E (eV)	$N_A^\uparrow$	$N_A^\downarrow$	$N_B^\uparrow$	$N_B^\downarrow$
restricted	-63.489 $= 2 \cdot E_S$	1.0000	1.0000	1.0000	1.0000
unrestricted	-63.489 $= 2 \cdot E_S$	1.0000	1.0000	1.0000	1.0000
FSM 0.0	-63.489 $= 2 \cdot E_S$	1.0000	1.0000	1.0000	1.0000
FSM 2.0	-53.223 $= E_S + E_T$	2.0000	0.0000	1.0000	1.0000
FSM 4.0	-42.956 $= 2 \cdot E_T$	2.0000	0.0000	2.0000	0.0000
SC SS	-63.489 $= 2 \cdot E_S$	1.0000	1.0000	1.0000	1.0000
SC ST	-53.223 $= E_S + E_T$	1.0000	1.0000	1.9999	0.0001
SC TS	-53.222 $= E_S + E_T$	1.9999	0.0001	1.0000	1.0000
SC TT	-42.955 $= 2 \cdot E_T$	1.9999	0.0001	1.9999	0.0001

Table 12.2: Total energies of two hydrogen molecules separated by 7 Å as a function of the spin configuration. The restricted and unrestricted calculations both yield non-spin-polarized hydrogen molecules and the total energy is twice the energy of the isolated restricted molecule. The fixed-spin-moment calculations (FSM) set the total spin of the system and yield the spin configurations given in the last four columns. The asymmetric spin configuration for the total spin of 2.0 is a result of the default start spin distribution in DMol^3 trapping the system in a local spin minimum. In the spin-constrained (SC) calculations the occupations are fixed from the beginning to singlet (S) or triplet (T) for the individual molecules. Occupations of 0.0001 for the minority spin have to be used to determine the Fermi energies. All energies are also assigned to combinations of the energies of the free singlet (E_S) and triplet (E_T) molecules. A H_2 bond length of 0.752 Å is used for all calculations.

Now we can use the spin-constrained DFT method to divide the total system into two subsystems each of which is formed by one hydrogen molecule. We will call the subsystems $H_{2,A}$ and $H_{2,B}$. We want to switch molecule A from a singlet to a triplet state while molecule B stays in a singlet state and vice versa. The overall spin of the system then should be a triplet. In contrast to a fixed-spin-moment calculation with the same overall spin, we now can exactly specify which spin is assigned to which molecule. For the spin-constrained calculations we use the occupations $N_A^\uparrow = 1.9999$, $N_A^\downarrow = 0.0001$[3], $N_B^\uparrow = 1.0000$ and $N_B^\downarrow = 1.0000$. By exchanging the occupation numbers it is possible to keep subsystem A in a singlet state and to switch subsystem B to the triplet spin configuration. The results of some test calculations are summarized in Table 12.2.

The results show that the total energies obtained from the spin-constrained (SC) calculations are exactly the sums of the energies of the free molecules with the respective spin configurations and the spins on both molecules can be switched in an arbitrary way. The fixed-spin-moment calculation with an overall triplet spin (FSM 2.0) does not lead to two doublet states on both molecules because in DMol^3 by default the start spin-density to initialize a spin-polarized calculation is located on one single atom. Therefore the initial symmetry is broken and the system gets trapped in a local spin minimum. For this simple system this could be avoided by choosing another initial spin configuration. However, in the general case of more complex sys-

[3]To determine the Fermi energies it is necessary to fill a small fraction of an electron in the spin-down states of subsystem A. We checked that this has no influence on the total energy.

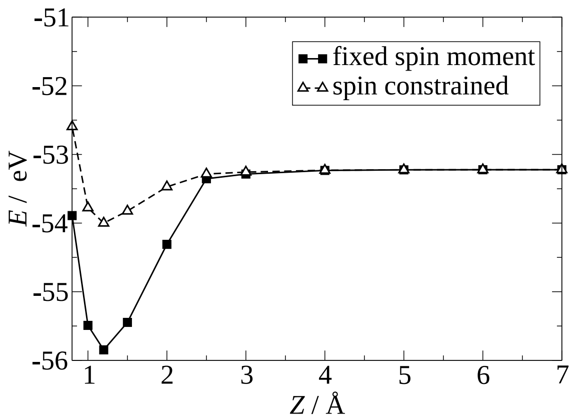

Figure 12.6: Comparison of the total energies of a system consisting of two hydrogen molecules. The total energy is given as a function of the intermolecular distance. The energies have been calculated with the fixed-spin-moment approach (FSM) confining the total spin to a triplet and with a spin-constraint forcing a triplet state on one molecule and a singlet state on the other molecule.

tems, the state we are interested in will not necessarily be a local minimum and thus not accessible by fixed-spin-moment calculations, while it still can be calculated using the spin-constraint.

Another possibility apart from the total energy to identify the physical states of the two subsystems of the spin-constrained calculations is to compare the composition of the eigenvectors and the eigenvalues with the corresponding values of the free molecules. Also these tests show clearly that the spin states enforced by the constraint are identical to those of the free singlet and triplet molecules.

So far, the two hydrogen molecules have been separated by 7 Å to avoid interactions between the subsystems. Now we want to investigate the effect of interactions. For this purpose we reduce the distance between the molecules and monitor the potential-energy for a fixed-spin-moment of an overall triplet spin and a spin-constraint of a triplet located on one molecule and a singlet on the other one. The energies are shown as a function of the distance between the two molecules in Fig. 12.6. For larger separations the energies and spin configurations are the same in both cases, i.e. one molecule is in a triplet state and one is in a singlet state. For a distance smaller than 3 Å, the molecules start to interact and in case of the fixed-spin-moment calculation the spin delocalizes on both molecules, because due to the wave-function overlap the system can escape the local spin minimum mentioned above. This flexibility is the reason for the lower total energy in case of the fixed-spin-moment calculation for small separations. The spin-constrained calculation fixes the triplet on one molecule in all calculations. This additional constraint is the reason for the higher energy.

The calculations on the hydrogen molecules clearly show that the spin-constrained density-functional method is working reliably. Thus, we now can start applying this approach to investigate the dissociation of oxygen molecules on the Al(111) surface.

Chapter 13

The Spin-Triplet Potential-Energy Surface

13.1 Calculation of the Triplet Potential-Energy Surface

The calculation of the triplet potential-energy surface employing the spin-constrained density-functional method introduced in Chapter 12 is done in the same way as has been described in Chapter 10 for the adiabatic potential-energy surface. For both functionals, RPBE and PBE, 38 elbow plots with the molecular configurations shown in Appendix C have been calculated[1]. For both functionals six representative elbow plots are shown in Fig. 13.1 and 13.2, respectively. In contrast to the adiabatic PES sizeable energy barriers exist with heights of up to about 0.9 eV as assumed in the model introduced in Chapter 11. In general, for the RPBE functional the height of the barriers is larger by about 0.3-0.4 eV compared to the PBE functional. A functional-dependence of this order of magnitude has not been found for the adiabatic potential-energy surface. The reason for the larger deviations between the two functionals in case of the barrier heights of the triplet PES might be that the different functional

[1]To reduce the CPU time required for the mapping of the six-dimensional triplet potential-energy surface only the PBE energies have been calculated fully self-consistently. Based on these self-consistent charge densities one DFT iteration using the RPBE functional has been calculated to obtain the RPBE energies. This procedure has been used frequently in the literature before [74] with only small uncertainties in the resulting relative energies. Errors could arise, if pseudopotentials are used [245], which does not pose a problem for the all-electron calculations in the present work. To check the applicability of this approach, all in all 96 different molecular configurations distributed over 12 elbow plots, with particular emphasis on the barrier region, have been calculated fully self-consistently using the RPBE functional and also non-selfconsistently starting from the PBE densities. A comparison shows that the average error in energy differences is 1.3 meV while the maximum error found is 6 meV. This is at least one order of magnitude smaller than the barriers at which we eventually aim. Correspondingly, we concluded that the much less time-consuming non-self-consistent calculations do not introduce a significant error in this case.

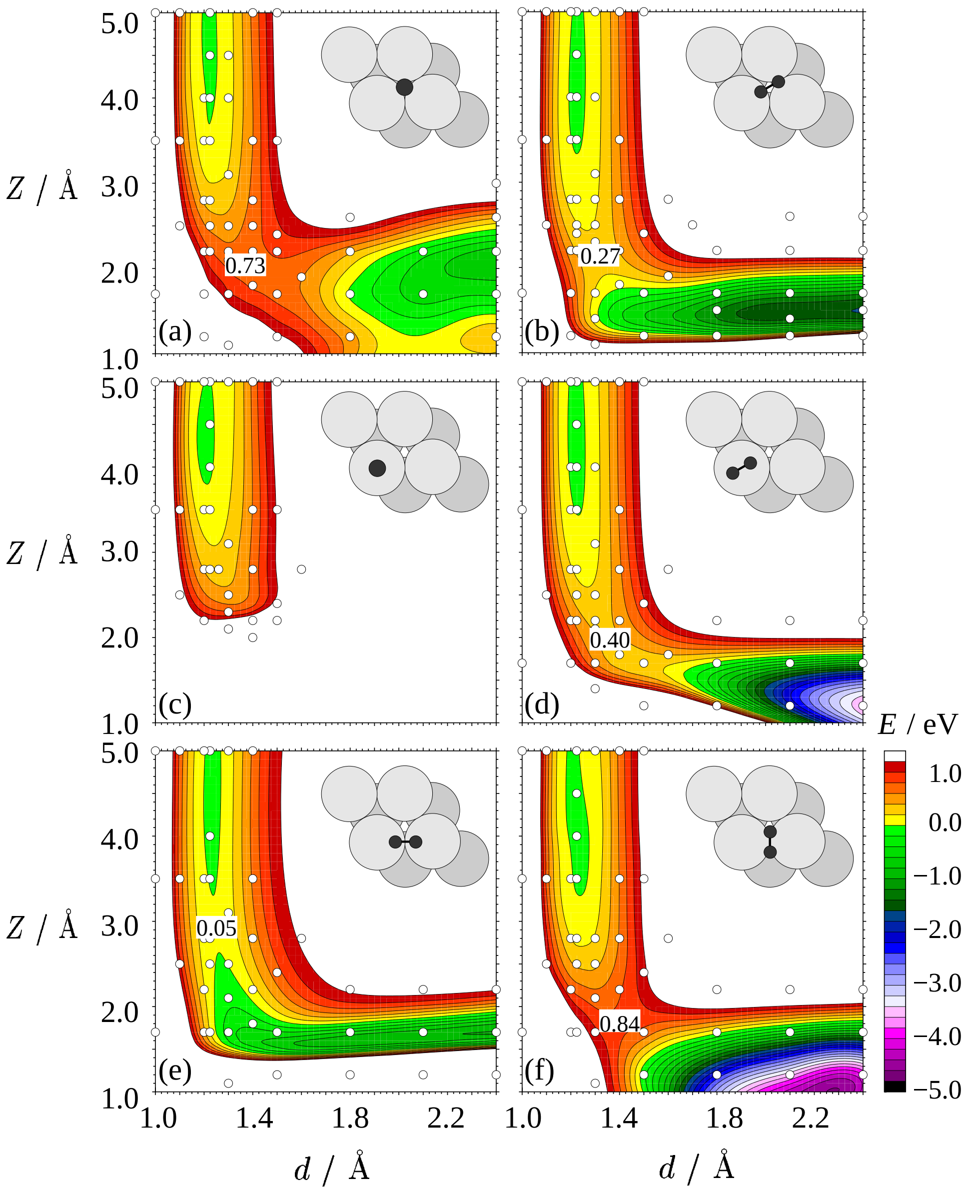

Figure 13.1: Two-dimensional cuts through the six-dimensional spin-triplet potential-energy surface calculated using the RPBE functional. The white dots represent the calculated DFT energies. The substrate has been frozen in the geometry of the bulk-truncated surface. The energy zero point corresponds to an oxygen molecule in the triplet ground state at an infinite distance from the surface without any charge transfer.

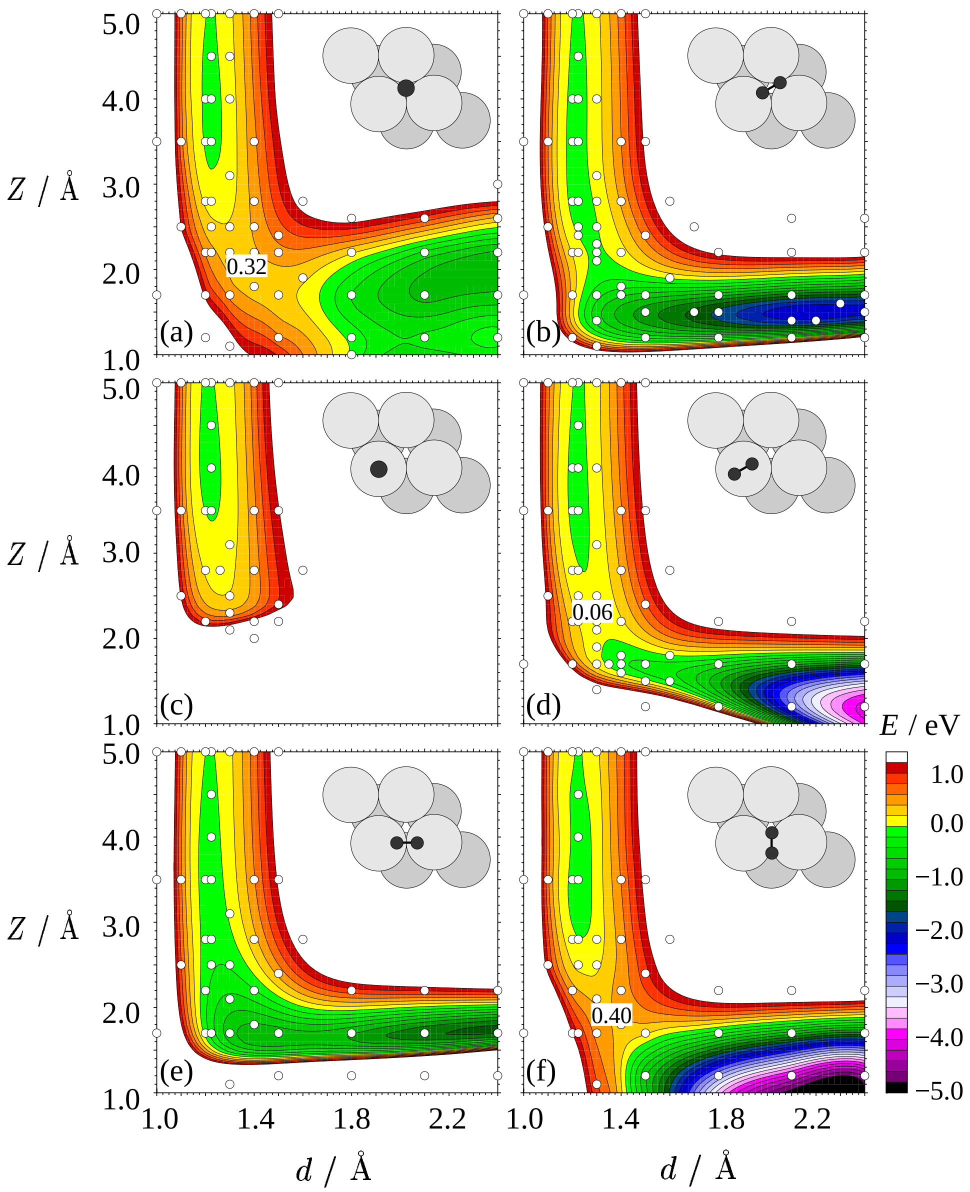

Figure 13.2: Two-dimensional cuts through the six-dimensional spin-triplet potential-energy surface calculated using the PBE functional. The white dots represent the calculated DFT energies. The substrate has been frozen in the geometry of the bulk-truncated surface. The energy zero point corresponds to an oxygen molecule in the triplet ground state at an infinite distance from the surface without any charge transfer.

form of the exchange part in both functionals [74] is particularly sensitive to the spin configuration of the system, which is significantly different between the adiabatic PES and the spin-triplet PES in the region where the maxima of the energy barriers are located. In the adiabatic PES most of the spin has already disappeared in this region, while in case of the triplet potential-energy surface the full triplet is still conserved. As has been found for example for the adsorption of CO and NO molecules on transition metal surfaces [74], the PBE functional is more attractive than the RPBE functional, which is in agreement with our findings. As a consequence of this difference in binding, the spin-triplet potential-energy surface calculated with the PBE functional does not show energy barriers with respect to the infinitely separated subsystems for 6 of the 38 calculated elbow plots. In all 6 geometries the molecule is oriented parallel to the surface and its center of mass is above an fcc, hcp or bridge site (geometries 2, 3, 5, 6, 11 and 13 in Appendix C).

Apart from the functional, the height of the barriers depends strongly on the molecular orientation and lateral position. Therefore, a more detailed mapping of the barrier region than in the adiabatic case has been done to ensure an accurate description of the potential-energy surface for the subsequent molecular dynamics simulations. As shown in Fig. 13.3, apart from the high symmetry fcc, hcp, top and bridge sites energy points with a bond length of 1.3 Å and a center of mass distance from the surface of 2.1 Å have been calculated for all possible angular orientations of the molecule at 11 additional "off-symmetry" sites by sampling the angles θ and ϕ in 30° intervals. The bond length and the distance to the surface of these points have been chosen such that they are located on the energy barriers for most molecular configurations. The six-dimensional shape of the energy barrier towards dissociation is in turn mapped very accurately, which allows to properly account for steering effects in the molecular dynamics simulations.

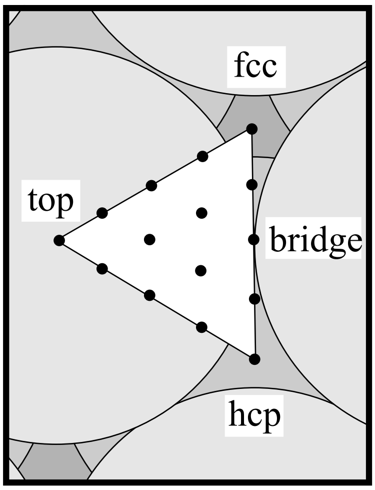

Figure 13.3: Surface sites within the irreducible part of the unit cell used for the mapping of the barrier region of the potential-energy surface.

Having calculated the spin-triplet potential-energy surface it is instructive to analyze the charge and spin distributions between the two subsystems. Fig. 13.4 shows the total spin and charge of the oxygen molecule as a function of the center of mass distance from the surface. The numbers have been obtained for a molecule in a parallel orientation towards the surface above a fcc site (geometry 2 in Appendix C) using the PBE functional. For comparison the corresponding numbers of the adiabatic calculations are also included (cf. Fig. 10.4). As can clearly be seen, the spin obtained from the Mulliken analysis corresponds to an ideal triplet for all molecule-surface separations in contrast to the adiabatic calculation, in which the spin decreases with the distance to the surface. However, also for the triplet calculations the Hirshfeld spin is decreasing for distances below 3 Å. This is a consequence of the way the spins are assigned to the two subsystems in the Hirshfeld analysis. In the latter the spin at each point in space is distributed among all atoms in a ratio that corresponds to the ratios of the electron densities of the free atoms in the same configuration, which is in conflict with our projection onto atomic orbitals. Nevertheless, in contrast to the adiabatic PES also in case of the Hirshfeld analysis of the triplet PES the full triplet is conserved, but an increasing part of the spin is assigned to the aluminium. The Mulliken analysis is based on the same philosophy as our projection technique and therefore reproduces exactly the triplet spin on the oxygen molecule. The same arguments also hold for the charge distribution. It is interesting to note that the artificial charge transfer from the metal to the oxygen molecule at large separations, which is due to the energetic position of the oxygen $2\pi^{*\downarrow}$ orbitals as discussed in Chapter 10, completely disappears when the constrained DFT is used, because now the occupations are fully controlled and these states are shifted above the Fermi level. Consequently, the total energy of the system converges to a constant value for separations larger than 6 Å, as can be seen in Fig. 13.4(c). This distance can therefore be identified as the separation at which the molecule-surface interaction sets in within our DFT description keeping in mind that van der Waals interactions are not properly included in density-functional theory [275].

In order to investigate the origin of the energy barriers of the triplet PES it is instructive to analyze the spin-density for a molecular configuration at the energy barrier. This is shown in Fig. 13.6 for a molecule parallel to the surface above an fcc site employing the RPBE functional. The molecular configuration corresponds to the point (d = 1.3 Å, Z = 2.1 Å) in Fig. 13.1(b). The positions of all atoms in the two-dimensional cut are shown in Fig. 13.5. In Fig. 13.6(a) the spin-density of an isolated oxygen molecule in its spin-triplet ground state without the aluminium slab is given for reference. In (b) the strongly reduced spin-density of an adiabatic calculation is shown. The integrated adiabatic spin-density amounts to 0.064 instead of 2.0 for the ideal triplet. The spin-density in (c) corresponds to a triplet fixed-spin-moment calculation. Although the integrated spin-density still corresponds to a triplet, a large amount of the spin has been transferred to the aluminium slab, which is the reason why the fixed spin moment calculations in Chapter 12 did not yield an energy barrier. In (d) the spin-density for the triplet spin-constrained DFT calculation is plotted. The spin-triplet is localized on the oxygen molecule causing a depletion of spin-up-density in the surrounding region of the metal surface shown in blue due to the Pauli repulsion of like spins. This Pauli repulsion is the origin of the energy barrier. As the metal surface is in an overall singlet state, the displaced aluminium spin-up-density is delocalized in the slab, but no overall net magnetization of the slab is present. On the other hand, in the fixed-spin-moment calculations the triplet spin is located on the slab to a large extent, while the spin of the molecule is significantly reduced.

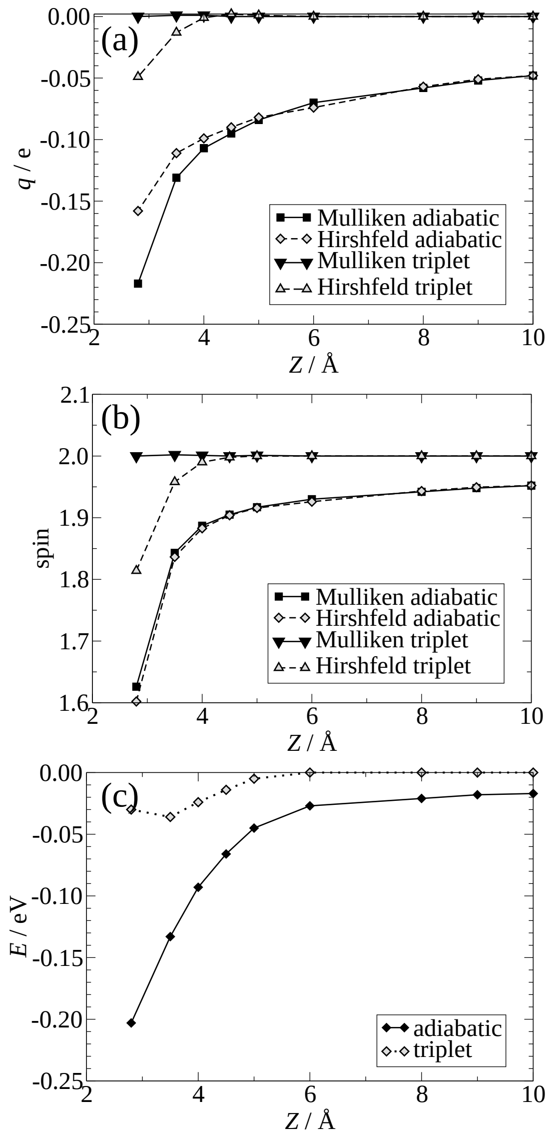

Figure 13.4: Charge, spin and energy as a function of the molecular distance Z from the surface obtained from the adiabatic and the triplet spin-constrained calculations. (a) shows the total charge q of the oxygen molecule obtained from a Mulliken population analysis (black line) and from a Hirshfeld analysis (dashed line). In (b) the total spins of the oxygen molecule are shown for these two methods. In (c) the energy of the system is plotted with respect to the triplet energy, which is converged for $Z > 6$ Å. The values have been obtained with the PBE functional for a molecule oriented parallel to the surface above an fcc site (geometry 2 in Appendix C, $\theta = 90°$, $\phi = 30°$).

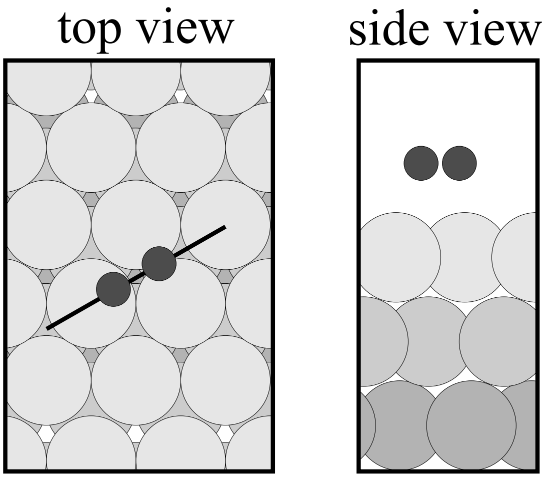

Figure 13.5: Orientation of the two-dimensional cut through the slab and atomic positions for the spin-density plot in Fig. 13.6.

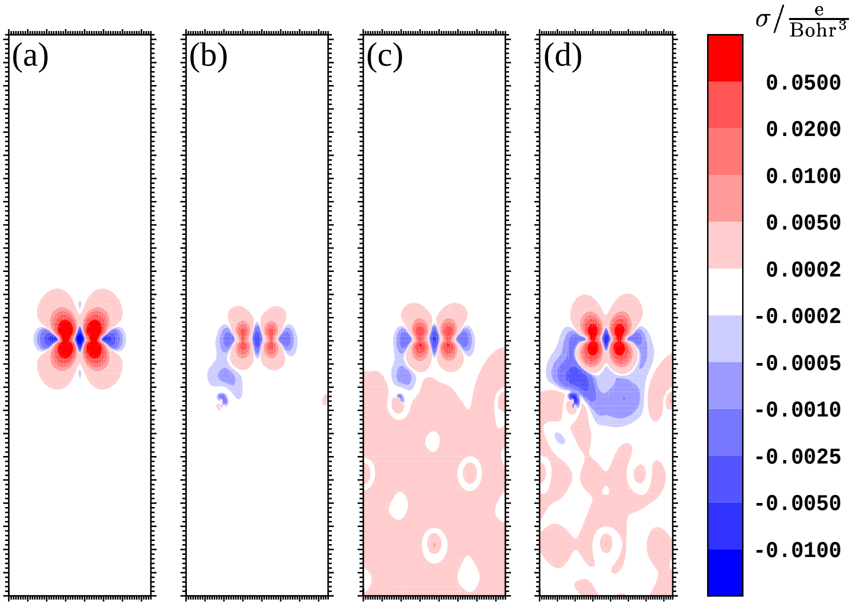

Figure 13.6: Spin-density plots for a molecule with a bond length of 1.3 Å oriented parallel to the surface 2.1 Å above an fcc site (geometry 2 in Appendix C) obtained with the RPBE functional. This molecular configuration corresponds to a position on the triplet energy barrier. In (a) the spin-density of a free O_2 molecule in its triplet ground state without the aluminium slab is shown. (b) gives the reduced spin-density in the adiabatic calculation. In (c) the spin-density distribution for a triplet fixed-spin-moment calculation is shown, while (d) refers to a triplet spin-constrained calculation. The position of the atoms is shown in Fig. 13.5

13.2 Interpolation of the Triplet Potential-Energy Surface

The preparation of the DFT data sets for the neural network interpolation is done in the same way as described in Chapter 10. In total 2870 *ab initio* points are available for the RPBE functional and 2917 points for the PBE functional. Adding high energy points in parts of the potential-energy surface not accessible for the molecular dynamics and extending the energy surface up to $Z = 10$ Å into the vacuum as described in Chapter 10 finally yields 3768 points for the RPBE functional and 3819 points for the PBE functional. In case of the RPBE functional 96 of the DFT energy points are chosen randomly and used as independent test set to control the prediction capability of the network, for the PBE functional the test set consists of 97 points.

To find an accurate fit of the spin-triplet PES, for the RPBE PES 64 fits using different network architectures, weight assignments and parameters have been performed. For the PBE functional 48 fits have been carried out. For the RPBE functional the best fit found results from a 11-40-40-1-tl network employing the same set of weights that has been used in the fitting of the adiabatic PBE energy surface (Table 10.1). The parameters of the Kalman filter, which has not been used in its adaptive version, are $\lambda(0)$ =0.98000 and λ_0 =0.99770. The mean absolute deviation for the training and test data points are 0.023 eV and 0.033 eV, respectively. In case of the PBE PES the best fit found is also based on a 11-40-40-1-tl network architecture, but a different set of fitting weights for the data points listed in Table 13.1 has been used. In this case the adaptive Kalman filter has been employed with the parameters $\lambda(0)$ =0.98000 and λ_0 =0.99670. The obtained mean absolute deviations are 0.035 eV for the training set and 0.031 eV for the test set. Surprisingly, here the average error of the test data points is smaller than the error of the training points. This is because most of the test points are located close to the minimum energy path and the barrier region, which are both much better fitted than the rather large amount of high energy points in the training set.

The analysis of the fit quality has been done in the same way as for the adiabatic potential-energy surface. All 38 calculated elbow plots, but also the additional points at off-symmetry sites are accurately reproduced. The mean absolute deviations for several groups of data points are given in Table 13.2. It can be seen that the part of the potential-energy surface with $E < 1$ eV is fitted very accurately, while the less important high energy part has an approximately 4 times higher average error. To illustrate the precision of the neural network fit in the barrier region, for a point ($d = 1.3$ Å, $Z = 2.1$ Å), which is located close to the maximum of the barrier for most molecular orientations, the neural network energies are compared to the DFT energies for the 38 calculated RPBE elbow plots in Fig. 13.7. The comparison shows an excellent agreement and all energies are accurately reproduced. The energy value of geometry 11 is slightly negative because for this molecular orientation (parallel to the surface above a bridge site) the barrier is located at a larger distance from the

Points	ω
E <1 eV	2.0
d = 1.224 Å ∧ Z >2.8 Å	1000.0
(1.21 Å < d < 1.49 Å) ∧ (1.5 Å ≤ Z < 2.6 Å) ∧ (-1.0 eV < E < +1.0 eV)	11.0
d = 1.3 Å ∧ Z = 2.1 Å	167.0

Table 13.1: Set of weights assigned to the data points for fitting the spin-triplet potential-energy surface obtained with the PBE functional.

		RPBE		PBE	
Group	Points	Points	MAD (eV)	Points	MAD (eV)
1	E <1 eV	2778	0.0117	2994	0.0201
2	E >1 eV	990	0.0568	825	0.0874
3	d = 1.224 Å ∧ Z > 2.8 Å	1336	0.0014	1338	0.0016
4	d = 1.300 Å ∧ Z = 2.1 Å	315	0.0160	314	0.0314
5	d = 1.500 Å ∧ Z = 2.4 Å	46	0.0457	46	0.0343
6	d = 1.200 Å ∧ Z = 2.2 Å	46	0.0360	46	0.0313
7	d = 1.200 Å ∧ Z = 2.8 Å	44	0.0052	44	0.0137
8	d = 1.400 Å ∧ Z = 2.8 Å	46	0.0288	46	0.0235
9	d = 1.200 Å ∧ Z = 1.7 Å	45	0.0551	45	0.0509
10	d = 1.500 Å ∧ Z = 1.7 Å	45	0.0616	45	0.0692
11	d = 1.400 Å ∧ Z = 1.8 Å	45	0.0355	45	0.0583
12	d = 1.300 Å ∧ Z = 2.5 Å	46	0.0108	46	0.0181
13	d = 1.224 Å ∧ Z = 3.5 Å	118	0.0023	119	0.0032
14	d = 1.224 Å ∧ Z = 2.8 Å	118	0.0041	117	0.0038

Table 13.2: Mean absolute deviations (MAD) of different groups of points for the best fit of the spin-triplet potential-energy surface calculated with the RPBE and the PBE functional.

surface at about Z =3.0 Å (cf. Fig. 13.1 (e)).

13.3 Molecular Dynamics on the Triplet Potential-Energy Surface

Based on these fits, molecular dynamics simulations have been done on the spin-triplet potential-energy surface for both functionals. These simulations are complementary to the molecular dynamics simulations on the adiabatic potential-energy surface in that the latter allows for instantaneous charge transfer and spin reduction when the molecule approaches the surface, while for the triplet molecular dynamics no charge transfer and no change in spin is allowed at all. This corresponds therefore to an infinite lifetime of the molecule on the diabatic triplet energy surface. The real adsorption process might be somewhere in between these two limits since transitions might occur, but in order to evaluate the relevance of non-adiabatic effects it has to be shown first that motion on the triplet potential-energy surface can yield a reduced

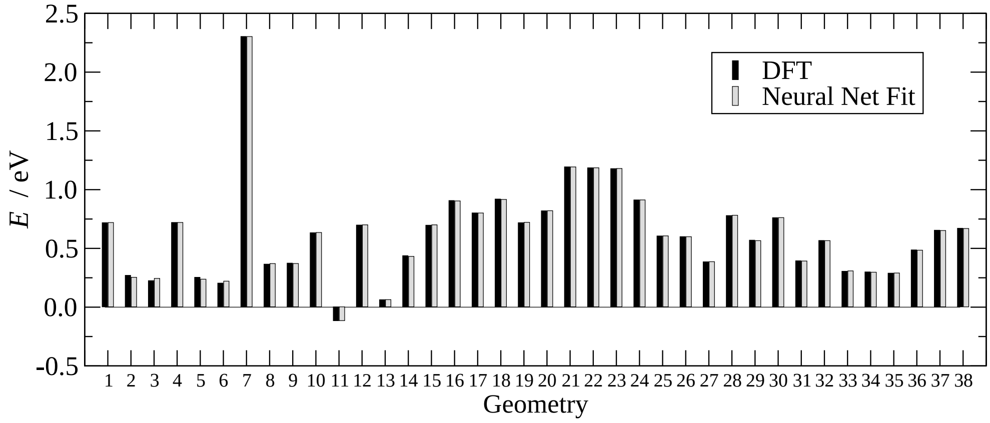

Figure 13.7: Comparison of the fitted and the RPBE DFT energies for a point in the typical barrier region ($d = 1.3$ Å, $Z = 2.1$ Å) for 38 different molecular geometries (cf. Appendix C).

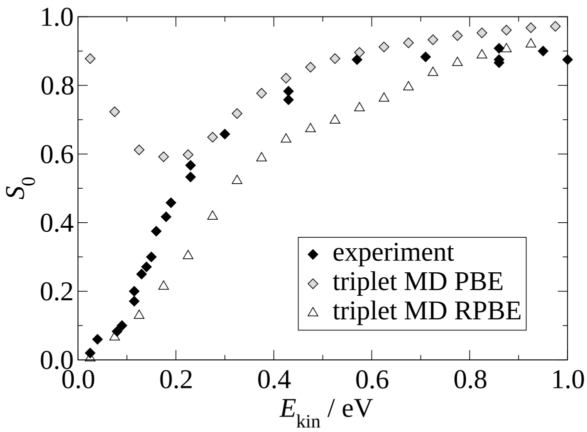

Figure 13.8: Sticking curves obtained from molecular dynamics runs on the spin-triplet potential-energy surface. The black diamonds represent the experimental data. The grey diamonds represent the sticking probabilities obtained with the PBE functional and the empty triangles the RPBE sticking probabilities.

sticking probability at all. The resulting sticking curves are shown in Fig. 13.8 and compared to the experimental sticking data. For each kinetic energy 2000 trajectories with random initial configuration starting at $Z = 9.5$ Å have been calculated. For both functionals a significant reduction of the sticking probability compared to the adiabatic case can be observed (cf. Fig. 10.10). However, at first sight the two sticking curves seem to be qualitatively different. The RPBE sticking curve reproduces the shape of the experimental sticking curve very well, since due to the presence of energy barriers for all molecular orientations the sticking probability of thermal molecules is basically zero. With increasing kinetic energy the barriers can be overcome for more and more molecular orientations and the sticking probability is rising to a value of about 90 %, which is very similar to the experimental saturation value.

The sticking curve based on the PBE triplet PES is very similar to the RPBE curve for medium and high kinetic energies. The upshift compared to the RPBE curve can be explained with the systematically lower energy barriers in case of the PBE functional and provides a kind of "DFT error bar". However, in contrast to both, the RPBE curve and the experimental sticking curve, for thermal molecules the PBE sticking probability is also very high, about 87 %. The reason for this high sticking probability is the absence of energy barriers for a few molecular orientations. Thermal molecules approach the surface very slowly and have sufficient time to change their orientation and lateral position corresponding to the shape of the surface potential. The majority of low energy molecules is therefore steered into the barrier-free entrance channels and can adsorb on the surface. This steering effect becomes less efficient with increasing kinetic energy, because then the molecules have less time to reorient, and consequently the sticking probability drops to about the experimental sticking curve. This difference in the sticking probabilities of thermal molecules obtained with the two functionals illustrates how critical small energy differences in the potential-energy surface can be for the resulting sticking curve. Although the PBE triplet energy surface is clearly less attractive than the adiabatic potential-energy surface, in the typical barrier region the energy of some configurations is only about -20 meV yielding no net barrier. If this energy would be only by about 50 meV higher, both functionals would yield qualitatively the same triplet sticking curve, because then thermal molecules could not adsorb on the surface. However, state-of-the-art density-functional theory is apparently not able to provide the required accuracy here, and it would be desirable to calculate the barrier heights with more precise methods like local correction schemes for an improved description of exchange and correlation [276, 277]. Nevertheless, the qualitative reduction of the sticking probability based on the diabatic triplet PES, which cannot be obtained from the adiabatic PES using either functional, is untouched by these uncertainties.

As mentioned above, the triplet sticking curve forms just one extreme case in which all types of transitions to other diabatic energy surfaces are neglected. Clearly, these transitions will occur, at least if both atoms are adsorbed on the surface according to a "normal" dissociative adsorption mechanism, because adsorbed oxygen atoms are in a singlet state and charge transfer from the metal to the oxygen atoms takes place. The consequences of these transitions for the sticking curve will be discussed in Chapter 15.

This chapter will be concluded by some remarks on the reliability of the sticking curves with respect to the fit and statistical arguments. So far each sticking curve was derived from one particular fit which is expected to represent the six-dimensional potential-energy surface accurately. This fit has been carefully selected in all cases but a quantitative measure for the deviations in the sticking curves for different fits would be desirable. In Fig. 13.9 the sticking curve based on the RPBE triplet potential-energy surface obtained from two independent fits of the same accuracy is compared. "Fit1" is the fit described above, and "fit2" employs a 11-40-40-1-tl network, an

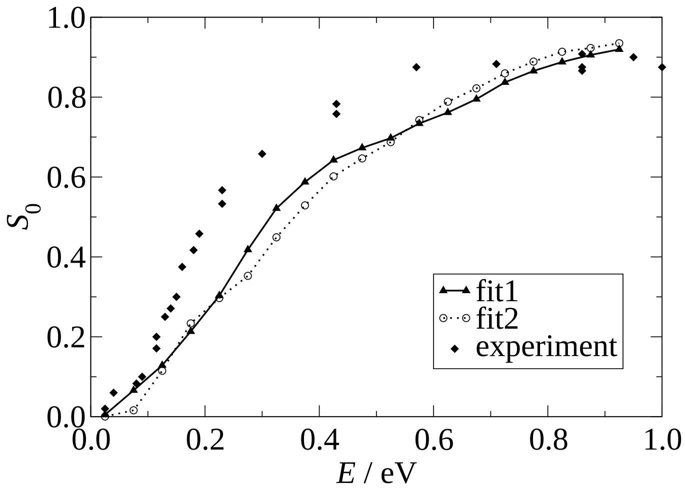

Figure 13.9: Sticking curves for two different neural network fits. The data have been obtained by molecular dynamics runs on the spin-triplet potential-energy surface using the RPBE functional.

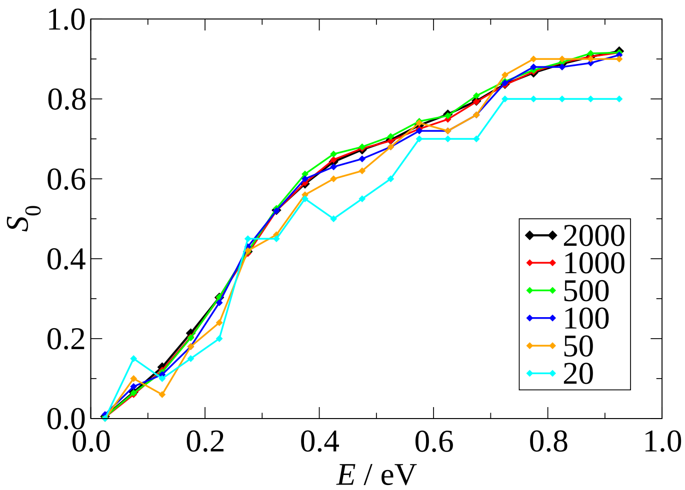

Figure 13.10: Sticking curves for different numbers of trajctories per kinetic energy. The data have been obtained by molecular dynamics runs on the spin-triplet potential-energy surface using the RPBE functional.

Points	ω
E <1 eV	25.0
d = 1.224 Å $\wedge$ Z >2.8 Å	500.0
d = 1.3 Å $\wedge$ Z = 2.1 Å	167.0
d >1.6 Å	10.0

Table 13.3: Set of weights assigned to the data points for fit 2 in Fig. 13.9.

adaptive Kalman filter with the parameters $\lambda(0)$ =0.98000 and λ_0 =0.99770 and the weights given in Table 13.3. Although the network architecture is the same in both fits, the network weights are completely different due to the different use of the Kalman filter and the fitting error weights. The two sticking curves are very similar and it can be concluded that the uncertainty in the sticking probabilities with respect to the applied fit is about 5 %. Tests with a number of other fits confirmed this uncertainty estimate. Another question is if the 2000 random trajectories at each kinetic energy are sufficient to obtain statistically reliable sticking curves. In Fig. 13.10 the RPBE triplet sticking curve is shown for different numbers of trajectories. For less than 100 trajectories per energy strong oscillations appear, but then the sticking curve converges and the curves based on 1000 and 2000 trajectories are basically indistinguishable.

Chapter 14

Further Diabatic Potential-Energy Surfaces

To obtain a more realistic picture of the dissociation process, transitions from the initial neutral spin-triplet PES to other diabatic PESs have to be included in the model. Two important alternative diabatic PESs are e.g. the singlet potential-energy surface, which corresponds to the ground state spin of the adsorbed atoms, and an ionic potential-energy surface, which emerges if one electron is transferred from the metal to the oxygen molecule. By transferring further electrons a series of ionic PESs can be constructed, but here we will focus on the first transfer only, and in short this PES will be called the "ionic PES". The energetic order of the singlet PES and the ionic PES determines the coupling to the triplet energy surface at large molecule-surface distances, and thus ensuing transitions between these states when the molecule approaches the metal surface.

The constrained density-functional method derived in Chapter 12 is very general and allows in principle to calculate any spin and charge state by distributing electrons accordingly into the oxygen and aluminium spin-up and spin-down subsystems. Consequently, this method is not limited to the calculation of the neutral spin-triplet potential-energy surface, but should also allow to calculate further diabatic potential-energy surfaces. In the following sections its applicability to the singlet PES and the ionic PES will be explored.

14.1 The Singlet Potential-Energy Surface

The singlet potential-energy surface is defined by a spin-singlet on the oxygen molecule and also on the metal surface. Standard density-functional theory offers two ways to calculate this energy surface. The first way is to perform spin-restricted, i.e. non-spin-polarized, DFT calculations. In this method the individual spin-up and spin-down densities are the same since the spatial orbitals for both spin orientations are identical. As described in detail in Section 9.1 these calculations do not allow to distinguish between the $^1\Delta_\mathrm{g}$ and $^1\Sigma_\mathrm{g}^+$ singlet states and the low-spin triplet in current implementations of DFT since these states have the same charge density. The second possibility for the calculation of the singlet energy surface would be the use of fixed-spin-moment calculations with an overall singlet spin, i.e. $N^\uparrow - N^\downarrow = 0$. However, we found that these calculations are very sensitive to local spin minima for large molecule-surface separations. Depending on the spin-density used to initialize the DFT calculation for large molecule-surface separations these local minima can correspond to a triplet oxygen molecule whose spin is compensated by an opposite spin-density in the metal surface. This is clearly not the singlet energy surface we want to calculate. On the other hand, if by choosing a suitable starting density in the fixed-spin-moment approach a singlet oxygen molecule is obtained, i.e. $N^\uparrow_{\mathrm{O}_2} = N^\downarrow_{\mathrm{O}_2}$, the calculation reduces to the spin-restricted result[1] with degenerate spin-up and spin-down orbitals having the same spatial part. The fixed-spin-moment approach does therefore not offer any advantages over spin-restricted calculations and will not be used in this work.

Another possibility to calculate the singlet potential-energy surface is to employ the spin-constrained density-functional approach in a similar way as in the calculation of the triplet PES, but to assign the same number of electrons to spin-up and spin-down orbitals in both subsystems. For the (3×3) supercell used in this work containing 63 aluminium atoms and two oxygen molecules the occupation numbers of the subsystems are accordingly: $N^\uparrow_{\mathrm{O}_2} = N^\downarrow_{\mathrm{O}_2} = 16$, and $N^\uparrow_{\mathrm{Al}} = N^\downarrow_{\mathrm{Al}} = 409.5$. The main question is, whether it is possible to decouple the oxygen molecule completely from the surface as it has been achieved in case of the $^3\Sigma_\mathrm{g}^-$ triplet ground state. In Fig. 14.1 two elbow plots obtained using the RPBE functional are shown for the spin-restricted and for the singlet spin-constrained density-functional calculations. All in all, 4 elbow plots (geometries 1, 2, 8 and 12 in Appendix C) have been calculated using spin-constrained DFT and 12 elbow plots (geometries 1-12 in Appendix C) using spin-restricted DFT for the PBE and the RPBE functional employing the same parameter set as for the adiabatic and the spin-triplet PESs.

According to Fig. 14.1 for large molecule-surface separations the spin-restricted PES has a significantly higher energy than the singlet obtained from the spin-constrained DFT calculation. For Z=6 Å the energy differences to the spin-triplet PES are 0.937 eV and 0.397 eV, respectively, independent of the molecular orientation. The difference between these energies can be understood by a comparison to the results obtained for the free oxygen molecule in Section 9.1. Using the RPBE functional, the free spin-restricted oxygen molecule has a singlet-triplet splitting of ΔE_ST=1.171 eV, and the unrestricted calculation yields a splitting of ΔE_ST=0.393 eV (cf. Table 9.4) with respect to the triplet ground state, while the experimental singlet-triplet splitting is about 0.98 eV [210]. Obviously, the spin-constrained singlet calculation yields an oxygen state corresponding to the spin-unrestricted calculation of the free molecule, with a similarly too low singlet-triplet splitting. This has been confirmed by compar-

[1] The computational costs are doubled compared to a restricted calculation due to the formally unrestricted calculation.

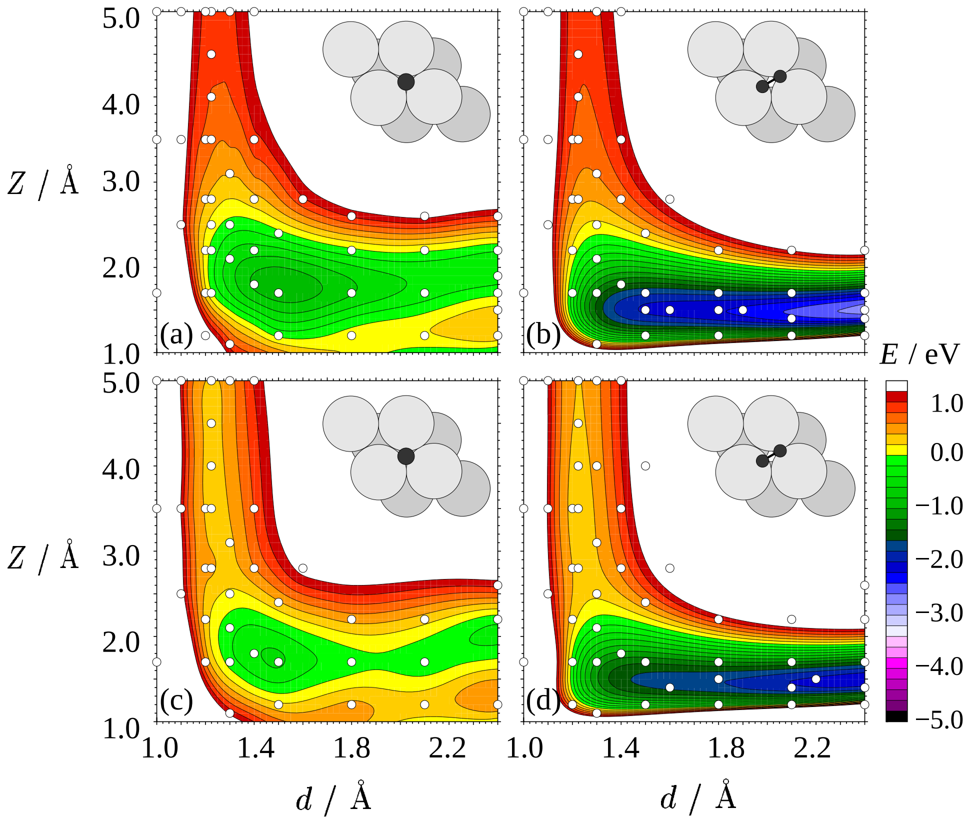

Figure 14.1: Singlet elbow plots for two different molecular orientations (geometries 1 and 2 in Appendix C) calculated using two different methods. (a) and (b) have been obtained by standard restricted (non-spinpolarized) DFT calculations, and (c) and (d) by singlet spin-constrained DFT. All shown elbow plots have been obtained using the RPBE functional, and the zero point of the energy is the same as for all potential-energy surfaces in this work. The white dots represent the calculated energy points. The substrate has been frozen in the geometry of the bulk-truncated surface. The energy zero point corresponds to an oxygen molecule in the triplet ground state at an infinite distance from the surface without any charge transfer.

ing the energy levels and occupations in both cases, and the obtained state for large molecule-surface separations corresponds exactly to a superposition of the undisturbed energy levels of the metal surface and the free unrestricted "singlet" molecule, which in fact corresponds to a mixture of the $^1\Sigma_g^+$ singlet state and the low-spin triplet O_2. Consequently, using the spin-constrained DFT method, we can control the state of the oxygen molecule basically in the same way as for the free molecule. This would exactly be what we need, but on the other hand, as explained in Section 9.1, the description of the singlet state with current gradient-corrected exchange-correlation functionals is very poor. By approximating the singlet state with a single-determinant wave-function, which is equivalent to using a symmetry-broken density, we therefore necessarily have to deal with the adherent severe underestimation of the singlet-triplet splitting.

Further inspection of Fig. 14.1 shows that close to the surface the spin-restricted energy is lower than the energy obtained from the spin-constrained calculations. This is because, like in case of the triplet PES, the spin-constrained singlet PES does not allow for charge transfer from the metal surface to the molecule at all distances. Thus, the spin-constrained singlet PES does not represent the ground state of the system when the oxygen atoms are adsorbed on the surface and further ionic PESs would have to be taken into account for a complete description. The spin-restricted PES, on the other hand, does not include any constraint concerning the charge distribution, and has the same energy as the adiabatic PES close to the surface. In terms of charge the spin-restricted PES is "adiabatic" in that always the lowest energy charge distribution is obtained. This rises the question if like in case of the adiabatic PES a finite charge transfer from the metal to the oxygen molecule occurs even at very large molecule-surface separations. This is indeed the case. For Z=6 Å a sizeable charge transfer of about 0.12 e has been found, which is approximately 10 times larger than in case of the adiabatic PES for the same molecular configuration (cf. Chapter 10). In order to estimate the charge transfer for an infinite molecule-surface separation, like in case of the adiabatic PES, calculations of a charged free spin-restricted oxygen molecule have been carried out. In Fig. 14.2 the energetic position of the $2\pi^*$ level is shown as a function of the molecular charge[2]. In excellent agreement with the slab calculation the $2\pi^*$ level is aligned with the Fermi level of the clean Al(111) slab ($\epsilon_{\mathrm{F,Al}}$=-4.522 eV) for a charge transfer of about 0.12 e. This comparably large charge transfer lowers the total energy of the spin-restricted PES and is the reason for the reduced singlet-triplet splitting of 0.937 eV mentioned above, compared to the value of 1.171 eV for the free restricted molecule. The good agreement of the singlet-triplet splitting with experiment is therefore just due to an error cancellation in that the charge transfer lowers the energy while the admixture of the ${}^1\Sigma_{\mathrm{g}}^+$ state and the low-spin triplet O_2 increases the total energy.

In summary, the singlet PES obtained from spin-constrained DFT has a clearly too low energy for medium and large molecule-surface separations, i.e. in the region of the PES we have identified before as most important for molecular sticking. This is a consequence of the single-determinant approximation to the underlying state yielding a symmetry-broken spin-density as described in Section 9.1. Close to the surface the energy is higher than the adiabatic ground state due to the absence of charge transfer. This indicates that further diabatic PESs should be included for a complete model. It is *a priori* not clear, if the spin-constrained singlet PES provides more reliable energies in this region, because the present strong hybridization has two consequences: On the one hand the oxygen molecule is not well defined anymore making the inaccuracies in the description of the singlet state obsolete. On the other hand the projection of the Kohn-Sham states on the atomic orbitals becomes, although mathematically well defined, an arbitrary choice to define the oxygen and aluminium subsystems. For large

[2]In case of a restricted calculation the $2\pi^{*\uparrow}$ and $2\pi^{*\downarrow}$ orbitals are degenerate and no distinction is possible.

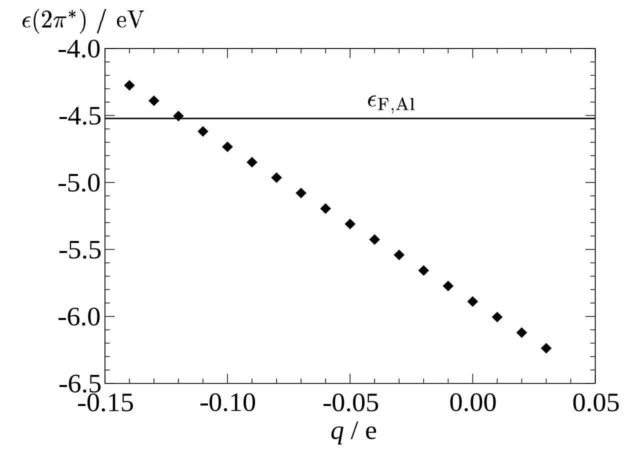

Figure 14.2: Energetic position of the $2\pi^*$ orbital of a free spin-restricted oxygen molecule as a function of the molecular charge q. The black line indicates the Fermi level $\epsilon_{\mathrm{F,Al}}$ of a clean Al(111) slab. The zero point of the energy corresponds to the vacuum level in the calculation of the free molecule, which is very close to the vacuum level of the potential in the Al(111) slab calculation.

molecule-surface separations the spin-restricted PES is energetically a much better approximation to the $^1\Delta_{\mathrm{g}}$ state, but only due to a fortuitous error cancellation. Yet, even without the energy lowering as a consequence of the unphysical charge transfer the singlet-triplet splitting would be significantly closer to experiment than in case of the spin-constrained result. Close to the surface a basically adiabatic charge transfer reduces the spin-restricted energy to the adiabatic ground state. This implies that, as mentioned above, the spin-restricted PES is in fact a mixture of several diabatic PESs of different charge. From this analysis it can be concluded that there is no easy way to obtain *the* singlet PES from present-day density-functional theory. A more detailed discussion of the consequences for the transition probability from the triplet to the singlet PES will be given in Chapter 15.

14.2 The Ionic Potential-Energy Surface

Another diabatic potential-energy surface, which has been suggested to play an important role in the oxygen dissociation on Al(111) [28], is the ionic potential-energy surface. It can be obtained by transferring one electron from the metal surface to the oxygen molecule, which therefore is in a spin-doublet state. In principle, the calculation of this energy surface can be done using the constrained density-functional method by assigning the corresponding electron numbers to the two subsystems ($N^{\uparrow}_{\mathrm{O}_2} = 18$, $N^{\downarrow}_{\mathrm{O}_2} = 16$, and $N^{\uparrow}_{\mathrm{Al}} = N^{\downarrow}_{\mathrm{Al}} = 408.5$). This has been done for five molecular orientations (geometries 1, 2, 8, 11 and 12 in Appendix C) for the PBE and the RPBE functionals. Two examples are shown in Fig. 14.3 for the RPBE functional. Close to the surface the energy is rather low because of a charge transfer comparable to

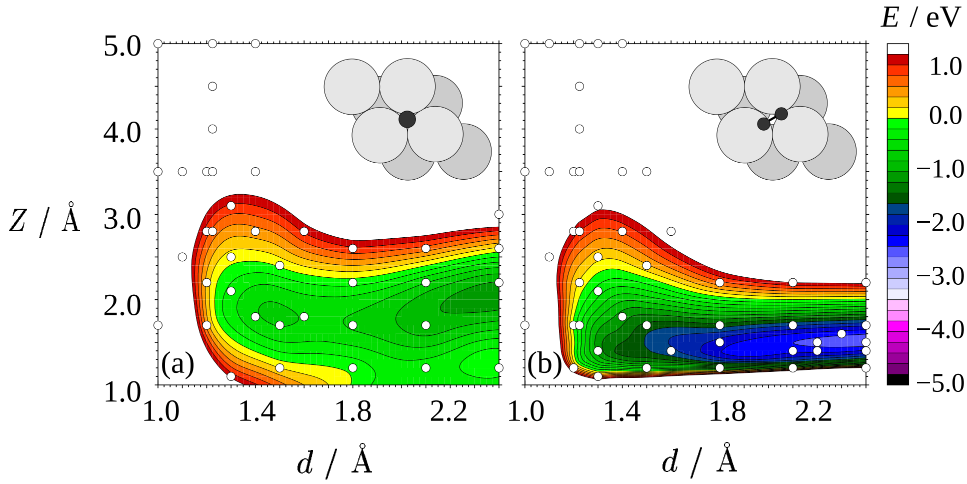

Figure 14.3: Ionic elbow plots for two different molecular orientations (geometries 1 and 2 in Appendix C) calculated using the constrained DFT method. All calculations have been done using the RPBE functional. The white dots represent the calculated energy points. The substrate has been frozen in the geometry of the bulk-truncated surface. The energy zero point corresponds to an oxygen molecule in the triplet ground state at an infinite distance from the surface without any charge transfer.

the ground state of the system. At Z=2.5 Å the energy starts to rise strongly with increasing molecule-surface separation.

However, the obtained energies have again to be treated with care for several reasons. For large separations the potential-energy should correspond to the difference between the work function of the Al(111) surface (4.24 eV [256]) and the electron affinity of the oxygen molecule (0.440 eV [225, 278]), i.e. approximately 3.8 eV according to experiment. This energy should be obtained also from the constrained DFT calculations, because for large molecule-surface separations the oxygen and aluminium states are well defined due to the absence of hybridization. The problem that arises is a consequence of the supercell approach chosen to model the aluminium surface in this work. While the (3×3) unit cell consisting of 7 aluminium layers is definitely large enough to obtain reliable energies when large electrostatic charges are absent, this is not necessarily true for the ionic energy surface due to the rather long range of the Coulomb potential. An additional complication is that oxygen is adsorbed on both sides of the slab. When an electron is transferred from the surface to each of the molecules, the slab becomes therefore doubly charged, which is energetically very unfavorable. At large molecule-surface separations we correspondingly find too high potential-energies, e.g. 5.8 eV at Z=5 Å practically independent of the molecular orientation. This suggests to interpret the obtained results on the ionic potential-energy surface only in a qualitative way. A more accurate determination of this surface would require a slab without inversion symmetry to avoid the doubly charged aluminium. This, however, cannot be handled in the present version of DMol^3 because of the missing dipole correction [259]. Most probably also larger supercells would be required to reduce the electrostatic interaction between the neighbored unit cells.

Yet, despite all these deficiencies, also according to experiment the ionic PES should be approximately 3 eV higher in energy than the $^1\Delta_g$ singlet state at large molecule-surface separations. Consequently, the latter is expected to couple much stronger to the triplet PES, and thus should be more important for the sticking probability of thermal molecules in the region of the barrier onset.

Chapter 15

The Role of Electronic Transitions

Up to now our molecular dynamics simulations have been restricted to two extremes, the adiabatic limit corresponding to an instantaneous relaxation of the electronic structure to the ground state, and the spin-triplet limit without any change in the charge or spin state. These two extreme cases allowed to answer the question if non-adiabatic effects could in principle account for the low sticking probability of oxygen on Al(111), i.e. do barriers exist and how do they affect the sticking curve if no transitions occur. A more refined model has to include transitions between different diabatic energy surfaces. At least at some energy range this will most likely increase the absolute values of the sticking probability. In principle, the adiabatic PES is a combination of all diabatic states, and the molecule is moving simultaneously on all of them with a certain amplitude. A slow molecule will therefore follow the adiabatic potential, if a strong coupling and consequently a high transition probability is present. To include these effects, the final intention must be to perform molecular dynamics simulations simultaneously on all suitably coupled diabatic PESs to obtain a quantitatively correct sticking curve over the whole kinetic energy range of interest. This is a very ambitious goal that requires the knowledge of all relevant diabatic PESs and their couplings. In this chapter the progress made in the present work is evaluated in the context of a possible strategy towards this goal.

The first step necessarily must aim to provide accurate potential-energy surfaces. These attempts up to now have been exclusively based on density-functional theory, usually in the adiabatic limit [22, 24, 70–73]. The constrained DFT approach introduced in the present work allows now to also calculate arbitrary diabatic PESs with DFT accuracy. Another approach is the extension of the ΔSCF method [118] to surfaces, currently being developed by Lundqvist and coworkers [268, 269][1]. From the

[1]In the surface-extended ΔSCF method first an adiabatic DFT calculation is carried out. Then the occupations of the states are modified in that one electron in a particular state is removed and filled into a formerly unoccupied state. Under the constraint of these occupations a self-consistent calculation is performed. The clear drawback of this method is that, in contrast to the constrained DFT method introduced in the present work, in case of interacting subsystems the hybridization is completely neglected, which can significantly affect the obtained energies.

diabatic and the adiabatic energies the coupling $|H'_{12}|$ between two diabatic states can be obtained. For a two-level system Eq. (3.1) holds, and one needs three of the four energies, two adiabatic energies $E^{\mathrm{a}}_{1,2}$ and two diabatic energies $E^{\mathrm{d}}_{1,2}$. Rearranging Eq. (3.1) yields

$$|H'_{12}| \quad = \quad \sqrt{\left(\frac{1}{2}\left(E^{\mathrm{d}}_1 + E^{\mathrm{d}}_2\right) - E^{\mathrm{a}}_1\right)^2 - \frac{1}{4}\left(E^{\mathrm{d}}_1 - E^{\mathrm{d}}_2\right)^2} \quad . \tag{15.1}$$

However, this expression is valid only for a two-level system, and becomes more complex in the general case of N diabatic PESs. The Hamiltonian in the diabatic representation is then

$$\mathbf{H}' = \begin{pmatrix} H'_{11} & H'_{12} & \cdots & H'_{1N} \\ H'_{21} & H'_{22} & & \vdots \\ \vdots & & \ddots & \vdots \\ H'_{N1} & \cdots & \cdots & H'_{NN} \end{pmatrix} \quad . \tag{15.2}$$

Basically, for each pair of diabatic PESs an individual coupling strength H'_{ij} has to be determined, which depends on the molecular configuration. Another, yet unsolved, problem is that for a large number of diabatic states an under-determined set of equations arises, because the number of coupling matrix elements is higher than the number of diabatic energy surfaces.

The configuration dependence of the couplings enters via the respective PESs, which are therefore of fundamental importance. In Fig. 15.1 the adiabatic ground state energy and several diabatic energies obtained in this work are shown for the PBE and the RPBE functional. The energies correspond to molecular configurations along the reaction paths on the initial spin-triplet PES for two different molecular orientations, above an fcc site oriented perpendicular and parallel to the surface. The corresponding triplet elbow plots are shown in Fig. 15.1(a) and (d), respectively. In the energy diagrams in Fig. 15.1(b), (c), (e) and (f) the energies along the reaction path have been projected on the Z-axis for molecule-surface separations between 2 and 5 Å. (b) and (c) refer to the perpendicular orientation in elbow plot (a), while (e) and (f) are assigned to the parallel orientation in elbow plot (d). At all distances, the adiabatic PES has by definition the lowest energy. At molecule-surface separations larger than 3 Å the triplet PES is energetically the most favorable of all diabatic PESs. Between 2.5 and 3 Å above the surface other diabatic PESs cross the triplet state. It is interesting to note that the sequence of these crossings is very similar for both functionals, but the energies are systematically higher for the RPBE functional. This increase of energy barriers using the RPBE functional has also been found for other systems [279, 280]. As a consequence, the relative energies of the two functionals are similar and the couplings are not expected to depend qualitatively on the functional.

Initially, at large molecule-surface separations, the oxygen molecule moves on the triplet PES, which should be identical to the adiabatic ground state. However, this

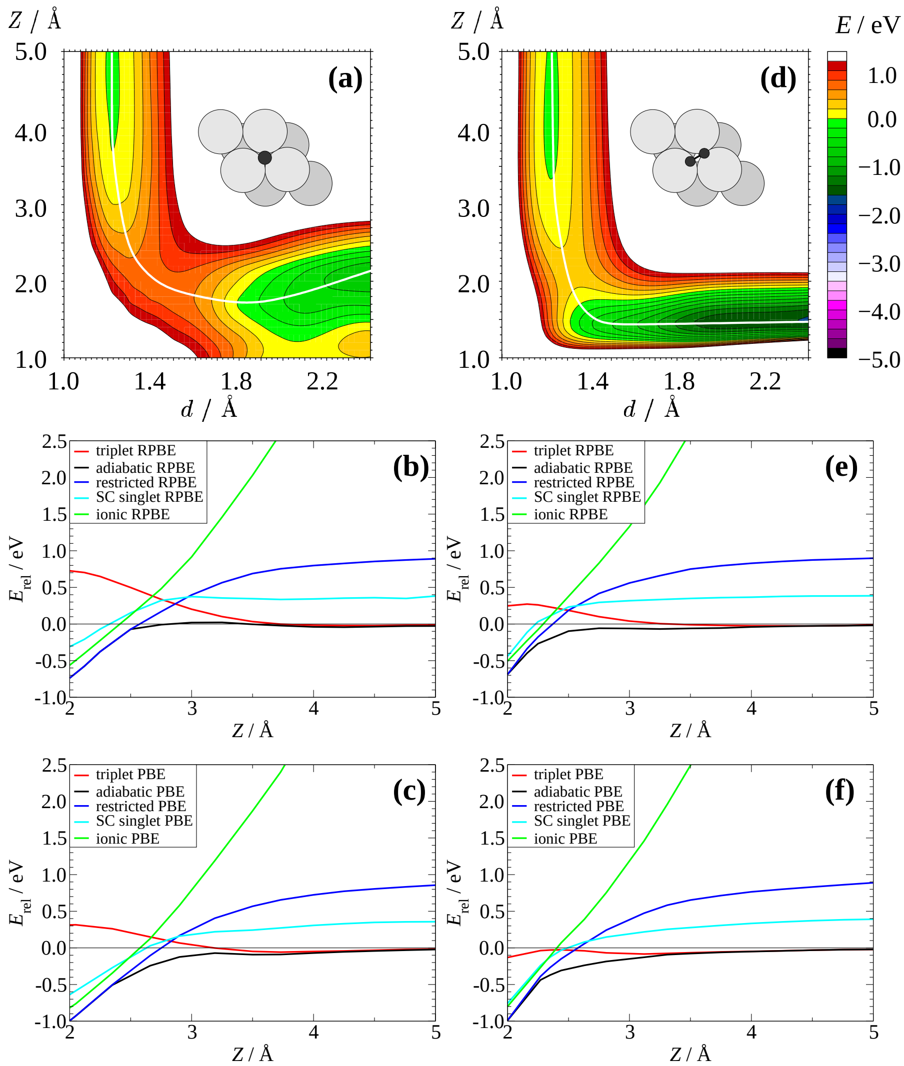

Figure 15.1: Energies along the reaction path for two different molecular configurations calculated using the PBE and the RPBE functional and projected on the Z-axis for molecule-surface separations between 2 and 5 Å. (a) shows the reaction path (white line) on the RPBE-triplet elbow plot for a molecule oriented perpendicular to the surface above an fcc site. In (b) the energies of all considered diabatic PESs along this path are shown for the RPBE functional. (c) contains the energies for the PBE functional using configurations on the very similar PBE-triplet reaction path (not shown). In (d) the reaction path for a molecule oriented parallel to the surface above an fcc site is shown for the RPBE functional. The corresponding diabatic energies are shown in (e), while (f) contains the PBE energies. "SC" denotes the spin-constrained singlet PES and "ionic" the superoxide PES with one electron transferred from the aluminium to the molecule.

is not the case in the adiabatic calculations due to the artificial charge transfer from the surface to the molecule discussed in Chapter 10. The adiabatic PES is therefore too low in energy and converges at an infinite distance from the surface to the wrong energy, which is approximately 20 meV lower than the triplet energy. This yields an unphysical coupling at all distances from the surface, because according to Eq. (15.1) the coupling between the triplet and any other diabatic PES is zero only if the triplet energy is exactly identical to the adiabatic ground state. Consequently, it cannot be identified, at which molecule-surface separation a physically reasonable, although initially weak, coupling sets in. Another uncertainty in the energies far away from the surface and affecting all PESs is the incorrect treatment of van der Waals interactions in DFT since present-day exchange-correlation functionals depend only on the local density and density gradients, while van der Waals interactions are non-local in nature. Still, many functionals yield an energy lowering which could be interpreted as a physisorption well caused by an overlap of charge densities, as has been shown for example in studies on rare gas dimers [275]. The resulting energy changes are very small, typically well below 0.1 eV and irrelevant for the interpretation of DFT energies, but for molecule-surface separations of more than about 3 Å this is the same order of magnitude as the energy difference between the adiabatic and the triplet PESs. However, at a distance of 6 Å the overlap of charge densities becomes very small having no effect on the energy any more, as has been shown for the spin-constrained singlet and triplet calculations, which reach a constant energy beyond Z=6 Å.

The next major question that arises is which diabatic PES gives rise to the splitting between the triplet and the adiabatic PES by coupling to the triplet state. As discussed in Chapter 11 there are two simplified models, a charge transfer model and a spin-flip model for the non-adiabatic effects. To assess the role of charge transfer a series of ionic PESs can be calculated, i.e. the superoxide PES "$\mathrm{Al(111)^+ + O_2^-}$", the peroxide surface "$\mathrm{Al(111)^{2+} + O_2^{2-}}$" and further ionic states of the adsorbed atoms [21]. These are not accessible by standard DFT, but a calculation is possible using the ΔSCF method if hybridization effects are neglected, which however can be a strong and uncontrolled approximation [269]. In the previous section it has been shown that the "superoxide" ionic PES in principle is also accessible using the constrained DFT formalism, but for accurate energies a larger supercell would be required (like in the ΔSCF method). Nevertheless, for large molecule-surface separations the ionic PESs are significantly higher in energy than the $^1\Delta_\mathrm{g}$ singlet state. The $^1\Delta_\mathrm{g}$ state is therefore a more likely diabatic coupling state at a large molecule-surface distance and has been investigated in more detail in the present work. As can be seen in Fig. 15.1, the uncertainty in energy with respect to this state is unfortunately particularly large, since far from the surface the spin-restricted and the spin-constrained (SC) singlet differ significantly. As discussed in Chapter 14 the spin-constrained singlet calculation yields a far too low singlet-triplet gap, while the spin-restricted calculation includes also a sizeable charge-transfer contribution. Consequently, a reliable singlet PES is presently not available, and these uncertainties in both the singlet and in the adiabatic energy as well as the functional-dependence of the barrier heights of the triplet PES so far prohibit a straightforward application of the two-state model described in Chapter 11.

Still, from Fig. 15.1 it can be concluded qualitatively that the crossing between the triplet and other diabatic PESs occurs roughly at a distance between 2.5 and 3 Å above the surface with a slight dependence on the molecular orientation. The coupling is largest at the crossing, which is clearly closer to the surface than the onset of the barriers. The latter exhibit a strong functional dependence, as shown in Chapter 13, adding further uncertainty to the exact position and energetics of the level crossings. Most of these problems are related to the implementation of exchange and correlation in present-day DFT, and obviously this is as far as one can get with current functionals. Before the coupling of the diabatic states can be addressed, a more precise way to determine the diabatic energies using a different treatment of exchange and correlation has to be found. The price of going beyond DFT is unfortunately a significantly higher computational demand of the calculations, and a high-level treatment of electron correlation like in configuration interaction [100] or coupled cluster approaches [100] is currently unfeasible for a direct mapping of six-dimensional PESs of surface systems. Still, an assessment of the barrier heights could be done for representative configurations, particularly exploiting the near-sightedness concept, i.e. using the higher level calculations only for corrections of the DFT total energies [276, 277]. With our present understanding from Chapter 13 this is most important for the triplet PES, but also some functional dependence in the shape of the adiabatic PES could be resolved (cf. Chapter 10). Concerning the triplet PES a suitable way to constrain the occupations in the wave-function based calculations would have to be found. As the constrained DFT approach described in Chapter 12 is by construction not limited to DFT, in principle it should be applicable to other electronic structure methods based on localized basis functions as well.

Concluding that the quantitative calculation of coupling matrix elements is currently limited by the approximate DFT energetics, some qualitative considerations can still be done. In Fig. 15.2 the energy diagram of Fig. 15.1(b) is shown. Additionally, the turning points of a thermal molecule and of a molecule with a medium kinetic energy of 0.25 eV are included. The singlet PES is represented by the spin-restricted calculations, keeping in mind the too low energy due to charge transfer with adherent uncertainty of the exact location of the crossing point. Due to the still comparably large energy difference to the singlet PES the part of the triplet PES accessible to the thermal molecule is expected to couple only weakly to the singlet state. Consequently, the transition probability[2] is expected to be very small. This suggests that the molecule would be confined to the triplet PES, cannot get close to the surface and is finally reflected into the gas phase. On the other hand, the medium

[2]The probability of a transition between the $^1\Delta_g$ and the $^3\Sigma_g^-$ state for an oxygen molecule in the gas phase due to spin-orbit coupling is very small. In experiment it has been found that the lifetime of the $^1\Delta_g$ state is about 45 minutes at low gas pressures [223].

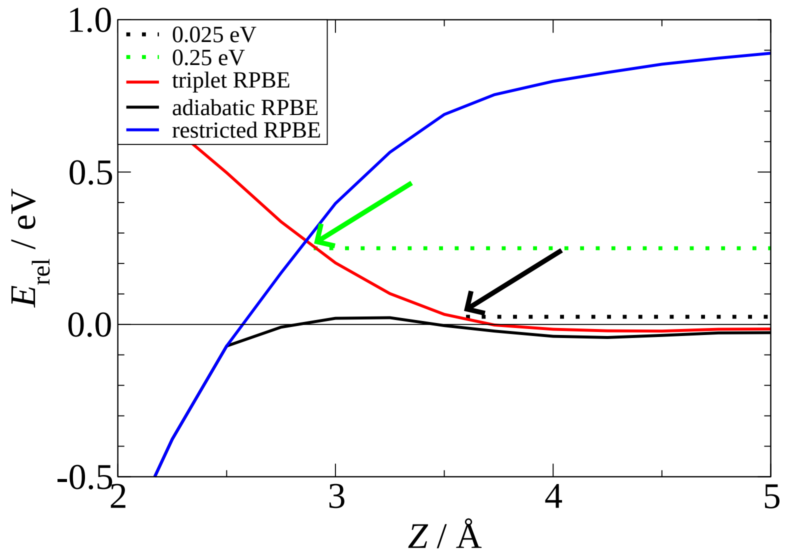

Figure 15.2: Turning points of a thermal (E=0.025 eV) and a medium energy (E=0.25 eV) oxygen molecule approaching the Al(111) surface on the triplet PES oriented perpendicular to the surface above an fcc site (cf. Fig. 15.1(b)). The thermal molecule cannot get closer than 3.5 Å to the surface. At this distance the coupling to the singlet PES, here represented by the spin-restricted PES, is rather small. The medium energy molecule is getting very close to the crossing point where the maximum coupling between the diabatic PESs is present.

energy molecule can get much closer to the crossing point where the strongest coupling is present. Consequently, eventually induced transitions might increase the sticking probability for this kinetic energy. Higher energy molecules ($E > 0.9$ eV) can overcome all barriers on the triplet PES and stick on the surface regardless of whether or not transitions take place. In summary, this implies that a significant change of the sticking probability is only expected for medium kinetic energies, leaving the low sticking probability found for thermal molecules in the triplet limit untouched by transitions. However, as long as the exact position of the curve crossing and the exact barrier height on the triplet PES are not known, this simple model cannot be confirmed. Still, there is some experimental evidence that the $^3\Sigma_g^-$ state of O_2 can have a very long lifetime (defined as the inverse of the transition probability) even in the presence of a metal surface. Menzel and coworkers [281] identified for example an oxygen molecule in its paramagnetic triplet state physisorbed on the Pt(111) surface below 30 K.

Assuming that the PESs could be obtained accurately by a different treatment of exchange and correlation, the next step towards a quantitative sticking curve would be to include transitions between the diabatic PESs. For the oxygen dissociation on Al(111) two studies based on simple model potentials have been done in this direction [21, 28].

Katz *et al.* [21, 29, 68] used wave packet dynamics to obtain populations of four diabatic PESs, the neural physisorption PES, the superoxide PES, the peroxide PES, and a PES describing the adsorbed atoms. Due to the lack of precise potentials, the diabatic states have been modelled by empirical functions. The atomic structure of the surface was furthermore completely neglected, reducing the dimensionality of the problem to three. Additionally, for the non-adiabatic coupling between each pair of states estimated parameters have been used in a combination with a function decaying exponentially with increasing distance from the surface. This generic model underlines the need for precise *ab initio* potentials, but also gives an idea what could be done by combining suitable PESs with quantum dynamics[3].

In the second study Hellman *et al.* [28] estimated the sticking probability from a simple one-dimensional model based on a combination of DFT using the Thomas-Fermi-Weizsäcker approximation to the kinetic energy functional [107, 108] and empirical functions. They took into account the neutral physisorption state as well as the ionic superoxide PES, and included transitions by an empirical function introduced by Langreth and Nordlander [282] that decays exponentially with the distance from the surface, which in turn was represented by a jellium model.

Both studies yield a reduced sticking probability for thermal molecules. However, due to their empirical character, i.e. parameters fitted to experiment and the neglect of most degrees of freedom, a more precise calculation of the sticking curve based on high-dimensional *ab initio* PESs is highly desirable. This holds in particular since it has been shown in Chapter 13 that small changes in the PES can have a large impact on the sticking curve. The strong surface-site dependence of the PESs, which has been neglected in both studies, is out of question. Both models also have in common that they assume an exponentially increasing transition probability when the molecule approaches the surface. For a model containing only a small number of coupling states this would be in contrast to the fact that the coupling is highest at the curve crossing. Yet, this probably does not introduce large errors, as closer to the surface many curve crossings might occur that open many ways for electronic transitions. An alternative approach yielding the same conclusion is to use the width of the oxygen $2\pi^*$ levels in the DOS as a measure for the electronic interaction with the surface. From the peak width Γ the lifetime $\tau = \frac{\hbar}{\Gamma}$ could be estimated. This has been done within our calculational setup for a molecule oriented perpendicular to the surface above an fcc site. The lifetime at a certain distance was found to be in the same order of magnitude as the time the molecule spends closer to the surface than this point. All in all the trajectory from the onset of noticeable level broadening to the turning point and back to the vacuum takes less than 1 ps for a thermal molecule on the triplet PES. Still, this simple DOS model does not account for spin-flip effects as the DOS only indicates electronic interaction in general, i.e. for example exchange of electrons with the surface. In this context a spin-flip within the molecule could be

[3]Wave packet dynamics for other systems, e.g. the laser induced desorption of NO from a NiO(100) surface, have been carried out by Klüner *et al.* [171]. These calculations have been based on accurate low-dimensional PESs obtained from CI calculations.

realized by an exchange of an electron with the surface in that an electron of spin α is transferred from the molecule to the surface and in return an electron of β spin reduces the former triplet to a singlet. This process, however, is energetically activated since the unoccupied $2\pi^{*\downarrow}$ orbital is higher in energy than the formerly occupied $2\pi^{*\uparrow}$ orbital.

A very promising method to perform dynamical studies on several coupled PESs including transitions is the surface hopping method of Tully and coworkers [283, 284]. It is a mixed quantum-classical dynamics method in which the atoms move classically on multi-dimensional PESs, while the electronic degrees of freedom are treated quantum mechanically. The essential component is a self-consistent treatment of the classical and the quantum subsystems in that the Hamiltonian acting on the electrons depends on the nuclear coordinates, so that in turn the forces on the nuclei are determined by the quantum state of the system. The wave-function of the system is a linear combination of basis functions, which can either be the diabatic or the adiabatic states. For each quantum state there is a distinct classical path, and the transitions between these states are determined by a non-adiabatic coupling vector. While the molecule moves on the PES of one particular quantum state, the amplitude of each electronic quantum state is calculated. By choosing a suitable hopping algorithm it is ensured that a large number of trajectories yields the correct population of each state [86]. However, due to the lack of accurate potentials, the surface hopping method has not been applied to the dissociation of molecules on surfaces so far.

In summary, the bottleneck towards simultaneous multi-dimensional dynamics on several PESs is presently the accuracy of the underlying potential-energies. Before the present work was begun, to our best knowledge no method had been implemented to calculate diabatic PESs from first-principles. By the introduction of the constrained DFT method this has now in principle become possible. Still, deficiencies of present-day DFT prevent the calculation of most diabatic PESs with sufficient accuracy forming now the main obstacle on the way to a quantitatively correct sticking curve.

Chapter 16

The Adsorption Mechanism

Finally, in this chapter some aspects of the adsorption mechanism will be discussed. The two most prominent models for the dissociation process these days are abstraction [1, 2, 68], in which one atom is adsorbed on the surface and the other atom is reflected back into the gas phase, and "normal" dissociation with both atoms being adsorbed close to each other on the surface [3] (cf. Fig. 2.2). While the calculations performed during this project certainly do not allow for conclusive statements about the mechanism, we briefly touch on aspects concerning the energetics, the substrate mobility and the final spin state, which already provide some basis for ensuing investigations directly addressing the nature of the adsorption mechanism.

Concerning the energetics, both mechanisms are exothermic and therefore allowed. The energetics of the abstraction mechanism is illustrated in Fig. 16.1 showing the energy of an oxygen atom as a function of its distance from an unrelaxed (3×3) slab at three different high symmetry sites for the PBE and the RPBE functionals. In order to obtain the same zero point for the energy as for the six-dimensional potential-energy surfaces calculated so far, a second oxygen atom has been included, which is located very far from the surface in its ^{3}P ground state. Consequently, this energy diagram can be regarded as an extension to the adiabatic potential-energy surface for molecules oriented perpendicularly to the surface having a very large bond length. The energy gain upon adsorption at the most stable fcc site is about 1.1 eV and about 0.3 eV at the bridge site, while adsorption at the top site is energetically not possible, because the binding energy at the top site is approximately 2 eV lower than the dissociation energy of the oxygen molecule. The energy differences between the PBE and the RPBE functional are surprisingly small since the higher binding energy in the oxygen molecule in case of the PBE functional is almost perfectly compensated by the higher oxygen adsorption energy on the surface. Relaxing the surface would lower the energies by approximately 0.5 eV, which has been determined in Section 9.3 by relaxing a (3×3) slab with one oxygen atom adsorbed in a fcc site. In total, in case of an abstraction mechanism the excess energy therefore amounts to approximately 1.5 eV, while for a "normal" dissociative chemisorption event about 8.5 eV are gained due to the additional binding energy of the second atom to the surface.

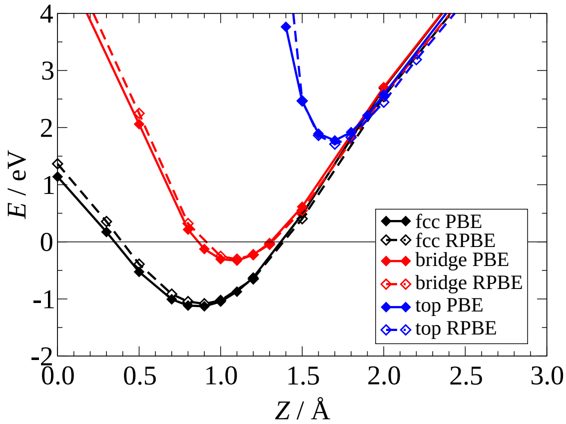

Figure 16.1: Potential of an oxygen atom above the fcc, bridge and top sites as a function of the distance from the unrelaxed surface. The second oxygen atom of the oxygen molecule is located at an infinite distance from the surface in its triplet ^{3}P ground state. The energy zero point corresponds to an oxygen molecule in the triplet ground state at an infinite distance from the surface without any charge transfer.

The adsorption energy can be dissipated by transferring energy to the aluminium atoms, i.e. by eventually exciting phonons[1] [85]. These effects of substrate mobility have been neglected in the six-dimensional molecular dynamics simulations employing the frozen surface approximation, since they are not relevant for the sticking of thermal molecules as explained in Chapter 10. As a consequence, the energy is completely converted into kinetic energy of the dissociating oxygen atoms yielding too high final velocities. Apart from providing a mechanism for energy dissipation, the mobility of the substrate atoms gives rise to very complex trajectories due to multiple atomic collisions and local structural changes, which can strongly affect the dissociation mechanism. This has been shown by high-dimensional *ab initio* molecular dynamics simulations in Section 10.5. However, the main purpose of these high-dimensional studies was to investigate the applicability of the frozen surface approximation to the calculation of the sticking curve at large molecule-surface separations. To obtain detailed information on the dissociation mechanism much longer runtimes would be required to identify oxygen atoms eventually leaving the surface. Finally, these molecular dynamics simulations can also not be based on a single energy surface. To cover the full trajectories from the initial triplet ground state of the molecule far from the surface to the final dissociation products, eventual transitions between several diabatic PESs would have to be included in addition to the substrate mobility, which is a formidable task.

Apart from the energetics and the substrate mobility another important aspect is the different final spin state of the oxygen atoms in the abstraction and the "normal"

[1]In principle, the energy would even be sufficient to completely remove aluminium atoms from the surface, which costs about 3.5 eV per atom.

dissociation mechanism. In the “normal” dissociative chemisorption both atoms are adsorbed on the surface and the spin of the system changes from triplet to singlet. In the abstraction mechanism all in all no spin-flip is required since the ground state of the ejected neutral oxygen atom is a ^{3}P triplet state and the initial spin of the molecule can be carried away from the surface without a change in the spin state. This might well be the reason for the apparent dominance of the abstraction mechanism for thermal oxygen molecules found in experiment [2].

This assessment is vaguely supported by the following analysis of the triplet-PES. In Fig. 16.2(b) the spin distribution between two oxygen atoms as obtained from a Mulliken analysis is shown for several molecular configurations along a reaction path in an elbow plot of the RPBE triplet-PES. In this elbow plot, which is shown in Fig. 16.2(a), the molecule is oriented perpendicular to the surface corresponding to an abstraction process. Far away from the surface the spin is equally shared by both oxygen atoms. For a strongly elongated bond length closer to the surface the majority of the spin is transferred to the oxygen atom with the larger distance to the surface. This corresponds to the initial state of the formation of a free oxygen atom in its triplet ^{3}P ground state. In Fig. 16.2(c) the spin distribution is shown for the adiabatic case and the same molecular configurations. For large molecule-surface separations the adiabatic spins are very similar to the triplet case except for a slight reduction of the total spin due to the artificial charge transfer from the surface discussed in Chapter 10. Closer to the surface the spin is reduced and completely vanishes below Z=2 Å. Then, the spin is recovered for bond lengths larger than about 1.8 Å, and like in the triplet case the majority of the spin is located on the oxygen atom being farther away from the surface. Both trajectories, on the adiabatic as well as on the spin-triplet PES, would therefore yield an abstraction mechanism if the molecule was confined to this elbow plot.

The real dissociation process, however, does not correspond to this simple picture. This becomes obvious when looking at the barrier heights at the initial spin-triplet PES. The lowest barriers are found for molecules oriented parallel to the surface, but these trajectories would not yield abstraction. Therefore, a complex molecular steering would be required, and very close to the surface the molecules would have to end up in a perpendicular orientation. This cannot be studied without taking into account the surface degrees of freedom. Another prerequisite for an abstraction process based exclusively on the spin-triplet PES is that the transition probability to other diabatic potential-energy surfaces has to be very low even in regions close to the surface that have to be passed by any dissociating molecule. Whether this is true is unknown since the transition probabilities are not yet available. However, once a molecule has overcome the barriers on the triplet PES, an abstraction mechanism could also occur after a transition to the adiabatic PES. Still, this applies only to a very small fraction of all impinging thermal molecules since the majority does not dissociate at the surface due to the energy barriers on the triplet PES.

In summary, the six-dimensional potential-energy surfaces calculated in this work provide only a very limited insight into the adsorption mechanism. They have been

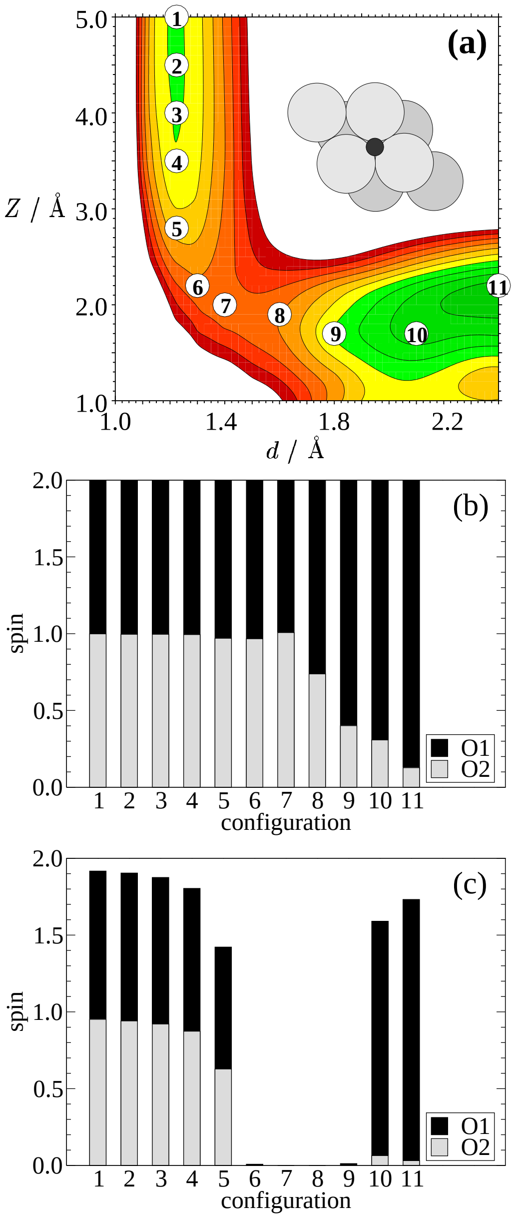

Figure 16.2: Spin on the two atoms O1 and O2 of an oxygen molecule oriented perpendicular to the surface above an fcc site (O2 is the atom being closer to the surface). In (a) the triplet spin-constrained elbow plot obtained with the RPBE functional is shown. The white circles represent DFT data points close to the reaction path. In (b) for these configurations the spins on the two oxygen atoms for the triplet spin-constrained calculations are shown. For all configurations they add up to a full triplet spin. Configuration 1 corresponds to a nearly free oxygen molecule and the spin is equally distributed on both atoms. For configuration 11, which has a strongly elongated bond length, the majority of the spin is centered at the atom farther away from the surface. In (c) the corresponding spins in the adiabatic case are shown. Far away from the surface the spin is slightly lower than a triplet due to charge transfer. For configurations 6-9 basically no spin-polarization exists, but for strongly elongated bond lengths like in the spin-constrained calculation a free oxygen atom in the ^{3}P state emerges.

obtained and applied under the assumption that the mobility of the substrate atoms is negligible, which is fulfilled for molecule-surface separations above about 2.5 Å. Closer to the surface the complexity increases drastically, as energy dissipation, electronic transitions between several diabatic energy surfaces and the motion of metal atoms have to be included to be able to follow the dissociation process until the dissociation products can be identified unambiguously. The required high-dimensional potential-energy surfaces cannot yet be mapped systematically, and consequently the only available technique would be direct "on-the-fly" *ab initio* molecular dynamics simulations extended to include energy dissipation and electronic transitions, which is beyond what is possible by present-day first-principle methods. Accordingly, only a few studies directly addressing the adsorption mechanism based on empirical diabatic potentials and completely neglecting the atomic structure of the surface have been performed to date [21].

Chapter 17

Summary and Outlook

The present work attempts reaching a better understanding of the dissociation process of oxygen molecules impinging on the Al(111) surface. Due to its fundamental importance, the main focus has been on the determination of the sticking coefficient, which is defined as the ratio of sticking events to the total number of molecule-surface collisions. In order to explain the experimentally determined low sticking probability of thermal oxygen molecules [9], many aspects of the adsorption event have been investigated systematically employing established methods as well as techniques, which have been developed in the course of this project.

In the first part of this work the six-dimensional adiabatic potential-energy surface (PES) representing the molecular degrees of freedom during the dissociation process has been calculated in detail. All calculations on the oxygen-aluminium system done so far have been based on density-functional theory, but the reliability of DFT for systems involving oxygen has been questioned due to the significant overestimation of the binding energy of the free molecule by present-day functionals. Thus, several exchange-correlation functionals have been tested for the free oxygen molecule. The PBE [114] and the RPBE [74] functional have been found to represent two extremes within the gradient-corrected functionals, yielding the strongest and the lowest overbinding, respectively. Consequently, all calculations in this work have been done using both functionals to somehow estimate the functional dependence of the obtained results. The absence of sizeable energy barriers towards dissociation found in previous studies of parts of the adiabatic PES [22, 24, 70–73] could be confirmed. While the PBE functional does not yield any barriers, in case of the RPBE functional a few shallow barriers of up to 0.1 eV have been identified. Still, the energetic differences between both functionals are far smaller than in case of the free molecule. This indicates an efficient error cancellation, which occurs because for these barriers only energy differences between parts of the PES matter that represent energies of very similar configurations of the oxygen molecule. Only close to the surface the oxygen-oxygen bond is significantly elongated due to a very strong hybridization with the Al(111) surface density, constituting then a situation very different from the dissociation of a free molecule. In conclusion, the sticking coefficients based on the adiabatic

PES should be quite reliable in particular since no significant differences between the PBE and the RPBE functional were found.

The sticking probability is a statistically averaged dynamic quantity. Consequently, a mere inspection of low-dimensional cuts through the adiabatic PES is not sufficient to account for dynamical steering effects, and only a large number of molecular dynamic simulations can yield a reliable sticking curve. This had not been done for this system before the course of this work. In order to calculate the sticking curve, a continuous representation of the adiabatic PES has been obtained using a neural network interpolation scheme [26, 27, 201], which has proven to reproduce the DFT energies very accurately. To incorporate the symmetry efficiently, a new method based on Fourier functions has been implemented and tested in the neural network code. This representation of the PES enabled to perform a large number of molecular dynamics simulations to obtain a statistically reliable sticking curve for the oxygen dissociation on Al(111) from first-principles. The sticking probability was found to be close to unity independent of the kinetic energy of the molecule, and independent of the exchange-correlation functional. Due to the absence of sizeable barriers in the PES, this result was somewhat expected, but remains in contrast to experiment. Consequently, dynamical steering towards non-dissociative pathways could be excluded as origin of the low sticking probability.

A possible source of error in the molecular dynamics simulations is the applied frozen surface approximation, i.e. only the degrees of freedom of the oxygen atoms have been taken into account. Due to the very similar masses of the oxygen molecule and the aluminium atoms the validity of this approximation cannot be taken for granted, and the mobility of aluminium atoms might strongly affect the molecular trajectories. The applicability of the frozen surface approximation has therefore been investigated by extensive high-dimensional *ab initio* molecular dynamics simulations, which took the mobility of the aluminium atoms explicitly into account. In all trajectories the approaching oxygen molecule had a significant influence on the substrate motion only for molecule-surface separations well below 2.5 Å, which is in turn much closer to the surface than the typical position of energy barriers towards dissociation. This suggests that the frozen surface approximation is justified in this case, eliminating another possible explanation for the experiment-theory discrepancy.

Having confirmed that the low sticking probability of thermal oxygen molecules cannot be explained by state-of-the-art adiabatic DFT, the possible role of non-adiabatic effects was explored. A simple two-state model has been developed based on the different spin states of the free molecule and the adsorbed atoms. While the free molecule has a spin-triplet ground state, the adsorbed atoms are in a singlet state and thus a spin-flip has to occur at some stage during the adsorption event, if both atoms are adsorbed. Assuming that the probability for a spin-flip from the triplet state to the singlet state is very low far away from the surface, an approaching oxygen molecule might be confined to the initial neutral spin-triplet PES for some time. If the latter PES exhibits energy barriers in this region, this might well explain the experimental low sticking probability. Unfortunately, before the present work was begun no method to calculate the diabatic triplet PES was available. The only standard technique to fix the spin of a system to a certain value has been the fixed-spin-moment approach [272]. The applicability of this method was carefully examined, but it was found that although the total spin of the system can be confined to a triplet, for small molecule-surface separations the majority of the spin-density is delocalized in the aluminium slab. The diabatic spin-triplet PES we are interested in, however, is characterized by a spin-triplet centered at the oxygen molecule and an aluminium surface in a singlet state for all molecular configurations.

With no available technique allowing for a calculation of the triplet PES, a constrained DFT method in the spirit of Dederichs *et al.* [34] has been developed, implemented, tested and applied to the oxygen dissociation on Al(111). The basic idea of this approach is to split up the system into an oxygen and an aluminium subsystem making efficient use of the localized basis set of the DMol^3 code. The occupations of each spin orientation in both subsystems can be controlled by a projection technique, that allows for a self-consistent solution of the Kohn-Sham equations under arbitrary constraints on the spin and charge states of the subsystems. This constrained DFT method has been applied to calculate the diabatic spin-triplet PES in all six molecular dimensions. This triplet PES shows sizeable energy barriers towards dissociation up to 0.9 eV for most molecular orientations. To evaluate if these barriers could account for the low sticking probability of thermal oxygen molecules, molecular dynamics simulations based on a neural network interpolation have been carried out. The obtained sticking curve shows unambiguously a significant reduction of the sticking probability. For kinetic energies higher than about 0.2 eV the qualitative agreement with experiment is excellent and independent of the chosen functional. However, for thermal molecules the sticking probability exhibits a strong functional dependence caused by dynamic steering effects together with the varying barrier heights on the triplet PES. While the RPBE functional yields barriers for all molecular orientations and consequently gives rise to a sticking probability of basically zero for thermal molecules, in case of the PBE functional a few barrier-free entrance channels exist. Slow, thermal molecules are then steered to these channels and stick on the surface in most cases. To obtain an accurate quantitative sticking probability for thermal molecules, more precise barriers would therefore be required than can be provided by present-day gradient-corrected DFT functionals. Still, the main conclusion is that sizeable energy barriers on the adiabatic PES do not exist. Only taking into account non-adiabatic effects, i.e. an initial confinement of the molecule to the neutral spin-triplet PES, yields a reduced sticking probability.

The molecular dynamics simulations on the triplet PES represent only the limit of an infinite lifetime of the molecule on this PES and can be regarded as being complementary to the adiabatic case, in which an instantaneous relaxation of the charge and spin state occurs at all nuclear positions. It is tempting to conclude that the triplet limit might be a reasonable approximation for thermal molecules, which cannot get closer than 3 to 3.5 Å to the surface due to the emerging energy barriers. At this distance the energy of other diabatic PESs is still clearly higher resulting in only a weak coupling. However, this has to be proven in future work, and a more refined model would have to include also further diabatic PESs like the singlet PES and several ionic PESs as well as the coupling of these states. This would enable to perform dynamics simultaneously on all of these PESs, which will be required to obtain a quantitative agreement with the experimental sticking curve. In principle, the constrained DFT approach also allows for the calculation of other diabatic states like the singlet or the ionic PES. While the latter is not expected to pose a general problem when large enough supercells are used, the description of the $^1\Delta_g$ singlet state in DFT-GGA is very poor, yielding a far too low singlet-triplet splitting. As an alternative model for this state spin-restricted DFT calculations have been tested. Due to an artificial charge transfer from the surface to the molecule accurate energies could unfortunately not be obtained, the energy lowering being about 0.2 eV for very large molecule-surface separations. In the adiabatic case this energy lowering induced by the charge transfer amounts to about 0.02 eV.

In summary, the accurate determination of diabatic PESs remains an important and most challenging task towards a quantitatively correct sticking curve. In the present work it has been shown, that non-adiabatic effects might well provide an explanation for the experimentally found low sticking probability of thermal oxygen molecules. However, present-day density-functional theory does not provide the accuracy to determine reliable barrier heights, which are decisive for the precise shape of the sticking curve, in particular at low kinetic energies. The situation might be improved by local correction schemes [276, 277], but these so far have not been applied to diabatic states and suitable constraints might be necessary. Only when the problems concerning the sticking probability have been fully solved, a reliable assessment of further questions like the adsorption mechanism will become possible. Still, in this case new difficulties emerge in that the investigation of the adsorption mechanism requires to follow the trajectory also in the region of the PES, where substrate mobility and dissipation effects play an important role.

Apart from these theoretical challenges also further experiments could help to shed light on the role of non-adiabatic effects in the oxygen dissociation on metal surfaces. To investigate the role of the singlet state of the oxygen molecule, the energy-resolved sticking curve of a beam of oxygen molecules in the $^1\Delta_g$ singlet state would be very helpful. According to the qualitative shape of the singlet PES calculated so far, a very high sticking probability independent of the kinetic energy would be expected since no energy barriers seem to be present on this PES. Additionally, energy resolved sticking curves on further *sp* metals like e.g. magnesium would be important to explore trends in the periodic table. Similar to the Al(111) surface also for magnesium chemiluminescence and exoelectron emission have been observed in the presence of oxygen [89], which are commonly accepted as indication for non-adiabatic effects. Unfortunately, these elements are very hard to handle because of their comparably low melting points and high affinity to impurities.

Experimental indications for non-adiabatic processes in the oxygen-dissociation on many other metal surfaces like cesium [88], lithium [90] and silver [91] exist, and also other diatomic molecules, e.g. Cl_2 [20] and NO [285] show non-adiabatic effects opening up a wide and to a large extent unexplored field for further experimental and theoretical studies.

The outcome of any serious research
can only be to make two questions grow
where only one grew before.

Thorstein Veblen

Part III

Appendix

Appendix A

Benchmarks

A.1 Introduction

The aim of this benchmark was to find an appropriate DFT code for the calculation of the six-dimensional potential-energy surface for the dissociation of oxygen molecules on the Al(111) surface. Results obtained for bulk aluminium as well as for clean and oxygen-covered Al(111) slabs using different DFT codes were therefore compared. The ideal code has to provide a high accuracy, since an accurate determination of barrier heights is very important for the dynamics of the adsorption process. Additionally, it should be very fast, because thousands of energy points have to be calculated to map the potential-energy surface reliably.

In case of bulk aluminium the physical quantities of interest were the cohesive energy E_{coh} and the equilibrium lattice constant a_0. The experimental values are $E_{\mathrm{coh}} = 3.39$ eV/atom [121] and $a_0 = 4.0496$ Å [225]. These quantities have been determined at two different levels of accuracy. The measure for the accuracy of a calculation was the difference between the cohesive energy of the actual calculation and the best cohesive energy that can be obtained ("*converged*") with a very large basis set for each DFT code. A "*coarse*" calculation should have an error in the cohesive energy less than or equal to 100 meV with respect to this reference value, an "*accurate*" calculation should have an error of 20 meV or less. For the Al(111) surface the quantity of interest was the oxygen binding energy of a full monolayer of oxygen atoms in a (1×1) cell, and of a quarter monolayer in a (2×2) cell.

The tested codes were the all-electron codes DMol^3 [133] and WIEN2k [136] (employing the LAPW and the APW+lo methods), as well as the pseudopotential code fhi98md [95][1]. All calculations have been carried out using the PBE functional [114] for exchange and correlation.

On the computational side the memory requirements and the CPU time were of interest. Unless stated otherwise, all calculations have been carried out on a Compaq

[1]The LAPW calculations have been performed by Mira Todorova, the APW+lo calculations by Jutta Rogal, and the fhi98md calculations by Cathy Stampfl.

ES45 workstation (4× ev68 1000 MHz CPUs, 4GB RAM per CPU). The measurement of the CPU time has been done on a fully loaded machine, i.e. 4 running calculations, one of them for the benchmark, to simulate a realistic working environment.

The tables in the following sections contain the parameters used for the different codes, as well as the results. In the DMol^3 calculations the parameters *rmaxp* and *s* control the radial part of the integration mesh, and *iomax* and *iomin* control the angular part. The accuracy parameter *thres* determines the actually used integration quality and r_{cut} is the real space cutoff for the basis functions. In the WIEN2k calculations $E^{\mathrm{pw}}_{\mathrm{cut}}$ is the applied plane wave cutoff and $G^2_{\max}$ is the cutoff for the potential expansion, both refer to the interstitial region. $LM_{\max}$ is the maximum angular momentum for the potential expansion and $l_{\max}$ is the maximum angular momentum for the wave-function expansion inside the muffin tin spheres. $l_{\mathrm{ns}_{\max}}$ is the maximum angular momentum for off-diagonal matrix elements in the Hamiltonian. R_{MT} is the muffin tin radius separating the muffin tin region from the interstitial. The value ΔE_{coh} indicates the derivation of the calculated cohesive energies from the reference value obtained with a highly converged parameter set for each code. The Al-pseudopotential used in the fhi98md calculations has been tested previously [286].

A.2 Bulk Aluminium

To determine the equilibrium lattice constant using the Murnaghan equation (cf. Section 9.2) calculations for 9 different lattice constants from 0.96 a_0 to 1.04 a_0 in steps of 0.01 a_0 have been carried out for the coarse and accurate parameter set. In order to calculate the cohesive energy, the total energy of an aluminium atom E_{atom} is required. As the atomic calculations in DMol^3 are very fast (a few seconds at most) and since in DMol^3 the total energies of atoms converge slower with increasing basis function cutoff than the energies of bulk calculations, the atomic reference energies have been calculated with a highly converged parameter set (cf. Table A.1) using occupations according to Hund's rule. The resulting atomic energy has been used as reference for all calculations. The bottleneck for the determination of the cohesive energies with DMol^3 is the slower bulk calculation. For the other codes the atomic reference requires expensive calculations, because the atom has to be calculated in an asymmetric large unit cell employing periodic boundary conditions. In all other codes the atomic reference calculations have therefore been carried out with the same parameter set as in the bulk calculations. The employed unit cell has dimensions of 13×14×15 bohr^3. The parameters used for the atomic and bulk calculations are listed for DMol^3 in Table A.1, for the LAPW method in Table A.2, for the APW+lo method in Table A.3 and for the fhi98md code in Table A.4. The equilibrium lattice constants, cohesive energies and required computer resources are summarized in Table A.5.

The obtained lattice constants and cohesive energies are very similar for all codes. Only in case of the fhi98md code the lattice constant is slightly larger than for the all-electron methods. The fastest code for the bulk calculations is the fhi98md code, but

	free atom	bulk aluminium	
		coarse	accurate
basis set	*dnp*	*dnd*	*dnp*
r_{cut} (bohr)	17	9	10
k-points	none	4×4×4	10×10×10
iomax	7	5	7
iomin	1	1	1
thres	0.000001	0.0001	0.000001
rmaxp	17	9	10
s	2.000	1.000	1.500
total CPU time (s)	10	56	750
memory (MB)	26	56	117
iterations	12	9	9

Table A.1: Parameters and results for the free aluminium atom and bulk aluminium using the DMol^3 code.

	atom in box		bulk aluminium	
	coarse	accurate	coarse	accurate
R_{MT} (bohr)	1.7	1.7	1.7	1.7
G^2_{max} (Ry)	196	196	196	196
LM_{max}	6	6	6	6
l_{max}	12	12	12	12
$l_{\mathrm{ns_{max}}}$	6	6	6	6
$E^{\mathrm{pw}}_{\mathrm{cut}}$ (Ry)	16	20	16	20
k-points	1×1×1	1×1×1	6×6×6	10×10×10
total CPU time (s)	2324	24868	48	83
memory (MB)	152	243	39	40
iterations	14	52	11	11

Table A.2: Parameters and results for the aluminium atom in a box and bulk aluminium using the WIEN2k code employing the LAPW method.

also the WIEN2k code is significantly faster than DMol^3. This is, on the other hand, compensated by the very fast atomic calculations, which are very time-consuming with WIEN2k. The CPU times for the atomic and bulk calculations are compared in Fig. A.1, and the obtained cohesive energies and lattice constants are shown in Fig. A.2.

	atom in box		bulk aluminium	
	coarse	accurate	coarse	accurate
R_{MT} (bohr)	1.7	1.7	1.7	1.7
G^2_{max} (Ry)	196	196	196	196
LM_{max}	6	6	6	6
l_{max}	12	12	12	12
$l_{\mathrm{ns_{max}}}$	6	6	6	6
$E^{\mathrm{pw}}_{\mathrm{cut}}$ (Ry)	10	15	10	15
k-points	1×1×1	1×1×1	6×6×6	10×10×10
total CPU time (s)	378	2687	34	47
memory (MB)	77	137	39	39
iterations	11	11	7	7

Table A.3: Parameters and results for the aluminium atom in a box and bulk aluminium using the WIEN2k code employing the APW+lo method.

	atom in box		bulk aluminium	
	coarse	accurate	coarse	accurate
$E^{\mathrm{pw}}_{\mathrm{cut}}$ (Ry)	10	20	10	20
k-points	1×1×1	1×1×1	4×4×4	6×6×6
total CPU time (s)	(14)	(36)	(5)	(25)
memory (MB)	14	26	5	7
iterations	7	10	10	21

Table A.4: Parameters and results for the aluminium atom in a box and bulk aluminium using the fhi98md code. The bracketed CPU times have been scaled since the numbers have been obtained on another machine which is roughly a factor of 1.5 slower than the ES45 used for the other codes.

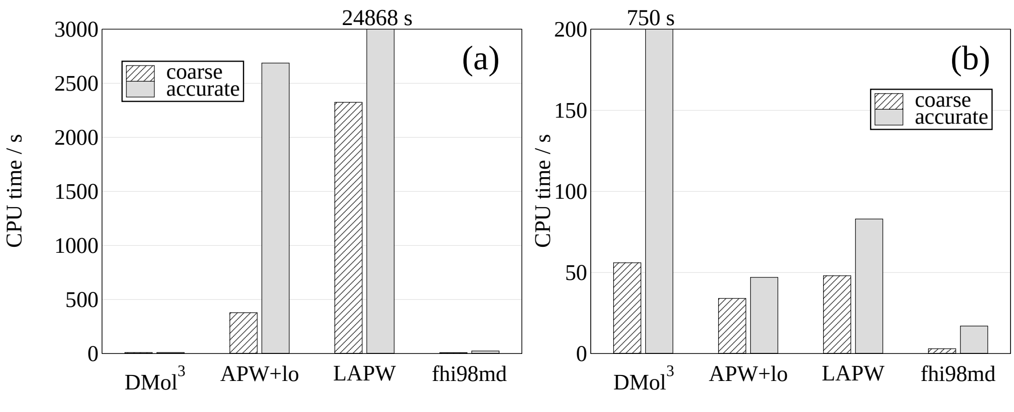

Figure A.1: Total CPU time requirements to reach self-consistency for the aluminium atoms (a) and for the bulk calculations (b).

	DMol^3		WIEN2k LAPW	
	coarse	accurate	coarse	accurate
a_0 (Å)	4.037	4.030	4.021	4.032
a_0 (a_{exp})	0.998	0.995	0.993	0.996
E_{coh} (eV)	-3.477	-3.399	-3.374	-3.377
ΔE_{coh} (eV)	0.063	-0.015	0.021	0.018
total CPU time (s)	56	750	48	83
memory (MB)	56	117	39	40
iterations	9	9	11	11
	WIEN2k APW+lo		fhi98md	
	coarse	accurate	coarse	accurate
a_0 (Å)	4.063	4.034	4.059	4.054
a_0 (a_{exp})	1.003	0.996	1.002	1.001
E_{coh} (eV)	-3.501	-3.390	-3.331	-3.387
ΔE_{coh} (eV)	0.099	0.012	0.074	0.018
total CPU time (s)	34	47	5	25
memory (MB)	39	39	5	7
iterations	7	7	10	21

Table A.5: Equilibrium lattice constants, cohesive energies and hardware requirements obtained with the different DFT codes.

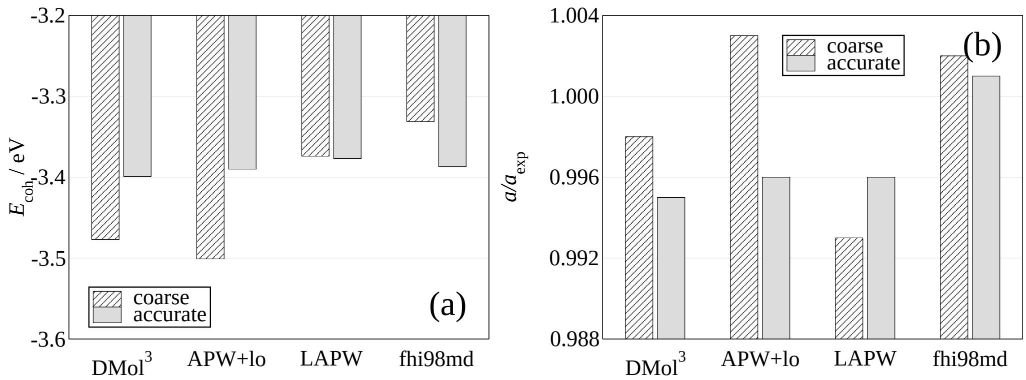

Figure A.2: Cohesive energies (a) and equilibrium lattice constants (b) obtained for bulk aluminium.

A.3 The Clean and the Oxygen-Covered Al(111) Surface

The oxygen binding energy, which has been used as a measure for the accuracy of the slab calculations, has been obtained using the equation

$$E_{\mathrm{bind}} = \frac{1}{N_{\mathrm{O}}} \left(E_{\mathrm{OAl}} - N_{\mathrm{O}} \cdot E_{\mathrm{O}} - E_{\mathrm{Al}} \right) \quad . \tag{A.1}$$

N_{O} is the number of oxygen atoms adsorbed per unit cell, E_{OAl} is the total energy of the adsorbate system, E_{O} is the energy of an isolated oxygen atom and E_{Al} is the energy of the clean aluminium slab. The slab consists of 7 aluminium layers and the atoms are fixed at their bulk positions. The oxygen atom is located 0.709 Å above the fcc site. To determine the oxygen binding energy, the energy of the free oxygen atom has to be calculated. This has been done in the same way as described for the aluminium atom in the preceding section. The parameters and results for the calculations on the oxygen atom are listed in Tables A.6 for DMol^3, Table A.7 for the LAPW method, Table A.8 for the APW+lo method and in Table A.9 for the fhi98md code.

basis set	*all*
r_{cut} (bohr)	20
k-points	—
iomax	7
iomin	1
thres	0.000001
rmaxp	20
s	2.000
total CPU time (s)	7
memory (MB)	27
iterations	11

Table A.6: Parameters and results for the calculation of the oxygen atom using DMol^3.

The parameters and results for the clean and oxygen-covered (1×1) slabs are listed in Tables A.10, A.11, A.12 and A.13 for the different codes. The corresponding values for the clean and oxygen-covered (2×2) slabs are given in Tables A.14, A.15, A.16 and A.17. The required CPU times for the oxygen-covered (1×1) and (2×2) slabs are compared in Fig. A.3, the oxygen binding energies are shown in Fig. A.4. For the (1×1) slabs DMol^3 is faster than all other benchmarked codes. For the (2×2) slabs the difference in performance between DMol^3 and LAPW in case of the accurate calculations is about a factor of 35, and a factor of 28 with respect to the APW+lo method. The obtained binding energies are very similar. The highest binding energy is found for the fhi98md code for the (1×1) and for the (2×2) slabs. The lowest binding energy results from the APW+lo method in both cases, but the LAPW values are

	coarse		accurate	
	for (1×1)	for (2×2)	for (1×1)	for (2×2)
$R_{\mathrm{MT}}^{\mathrm{O}}$	1.3	1.3	1.3	1.3
$E_{\mathrm{cut}}^{\mathrm{pw}}$ (Ry)	19	20	25	25
k-points	1×1×1	1×1×1	1×1×1	1×1×1
G_{max}^2 (Ry)	196	196	196	196
l_{max}	12	12	12	12
$l_{\mathrm{ns_{max}}}$	6	6	6	6
total CPU time (s)	5990	6885	18947	18974
memory (MB)	215	242	401	401
iterations	15	14	14	14

Table A.7: Parameters and results for the calculation of the oxygen atom employing the LAPW method.

	coarse	accurate
$R_{\mathrm{MT}}^{\mathrm{O}}$	1.3	1.3
$E_{\mathrm{cut}}^{\mathrm{pw}}$ (Ry)	17	20
k-points	1×1×1	1×1×1
G_{max}^2 (Ry)	196	196
l_{max}	12	12
$l_{\mathrm{ns_{max}}}$	6	6
total CPU time (s)	3620	5820
memory (MB)	172	242
iterations	15	12

Table A.8: Parameters and results for the calculation of the oxygen atom employing the APW+lo method.

	coarse	accurate
$E_{\mathrm{cut}}^{\mathrm{pw}}$ (Ry)	48	62
k-points	1×1×1	1×1×1
total CPU time (s)	157	235
memory (MB)	85.4	128
iterations	4	4

Table A.9: Parameters and results for the oxygen atom using the fhi98md code.

very similar. The binding energies obtained with DMol^3 are about 1 % higher than the WIEN2k results.

	Clean Slab		O-covered Slab	
	coarse	accurate	coarse	accurate
basis set oxygen	—	—	*all*	*all*
basis set aluminium	*dnd*	*all*	*dnd*	*all*
r_{cut} (bohr)	8	9	8	9
k-points	7×7×1	7×7×1	7×7×1	7×7×1
iomax	5	5	5	5
iomin	1	1	1	1
thres	0.0001	0.0001	0.0001	0.0001
rmaxp	8	9	8	9
s	1.000	1.000	1.000	1.000
E_{bind} (eV)	—	—	-7.747	-7.829
ΔE_{bind} (eV)	—	—	0.086	0.004
total CPU time (s)	342	1384	660	2529
memory (MB)	53	106	62	118
iterations	17	17	19	21

Table A.10: Parameters and results for the (1×1) slab calculations for DMol^3.

	Clean Slab		O-covered Slab	
	coarse	accurate	coarse	accurate
$R_{\mathrm{MT}}^{\mathrm{Al}}$	1.7	1.7	1.7	1.7
$R_{\mathrm{MT}}^{\mathrm{O}}$	—	—	1.4	1.3
$E_{\mathrm{cut}}^{\mathrm{pw}}$ (Ry)	19	25	19	25
k-point mesh	8×8×1	12×12×1	8×8×1	12×12×1
G_{max}^2 (Ry)	196	196	196	196
l_{max}	12	12	12	12
$l_{\mathrm{ns_{max}}}$	6	6	6	6
E_{bind} (eV)	—	—	-7.827	-7.776
ΔE_{bind} (eV)	—	—	0.056	0.005
total CPU time (s)	8118	44978	8509	53737
memory (MB)	182	238	182	239
iterations	23	22	26	24

Table A.11: Parameters and results for the (1×1) slab calculations employing the LAPW method.

	Clean Slab		O-covered Slab	
	coarse	accurate	coarse	accurate
$R_{\mathrm{MT}}^{\mathrm{Al}}$	1.7	1.7	1.7	1.7
$R_{\mathrm{MT}}^{\mathrm{O}}$	—	—	1.3	1.3
$E_{\mathrm{cut}}^{\mathrm{pw}}$ (Ry)	17	20	17	20
k-point mesh	5×5×1	8×8×1	5×5×1	8×8×1
G_{max}^2 (Ry)	196	196	196	196
l_{max}	12	12	12	12
$l_{\mathrm{ns_{max}}}$	6	6	6	6
E_{bind} (eV)	—	—	-7.798	-7.754
ΔE_{bind} (eV)	—	—	0.043	0.001
total CPU time (s)	2634	8659	3142	9695
memory (MB)	182	182	182	182
iterations	22	21	24	22

Table A.12: Parameters and results for the (1×1) slab calculations employing the APW+lo method.

	Clean Slab		O-covered Slab	
	coarse	accurate	coarse	accurate
$E_{\mathrm{cut}}^{\mathrm{pw}}$ (Ry)	48	62	48	62
k-points	6×6×1	6×6×1	6×6×1	6×6×1
E_{bind} (eV)	—	—	-7.858	-7.921
ΔE_{bind} (eV)	—	—	0.080	0.017
total CPU time (s)	1807	3632	2702	5666
memory (MB)	105	159	137	203
iterations	38	39	41	44

Table A.13: Parameters and results for the (1×1) slab calculations using the fhi98md code.

	Clean Slab		O-covered Slab	
	coarse	accurate	coarse	accurate
basis set oxygen	—	—	*all*	*all*
basis set aluminium	*dnd*	*all*	*dnd*	*all*
r_{cut} (bohr)	8	9	8	9
k-points	6×6×1	8×8×1	6×6×1	8×8×1
iomax	5	7	5	7
iomin	1	1	1	1
thres	0.0001	0.000001	0.0001	0.000001
rmaxp	8	9	8	9
s	1.000	1.500	1.000	1.500
E_{bind} (eV)	—	—	-7.192	-7.232
ΔE_{bind} (eV)	—	—	0.041	0.001
total CPU time (s)	1682	18573	2236	21275
memory (MB)	91	269	86	238
iterations	17	19	21	22

Table A.14: Parameters and results for the (2×2) slab calculations using DMol^3.

	Clean Slab		O-covered Slab	
	coarse	accurate	coarse	accurate
$R_{\mathrm{MT}}^{\mathrm{Al}}$	1.7	1.7	1.7	1.7
$R_{\mathrm{MT}}^{\mathrm{O}}$	—	—	1.3	1.3
$E_{\mathrm{cut}}^{\mathrm{pw}}$ (Ry)	20	25	20	25
k-point mesh	4×4×1	10×10×1	4×4×1	10×10×1
G_{max}^2 (Ry)	196	196	196	196
l_{max}	12	12	12	12
$l_{\mathrm{ns_{max}}}$	6	6	6	6
E_{bind} (eV)	—	—	-7.158	-7.188
ΔE_{bind} (eV)	—	—	0.007	0.023
total CPU time (s)	588404	3286368	394250	2506789
memory (MB)	882	1512	883	1513
iterations	46	38	37	28
Using Iterative Diagonalization:				
E_{bind} (eV)	—	—	-7.099	-7.188
ΔE_{bind} (eV)	—	—	0.066	0.023
total CPU time (s)	164764	908984	88982	758087
memory (MB)	882	1512	883	1513
iterations	47	48	25	34

Table A.15: Parameters and results for the (2×2) slab calculations employing the LAPW method.

	Clean Slab		O-covered Slab	
	coarse	accurate	coarse	accurate
$R_{\mathrm{MT}}^{\mathrm{Al}}$	1.7	1.7	1.7	1.7
$R_{\mathrm{MT}}^{\mathrm{O}}$	—	—	1.3	1.3
$E_{\mathrm{cut}}^{\mathrm{pw}}$ (Ry)	17	20	17	20
k-point mesh	3×3×1	11×11×1	3×3×1	11×11×1
G_{max}^2 (Ry)	196	196	196	196
l_{max}	12	12	12	12
$l_{\mathrm{ns_{max}}}$	6	6	6	6
E_{tot} (eV)	-185001.491	-185001.644	-189100.060	-189100.996
E_{bind} (eV)	—	—	-7.127	-7.174
ΔE_{bind} (eV)	—	—	0.027	0.020
ϕ (eV)	-3.901	-4.046	-3.837	-3.904
total CPU time (s)	124264	807465	115648	1025995
memory (MB)	636	896	639	898
iterations	31	21	29	26
Using Iterative Diagonalisation:				
E_{bind} (eV)	—	—	-7.125	-7.171
ΔE_{bind} (eV)	—	—	0.029	0.017
total CPU time (s)	100949	763498	82106	596160
memory (MB)	699	987	701	988
iterations	66	61	51	45

Table A.16: Parameters and results for the (2×2) slab calculations employing the APW+lo method.

	Clean Slab		O-covered Slab	
	coarse	accurate	coarse	accurate
$E_{\mathrm{cut}}^{\mathrm{pw}}$ (Ry)	48	62	48	62
k-points	4×4×1	6×6×1	4×4×1	6×6×1
E_{bind} (eV)	—	—	-7.297	-7.318
ΔE_{bind} (eV)	—	—	0.001	0.020
total CPU time (s)	16969	78726	42331	172312
memory (MB)	656	1498	599	1814
iterations	34	54	136	136

Table A.17: Parameters and results for the (2×2) slab calculations using the fhi98md code.

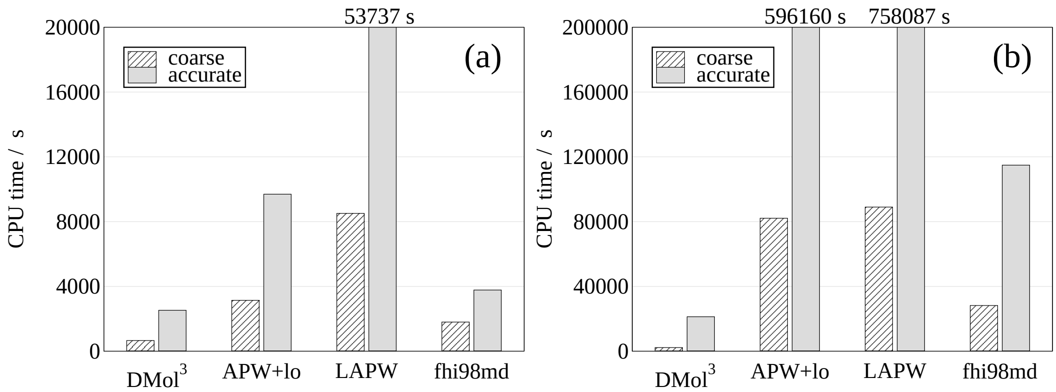

Figure A.3: Total CPU time requirements to reach self-consistency for the oxygen-covered (1×1) (a) and (2×2) (b) slabs.

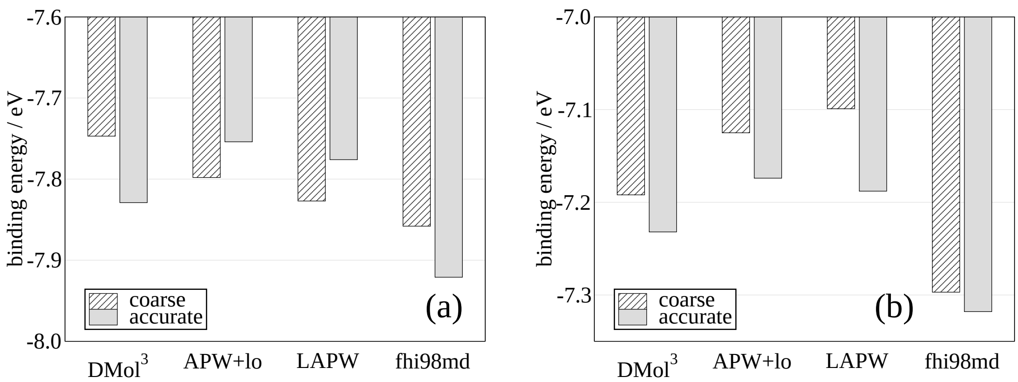

Figure A.4: Oxygen binding energies in the (1×1) (a) and (2×2) (b) slabs.

A.4 Conclusion

Even in an extensive benchmark project it is impossible to test all parameters that might have an influence on the accuracy and on the performance. One example is the mixing factor for the charge density, which can significantly change the number of iterations necessary to reach self-consistency. However, it will not change the final results. In all calculations a reasonable constant value (usually 0.1) has been chosen. Further parameters, which have not been tested, are the box dimensions for the atomic calculations using WIEN2k and fhi98md. Additionally, the muffin tin radius in case of WIEN2k, which can have a strong influence on the performance, as well as the pseudopotentials in case of fhi98md remained unchecked. In case of DMol^3 the 5 parameters defining the integration mesh have not been tested individually, but have been increased simultaneously in a consistent way. Additionally, only built-in basis sets have been used. As the calculations using the fhi98md code have been done on a different machine, an estimated scaling factor of 1.5 has been applied to convert the CPU times.

Several other physical quantities have also been tested to compare the different codes. For the bulk calculations the density of states, the band structure and the bulk modulus have been determined. For the slab calculations the density of states, the work function and in case of the (2×2) slabs with a quarter monolayer of adsorbed oxygen atoms also the forces on the oxygen atom and the top layer aluminium atoms have been checked. The overall agreement between all tested codes is excellent with slight deviations for the pseudopotential code fhi98md. While the CPU time requirements for the bulk calculations are comparably high for DMol^3, for larger systems like the (1×1) and in particular the (2×2) slabs the DMol^3 code is much faster than the WIEN2k code using the LAPW and APW+lo methods, but also clearly faster than the fhi98md code.

All in all there are no significant differences in the obtained results. However, the fastest code for large systems is clearly DMol^3. As the calculation of the six-dimensional potential-energy surface is done using larger (3×3) supercells, the difference can be expected to be even larger. In conclusion, for all calculations in this project the DMol^3 density-functional code is used.

Appendix B

Convergence Tests

B.1 Introduction

One of the main sources of error in a DFT calculation is the approximate exchange-correlation functional. However, the numerical accuracy of density-functional calculations depends also on many parameters that are specific for the actually chosen implementation of density-functional theory. One of the most important quantities in this respect is the basis set. In $DMol^3$ the basis functions are atomic orbitals and the available basis sets are formed by groups of these atomic orbitals as described in Chapter 6. Consequently, in contrast to DFT codes using for example plane waves as basis functions, in $DMol^3$ the basis set cannot be improved systematically, and the convergence of the physical properties has to be tested using many different basis sets. Two quantities are related to the basis set: the basis function cutoff r_{cut}, which determines the spatial extension of the basis functions, and the integration grid within this cutoff radius. The integration grid is specified by 5 parameters (cf. Chapter 6). The parameters *iomin* und *iomax* define the lower and upper bound for the angular point distributions on the spherical integration shells. The actually used scheme is determined internally according to a numerical precision parameter *thres*. The spatial extension of the integration grid is determined by *rmaxp*, which is generally set equal to the basis function cutoff r_{cut} in this work. The radial density of shells can be scaled by the factor s according to Eq. (6.8). In addition, the Brillouin zone has to be represented accurately by a set of discrete k-points. Besides these implementation-dependent parameters also the slab geometries have to be chosen in a suitable way for the problem of interest. This mainly refers to structural parameters like the slab thickness, the vacuum size between the slabs and also the lateral dimension of the supercell.

Many tests have been performed at all stages of this project to ensure that the obtained results are converged with respect to these parameters. In the following sections some examples of the parameter determination will be given for bulk aluminium, for oxygen-covered (1×1) aluminium slabs and for the (3×3) supercell used in the calculation of the potential-energy surfaces for the oxygen dissociation on Al(111). All tests have been carried out using the PBE functional only, because the convergence with respect to the k-points and to the basis set does not depend much on the actually chosen functional.

B.2 Bulk Aluminium

As already described for the benchmark calculations in Appendix A, the cohesive energy of aluminium has been used as a measure for the precision of the bulk calculations. In Fig. B.1 the convergence of the cohesive energy obtained from Eq. (9.6) is shown as a function of the k-point-mesh for basis function cutoffs from 8 to 12 bohr. The largest basis set available for aluminium (*dnp*) has been used in combination with a dense integration grid (*iomin*=1, *iomax*=7, *thres*=0.000001, *rmaxp*=r_{cut}, *s*=1.5). The calculations have employed the experimental lattice constant of 4.041 Å [225] and the primitive unit cell containing just one aluminium atom instead of the conventional cubic cell consisting of 4 atoms. The cohesive energy obtained for the highest cutoff and the largest number of k-points (17×17×17 mesh, 165 k-points in the irreducible wedge of the Brillouin zone) is -3.413 eV per atom (experiment: -3.36 eV [225]). According to Fig. B.1 a basis function cutoff of 9 bohr and a k-point mesh of 12×12×12 k-points (72 points in the irreducible wedge) are sufficient to reproduce the cohesive energy with an error of less than 30 meV. For this cutoff a less dense integration grid with the parameters *iomin*=1, *iomax*=5, *thres*=0.0001, *rmaxp*=r_{cut} and *s*=1.0, which is the default grid in DMol^3, yields only a small uncertainty of about 10 meV. Finally, the basis set has been tested with this set of parameters. In DMol^3 four built-in aluminium basis sets are available. The *minimal* and *dn* basis sets are not sufficiently accurate due to the absence of polarization functions. However, the *dnd* basis yields a cohesive energy of -3.422 eV, which is very close to the *dnp* value of -3.413 eV. Therefore, the *dnd* basis has been used for all bulk calculations.

B.3 Al(1×1) Slabs

To determine the required basis function cutoff, the k-point mesh, the basis set and the integration grid for calculations on oxygen-covered (1×1) slabs, three different (1×1) slabs consisting of 7 aluminium layers and a vacuum of 30 Å have been constructed. In these slabs a full monolayer of oxygen atoms is placed 0.7 Å above the fcc site, 0.7 Å above the hcp site and 1.8 Å above the top site, respectively, which corresponds to the approximate equilibrium distances at these adsorption sites. In order to determine the accuracy of the calculations, the oxygen binding energy at these three adsorption sites as defined by Eq. (9.9) has been monitored as a function of the calculational parameters. Additionally also the convergence of the binding energy difference between the hcp and the fcc site as well as between the top and the fcc site

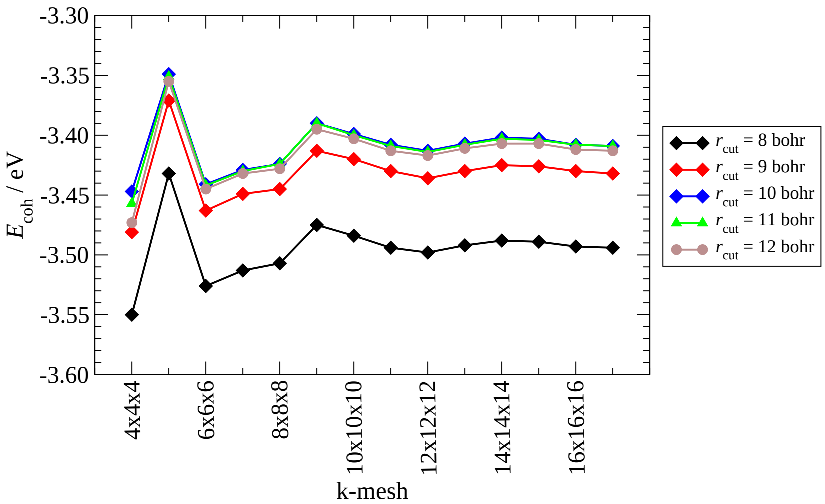

Figure B.1: Convergence of the cohesive energy E_{coh} of bulk aluminium for several basis function cutoffs as a function of the k-point mesh calculated with the PBE funtional and a *dnp* basis set employing the experimental lattice constant.

has been checked.

To find a suitable basis set, calculations employing different basis sets, a basis function cutoff of 10 bohr, a k-point mesh of 12×12×1 k-points (19 k-points in the irreducible wedge of the unit cell) and the default integration mesh (*iomin*=1, iomax=5, *thres*=0.0001, *rmaxp*=r_{cut}, *s*=1.0) have been carried out. The results are shown in Fig. B.2. To obtain reliable oxygen binding energies a *dnd* basis is sufficient to describe the aluminium atoms. This basis set has also been used for the determination of the lattice constant and therefore does not introduce any strain in the slab (the larger *dnp* basis set yields basically the same lattice constant). For oxygen the largest available *all* basis will be used, which yields slightly improved values compared to the *dnd* basis for this element. Due to the small number of oxygen atoms in the system using the largest oxygen basis set does not increase the computational demand significantly. With this combination of basis sets the absolute oxygen binding energies have an uncertainty of about 80 meV (1 % of the binding energy) with respect to the *all* basis set, and the binding energy differences for different sites are converged to about 20 meV.

To determine the required basis function cutoff the same parameters as for the basis set tests have been employed. An *all* basis has been used for oxygen and aluminium. The obtained binding energies and binding energy differences are shown in Fig. B.3 for basis function cutoffs from 7 to 12 bohr. For a cutoff of 9 bohr the binding energy differences are converged to about 20 meV and the absolute binding energies to within 40 meV. Therefore, this cutoff is used in all calculations.

The convergence of the binding energies and binding energy differences as a function of the k-point mesh is shown in Fig. B.4. The same parameters as for the basis set tests

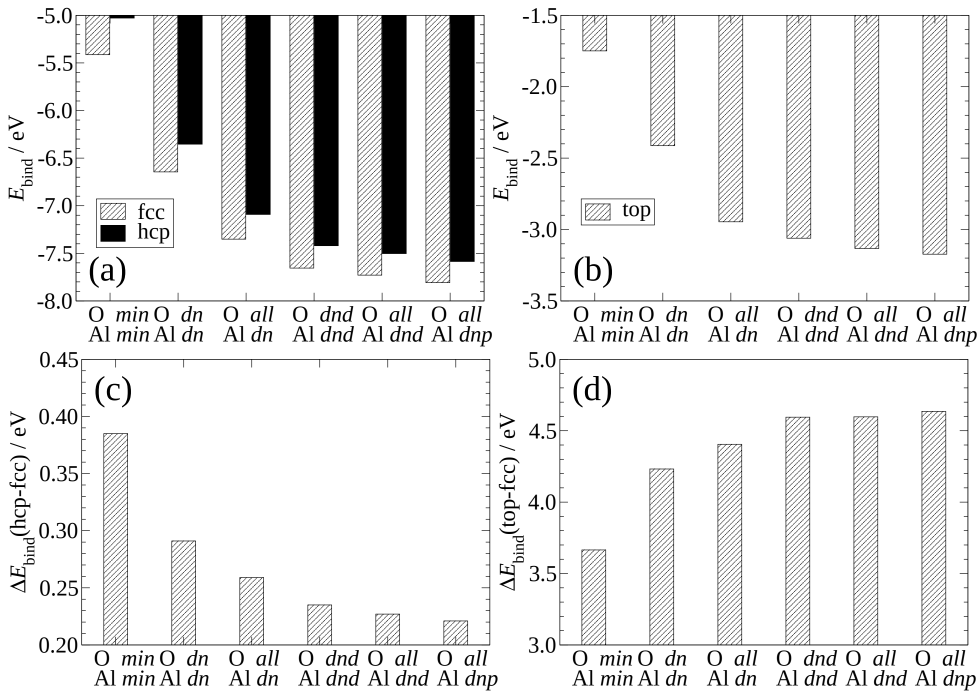

Figure B.2: Determination of the basis set required to describe a monolayer of oxygen atoms in a (1×1) supercell. In (a) the binding energies for oxygen atoms adsorbed at the fcc and the hcp sites are shown for different basis sets. In (b) the binding energy above a top site is plotted. In (c) the difference between the oxygen binding energy at the fcc site and the hcp site is shown, and in (d) the binding energy difference between the top site and the fcc site is given.

have been employed, and an *all* basis has been chosen for oxygen and aluminium. For a mesh of 12×12×1 k-points the absolute binding energies are converged to within 20 meV and binding energy differences to about 10 meV with respect to a much denser mesh. Additionally, a 12×12×1 mesh has the advantage that it permits the calculation of larger supercells with a commensurable k-points distribution, i.e. a 6×6×1 mesh for a (2×2) slab, a 4×4×1 mesh for a (3×3), and a 3×3×1 mesh for a (4×4) slab yield directly comparable energies due to equivalent k-point positions covering all cell sizes of interest in this thesis.

The noise of the obtained binding energies due to the numerical evaluation of the matrix elements has been estimated by using several integration meshes of different point densities. The list of employed meshes is given in Table B.1 and the resulting binding energies and binding energy differences are shown in Fig. B.5. For these calculations a k-points mesh of 12×12×1 points, a cutoff of 9 bohr as well as an *all* basis for oxygen and a *dnd* basis for aluminium have been chosen as determined above, because it is important to make sure that the integration grid is appropriate for the actually employed cutoff. The results show that for a cutoff of 9 bohr basically all tested integration meshes yield errors in the oxygen binding energies and binding

Mesh	*iomin*	*iomax*	*thres*	*rmaxp*	*s*
M1	1	4	0.0001	9	1.0
M2	1	5	0.0001	9	1.0
M3	1	6	0.00001	9	1.5
M4	1	7	0.000001	9	1.5
M5	1	8	0.000001	9	2.0

Table B.1: Parameters of the integration meshes tested for a full monolayer of oxygen atoms adsorbed in a (1×1) slab.

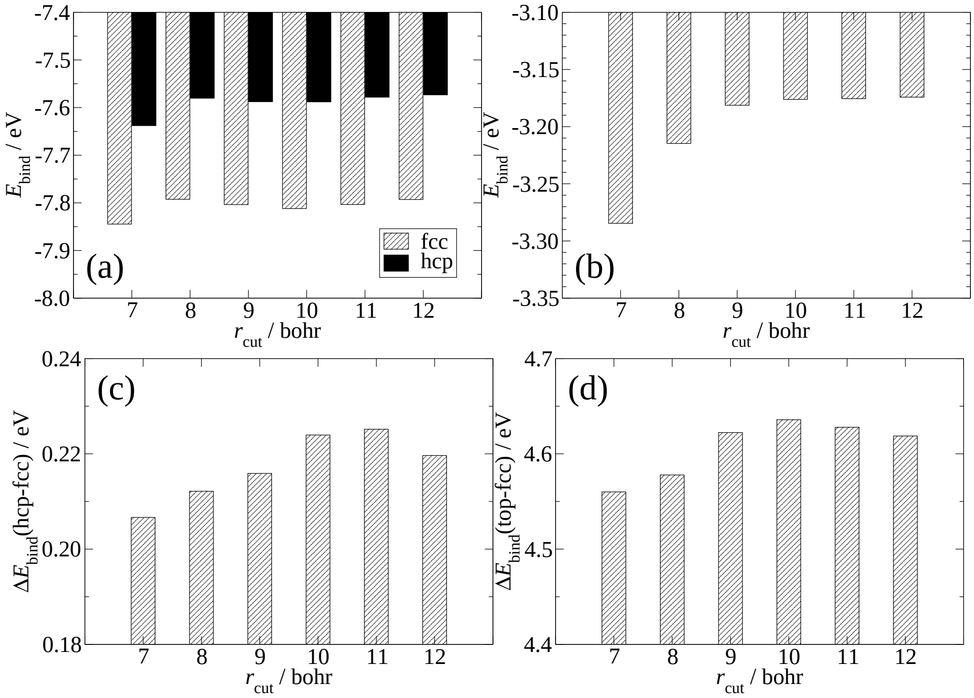

Figure B.3: Determination of the basis function cutoff required to describe a monolayer of oxygen atoms adsorbed in a (1×1) supercell. In (a) the binding energies for oxygen atoms adsorbed at the fcc and the hcp sites are shown as a function of the basis function cutoff. In (b) the binding energy above the top site is plotted. In (c) the difference between the oxygen binding energy at the fcc and the hcp site is shown, and in (d) the binding energy difference between the top site and the fcc site is given.

energy differences of well below 10 meV. Therefore mesh M2 has been chosen, which corresponds to the default mesh of $DMol^3$.

For all tests carried out so far a reasonable slab geometry consisting of 7 aluminium layers separated by a large vacuum of 30 Å has been employed. However, also these structural parameters have to be tested to avoid interactions between the oxygen atoms through the slab or through the vacuum. In Fig. B.6 the oxygen binding energy at an fcc site is shown as a function of the number of aluminium layers in

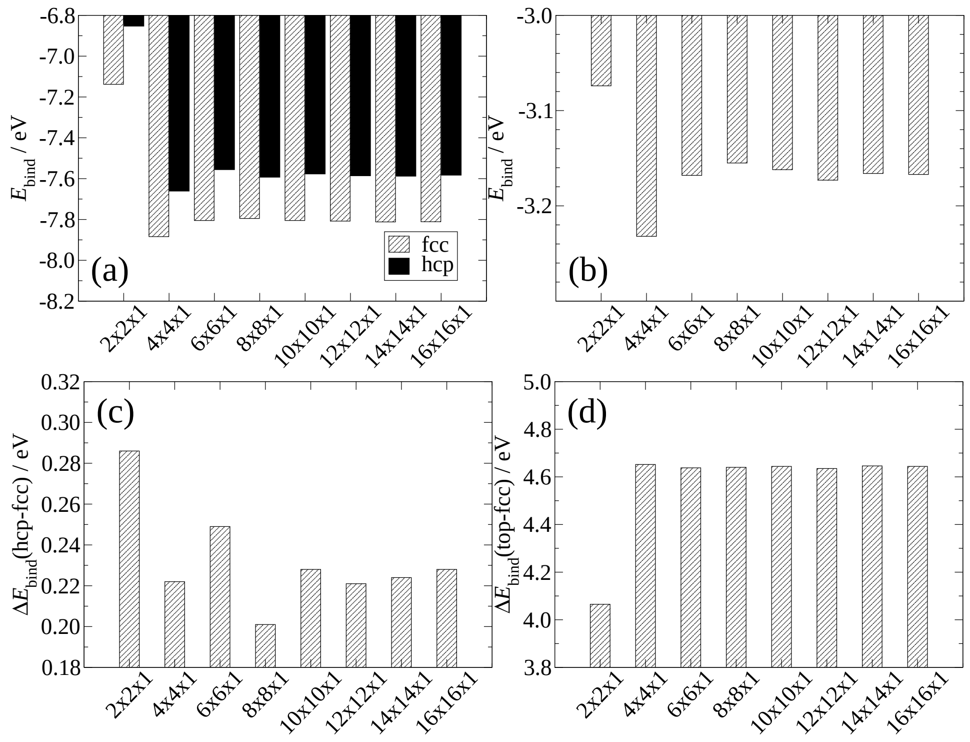

Figure B.4: Determination of the k-point mesh required to describe a monolayer of oxygen atoms adsorbed in a (1×1) supercell. In (a) the binding energies for oxygen atoms adsorbed at the fcc and the hcp sites are shown as a function of the mesh size. In (b) the binding energy above a top site is plotted. In (c) the difference between the oxygen binding energy at a fcc site and a hcp site is shown, and in (d) the binding energy difference between the top site and the fcc site is given.

the slab. A slab consisting of 7 aluminium layers is thick enough to obtain a binding energy converged to within 20 meV. In Fig. B.7 the total energy for a slab with oxygen adsorbed at the fcc sites is given as a function of the vacuum thickness for a 7 layer aluminium slab. The zero point for the energy has been chosen for a very large vacuum size. For a vacuum larger than 6 Å the energy is converged to within 10 meV, but in general a larger vacuum will be chosen, because this does not increase the computational demand of the calculations using a localized atomic orbital basis set of finite spatial extent.

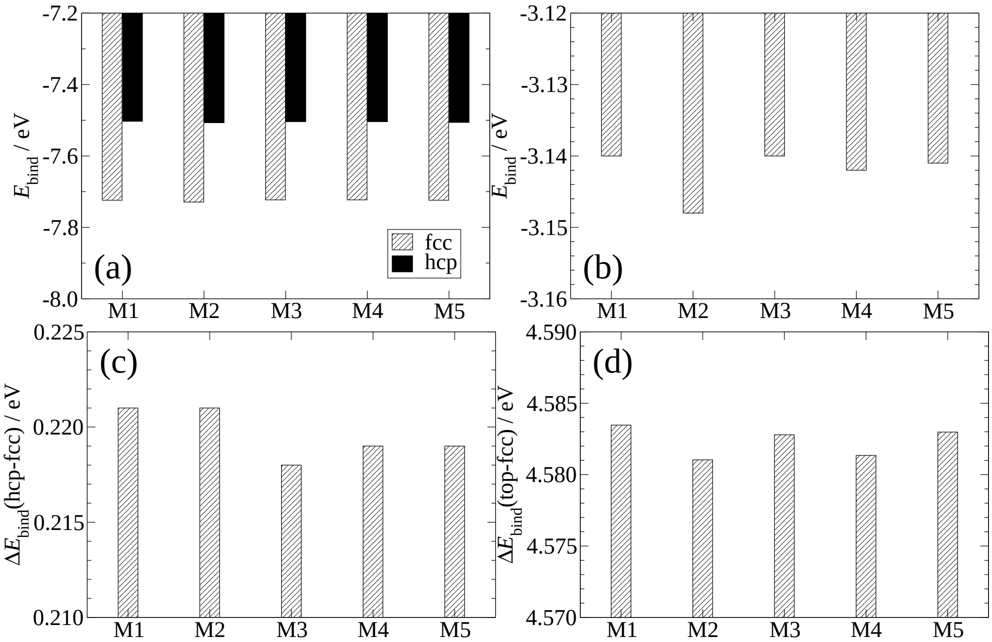

Figure B.5: Determination of the integration mesh required to describe a monolayer of oxygen atoms adsorbed in a (1×1) supercell. In (a) the binding energies for oxygen atoms adsorbed at the fcc and the hcp site are shown for the meshes listed in Table B.1. In (b) the binding energy above the top site is plotted. In (c) the difference between the oxygen binding energy at a fcc site and a hcp site is shown, and in (d) the binding energy difference between the top site and the fcc site is given.

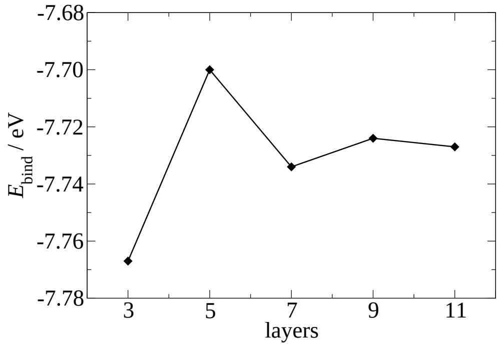

Figure B.6: Binding energy of an oxygen atom adsorbed in the fcc hollow site of a (1×1) slab as a function of the number of aluminium layers in the slab.

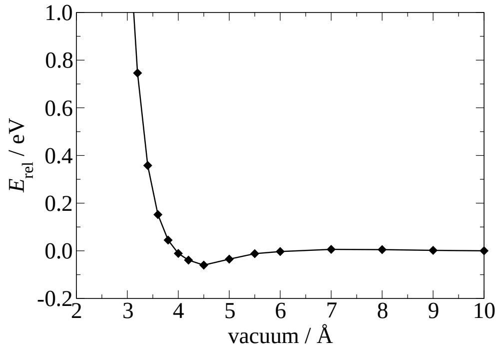

Figure B.7: Total energy of a (1×1) aluminium slab with oxygen adsorbed in the fcc hollow site as a function of the vacuum thickness.

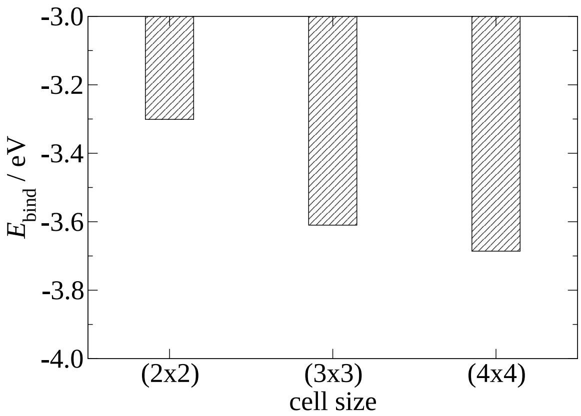

Figure B.8: Convergence of the oxygen binding energy for a molecule oriented parallel to the surface 1.5 Å above an fcc site and a bond length of 2.4 Å as a function of the supercell size.

B.4 Al(3×3) Slabs

The determination of accurate but efficient parameters for the calculation of the oxygen binding energies in the (3×3) supercell employed for the mapping of the potential-energy surface is of particular importance, because many thousand calculations will be performed with this parameter set.

To investigate the adsorption process of a single oxygen molecule, lateral interactions between the oxygen molecule and its periodic images have to be avoided by choosing a large enough supercell. The strongest interactions can be expected when the molecule is oriented parallel to the surface with a bond length of 2.4 Å, which is the largest bond length that is employed in the calculation of the potential-energy surfaces. For a molecule located 1.5 Å above an fcc site parallel to the surface (geometry 3 in Appendix C) the binding energy has been calculated for several supercells of different size. The calculations have been carried out using the same basis set parameters as for the calculations of the (1×1) slabs and a 4×4×1 k-point mesh employing the PBE functional. The obtained binding energies are shown in Fig. B.8 as a function of the supercell size. While for this molecular geometry remarkable lateral interactions are still present in a (2×2) cell, the change in binding energy between a (3×3) and a (4×4) supercell is only about 70 meV even for this extremely stretched oxygen molecule. Therefore a (3×3) slab is large enough to model accurately the potential-energy surface, the most important parts of which will have a far smaller remaining interaction due to a shorter oxygen-oxygen bond length.

While the required number of aluminium layers in the slab is not expected to differ from the oxygen-covered (1×1) slabs tested above, the vacuum size has to be chosen large enough to allow for the mapping of the potential-energy surface also for very large molecule-surface separations up to 10 Å. The required vacuum thickness depends on two interactions, first the interaction of the oxygen molecule with the surface and second the interaction between two oxygen molecules in neighbored slabs through the vacuum due to the inversion symmetry of the system. As can be seen in Fig. 13.4 in case of the adiabatic potential-energy surface the energy only asymptotically reaches a constant value, when the molecule-surface separation is increased. This is due to the charge transfer from the metal to the molecule described in Chapter 10. At a molecule-surface separation of 10 Å the remaining interaction is sufficiently small (below 20 meV). Therefore, the required vacuum size due to the molecule-surface separation on both sides of the slab is 20 Å in total. The remaining interaction between the two oxygen molecules through the vacuum can be described to an excellent approximation by the interaction between two free oxygen molecules. This is because the two oxygen molecules in the neighbored supercells are closest when their distance to the surface is largest, i.e. when the charge transfer is very small. The energy of a system of two interacting oxygen molecules is shown in Fig. B.9 as a function of the center of mass distance of the molecules. Both molecules have the equilibrium bond length of 1.224 Å of the free molecule and their bonds have been aligned to minimize the distance of the closest atoms for a given center of mass distance. The calculations have been done using a basis function cutoff of 9 bohr, an *all* basis and the PBE functional, i.e. under the same conditions as the potential-energy surface. Periodic boundary conditions have not been applied. As can be seen, the interaction becomes negligible at a center of mass separation of 6 Å. Therefore, a total vacuum thickness of 30 Å between the aluminium slabs should be absolutely sufficient for the calculation of the potential-energy surface for molecule-surface separations of up to 10 Å.

The convergence of the binding energy of an oxygen molecule in a (3×3) supercell as a function of the calculational parameters is expected to be very similar to the (1×1) cells. Nevertheless, due to the fundamental importance of these parameters for the mapping of the potential-energy surface, the convergence has been tested using two different molecular configurations, (d=2.4 Å, Z=1.5 Å) and (d=1.0 Å, Z=1.7 Å), for a molecule parallel to the surface above an fcc site (geometry 3 in Appendix C). In Fig. B.11 the basis set test is shown. Fig. B.10 illustrates the dependence of the binding energy on the k-point mesh, and Fig. B.12 shows the convergence with respect to the basis function cutoff. In agreement with the tests on the (1×1) slabs a *dnd* basis for aluminium combined with an *all* basis for oxygen, a k-point mesh of 4×4×1 k-points and a basis function cutoff of 9 bohr provide a reliable description of the potential-energy surface for the oxygen dissociation on Al(111).

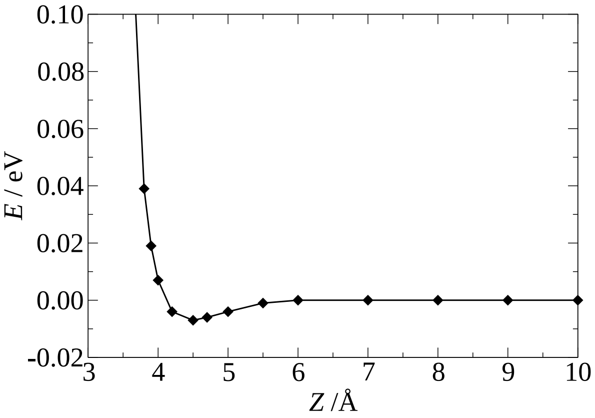

Figure B.9: Convergence of the interaction energy of two neutral oxygen molecules as a function of their center of mass distance.

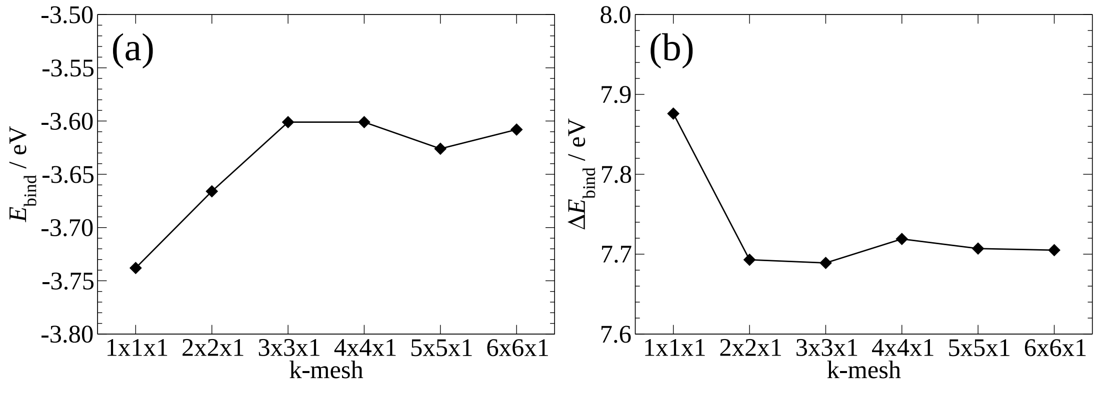

Figure B.10: Convergence of the binding energy of an oxygen molecule with respect to the k-point mesh in a (3×3) cell. In (a) the binding energy of an oxygen molecule parallel to the surface (d=2.4 Å, Z=1.5 Å, geometry 3 in Appendix C) above an fcc site is shown. In (b) the binding energy difference between two different configurations (E(d=1.0 Å, Z=1.7 Å)-E(d=2.4 Å, Z=1.5 Å)) is plotted.

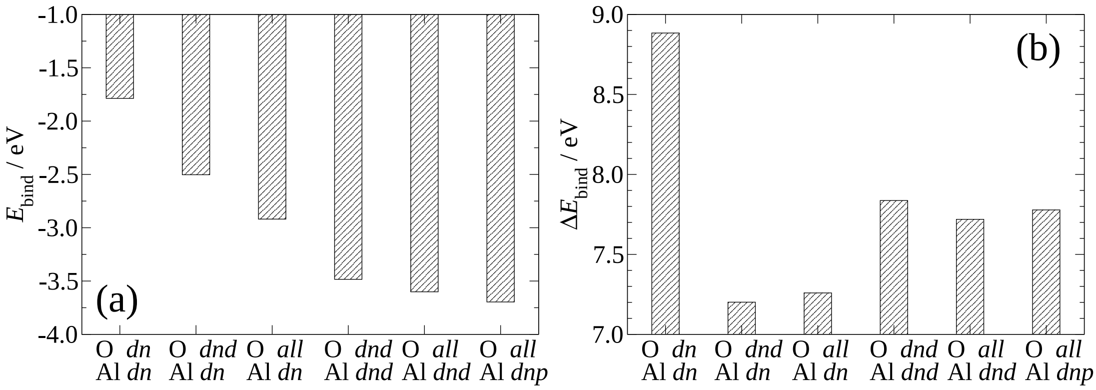

Figure B.11: Convergence of the binding energy of an oxygen molecule in a (3×3) supercell with respect to the basis sets chosen for the description of the oxygen and aluminium atoms. In (a) the binding energy of an oxygen molecule parallel to the surface (d=2.4 Å, Z=1.5 Å, geometry 3 in Appendix C) above an fcc site is shown. In (b) the binding energy difference between two different configurations (E(d=1.0 Å, Z=1.7 Å)-E(d=2.4 Å, Z=1.5 Å)) is plotted.

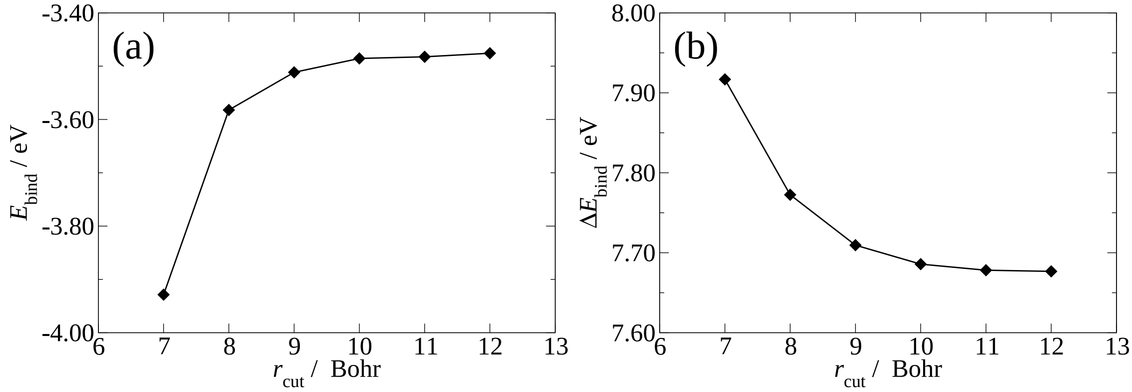

Figure B.12: Convergence of the binding energy of an oxygen molecule in a (3×3) supercell with respect to the basis function cutoff. In (a) the binding energy of an oxygen molecule parallel to the surface (d=2.4 Å, Z=1.5 Å, geometry 3 in Appendix C) above an fcc site is shown. In (b) the binding energy difference between two different configurations (E(d=1.0 Å, Z=1.7 Å)-E(d=2.4 Å, Z=1.5 Å)) is plotted.

Appendix C

Sampling of Potential-Energy Surfaces

For the mapping of the six-dimensional potential-energy surfaces of various spin states elbow plots have been calculated for 38 different molecular orientations. The geometries are listed below. The coordinates refer to Fig. 8.2. The top view shows only a few of the surface atoms of the (3×3) supercells that have been used in the calculations. Taking into account the symmetry of the surface these orientations cover the full orientational configuration space for all combinations of θ and ϕ in 30° steps above the top, fcc and hcp sites. Due to its reduced symmetry, not all of these combinations are covered in case of the bridge site.

Geometry 1

$$\begin{aligned} X/a &= 0.5 \\ Y/a &= 1/(2\cdot\sqrt{3}) \\ \theta &= 0^\circ \\ \phi &= 0^\circ \end{aligned}$$

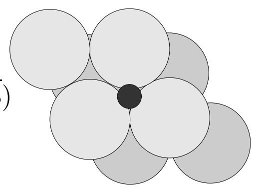

Geometry 2

$$\begin{aligned} X/a &= 0.5 \\ Y/a &= 1/(2\cdot\sqrt{3}) \\ \theta &= 90^\circ \\ \phi &= 30^\circ \end{aligned}$$

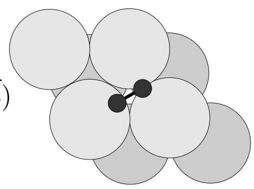

Geometry 3

$$\begin{aligned} X/a &= 0.5 \\ Y/a &= 1/(2\cdot\sqrt{3}) \\ \theta &= 90^\circ \\ \phi &= 60^\circ \end{aligned}$$

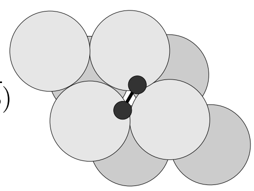

Geometry 4

$$\begin{aligned} X/a &= 0.0 \\ Y/a &= 1/\sqrt{3} \\ \theta &= 0^\circ \\ \phi &= 0^\circ \end{aligned}$$

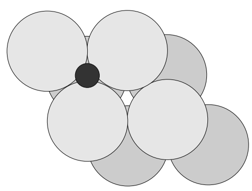

Geometry 5

$$\begin{aligned} X/a &= 0.0 \\ Y/a &= 1/\sqrt{3} \\ \theta &= 90^\circ \\ \phi &= 30^\circ \end{aligned}$$

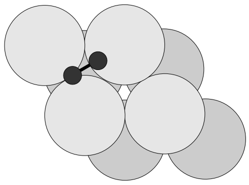

Geometry 6

$$\begin{aligned} X/a &= 0.0 \\ Y/a &= 1/\sqrt{3} \\ \theta &= 90^\circ \\ \phi &= 60^\circ \end{aligned}$$

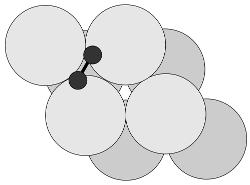

Geometry 7

$$\begin{aligned} X/a &= 0.0 \\ Y/a &= 0.0 \\ \theta &= 0^\circ \\ \phi &= 0^\circ \end{aligned}$$

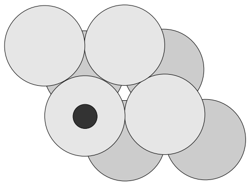

Geometry 8

$$\begin{aligned} X/a &= 0.0 \\ Y/a &= 0.0 \\ \theta &= 90^\circ \\ \phi &= 30^\circ \end{aligned}$$

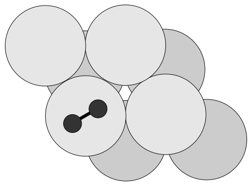

Geometry 9

$$\begin{aligned} X/a &= 0.0 \\ Y/a &= 0.0 \\ \theta &= 90^\circ \\ \phi &= 60^\circ \end{aligned}$$

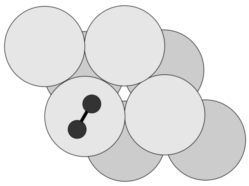

Geometry 10

$$\begin{aligned} X/a &= 0.5 \\ Y/a &= 0.0 \\ \theta &= 0^\circ \\ \phi &= 0^\circ \end{aligned}$$

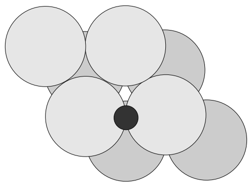

Geometry 11

$$\begin{aligned} X/a &= 0.5 \\ Y/a &= 0.0 \\ \theta &= 90^\circ \\ \phi &= 0^\circ \end{aligned}$$

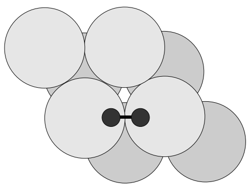

Geometry 12

$$\begin{aligned} X/a &= 0.5 \\ Y/a &= 0.0 \\ \theta &= 90^\circ \\ \phi &= 90^\circ \end{aligned}$$

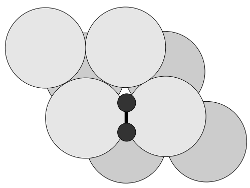

Geometry 13

$$\begin{aligned} X/a &= 0.5 \\ Y/a &= 0.0 \\ \theta &= 90^\circ \\ \phi &= 150^\circ \end{aligned}$$

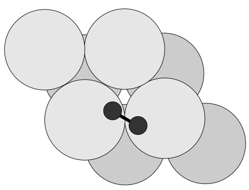

Geometry 14

$$\begin{aligned} X/a &= 0.5 \\ Y/a &= 0.0 \\ \theta &= 90^\circ \\ \phi &= 120^\circ \end{aligned}$$

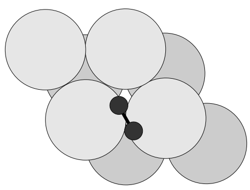

Geometry 15

$$\begin{aligned} X/a &= 0.5 \\ Y/a &= 1/(2\cdot\sqrt{3}) \\ \theta &= 30^\circ \\ \phi &= 210^\circ \end{aligned}$$

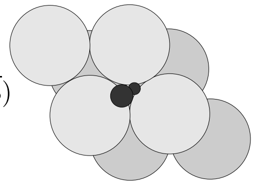

Geometry 16

$$\begin{aligned} X/a &= 0.5 \\ Y/a &= 1/(2\cdot\sqrt{3}) \\ \theta &= 30^\circ \\ \phi &= 30^\circ \end{aligned}$$

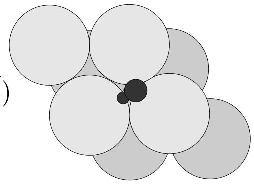

Geometry 17

$$\begin{aligned} X/a &= 0.5 \\ Y/a &= 1/(2\cdot\sqrt{3}) \\ \theta &= 30^\circ \\ \phi &= 240^\circ \end{aligned}$$

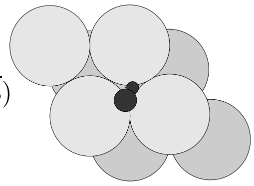

Geometry 18

$$\begin{aligned} X/a &= 0.0 \\ Y/a &= 1/\sqrt{3} \\ \theta &= 30^\circ \\ \phi &= 210^\circ \end{aligned}$$

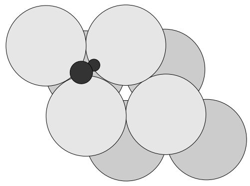

Geometry 19

$$\begin{aligned} X/a &= 0.0 \\ Y/a &= 1/\sqrt{3} \\ \theta &= 30^\circ \\ \phi &= 30^\circ \end{aligned}$$

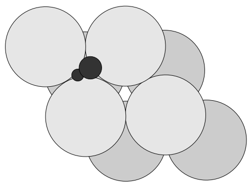

Geometry 20

$$\begin{aligned} X/a &= 0.0 \\ Y/a &= 1/\sqrt{3} \\ \theta &= 30^\circ \\ \phi &= 240^\circ \end{aligned}$$

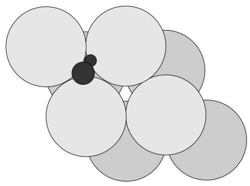

Geometry 21

$$\begin{aligned} X/a &= 0.0 \\ Y/a &= 0.0 \\ \theta &= 30^\circ \\ \phi &= 210^\circ \end{aligned}$$

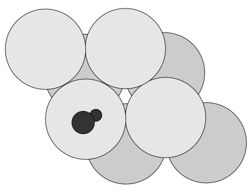

Geometry 22

$$\begin{aligned} X/a &= 0.0 \\ Y/a &= 0.0 \\ \theta &= 30^\circ \\ \phi &= 240^\circ \end{aligned}$$

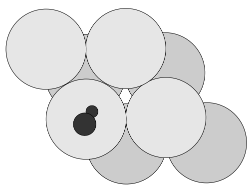

Geometry 23

$$\begin{aligned} X/a &= 0.0 \\ Y/a &= 0.0 \\ \theta &= 30^\circ \\ \phi &= 30^\circ \end{aligned}$$

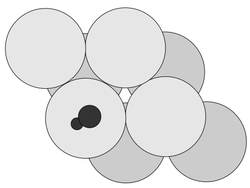

Geometry 24

$$\begin{aligned} X/a &= 0.5 \\ Y/a &= 0.0 \\ \theta &= 30^\circ \\ \phi &= 180^\circ \end{aligned}$$

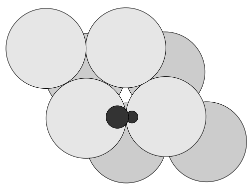

Geometry 25

$$\begin{aligned} X/a &= 0.5 \\ Y/a &= 0.0 \\ \theta &= 30^\circ \\ \phi &= 270^\circ \end{aligned}$$

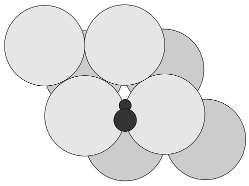

Geometry 26

$$\begin{aligned} X/a &= 0.5 \\ Y/a &= 0.0 \\ \theta &= 30^\circ \\ \phi &= 90^\circ \end{aligned}$$

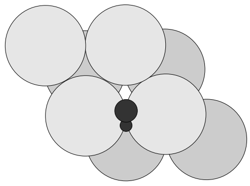

Geometry 27

$$\begin{aligned} X/a &= 0.5 \\ Y/a &= 1/(2 \cdot \sqrt{3}) \\ \theta &= 60^\circ \\ \phi &= 210^\circ \end{aligned}$$

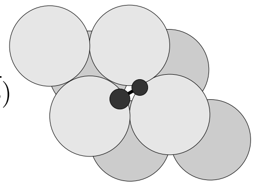

Geometry 28

$$\begin{aligned} X/a &= 0.5 \\ Y/a &= 1/(2 \cdot \sqrt{3}) \\ \theta &= 60^\circ \\ \phi &= 30^\circ \end{aligned}$$

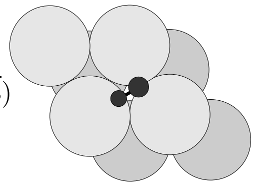

Geometry 29

$$\begin{aligned} X/a &= 0.5 \\ Y/a &= 1/(2 \cdot \sqrt{3}) \\ \theta &= 60^\circ \\ \phi &= 240^\circ \end{aligned}$$

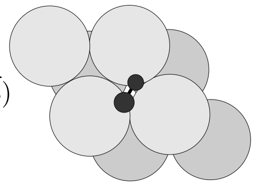

Geometry 30

$$\begin{aligned} X/a &= 0.0 \\ Y/a &= 1/\sqrt{3} \\ \theta &= 60^\circ \\ \phi &= 210^\circ \end{aligned}$$

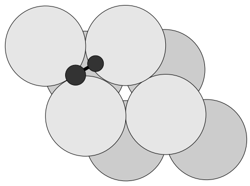

Geometry 31

$$\begin{aligned} X/a &= 0.0 \\ Y/a &= 1/\sqrt{3} \\ \theta &= 60^\circ \\ \phi &= 30^\circ \end{aligned}$$

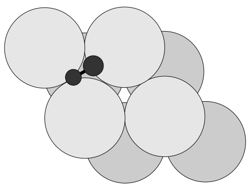

Geometry 32

$$\begin{aligned} X/a &= 0.0 \\ Y/a &= 1/\sqrt{3} \\ \theta &= 60^\circ \\ \phi &= 240^\circ \end{aligned}$$

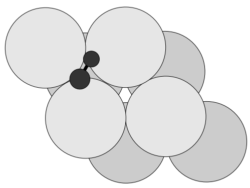

Geometry 33

$$\begin{aligned} X/a &= 0.0 \\ Y/a &= 0.0 \\ \theta &= 60^\circ \\ \phi &= 210^\circ \end{aligned}$$

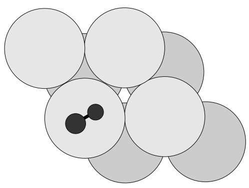

Geometry 34

$$\begin{aligned} X/a &= 0.0 \\ Y/a &= 0.0 \\ \theta &= 60^\circ \\ \phi &= 240^\circ \end{aligned}$$

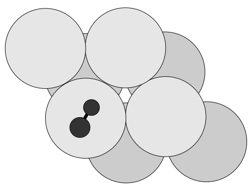

Geometry 35

$$X/a = 0.0$$
$$Y/a = 0.0$$
$$\theta = 60^\circ$$
$$\phi = 30^\circ$$

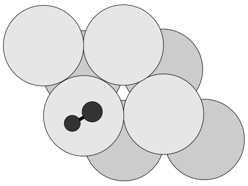

Geometry 36

$$X/a = 0.5$$
$$Y/a = 0.0$$
$$\theta = 60^\circ$$
$$\phi = 180^\circ$$

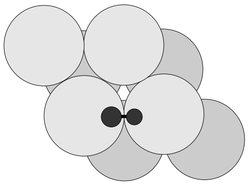

Geometry 37

$$X/a = 0.5$$
$$Y/a = 0.0$$
$$\theta = 60^\circ$$
$$\phi = 270^\circ$$

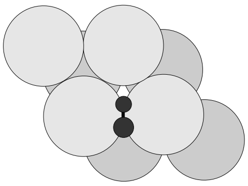

Geometry 38

$$X/a = 0.5$$
$$Y/a = 0.0$$
$$\theta = 60^\circ$$
$$\phi = 90^\circ$$

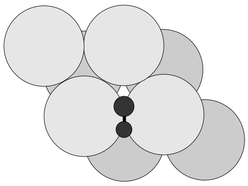

Bibliography

[1] M. Binetti, O. Weisse, E. Hasselbrink, A. J. Komrowski, and A. C. Kummel. *Faraday Diss.* ***117*** (2000), 313.

[2] A. J. Komrowski, J. Z. Sexton, A. C. Kummel, M. Binetti, O. Weisse, and E. Hasselbrink. *Phys. Rev. Lett.* ***87*** (2001), 246103.

[3] M. Schmid, G. Leonardelli, R. Tscheliessnig, A. Biedermann, and P. Varga. *Surf. Sci. Lett.* ***478*** (2001), L355.

[4] A. Kiejna, and B. I. Lundqvist. *Phys. Rev. B* ***63*** (2001), 85405.

[5] H. Brune, J. Wintterlin, R. J. Behm, and G. Ertl. *Phys. Rev. Lett* ***68*** (1992), 624.

[6] P. O. Gartland. *Surf. Sci.* ***62*** (1977), 183.

[7] A. M. Bradshaw, P. Hofmann, and W. Wyrobisch. *Surf. Sci.* ***68*** (1977), 269.

[8] H. Brune, J. Wintterlin, J. Trost, G. Ertl, J. Wiechers, and R. J. Behm. *J. Chem. Phys.* ***99*** (1993), 2128.

[9] L. Österlund, I. Zorić, and B. Kasemo. *Phys. Rev. B* ***55*** (1997), 15452.

[10] V. Zhukov, I. Popova, and J. T. Yates Jr. *J. Vac. Sci. Technol. A* ***17*** (1999), 1727.

[11] V. Zhukov, I. Popova, and J. T. Yates Jr. *Surf. Sci.* ***441*** (1999), 251.

[12] C. S. Lee, and T. M. Lin. *Surf. Sci.* ***471*** (2001), 219.

[13] R. G. Parr, and W. Yang. *Density-Functional Theory of Atoms and Molecules.* Oxford University Press, Oxford, 1989.

[14] R. M. Dreizler, and E. K. U. Gross. *Density Functional Theory.* Springer, Berlin, 1990.

[15] M. Kay, G. R. Darling, S. Holloway, J. A. White, and D. M. Bird. *Chem. Phys. Lett.* ***245*** (1995), 311.

[16] A. Eichler, G. Kresse, and J. Hafner. *Phys. Rev. Lett.* ***77*** (1996), 1119.

[17] A. Gross, S. Wilke, and M. Scheffler. *Phys. Rev. Lett.* ***75*** (1995), 2718.

[18] A. Gross. *Private Communication*.

[19] P. Kratzer, R. Russ, and W. Brenig. *Surf. Sci.* ***345*** (1996), 125.

[20] J. Strömquist, L. Hellberg, B. Kasemo, and B. I. Lundqvist. *Surf. Sci.* ***352-354*** (1996), 435.

[21] G. Katz, Y. Zeiri, and R. Kosloff. *J. Chem. Phys.* ***120*** (2004), 3931.

[22] K. Honkala, and K. Laasonen. *Phys. Rev. Lett.* ***84*** (2000), 705.

[23] D. J. Tozer, and N. C. Handy. *Phys. Chem. Chem. Phys.* ***2*** (2000), 2117.

[24] Y. Yourdshahyan, B. Razaznejad, and B. I. Lundqvist. *Phys. Rev. B* ***65*** (2002), 75416.

[25] M. Born, and J. R. Oppenheimer. *Ann. Phys.* ***84*** (1927), 457.

[26] S. Lorenz. *Reactions on Surfaces with Neural Networks*. PhD thesis, Techn. Universität Berlin, 2001.

[27] S. Lorenz, A. Gross, and M. Scheffler. *Chem. Phys. Lett.* ***395*** (2004), 210.

[28] A. Hellman, B. Razaznejad, Y. Yourdshahyan, H. Ternow, I. Zorić, and B. I. Lundqvist. *Surf. Sci.* ***532-535*** (2003), 126.

[29] G. Katz, Y. Zeiri, and R. Kosloff. *Surf. Sci.* ***425*** (1999), 1.

[30] V. L. Moruzzi, P. M. Marcus, K. Schwarz, and P. Mohn. *Phys. Rev. B* ***34*** (1986), 1784.

[31] H. Duschanek, P. Mohn, and K. Schwarz. *Physica B* ***161*** (1989), 139.

[32] P. M. Marcus, and V. L. Moruzzi. *J. Appl. Phys.* ***63*** (1988), 4045.

[33] P. M. Marcus, and V. L. Moruzzi. *Phys. Rev. B* ***38*** (1988), 6949.

[34] P. H. Dederichs, S. Blügel, R. Zeller, and H. Akai. *Phys. Rev. Lett.* ***53*** (1984), 2512.

[35] M. Kerkar, D. Fisher, D. P. Woodruff, and B. Cowie. *Surf. Sci.* ***271*** (1992), 45.

[36] L. Vitos, A. V. Ruban, H. L. Skriver, and J. Kollar. *Surf. Sci.* ***411*** (1998), 186.

[37] R. Stumpf, and M. Scheffler. *Phys. Rev. B* ***53*** (1996), 4958.

[38] I. P. Batra, and L. Kleinman. *J. Electr. Spec. Rel. Phen.* ***33*** (1984), 175.

[39] V. Zhukov, I. Popova, V. Fomenko, and J. T. Yates Jr. *Surf. Sci.* ***441*** (1999), 240.

[40] C. Berg, S. Raaen, A. Borg, J. N. Andersen, E. Lundgren, and R. Nyholm. *Phys. Rev. B* ***47*** (1993), 13063.

[41] S. A. Flodström, C. W. B. Martinsson, R. Z. Bachrach, S. B. M. Hagström, and R. S. Bauer. *Phys. Rev. Lett.* ***40*** (1978), 907.

[42] W. Eberhardt, and F. J. Himpsel. *Phys. Rev. Lett.* ***42*** (1979), 1375.

[43] A. Arranz, and C. Palacio. *Surf. Sci.* ***355*** (1996), 203.

[44] J. Stöhr, L. I. Johansson, S. Brennan, M. Hecht, and J. N. Miller. *Phys. Rev. B* ***22*** (1980), 4052.

[45] C. Astaldi, P. Geng, and K. Jacobi. *J. Electr. Spec. Rel. Phen.* ***44*** (1987), 175.

[46] J. G. Chen, J. E. Crowell, and J. T. Yates Jr. *Phys. Rev. B* ***33*** (1986), 1436.

[47] R. L. Strong, B. Firey, F. W. deWette, and J. L. Erskine. *Phys. Rev. B* ***26*** (1982), 3483.

[48] J. L. Erskine, and R. L. Strong. *Phys. Rev. B* ***25*** (1982), 5547.

[49] D. J. O'Connor, E. R. Wouters, A. W. D. van der Gonm, J. F. van der Veen, P. M. Zagwijn, and J. W. M. Frenken. *Surf. Sci.* ***296*** (1993), 131.

[50] D. J. O'Connor, E. R. Wouters, A. W. D. van der Gon, J. Vrijmoeth, P. M. Zagwijn, W. F. J. Slijkerman, J. W. M. Frenken, and J. F. van der Veen. *Surf. Sci.* ***287-288*** (1993), 438.

[51] B. C. Mitrovic, and D. J. O'Connor. *Surf. Sci.* ***405*** (1998), 261.

[52] J. Trost, H. Brune, J. Wintterlin, R. J. Behm, and G. Ertl. *J. Chem. Phys.* ***108*** (1998), 1740.

[53] B. G. Frederick, M. B. Lee, and N. V. Richardson. *Surf. Sci.* ***348*** (348), L71.

[54] P. S. Bagus, C. R. Brundle, F. Illas, F. Parmigiani, and G. Polzonetti. *Phys. Rev. B* ***44*** (1991), 9025.

[55] E. R. Wouters, D. J. O'Connor, J. F. van der Veen, P. M. Zagwijn, J. Vrijmoeth, W. Slijkerman, and J. W. M. Frenken. *Surf. Sci.* ***296*** (1993), 141.

[56] A. Kiejna, and B. I. Lundqvist. *Surf. Sci.* ***504*** (2002), 1.

[57] J. Neve, J. Rundgren, and P. Westrin. *J. Phys. C* ***15*** (1982), 4391.

[58] F. Soria, V. Martinez, M. C. Munoz, and J. L. Sacedon. *Phys. Rev. B* ***24*** (1981), 6926.

[59] L. I. Johansson, and J. Stöhr. *Phys. Rev. Lett.* ***43*** (1979), 1882.

[60] D.-S. Wang, A. J. Freeman, and H. Krakauer. *Phys. Rev. B* ***24*** (1981), 3092.

[61] G. Wahnström, A. B. Lee, and J. Strömquist. *J. Chem. Phys.* ***105*** (1996), 326.

[62] C. Engdahl, and G. Wahnström. *Surf. Sci.* ***312*** (1994), 429.

[63] D. E. Oner, R. Chakarova, I. Zoric, and B. Kasemo. *J. Chem. Phys.* ***113*** (2000), 8869.

[64] R. Chakarova, D. E. Oner, I. Zoric, and B. Kasemo. *Surf. Sci.* ***472*** (2001), 63.

[65] M. L. Neuburger, and D. P. Pullman. *J. Chem. Phys.* ***113*** (2000), 1249.

[66] Y. L. Li, D. P. Pullman, J. J. Yang, A. A. Tsekouras, D. B. Gosalvez, K. B. Laughlin, Z. Zhang, M. T. Schulberg, D. J. Gladstone, M. McGonigal, and S. T. Ceyer. *Phys. Rev. Lett.* ***74*** (1995), 2603.

[67] J. Jacobsen, B. Hammer, K. W. Jacobsen, and J. N. Nørskov. *Phys. Rev. B* ***52*** (1995), 14954.

[68] M. Binetti, O. Weisse, E. Hasselbrink, G. Katz, R. Kosloff, and Y. Zeiri. *Chem. Phys. Lett.* ***373*** (2003), 366.

[69] D. A. King, and M. G. Wells. *Surf. Sci.* ***29*** (1972), 454.

[70] T. Sasaki, and T. Ohno. *Surf. Sci.* ***454*** (2000), 337.

[71] T. Sasaki, and T. Ohno. *Surf. Sci.* ***435*** (1999), 172.

[72] T. Sasaki, and T. Ohno. *Phys. Rev. B* ***60*** (1999), 7824.

[73] Y. Yourdshahyan, B. Razaznejad, and B. I. Lundqvist. *Solid State Comm.* ***117*** (2001), 531.

[74] B. Hammer, L. B. Hansen, and J. Nørskov. *Phys. Rev. B* ***59*** (1999), 7413.

[75] O. Gunnarsson, and R. O. Jones. *Phys. Rev. B* ***31*** (1985), 7588.

[76] T. Greber. *Surf. Sci. Rep.* ***28*** (1997), 3.

[77] M. S. Child. *Molecular Collision Theory.* Academic Press, New York, 1974.

[78] C. Zener. *Proc. Roy. Soc. Lond. A* ***137*** (1932), 696.

[79] E. C. G. Stückelberg. *Helv. Phys. Acta* ***5*** (1932), 369.

[80] L. Landau. *Phys. Z. Sowj.* ***1*** (1932), 88.

[81] L. Landau. *Phys. Z. Sowj.* ***2*** (1932), 46.

[82] F. T. Smith. *Phys. Rev.* ***179*** (1969), 111.

[83] H. Nakamura. *Nonadiabatic Transitions.* World Scientific, Singapore, 2002.

[84] G. R. Darling, and S. Holloway. *Rep. Prog. Phys.* ***58*** (1995), 1595.

[85] J. C. Tully. *Ann. Rev. Phys. Chem.* ***51*** (2000), 153.

[86] A. Gross. *Theoretical Surface Science.* Springer, Berlin, 2003.

[87] L. Hellberg, J. Strömquist, B. Kasemo, and B. I. Lundqvist. *Phys. Rev. Lett.* ***74*** (1995), 4742.

[88] A. Böttcher, R. Imbeck, A. Morgante, and G. Ertl. *Phys. Rev. Lett.* ***65*** (1990), 2035.

[89] B. Kasemo. *Phys. Rev. Lett.* ***32*** (1974), 1114.

[90] T. Greber. *Chem. Phys. Lett.* ***222*** (1994), 292.

[91] V. P. Zhdanov. *Phys. Rev. B* ***55*** (1997), 6770.

[92] K. Kato, and T. Uda. *Phys. Rev. B* ***62*** (2000), 15978.

[93] K. Kato, T. Uda, and K. Terakura. *Phys. Rev. Lett.* ***80*** (1998), 2000.

[94] B. Kasemo, E. Törnqvist, J. N. Nørskov, and B. I. Lundqvist. *Surf. Sci.* ***89*** (1979), 554.

[95] M. Bockstedte, A. Kley, J. Neugebauer, and M. Scheffler. *Comp. Phys. Comm.* ***107*** (1997), 187.

[96] R. Car, and M. Parrinello. *Phys. Rev. Lett.* ***55*** (1985), 2471.

[97] A. Gross, M. Bockstedte, and M. Scheffler. *Phys. Rev. Lett.* ***79*** (1997), 701.

[98] D. R. Hartree. *Proc. Camb. Phil. Soc.* ***24*** (1928), 328.

[99] V. A. Fock. *Z. Phys.* ***61*** (1930), 126.

[100] A. Szabo, and N. S. Ostlund. *Modern Quantum Chemistry.* Dover, 1996.

[101] J. A. Pople. *Rev. Mod. Phys.* ***71*** (1999), 1267.

[102] C. Møller, and M. S. Plesset. *Phys. Rev.* ***46*** (1934), 618.

[103] B. O. Roos, and P. R. Taylor. *Chem. Phys.* ***48*** (1980), 157.

[104] W. Koch, and M. C. Holthausen. *A Chemist's Guide to Density Functional Theory.* Wiley-VCH, Weinheim, 2001.

[105] P. Hohenberg, and W. Kohn. *Phys. Rev. B* ***136*** (1964), 864.

[106] E. Fermi. *Nuovo Cimento* ***11*** (1934), 157.

[107] L. H. Thomas. *Proc. Camb. Phil. Soc.* ***23*** (1927), 542.

[108] E. Fermi. *Rend. Accad. Lincei* ***6*** (1927), 602.

[109] P. A. M. Dirac. *Proc. Camb. Phil. Soc.* ***26*** (1930), 376.

[110] W. Kohn, and L. J. Sham. *Phys. Rev. A* ***140*** (1965), 1133.

[111] D. M. Ceperley, and B. J. Alder. *Phys. Rev. Lett.* ***45*** (1980), 566.

[112] S. J. Vosko, L. Wilk, and M. Nusair. *Can. J. Phys.* ***58*** (1980), 1200.

[113] J. P. Perdew, Y. Wang. *Phys. Rev. B* ***45*** (1992), 13244.

[114] J. P. Perdew, K. Burke, and M. Ernzerhof. *Phys. Rev. Lett.* ***77*** (1996), 3865.

[115] M. Ernzerhof, and G. E. Scuseria. *J. Chem. Phys.* ***110*** (1999), 5029.

[116] J. P. Perdew, J. A. Chevary, S. H. Vosko, K. A. Jackson, M. R. Pederson, D. J. Singh, and C. Fiolhais. *Phys. Rev. B* ***46*** (1992), 6671.

[117] L. V. Slipchenko, and A. I. Krylov. *J. Chem. Phys.* ***117*** (2002), 4694.

[118] O. Gunnarsson, and B. I. Lundqvist. *Phys. Rev. B* ***13*** (1976), 4274.

[119] U. von Barth, L. Hedin. *J. Phys. C* ***5*** (1972), 1629.

[120] A. A. Ovchinnikov, C. F. Bender, and J. K. Labanowski. Recent developments and applications of modern density functional theory. Elsevier, Amsterdam, 1996, p. 359.

[121] C. Kittel. *Einführung in die Festkörperphysik.* Oldenbourg, Wien, 1999.

[122] P. E. Blöchl, O. Jepsen, and O. K. Andersen. *Phys. Rev. B* ***49*** (1994), 16223.

[123] E. Penev, P. Kratzer, and M. Scheffler. *J. Chem. Phys.* ***110*** (1999), 3986.

[124] M. Städele, M. Moukara, J. A. Majewski, P. Vogel, and A. Görling. *Phys. Rev. B* ***59*** (1999), 10031.

[125] W. Kohn, Y. Meir, and D. E. Makarov. *Phys. Rev. Lett.* ***80*** (1998), 4153.

[126] E. Hult, H. Rydberg, B. I. Lundqvist, and D. C. Langreth. *Phys. Rev. B* ***59*** (1999), 4708.

[127] T. Bredow, and A. R. Gerson. *Phys. Rev. B* ***61*** (2000), 5194.

[128] D. J. Singh. *Planewaves, Pseudopotentials and the LAPW Method.* Kluwer Academic Press, Boston, 1994.

[129] O. K. Andersen. *Phys. Rev. B* ***12*** (1975), 3060.

[130] O. K. Andersen. *Solid State Comm.* ***13*** (1973), 133.

[131] E. Sjöstedt, L. Nordström, and D. J. Singh. *Solid State Comm.* ***114*** (2000), 15.

[132] G. K. H. Madsen, P. Blaha, K. Schwarz, E. Sjöstedt, and L. Nordström. *Phys. Rev. B* ***64*** (2001), 195134.

[133] B. Delley. *J. Chem. Phys.* ***92*** (1990), 508.

[134] B. Delley. *J. Chem. Phys.* ***113*** (2000), 7756.

[135] B. Delley, and D. E. Ellis. *J. Chem. Phys.* ***76*** (1982), 1949.

[136] P. Blaha, K. Schwarz, G. K. Madsen, D. Kvasnicka, and J. Luitz. *WIEN2k, An Augmented Plane Wave + Local Orbitals Program for Calculating Crystal Properties.* K. Schwarz, Techn. Universität Wien, Austria, 2001. ISBN 3-9501031-1-2.

[137] R. F. W. Bader, and A. D. Bandrauk. *J. Chem. Phys.* ***49*** (1968), 1666.

[138] B. Delley. Modern density functional theory: A tool for chemistry. Elsevier, Amsterdam, 1995, p. 221.

[139] F. L. Hirshfeld. *Theor. Chim. Acta* ***44*** (1977), 129.

[140] A. D. Becke. *J. Chem. Phys.* ***88*** (1988), 2547.

[141] B. Delley. *J. Comp. Chem.* ***17*** (1996), 1152.

[142] V. I. Lebedev. *Zh. Vychisl. Mat. Mat. Fiz.* ***16*** (1976), 293.

[143] V. I. Lebedev. *Zh. Vychisl. Mat. Mat. Fiz.* ***15*** (1975), 48.

[144] V. I. Lebedev. *Sibirsk Mat. Zh.* ***18*** (1977), 132.

[145] P. P. Ewald. *Adv. Phys.* ***64*** (1921), 253.

[146] B. Delley. *J. Phys. Chem.* ***100*** (1996), 6107.

[147] W. H. Press, S. A. Teukolsky, W. T. Vetterling, and B. P. Flannery. *Numerical Recipes in Fortran 77.* Cambridge University Press, 1992.

[148] J. Harris. *Phys. Rev. B* ***31*** (1985), 1770.

[149] B. Delley, D. E. Ellis, A. J. Freeman, E. J. Baerends, and D. Post. *Phys. Rev. B* ***27*** (1983), 2132.

[150] I. J. Robertson, and B. Farid. *Phys. Rev. Lett.* ***66*** (1991), 3265.

[151] B. Farid, V. Heine, G. E. Engel, and I. J. Robertson. *Phys. Rev. B* ***48*** (1993), 11602.

[152] B. Delley. *J. Chem. Phys.* ***94*** (1991), 7245.

[153] R. P. Feynman. *Phys. Rev.* ***56*** (1939), 340.

[154] P. Pulay. *Mol. Phys.* ***17*** (1969), 197.

[155] D. D. Koelling, and B. N. Harmon. *J. Phys. C* ***10*** (1977), 3107.

[156] T. Takeda. *Z. Phys.* ***32*** (1978), 43.

[157] B. Delley. *Int. J. Quant. Chem.* ***69*** (1998), 423.

[158] P. Csaszar, and P. Pulay. *J. Mol. Struct.* ***114*** (1984), 31.

[159] P. Pulay. *Chem. Phys. Lett.* ***73*** (1980), 393.

[160] D. R. Bowler, and M. J. Gillan. *Chem. Phys. Lett.* ***325*** (2000), 473.

[161] J. Baker. *J. Comp. Chem.* ***7*** (1986), 385.

[162] J. Baker, and D. Bergeron. *J. Comp. Chem.* ***14*** (1993), 1339.

[163] M. D. Allen, and D. J. Tildesley. *Computer Simulation of Liquids.* Oxford University Press, Oxford, 1989.

[164] B. Delley. *Phys. Rev. B* ***66*** (2002), 155125.

[165] B. Delley. *Comp. Mat. Sci.* ***17*** (2000), 122.

[166] D. F. R. Brown, M. N. Gibbs, and D. C. Clary. *J. Chem. Phys.* ***105*** (1996), 7597.

[167] C. Crespos, M. A. Collins, E. Pijper, and G. J. Kroes. *Chem. Phys. Lett.* ***376*** (2003), 566.

[168] J. Hertz, A. Krogh, and R. G. Palmer. *Introduction to the Theory of Neural Computation.* Addison-Wesley, Reading, 1991.

[169] R. Rojas. *Theorie der Neuronalen Netze.* Springer, Heidelberg, 1996.

[170] D. E. Makarov, and H. Metiu. *J. Chem. Phys.* ***108*** (1998), 590.

[171] T. Klüner, H.-J. Freund, V. Staemmler, and R. Kosloff. *Phys. Rev. Lett.* ***80*** (1998), 5208.

[172] A. Gross, and M. Scheffler. *Phys. Rev. B* ***57*** (1998), 2493.

[173] G. Wiesenekker, G. J. Kroes, and E. J. Baerends. *J. Chem. Phys.* ***104*** (1996), 7344.

[174] C. M. Wei, A. Gross, and M. Scheffler. *Phys. Rev. B* ***57*** (1998), 15572.

[175] G. Kresse. *Phys. Rev. B* ***62*** (2000), 8295.

[176] H. F. Busnengo, A. Salin, and W. Dong. *J. Chem. Phys.* ***112*** (2000), 7641.

[177] C. Crespos, H. F. Busnengo, W. Dong, and A. Salin. *J. Chem. Phys.* ***114*** (2001), 10954.

[178] H. F. Busnengo, E. Pijper, M. F. Somers, G. J. Kroes, A. Salin, R. A. Olsen, D. Lemoine, and W. Dong. *Chem. Phys. Lett.* ***356*** (2002), 515.

[179] R. A. Olsen, H. F. Busnengo, A. Salin, M. F. Somers, G. J. Kroes, and E. J. Baerends. *J. Chem. Phys.* ***116*** (2002), 3841.

[180] A. Gross, M. Scheffler, M. J. Mehl, and D. Papaconstantopoulos. *Phys. Rev. Lett.* ***82*** (1999), 1209.

[181] A. Gross, A. Eichler, J. Hafner, M. J. Mehl, and D. A. Papaconstantopoulos. *Surf. Sci.* ***539*** (2003), L542.

[182] M. J. Mehl, and D. A. Papaconstantopoulos. *Phys. Rev. B* ***54*** (1996), 4519.

[183] R. E. Cohen, M. J. Mehl, and D. A. Papaconstantopoulos. *Phys. Rev. B* ***50*** (1994), 14694.

[184] M. S. Daw, and M. I. Baskes. *Phys. Rev. B* ***29*** (1984), 6443.

[185] M. S. Daw, S. M. Foiles, and M. I. Baskes. *Mat. Sci. Rep.* ***9*** (1993), 251.

[186] M. S. Daw, and M. I. Baskes. *Phys. Rev. Lett.* ***50*** (1983), 1285.

[187] M. I. Baskes. *Phys. Rev. Lett.* ***59*** (1987), 2666.

[188] B. Lehner, T. Hammerschmidt, K. Reuter, and M. Scheffler. *To be published.*

[189] W. S. McCulloch, and W. Pitts. *Bull. Math. Biophys.* ***5*** (1943), 115.

[190] F. Rosenblatt. *Psychol. Rev.* ***65*** (1958), 386.

[191] Y. Le Cun, L. D. Jackel, B. Boser, J. S. Denker, H. P. Graf, I. Guyon, D. Henderson, R. E. Howard, and W. Hubbard. *IEEE Comm. Mag.* ***27*** (1989), 41.

[192] M. T. Leung, W. E. Engeler, and P. Frank. Fingerprint processing using backpropagation neural networks. In *Proceedings of the International Joint Conference on Neural Networks I* (1990), p. 15.

[193] W. G. Baxt. *Neural Comp.* ***2*** (1990), 480.

[194] T. J. Sejnowski, B. P. Yuhas, M. H. Goldstein Jr., and R. E. Jenkins. *Adv. Neur. Inf. Proc. Sys.* ***2*** (1990), 232.

[195] J. M. Hutchinson. *A Radial Basis Function Approach to Financial Time Series Analysis.* PhD thesis, Massachusetts Institute of Technology, 1994.

[196] J. W. Shavlik, G. G. Towell, and M. O. Noordewier. *Int. J. Gen. Res.* ***1*** (1992), 81.

[197] C. F. Allex, J. W. Shavlik, and F. R. Blattner. *Bioinformatics* ***15*** (1999), 723.

[198] N. Qian, T. J. Sejnowski. *J. Mol. Biol.* ***202*** (1988), 865.

[199] G. Cybenko. *Math. Contr. Sign. Sys.* ***2*** (1989), 303.

[200] K. Hornik, M. Stinchcombe, and H. White. *Neural Networks* ***2*** (1989), 359.

[201] T. B. Blank, S. D. Brown, A. W. Calhoun, and D. J. Doren. *J. Chem. Phys.* ***103*** (1995), 4129.

[202] T. B. Blank, and S. D. Brown. *J. Chemometrics* ***8*** (1994), 391.

[203] R. E. Kalman. *J. Bas. Eng.* ***82*** (1960), 35.

[204] A. Gelb. *Applied Optimal Estimation.* MIT Press, Cambridge, 1974.

[205] D. P. Bertsekas. *SIAM J. Opt.* ***6*** (1996), 807.

[206] K. Watanabe, and S. G. Tzafestas. *J. Intel. Robot. Sys.* ***3*** (1990), 305.

[207] S. Haykin, A. H. Sayed, J. Zeidler, P. Yee, and P. Wei. *IEEE Trans. Sign. Proc.* ***45*** (1997), 1118.

[208] S. Haykin, P. Yee, and E. Derbez. *IEEE Trans. Sign. Proc.* ***45*** (1997), 2774.

[209] L. Salem, and C. Rowland. *Angew. Chem. Int. Ed.* ***11*** (1972), 92.

[210] G. Herzberg. *Molecular Spectra and Molecular Structure, I. Spectra of Diatomic Molecules.* van Nostrand Reinhold Company, New York, 1950.

[211] J. Gräfenstein, and D. Cremer. *Phys. Chem. Chem. Phys.* ***2*** (2000), 2091.

[212] M. Filatov, and S. Shaik. *J. Chem. Phys.* ***110*** (1999), 116.

[213] T. Ziegler, A. Rauk, and E. J. Baerends. *Theor. Chim. Acta* ***43*** (1977), 261.

[214] U. von Barth. *Phys. Rev. A* ***20*** (1979), 1693.

[215] O. Gunnarsson, and R. O. Jones. *J. Chem. Phys.* ***72*** (1980), 5357.

[216] R. O. Jones, and O. Gunnarsson. *Rev. Mod. Phys.* ***61*** (1989), 689.

[217] A. Eichler, and J. Hafner. *Phys. Rev. Lett.* ***79*** (1997), 4481.

[218] S. Y. Liem, J. H. R. Clarke, and G. Kresse. *Surf. Sci.* ***459*** (2000), 104.

[219] A. Eichler, F. Mittendorfer, and J. Hafner. *Phys. Rev. B* ***62*** (2000), 4744.

[220] P. M. W. Gill, B. G. Johnson, J. A. Pople, and M. J. Frisch. *Int. J. Quant. Chem. Suppl.* ***26*** (1992), 319.

[221] D. Feller, and K. A. Peterson. *J. Chem. Phys.* ***110*** (1999), 8384.

[222] D. Feller, and K. A. Peterson. *J. Chem. Phys.* ***108*** (1998), 154.

[223] A. F. Holleman, and E. Wiberg. *Lehrbuch der Anorganischen Chemie.* de Gruyter, Berlin, 1995.

[224] G. Herzberg. *Can. J. Phys.* ***30*** (1952), 185.

[225] R. C. Weast, Ed. *CRC Handbook of Chemistry and Physics*, 67th ed. CRC Press, Boca Raton, Florida, 1987.

[226] L. A. Curtiss, K. Raghavachari, P. C. Redfern, and J. A. Pople. *J. Chem. Phys.* ***106*** (1997), 1063.

[227] B. G. Johnson, P. M. W. Gill, and J. A. Pople. *J. Chem. Phys.* ***98*** (1993), 5612.

[228] M. V. Ganduglia-Pirovano, and M. Scheffler. *Phys. Rev. B* ***59*** (1999), 15533.

[229] Y. Zhang, and W. Yang. *Phys. Rev. Lett.* ***80*** (1998), 890.

[230] A. Badinski. Electronic correlation calculations of small molecules with quantum monte carlo methods. Master's thesis, Techn. Universität Berlin, 2004.

[231] J. C. Grossman. *J. Chem. Phys.* ***117*** (2002), 1434.

[232] J. Andzelm, and E. Wimmer. *J. Chem. Phys.* ***96*** (1992), 1280.

[233] A. A. Ovchinnikov, and J. K. Labanowski. *Phys. Rev. A* ***53*** (1996), 3946.

[234] W. J. Hehre, L. Radom, P. v. R. Schleyer, and J. A. Pople. *Ab Initio Molecular Orbital Theory.* Wiley, New York, 1986.

[235] A. D. Becke. *Phys. Rev. A* ***38*** (1988), 3098.

[236] D. C. Sorescu, K. D. Jordan, and P. Avouris. *J. Phys. Chem. B* ***105*** (2001), 11227.

[237] S.-P. Chan, G. Chen, X. G. Gong, and Z.-F. Liu. *Phys. Rev. Lett.* ***90*** (2003), 86403.

[238] K. Yamaguchi, F. Jensen, A. Dorigo, and K. N. Houk. *Chem. Phys. Lett.* ***149*** (1988), 537.

[239] B. F. Minaev, and V. A. Minaeva. *Phys. Chem. Chem. Phys.* ***3*** (2001), 720.

[240] J. M. Wittbrodt, and H. B. Schlegel. *J. Chem. Phys.* ***105*** (1996), 6574.

[241] T. Ziegler. Local density approximations in quantum chemistry and solid state physics. Plenum Press, New York, 1984, p. 273.

[242] J. C. Slater. *Adv. Quantum Chem.* ***6*** (1972), 1.

[243] F. D. Murnaghan. *Proc. Nat. Acad. Sci.* ***30*** (1944), 244.

[244] U. Scherz. *Quantenmechanik.* Teubner, Stuttgart, 1999.

[245] M. Fuchs, M. Bockstedte, E. Pehlke, and M. Scheffler. *Phys. Rev. B* ***57*** (1998), 2134.

[246] A. D. Corso, A. Pasquarello, and A. Baldereschi. *Phys. Rev. B* ***53*** (1996), 1180.

[247] H. B. Nielsen, and D. L. Adams. *J. Phys. C* ***15*** (1982), 615.

[248] J. R. Noonan, and H. L. Davis. *J. Vac. Sci. Techn.* ***8*** (1990), 2671.

[249] F. Jona, D. Sondericker, and P. M. Marcus. *J. Phys. C* ***13*** (1980), L155.

[250] C. J. Fall, N. Binggeli, and A. Baldereschi. *Phys. Rev. B* ***58*** (1998), R7544.

[251] W. R. Tyson, and W. A. Miller. *Surf. Sci.* ***62*** (1977), 267.

[252] W. Wawra. *Z. Metallkunde* ***66*** (1975), 395.

[253] F. R. de Boer, R. Boom, W. C. M. Mattens, A. R. Miedema, and A. K. Niessen. *Cohesion in Metals.* Elsevier, Amsterdam, 1988.

[254] H. L. Skriver, and N. M. Rosengaard. *Phys. Rev. B* ***46*** (1992), 7157.

[255] H. M. Polatoglou, M. Methfessel, and M. Scheffler. *Phys. Rev. B* ***48*** (1993), 1877.

[256] J. K. Grepstad, P. O. Gartland, and B. J. Slagsvold. *Surf. Sci.* ***57*** (1976), 348.

[257] K. Mednick, and L. Kleinman. *Phys. Rev. B* ***22*** (1980), 5768.

[258] F. Wagner, T. Laloyaux, and M. Scheffler. *Phys. Rev. B* ***57*** (1998), 2102.

[259] J. Neugebauer, and M. Scheffler. *Phys. Rev. B* ***46*** (1992), 16067.

[260] C. G. Broyden. *Math. Comp.* ***19*** (1965), 557.

[261] M. Kawata, C. M. Cortis, and R. A. Friesner. *J. Chem. Phys.* ***108*** (1998), 4426.

[262] D. D. Johnson. *Phys. Rev. B* ***38*** (1988), 12807.

[263] G. P. Srivastava. *J. Phys. A* ***17*** (1984), L317.

[264] J. P. Perdew. *Phys. Rev. B* ***33*** (1986), 8822.

[265] R. S. Mulliken. *J. Chem. Phys.* ***23*** (1955), 1833.

[266] A. C. Becker, U. Schurath, H. Dubost, and J. P. Galaup. *Chem. Phys.* ***125*** (1988), 321.

[267] L. C. Ciacchi, and M. C. Payne. *Phys. Rev. Lett.* ***92*** (2004), 176104.

[268] A. Hellman, B. Razaznejad, and B. I. Lundqvist. *J. Chem. Phys.* ***120*** (2004), 4593.

[269] A. Hellman et al. *To be published*.

[270] A. Hellman. *Electron Transfer and Molecular Dynamics at Metal Surfaces.* PhD thesis, Chalmers, Göteborg University, 2003.

[271] B. Ujfalussy, X.-D. Wang, D. M. C. Nicholson, W. A. Shelton, G. M. Stocks, Y. Wang, and B. L. Gyorffy. *J. Appl. Phys.* ***85*** (1999), 4824.

[272] K. Schwarz, P. Mohn. *J. Phys. F* ***14*** (1984), L129.

[273] M. Head-Gordon, P. E. Maslen, and C. A. White. *J. Chem. Phys.* ***108*** (1998), 616.

[274] E. Artacho, L. M. del Bosch. *Phys. Rev. A* ***43*** (1991), 5770.

[275] D. C. Patton, and M. R. Pederson. *Phys. Rev. A* ***56*** (1997), R2495.

[276] M. Scheffler. *Private Communication.*

[277] M. Scheffler. *Bull. Am. Phys. Soc.* ***49*** (2004), 1124.

[278] R. J. Celotta, R. A. Bennett, J. L. Hall, M. W. Siegel, and J. Levine. *Phys. Rev. A* ***6*** (1972), 631.

[279] B. Hammer. *Surf. Sci.* ***459*** (2000), 323.

[280] A. Eichler, and J. Hafner. *Chem. Phys. Lett.* ***343*** (2001), 383.

[281] W. Wurth, J. Stöhr, P. Feulner, X. Pan, K. R. Bauchspiess, Y. Baba, E. Hudel, G. Rocker, and D. Menzel. *Phys. Rev. Lett.* ***65*** (1990), 2426.

[282] D. C. Langreth, and P. Nordlander. *Phys. Rev. B* ***43*** (1991), 2541.

[283] J. C. Tully. *Farad. Disc.* ***110*** (1998), 407.

[284] D. S. Sholl, and J. C. Tully. *J. Chem. Phys.* ***109*** (1998), 7702.

[285] Y. Huang, C. T. Rettner, D. J. Auerbach, and A. M. Wodtke. *Science* ***290*** (2000), 111.

[286] M. Fuchs, J. L. F. Da Silva, C. Stampfl, J. Neugebauer, and M. Scheffler. *Phys. Rev. B* ***65*** (2002), 245212.

Acknowledgements

This thesis would not have been possible at all without the help and support of many people. First of all, I would like to thank my supervisor Matthias Scheffler for the chance to work on a challenging project in a very nice and stimulating environment, for his continuous support and advice and for making me feel home in the surface science community by giving me the opportunity to get in contact with so many people in this field, in Berlin as well as at many conferences. A special thanks also goes to Karsten Reuter for solving all the small and big problems that appear on the way to a PhD. He always took the time to help and taught me how science really works. I could not have imagined having a better advisor and mentor for my PhD. He almost succeeded in turning a chemist into a physicist, but I also met people calling him a chemist now.

For the nice time at the Fritz-Haber Institut, which is not yet over, I like to thank all my colleagues and friends, in particular Mira Todorova, Jutta Rogal, Cesar Lazo, Bernhard Lehner, Volker Blum and all other members of the theory department, which are too many to mention, as well as my past and present office mates Maria Elena Grillo, Alexander Badinski and Alexander Kleinsorge.

For valuable discussions I am indebted to Martin Fuchs, Peter Kratzer, Patrick Rinke, Klaus Hermann, Johan Carlsson, Youngho Shin, Christoph Friedrich and Sixten Boeck. Furthermore, I would like to gratefully acknowledge the advice of Bernard Delley. Without our countless discussions on many practical aspects of the DMol^3 code the implementation of the spin-constraint would have been a much harder task. A special thanks also goes to Sönke Lorenz for introducing me into the neural network technique and for sharing his enormous experience in fitting energy surfaces. Furthermore, I appreciated discussions with Axel Groß, Eckhardt Hasselbrink, Bengt Lundqvist, Mats Persson, Stephen Holloway, Andy Kummel, and Anders Hellman. I really enjoyed also the opportunity to participate in another very interesting project mainly carried out by Christian Ratsch reminding me that the periodic table is more than just oxygen and aluminium.

Additionally, I would like to thank the members of the committee at the Technical University of Berlin, Eckehard Schöll and Christian Thomsen, for taking the time for the exam and for reading this thesis.

Last not least, the biggest thanks goes to Alexandra and my family for their encouragement, support, endless patience and for forgiving me spending so much time in front of a computer screen.